NUCLEAR SPECTROSCOPY WITH THE IN-MEDIUM SIMILARITY RENORMALIZATION GROUP

By

Nathan Michael Parzuchowski

A DISSERTATION

Submitted to
Michigan State University
in partial fulfillment of the requirements
for the degree of

Physics – Doctor of Philosophy

2017

ABSTRACT

NUCLEAR SPECTROSCOPY WITH THE IN-MEDIUM SIMILARITY RENORMALIZATION GROUP

By

Nathan Michael Parzuchowski

The in-medium similarity renormalization group (IMSRG) is an *ab initio* many-body method which features soft polynomial scaling with system size and a Hermitian framework to create Hamiltonians tailored for use with low-level approximations such as Hartree-Fock (HF) theory or the random phase approximation (RPA). The flexibility that comes with these characteristics has made the IMSRG a mainstay in contemporary nuclear structure theory. However, spectroscopy with IMSRG calculations has been limited to scalar observables in nuclei accessible with shell model machinery, where the IMSRG is used to construct effective valence-space interactions.

In this thesis, we present two novel developments which have greatly extended the IMSRG's capability to perform spectroscopic calculations. First is the introduction of the equations-of-motion IMSRG (EOM-IMSRG), which uses an approximate, but systematically improvable diagonalization scheme in conjunction with the IMSRG to produce spectra and wave functions. The method does not suffer the model-space limitations of the shell model, but sacrifices some accuracy due to the approximate diagonalization. We benchmark this new method with the well established equations-of-motion coupled cluster and full configuration interaction methods, where we demonstrate that the method is indeed viable for closed-shell systems, encouraging expansion to open shells using a multireference formalism. We also introduce a perturbative framework to add systematic corrections to the EOM-IMSRG, showing results for closed shell nuclei and quantum dots.

The second development is a generalized effective operator formalism for the IMSRG, capable of consistently evolving non-scalar operators relevant for electroweak transitions and moments. This general framework is applicable to both the EOM-IMSRG and the valence-space IMSRG approaches. We benchmark electromagnetic transition strengths and moments using both of these methods, also comparing with the quasi-exact no-core shell model and experiment when available.

We demonstrate that consistent renormalization of observables is critical for precise computations with the IMSRG. We find that our methods perform well for transitions that are strongly single particle in nature, but for collective transitions involving many particles, we note that work remains to properly incorporate these effects in the IMSRG.

"...I must earnestly entreat both the patience and attention of the reader: his patience in order to examine a detail which may perhaps in some places appear unnecessarily tedious; and his attention in order to understand what may, perhaps, after the fullest explication which I am capable of giving of it, appear still in some degree obscure. I am always willing to run some hazard of being tedious in order to be sure that I am perspicuous; and after taking the utmost pains that I can to be perspicuous, some obscurity may still appear to remain upon a subject in its own nature extremely abstracted." - Adam Smith

ACKNOWLEDGMENTS

First and foremost, I would like to say thanks to my family. I want to thank my parents Scott and Mary, for teaching me how to behave like a well adjusted adult with integrity. Thank you also to my siblings Kristen and Kevin for being supportive and inspirational throughout my studies. I would be remiss if I didn't also mention the numerous other family members who have inspired me to care about stuff like physics. If you're related to me and you have bothered to read this, you've probably been a positive influence at some point. Most of all, I want to say thank you to Erica Yurk for being by my side for the whole thing, and never once agreeing with my constant insistence that I wasn't going to graduate. Thank you.

I would also like to thank my academic family. Most importantly my adviser Scott Bogner, who is the finest scientist I know. It has been a pleasure learning how to study physics under his guidance. Thanks also to my committee, Filomena Nunes, Morten Hjorth-Jensen, Piotr Piecuch and Alexandra Gade, who have all provided useful inputs and criticism during my journey. I'm also indebted to Heiko Hergert, Richard Cyburt, Gaute Hagen, Gustav Jansen, Jason Holt, Wayne Repko, Thomas Papenbrock, Carlo Barbieri, and numerous others who have willfully given their time so that I might not fail miserably.

Titus Morris, my predecessor from our group, has been an inspiration to me throughout this process. He is a good friend, a great physicist, and was a worthy adversary in our beloved group meetings. Likewise, Justin Lietz, Sam Novario, Fei Yuan, and Sushant More have been excellent companions in the quests to solve the problems of nuclear physics, and also in the equally worthy quest to distract ourselves from those problems. I should not forget Ragnar Stroberg, who has taught me how to do physics correctly. Thank you.

Finally I want to thank also the other friends that I've had along the way who have encouraged me and made life worth living. There are too many of them to name without forgetting a few and potentially offending them, but if you're reading this, and haven't seen your name yet, you should know that I added this paragraph just for you!

TABLE OF CONTENTS

LIST OF TABLES

LIST OF FIGURES

KEY TO ABBREVIATIONS

CC – coupled cluster

CCSD – coupled cluster with singles and doubles

CI – configuration interaction

COM – center-of-mass

EFT – effective field theory

EOM – equations-of-motion

EOM-CC – equations-of-motion coupled cluster

EOM-IMSRG – equations-of-motion in-medium similarity renormalization group

EM – Entem and Machleidt

EN – Epstein-Nesbet

FCI – full configuration interaction

HF – Hartree-Fock

HO – harmonic oscillator

IMSRG – in-medium similarity renormalization group

IPM – independent particle model

IT-NCSM – importance truncated no-core shell model

LECs – low-energy constants

MBPT – many-body perturbation theory

MP – Møller-Plesset

MR – multireference

NCSM – no-core shell model

NN – nucleon-nucleon

NO2B – normal-ordered two-body

N^2LO – next-to-next-to leading order

N^3LO – next-to-next-to-next-to leading order

PA – particle attached

PR – particle removed

QMC – quantum Monte Carlo

QCD – quantum chromodynamics

RG – renormalization group

RPA – random phase approximation

SCGF – self-consistent Green's function

SRG – similarity renormalization group

TDA – Tamm-Dancoff approximation

VS – valence-space

VS – valence-space in-medium similarity renormalization group

WIMPs – weakly interacting massive particles

WS – Woods-Saxon

3N – three-nucleon

CHAPTER 1

INTRODUCTION

It has been apparent for some time that an important forefront of nuclear theory lies in *ab initio* methods. These are approaches which seek to describe nuclear properties starting from first principles. Over the past fifteen years, we have seen an explosion of applicability for this brand of theory, growing from the lightest nuclei well into the medium-mass region, with contemporary investigations reaching as far as the tin isotopes.

It was not too long ago that the only reliable *ab initio* approaches for nuclear physics were quasi-exact methods such as the no-core shell model (NCSM) [16–18] or quantum Monte Carlo (QMC) [19–21]. At the time, approximate methods were not effectual because nucleon-nucleon potentials designed to reproduce elastic scattering phase shifts often exhibited strong short-range repulsion and tensor forces, which result in significant coupling to high-momentum modes, producing strongly correlated wave functions incapable of a perturbative description. While quasi-exact methods exhibited extraordinary success for nuclei existing in the lightest regions of the *p*-shell, the idea of one day computing a nucleus such as ^{100}Sn, or even a more modest system such as ^{56}Ni, was a veritable pipe dream. The brute-force nature of these quasi-exact methods results in exponential or factorial scaling with system size, and hence even with an optimistic view of Moore's law, the medium-mass region seemed completely inaccessible using only these approaches.

Meanwhile, the field of quantum chemistry enjoyed a much more bountiful array of *ab initio* methods. Along with the quasi-exact methods, chemists had employed approximate, but systematically improvable methods such as many-body perturbation theory (MBPT) and coupled-cluster (CC) theory [11, 22–28]. These methods employ various many-body truncations, where dynamic correlations beyond a certain level are omitted for reasons of computational feasibility. These truncations offer much more favorable polynomial scaling with system size at the expense of some precision. While these approaches were known in nuclear physics [29–31], their many-body truncations were ultimately their undoing in that field, as the highly nonperturbative interactions of

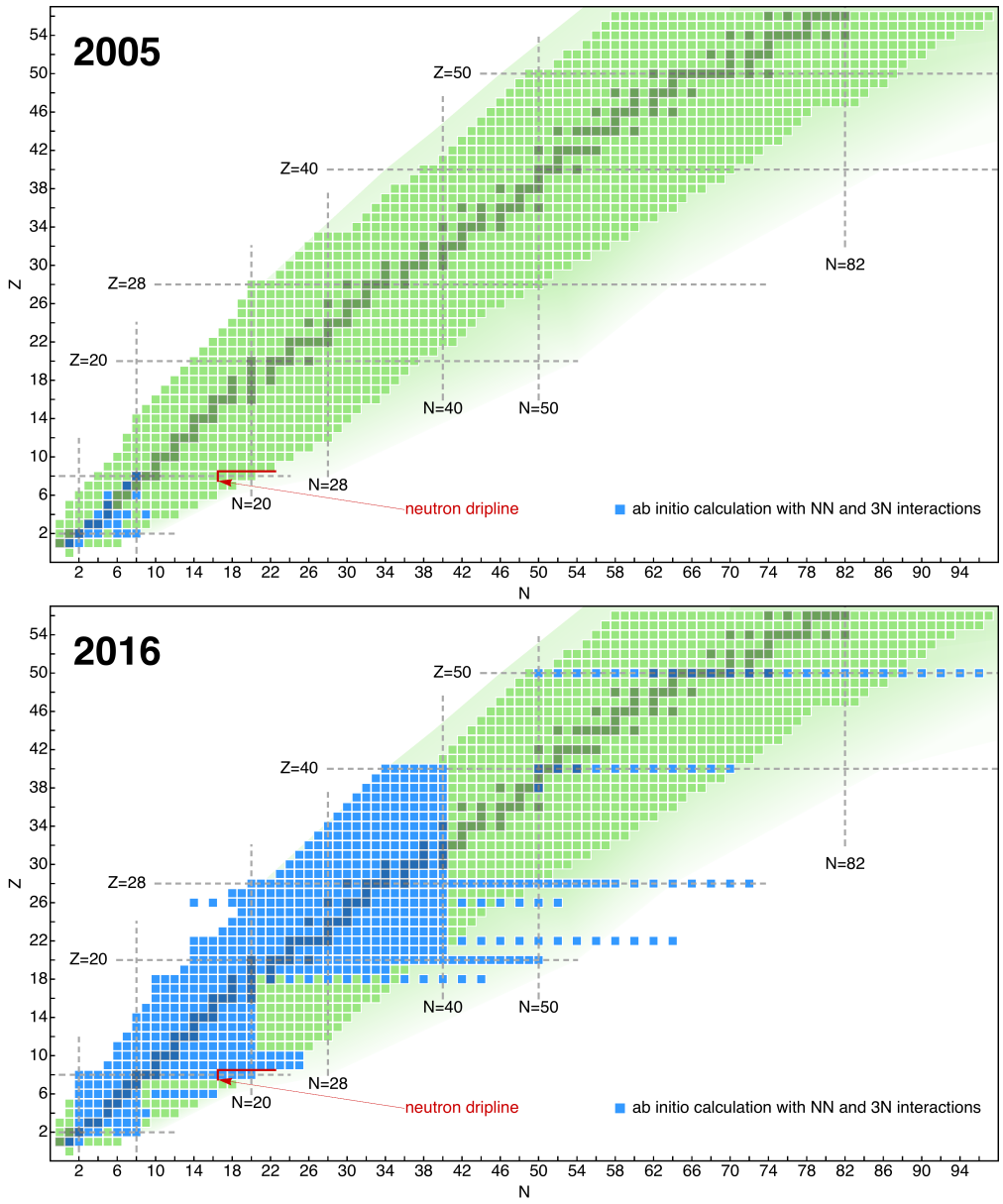

Figure 1.1 Taken from [3]. The progress of *ab initio* nuclear structure from 2005 to 2016.

the time resulted in crippling many-body truncation errors. In contrast, descriptions of the electronic systems of interest in quantum chemistry can typically treat inter-particle interactions as a perturbation on top of the dominant mean-field.

Owing to the difficulties associated with the interactions, the earliest attempts at *ab initio* nuclear theory primarily served as a means to draw loose connections between the more quantitative phenomenological models and the underlying inter-nucleon forces [32, 33]. Phenomenology such

as the empirical shell-model [34] and Skyrme energy density-functionals [35,36] have long offered a computationally elegant and numerically precise means to explain nuclear properties in regions of the nuclear landscape where experimental data can be used to constrain the models, but as the sights of experimenters turn to the exotic reaches of the nuclear chart, the utility of phenomenology is reduced drastically. These shortcomings stem from uncontrolled extrapolations beyond regions of known data; here artifacts of the fitting procedure are amplified, resulting in strongly model dependent predictions. Furthermore, phenomenological predictions for observables other than energies are a subtle matter, as there is no obvious way to *consistently* renormalize the operators with the fitted effective interactions of these methods.

A path forward was revealed by two revolutionary developments, which brought forth a renaissance in *ab initio* nuclear theory. The first was the arrival of chiral effective field theory (EFT) [37, 38], where two- and three-nucleon interactions (and consistent electroweak current operators) are constructed systematically via a consistent power-counting scheme which connects with the symmetries of quantum chromodynamics (QCD). The second breakthrough came with the increased popularity of renormalization group (RG) methods [39, 40] in the field, which have brought about a unitary softening mechanism for the nuclear interactions. With chiral EFT providing a consistently constructed starting point for both the inter-nucleon interactions and observables, RG methods act as a resolution dial for nuclear interactions. Here we can tune the strength of short-range correlations to construct a more perturbative interaction, where rudimentary approaches such as Hartree-Fock (HF) theory can then provide a reasonable starting point for approximate many-body methods.

With these developments on the interaction front, the quasi-exact NCSM has been pushed to new frontiers, reaching as far as the oxygen chain [40]. In regards to the proliferation of *ab initio* methods, the most meaningful consequence of these developments was the reintroduction of the polynomial scaling methods which had taken refuge in quantum chemistry. Techniques such as CC theory have re-emerged in nuclear physics, along with a plethora of new approaches, such as the in-medium similarity renormalization group (IMSRG) and the self-consistent Green's

function (SCGF) approach [41–60]. These methods, armed with the power of chiral EFT and RG softening, have pushed the boundaries of predictive *ab initio* nuclear structure to the entirety of the *sd* and pf-shells, and further beyond to the tin chain, as demonstrated in fig. 1.1. In this endeavor, significant progress has been made in including the effects of three-nucleon forces [60–64] and extending calculations to open-shell nuclei [44–46, 49, 51–53, 65, 66] through the clever use of various normal-ordering schemes and also through marriages of *ab initio* machinery with effective interaction ideas ported from phenomenology.

Ab initio efforts of the past decade have largely targeted energies and scalar observables such as nuclear radii. In recent years however, there has been a significant push to develop a more general effective operator formalism for these approximate *ab initio* methods, which includes tensor observables such as transitions and moments. A particularly crucial frontier is that of neutrinoless double β-decay, where a consistent and reliable prediction of the nuclear matrix element [67] for the process would be invaluable to experimental efforts and analyses in the event of a confirmed observation. There are many hurdles to be surpassed before the *ab initio* community can contribute confidently on this front; to start, the development of a reliable theory for electromagnetic transitions between excited states in heavier open-shell nuclei would be a needed step forward. While there have certainly been efforts to explain excited states and strength distributions in medium-mass nuclei [68–70], a versatile, lightweight framework for such explorations has not yet been formalized. In the IMSRG, extensions to excited states and observables come quite naturally, as the method offers a malleable and transparent Hermitian framework to renormalize various many-body correlations within the nuclear Hamiltonian. Of late, much of the IMSRG's progress on this front has been through construction of effective valence-space interactions for shell-model calculations [46, 51, 52]. In the valence-space IMSRG (VS-IMSRG), ground states and excited states are treated on the same footing and observables such as transition strengths follow from existing shell-model machinery. This description is restricted however by those limitations which are endemic to any diagonalization method, where larger nuclei or multi-shell excitations will eventually be confronted with the factorial scaling of the method.

An alternative approach is offered by the equations-of-motion (EOM) formalism [71]. EOM methods are systematically improvable approximate diagonalization methods. Much like the shell model, *ab initio* EOM is greatly improved when used jointly with the IMSRG, which softens couplings between various excitations in the Hamiltonian, and thus facilitates approximate diagonalizations. The equations-of-motion IMSRG (EOM-IMSRG) [72] utilizes Hamiltonians which have been softened by IMSRG decoupling, where one may use less sophisticated transformations than those needed for the VS-IMSRG, as the approximate diagonalization in the EOM calculation allows one to keep all particles active in the full model space. As such, the two methods are excellent complements; the VS-IMSRG shell-model diagonalization allows for more detailed descriptions where valence-space collectivity is important, such as in deformed nuclei, and the EOM-IMSRG allows for less restricted explorations of states where low-order excitations dominate. Both methods are growing in the scope of their applicability, as valence space decoupling techniques continue to be perfected, and systematic improvements are built into the EOM-IMSRG in both the manner of improved approximate diagonalization and decoupling schemes.

The EOM-IMSRG is an analog to the well established equations-of-motion CC (EOM-CC) theory [68, 69, 73–76], and thus we expect similar behavior from these methods. The promise of the EOM-IMSRG lies with the impending inclusion of generalized normal-ordering [77], which has been used to develop the multireference IMSRG (MR-IMSRG) [45, 47]. As of now, the MR-IMSRG has shown great potential as a method to obtain open-shell ground state observables for even-even nuclei. Extension of this method to the MR-EOM-IMSRG will enable the exploration of spectra in open-shells without any of the inherent limitations of the shell model method. Additionally, the MR-EOM-IMSRG can be extended to odd-even and odd-odd nuclei with a generalized EOM formalism. The application of generalized normal-ordering is a non-trivial task, so we have first demonstrated the principle and produced some novel results in a single-reference formulation, which is limited to nuclei near closed shells. In this work, we introduce and explore the strengths and limitations of the EOM-IMSRG as a method for obtaining excited states, and introduce a general effective operator formalism for the IMSRG, which is explored and benchmarked in both the

VS- and EOM-IMSRG for numerous light and medium-mass nuclei.

The rest of this dissertation is organized as follows. In chapter 2, we introduce the nuclear many-body problem, and much of the notation and terminology used in this work. In chapter 3, we formalize the IMSRG, introducing normal-ordering, the IMSRG equations, and the resummation of perturbation theory through IMSRG decoupling. In chapter 4, we discuss some of the major new developments brought about by this work, namely the direct computation of excited states methods in the EOM paradigm, first from the perspective of decoupling the 1p1h sector exactly, and second as a general formulation of the EOM-IMSRG. In chapter 5, we introduce a generalized effective-operator formalism for IMSRG, which was developed throughout the course of this work. This technical advance is applicable for all variants of the IMSRG, so we make comparisons between the VS-IMSRG and EOM-IMSRG. Here we seek to understand the strengths and weaknesses of the complementary methods, which are also benchmarked with NCSM and experiment where available. Finally we present conclusions in chapter 6. The technical advances which brought about the results in chapters 4 and 5 are showcased in the appendix.

CHAPTER 2

THE NUCLEAR MANY-BODY PROBLEM

Nuclei are self-bound collections of protons and neutrons, held together by complicated inter-particle interactions. If nucleons are taken to be the fundamental degrees of freedom for a nuclear structure problem, it is then necessary to take into consideration two-, three-, and up to A-body forces to account for the composite nature of the proton and neutron. Of course, such considerations are impractical for computation, so we must start from a heavily restricted approximation, and improve systematically from there.

In this chapter we explore the basic facets of the nuclear many-body problem. First we introduce inter-nucleon interactions and briefly discuss chiral effective field theory, which is used to produce the input two- and three-nucleon interactions used in this work. We review the independent particle model, and from there motivate the nuclear many-body problem. We introduce Hartree-Fock theory as a means of generating a suitable reference state, and then summarize the formalism of the popular configuration interaction method, many-body perturbation theory, and coupled cluster theory. These methods serve both as motivations and benchmarks for the in-medium similarity renormalization group, which is the focus of this thesis.

2.1 Nuclear Interactions

Perhaps the most daunting challenge for nuclear theory is to construct an accurate description of the inter-nucleon interaction. There are two classes of interactions used for the nuclear many-body problem; phenomenological interactions that are tuned to specific many-body methods and/or nuclei in a given mass range, and "realistic" interactions which accurately describe two- and three-nucleon systems in free-space, and can be used to describe any nucleus within any many-body framework. Phenomenological interactions are designed to perform well for a restricted set of nuclei and/or observables, and are fit to data within that region of the nuclear chart. Most prominent

among these phenomenological interactions is the USDB interaction [78], which has performed excellently in the reproduction of nuclear observables in the *sd*-shell [34], and the Skyrme force, which in modern parlance is a phenomenological parameterization of the nuclear energy density functional [35, 36]. Beyond the specific region targeted by phenomenological interactions, their predictive power becomes extremely limited, often exhibiting model dependent extrapolation properties. Moreover, if one wishes to explore observables other than energies, such as electromagnetic moments or strengths, a phenomenological renormalization procedure for the relevant operators is often ad hoc and uncontrolled. For this reason, *ab initio* approaches, where one starts from realistic two- and three-nucleon interactions in free-space and then solves the many-body Schrödinger equation as accurately as possible, have attracted increased attention in recent years.

Of course, the *ab initio* label raises a picture of interactions derived analytically from QCD, starting with quarks and gluons, and deriving from there the meson-exchange processes which govern the nuclear interactions. This is not possible at present, as the QCD Lagrangian is nonperturbative at low energies relevant to nuclear structure, in stark contrast to the lovely perturbative properties which have brought great success to quantum electrodynamics. While lattice QCD calculations offer a step forward, immense computational demands limit these explorations to 0*s* shell nuclei such as the deuteron and triton, where the pion mass is artificially large [79, 80].

A more practical starting point is from so-called "realistic" interactions, where all nucleons are treated as active, and the forces are fit to very light-mass nuclear data, such as nucleon-nucleon (NN) phase shifts, and binding energies from the triton and ^{4}He. Some early examples of these interactions are high-precision potentials [81–83] which use meson-exchange phenomenology to fit to elastic channel NN scattering. While these potentials have been extraordinarily successful in the description of light nuclei, they struggle as we enter the medium-mass region. Moreover, *ab initio* methods which use many-body truncations to access this region are subject to large errors resulting from the hard repulsive core featured in several of these interactions. These interactions also lack a formal consistency between two- and three-nucleon interactions, and offer no path to build consistent current operators for coupling to to external electroweak probes.

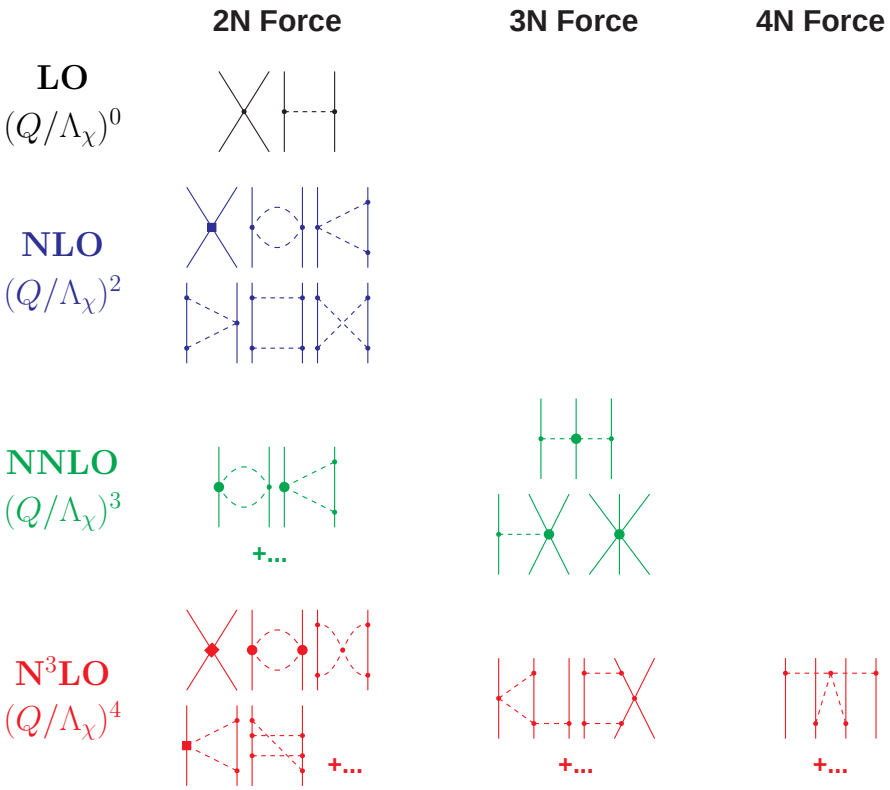

Figure 2.1 Chiral EFT forces up to N^{3}LO ($\nu = 4$). Solid and dashed lines represent nucleons and pions respectively. Vertex order Δ is 0 for small dots, 1 for filled circles, 2 for filled squares, and 4 for filled diamonds. Figure taken from [4].

An *ab initio* paradigm which has gained significant traction in the past decade is to use chiral effective field theory (EFT) to construct the inter-nucleon interactions systematically starting from an effective Lagrangian which is modeled after QCD. Chiral EFT preserves the symmetries of QCD, in particular chiral symmetry breaking [4, 84]. Chiral symmetry is exhibited by massless particles, where right-handed helicity states are completely decoupled from left-handed states. In the two-flavor QCD Lagrangian, the constituent up and down quarks are nearly massless in comparison to the hadronic masses at around 1 GeV/c^2 ($m_u = (2.5 \pm 0.8)$ MeV/c^2, $m_d = (5.0 \pm 0.9)$ MeV/c^2 [85, 86]). Therefore, the QCD Lagrangian exhibits approximate chiral symmetry, which is spontaneously broken in the axial-vector subgroup of the $SU(2)_L \times SU(2)_R$ chiral symmetry

group (see e.g. [38,87]). This spontaneous chiral symmetry breaking implies the existence of three massless Nambu-Goldsone bosons. In reality, the slight explicit breaking of chiral symmetry due to the non-zero quark masses results in massive, but unnaturally light psuedoscalar mesons in the place of the Nambu-Goldstone bosons, namely pions. The existence of pions implies a separation of scales in the hadronic degrees of freedom, as the pion mass $m_\pi \approx 140$ MeV/c^2 is significantly smaller than the mass of other vector mesons [86]. This separation is exploited to formulate chiral EFT.

In contrast to the quarks and gluons of QCD, chiral EFT employs nucleons and pions as the fundamental degrees of freedom,

$$\mathscr{L}_{\chi EFT} = \mathscr{L}_{\pi\pi} + \mathscr{L}_{\pi N} + \mathscr{L}_{NN} + \cdots . \tag{2.1}$$

Pions, being of significantly lighter mass than the other mesons exchanged in nuclear interactions, account for long-range interactions and are the only meson fields included in the Lagrangian. Short-range physics, the result of heavier meson exchange, is encoded in contact interactions with low energy constants (LECs) which must be fit to light-mass nuclear data. Treating short range physics in low-resolution such as this means that the theory is only valid for long-range physics whose characteristic energy scale Q is on the order of the pion mass. As such, the theory must be regulated by a cut-off at some momentum Λ, which suppresses high momenta on the order of the heavier meson masses. The EFT Lagrangian constitutes the most general expression which conserves the symmetries of QCD, and hence there are an infinite number of terms in the expansion, and with each term comes a myriad of LECs. Fortunately, the vertices may be organized by the number of terms proportional to the soft scale Q. This breaks down to the number of pion mass insertions or derivatives, d and nucleon fields n,

$$\Delta = d + n/2 - 2 , \tag{2.2}$$

and the problem may then be treated in chiral perturbation theory, where interaction terms are grouped in powers of (Q/Λ), which is ostensibly small. Thus a chiral EFT is specified by the order

ν of (Q/Λ) kept in the perturbative expansion, as well as the fitting procedure used to constrain the forces. For a given chiral order ν, there are a finite number of diagrams which may contribute to the nuclear forces. As a result, the chiral forces can in principle be calculated to any order.

Fig. 2.1 illustrates the chiral power counting for the EFT up to $\nu = 4$ or next-to-next-to-next-to leading order (N^3LO). Here you can see the number of nucleons A, loops L, and the vertex orders Δ_i factor into the chiral order of a given diagram,

$$\nu = -4 + 2A + 2L + \sum_i \Delta_i \,. \tag{2.3}$$

This figure also demonstrates the fact that many-body forces appear naturally as you increase the chiral order, with 3N forces appearing at N^2LO, 4N at N^3LO, and so on. Thus, we expect that for sufficiently small (Q/Λ), the importance of many-body forces decreases significantly with many-body operator rank. This is an important feature in *ab initio* calculations, as the diminished importance of these higher-body forces means that accurate computations are indeed feasible.

The most popular interaction in the literature is the NN interaction of Entem and Machleidt, computed to N^3LO [5], with a cutoff at Λ=500 MeV. Often coupled with this is the 3N force of Navrátil, which is computed to N^2LO at Λ=400 MeV [13]. This is of course inconsistent with the order and cutoff of the NN force, but 3N forces at N^3LO have not been computed until very recently [88], and it has been demonstrated that using a 500 MeV cutoff for the 3N interaction leads to large induced 4N forces upon SRG softening [63]. The so called NN+3N(400) force has been quite successful as a means to describe ground state energies up to the light constituents of the *sd*-shell. A notable shortcoming is the interaction's inability to produce ground states with proper radii. Radii are under predicted and significant overbinding is exhibited in heavier nuclei, but the effect seems to be filtered out by observables such as separation and excitation energies [55,89,90]. There have been numerous works in recent years to improve chiral EFT. Two main strategies have developed: a brute force approach to increase the chiral order [88, 91], and a re-evaluation of the fitting procedures at lower orders [92–94].

For this work we use almost exclusively the NN force of Entem and Machleidt, often including

the 3N force of Navrátil. We choose this interaction because of its preponderance in the literature. We refer to it as the standard NN+3N(400) force.

2.2 Independent Particle Model

The most elementary picture of nuclear structure can be constructed by neglecting the inter-nucleon forces, and instead treating the problem as a collection of independent particles subject to some empirical mean-field; this reduces the original problem of solving the many-body Schrödinger equation to that of a single particle moving in a potential well, a problem that is familiar from introductory quantum mechanics. An approximation for the ground state of the A-body nucleus can be made simply by filling the lowest A orbitals, where the highest single-particle energy corresponds to the Fermi energy ε_F. We then construct an antisymmetric product state in accordance with the Pauli exclusion principle. The resulting theory of nuclear structure is often referred to as the independent particle model (IPM). A standard choice for the mean-field potential is the Woods-Saxon (WS) potential [95], shown schematically in fig. 2.2 and given by

$$V(r) = -V_0 \left[1 + exp(\frac{r - R_0}{a}) \right]^{-1}, \tag{2.4}$$

where V_0 is the depth of the potential well, R_0 is the empirical nuclear radius, and a controls the gradient of the potential near $r = R_0$. These parameters are chosen to match observed properties of nuclei. In particular, the approximately uniform density (saturation density) which occurs within the interior of the nucleus is ensured by the flat region of the WS potential, and the sharp gradient in the potential near R_0 guarantees a strong binding force at the surface. The potential quickly goes to zero after R_0, which accounts for the finite range of the nuclear force. As the WS potential vanishes at infinity, the WS basis contains both discrete bound states in the potential well and scattering states within the continuum.

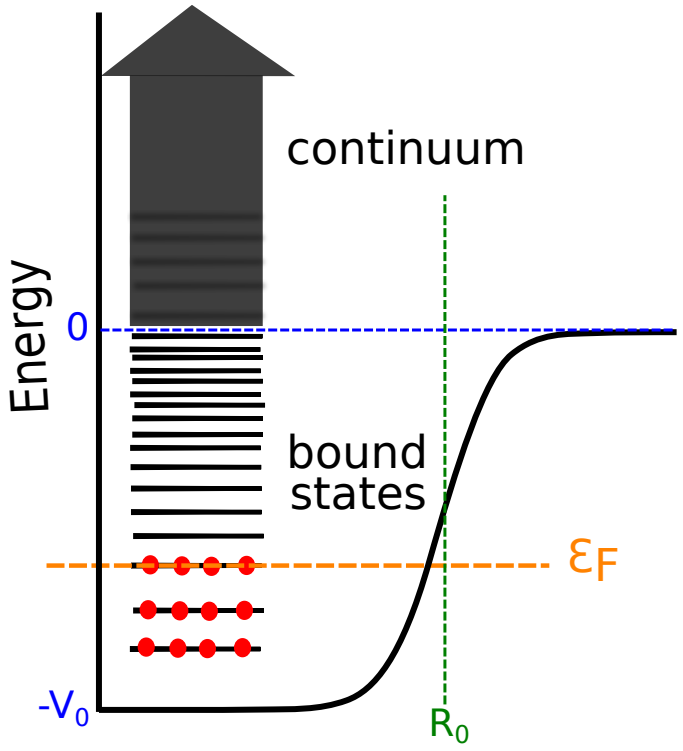

Figure 2.2 Schematic diagram of the Woods-Saxon potential. Discrete levels exist in the potential well, and a continuum of scattering states exist above it. Orbitals are filled up to the Fermi level, ε_F.

The constructed antisymmetric product state is called a Slater determinant,

$$\Phi_0(\mathbf{r}_1,\ldots,\mathbf{r}_A) = \frac{1}{\sqrt{A!}} \begin{vmatrix} \phi_1(\mathbf{r}_1) & \phi_1(\mathbf{r}_2) & \cdots & \phi_1(\mathbf{r}_A) \\ \phi_2(\mathbf{r}_1) & \phi_2(\mathbf{r}_2) & \cdots & \phi_2(\mathbf{r}_A) \\ \vdots & \vdots & \ddots & \vdots \\ \phi_A(\mathbf{r}_1) & \phi_A(\mathbf{r}_2) & \cdots & \phi_A(\mathbf{r}_A) \end{vmatrix}, \tag{2.5}$$

where ϕ_i are the WS orbitals. In the IPM, this is our approximation to the ground state wave function. Despite the IPM's extreme simplicity, it gives a remarkable account of the gross structure of nuclei; the method is able to produce shell structure and magic numbers, as well as nuclear properties such as ground state spins and magnetic moments in the vicinity of shell closures. Conversely, open-shell nuclei have strongly correlated ground states due to the presence of quasi-degenerate orbitals near ε_F, and hence a single Slater determinant fails to describe them even qualitatively. Moreover, the method is not systematically improvable without the inclusion of correlations.

When we do add correlations by restoring the inter-nucleon interactions and solving the many-body Schrödinger equation, the IPM offers a convenient starting point for nuclei near shell closures, from which we may build in dynamic correlations in the form of excitations brought about by the interactions. To compute solutions to the nuclear many-body problem, we must construct a many-body basis from the single-particle basis. Such a task may be accomplished by enumerating all possible A-body Slater determinants allowed within the chosen single-particle basis. The ground-state approximation from the mean-field picture is now referred to as the "reference state", and all other Slater determinants are particle-hole excitations on top of this reference.

While there is a continued effort to solve the nuclear many-body problem using idealized single-particle bases where bound and scattering states are treated on equal footing [96–99], most many-body methods at present focus primarily on bound states using the harmonic oscillator (HO) potential

$$V(r) = \frac{1}{2} m\omega^2 r^2 \tag{2.6}$$

as a starting point. The HO potential, despite allowing only bound states, exhibits desirable properties owing to a clean factorization of the center-of-mass and relative coordinates. This allows for convenient transformations between momentum and coordinate space, as well as access to intrinsic properties without spuriosities from the violation of translational invariance necessarily suffered when using a spherical basis. Despite some striking differences from the WS potential, the IPM with the HO basis is nonetheless able to recover fundamental properties of nuclei such as shell structure arising from its evenly spaced degenerate orbitals.

2.3 The Many-Body Basis and Hamiltonian

To include the dynamic correlations that are neglected by the independent particle model, we now formulate the interacting nuclear many-body problem in second quantization (see [100, 101]). The nuclear many-body problem boils down to solving the stationary Schrödinger equation,

$$H|\Psi_\nu\rangle = E_\nu|\Psi_\nu\rangle\,, \tag{2.7}$$

where Ψ_ν and E_ν are the wave function and energy for any stationary state of the system. The intrinsic A-body nuclear Hamiltonian H consists of a kinetic energy term, as well as two-, three- and up to A-nucleon forces,

$$H = T^{1b} + \sum_{n=2}^{A} V^{nb} - T^{1b}_{cm} - T^{2b}_{cm}. \tag{2.8}$$

Here we have subtracted contributions from the COM kinetic energy,

$$T_{cm} = \frac{\mathbf{P}^2}{2mA} = \sum_{i=1}^{A} \frac{\mathbf{p}_i^2}{2mA} + \frac{1}{2}\sum_{i\neq j}^{A} \frac{\mathbf{p}_i \cdot \mathbf{p}_j}{mA} = T^{1b}_{cm} + T^{2b}_{cm}, \tag{2.9}$$

which account for translation of the entire nucleus. In practice, finite computational power limits us to at most three-nucleon forces, so state-of-the-art many-body calculations use second-quantized Hamiltonians of the form

$$\begin{aligned} H = \sum_{pq}(1-\frac{1}{A})\langle p|T|q\rangle a_p^\dagger a_q + \frac{1}{4}\sum_{pqrs}\langle pq|V^{(2)} - \frac{\mathbf{p}_1\cdot\mathbf{p}_2}{mA}|rs\rangle a_p^\dagger a_q^\dagger a_s a_r \\ + \frac{1}{36}\sum_{pqrstu}\langle pqr|V^{(3)}|stu\rangle a_p^\dagger a_q^\dagger a_r^\dagger a_u a_t a_s. \end{aligned} \tag{2.10}$$

Here, we use antisymmetrized two- and three-body bras and kets. We will often use short-hand such as

$$T_{pq} \equiv (1-\frac{1}{A})\langle p|T|q\rangle\,, \tag{2.11}$$

$$V^{(2)}_{pqrs} \equiv \langle pq|V^{(2)} - \frac{\mathbf{p}_1\cdot\mathbf{p}_2}{mA}|rs\rangle\,, \tag{2.12}$$

$$V^{(3)}_{pqrstu} \equiv \langle pqr|V^{(3)}|stu\rangle\,, \tag{2.13}$$

for the antisymmetrized operators, where the subtraction of the center-of-mass kinetic energy has been absorbed into the interaction terms. $a^\dagger$ and a are fermion creation and annihilation operators, which are used to construct the many-body basis of antisymmetrized A-body product states, or Slater determinants:

$$|\Phi_0\rangle = \{\prod_{i=1}^{A} a_i^\dagger\}|0\rangle\,. \tag{2.14}$$

Here each $a_i^\dagger$ corresponds to the addition of the ith single-particle orbital to the antisymmetrized product. $|\Phi_0\rangle$ is the reference state, consisting of the A single-particle orbits which comprise

the Fermi sea. The Pauli exclusion principle is encoded here by the fermion anti-commutation relations,

$$[a_i^\dagger, a_j]_+ = \delta_{ij}, \qquad [a_i^\dagger, a_j^\dagger]_+ = [a_i, a_j]_+ = 0\,. \tag{2.15}$$

A complete many-body Hilbert-space can be constructed via the application of creation and annihilation operators,

$$|\Phi_i^a\rangle = a_a^\dagger a_i |\Phi_0\rangle\,, \qquad |\Phi_{ij}^{ab}\rangle = a_a^\dagger a_b^\dagger a_j a_i |\Phi_0\rangle\,, \qquad \text{etc}\ldots \tag{2.16}$$

Here we note that fermion creation and annihilation operators cannot create an already existing particle, or annihilate one which is already absent. Thus, when these cases arise, the creation and annihilation operators annihilate the state, which can be shown using eq. 2.15. In the definition 2.16, we see a single excitation and a double excitation from the reference state. The ellipses indicates that in order to construct the complete basis, we must include triples, quadruples and up to A-body excitations, corresponding to A creators and A annihilators acting on the reference state.

To simplify the discussion of the many-body basis, we develop the particle-hole nomenclature, where *particles* are created above the Fermi level, and *holes* are destroyed below it. In this work (except where otherwise noted), the indices $a, b, c, \ldots$ will refer to particles and $i, j, k, \ldots$ to holes. Unspecified orbitals will be referred to as $p, q, r, \ldots$ In this terminology, the reference state corresponds to a Slater-determinant filled with all hole states. A single excitation corresponds to a particle-hole excitation (1p1h) from the reference,

$$|\Phi_i^a\rangle = a_a^\dagger a_i |\Phi_0\rangle\,, \tag{2.17}$$

doubles to 2p2h, triples to 3p3h, and so on to ApAh excitations. This is shown schematically in fig. 2.3

As the reference state and all possible excitations constitute a complete basis, the eigenstates of eq. 2.7 can be written as a linear combination of these Slater determinants,

$$|\Psi_\nu\rangle = C_0|\Phi_0\rangle + \sum_{N=1}^{A} \frac{1}{N!} \sum_{\substack{i_1,\ldots,i_N \\ a_1,\ldots,a_N}} C_{i_1,\ldots,i_N}^{a_1,\ldots,a_N} a_{a_1}^\dagger \cdots a_{a_N}^\dagger a_{i_N} \cdots a_{i_1} |\Phi_0\rangle\,. \tag{2.18}$$

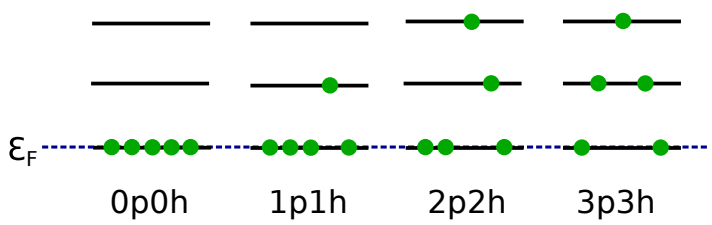

Figure 2.3 Schematic depiction of the reference state (0p0h), single (1p1h), double (2p2h) and triple (3p3h) excitations.

The goal of the nuclear structure theorist is then to solve for the coefficients C_α which describe the state of interest.

The single particle basis used to construct the many-body basis is specified by a truncation on the single-particle energies in the HO basis, e_{max}. It is not practical to solve the problem in m-scheme, where each orbital has good spin projection quantum number m, as the necessary model spaces for converged calculations ($e_{max} > 10$) would possess over 1000 orbitals, corresponding to billions of antisymmetrized two-particle states, and an astronomical number of three-particle states. We instead express the problem in J-scheme, exploiting the spherical symmetry of the Hamiltonian. For spherical nuclei, it is sufficient to only consider scalar matrix elements. To transition to J-scheme, all dependence on the spin projection m is summed out using the Wigner-Eckart theorem (see appendix for details). In J-scheme, the number of orbitals is reduced by roughly an order of magnitude. Even with this simplification, many-body problems involving hundreds of orbitals are far from trivial. Thus the matrix must be stored in such a way as to exploit every symmetry available, namely total angular momentum J, isospin projection T_z, and parity Π. Additionally, we note that observables must be expressed as Hermitian operators, reducing the size of the matrix by roughly a factor of two.

Even after these symmetries are exploited, it is often found that the number of unique non-zero three-body matrix elements requires many terabytes of storage even for light *sd*-shell nuclei. Thus an additional truncation E_{3max} is introduced, where

$$E_3 = e_1 + e_2 + e_3 \,. \tag{2.19}$$

Here the summed single particle energies for a three-body basis state are restricted to E_{3max}. Typical values are $E_{3max} = 12, 14, 16$, which limit the size of the three-body interaction to 1-100 GB. Ground state energies are dependent on this truncation for low values of the HO single-particle basis frequency $\hbar\omega$, but for *sd*-shell nuclei, $E_{3max} = 14$ is sufficient after $\hbar\omega$ = 20 MeV. The difference between $E_{3max} = 12$ and 14 is typically on the order of $1-2\%$ for the optimal $\hbar\omega$ [102].

Solution of the many-body problem often requires the storage of several copies of the interaction, and therefore it is rarely practical to include the three-body force, even after E_{3max} truncation. However, partial incorporation of the three-body force at the two-body level can be achieved through normal-ordering. Nuclear many-body operators are expressed in-medium through use of normal-ordering with Wick's theorem.

A normal ordered operator string is a string of N creation and annihilation operators (denoted generically by A_i) which are ordered in such a way that the reference state expectation value is zero,

$$\langle\Phi_0|\{A_1 A_2 \cdots A_N\}|\Phi_0\rangle = 0\,. \tag{2.20}$$

While this ordering may be achieved using the standard fermion anti-commutation relations, a more useful approach is through the use of Wick contractions

$$\overbrace{a_i^\dagger a_j} = a_i^\dagger a_j - \left\{a_i^\dagger a_j\right\}, \tag{2.21}$$

which are zero by construction for operator pairs which are already normal-ordered, and which correspond to the anti-commutator for pairs which are not. This is related to the convenient fact that all creation and annihilation operators within a normal-ordered string anti-commute, so exchanges only require a change of sign. For two strings of normal-ordered operators of length $2n$ and $2m$, Wick's theorem (see, e.g., [11]) relates their product to a linear combination of normal-ordered operator strings:

$$\begin{aligned}&\left\{a_{i_1}^\dagger \ldots a_{i_n}^\dagger a_{j_n} \ldots a_{j_1}\right\}\left\{a_{k_1}^\dagger \ldots a_{k_m}^\dagger a_{l_m} \ldots a_{l_1}\right\} = \\ &\quad (-1)^{m\cdot n}\left\{a_{i_1}^\dagger \ldots a_{i_n}^\dagger a_{k_1}^\dagger \ldots a_{k_m}^\dagger a_{j_n} \ldots a_{j_1} a_{l_m} \ldots a_{l_1}\right\}\end{aligned} \tag{2.22}$$

$$+(-1)^{m\cdot n}\overbrace{a^\dagger_{i_1}a_{l_1}}\{a^\dagger_{i_2}\dots a^\dagger_{k_m}a_{j_n}\dots a_{l_2}\}+\text{singles}$$
$$+(-1)^{m\cdot n}\overbrace{a^\dagger_{i_1}a_{l_1}}\overbrace{a^\dagger_{i_2}a_{l_2}}\{a^\dagger_{i_3}\dots a^\dagger_{k_m}a_{j_n}\dots a_{l_3}\}+\text{doubles}+\text{triples}+\cdots. \tag{2.23}$$

Here *singles*, *doubles*, and *triples* refer respectively to all possible single contractions, pairs and triplets of operator contractions in the two strings. The expansion continues until all terms are contracted in every way possible. The phase of each term is determined by the number of exchanges needed to bring the total operator string into the form shown, including the process of bringing contracted operators adjacent to one another. Note that we do not show contractions between two creation or two annihilation operators, as these anti-commute with one another, and thus their contractions vanish.

Normal ordering has the effect of mapping the second quantized Hamiltonian,

$$H=\sum_{pq}T_{pq}a^\dagger_p a_q+\frac{1}{4}\sum_{pqrs}V^{(2)}_{pqrs}a^\dagger_p a^\dagger_q a_s a_r+\frac{1}{36}\sum_{pqrstu}V^{(3)}_{pqrstu}a^\dagger_p a^\dagger_q a^\dagger_r a_u a_t a_s\,, \tag{2.24}$$

to a form where vertices contain density dependent elements of higher-body forces:

$$H=E_0+\sum_{pq}f_{pq}\{a^\dagger_p a_q\}+\frac{1}{4}\sum_{pqrs}\Gamma_{pqrs}\{a^\dagger_p a^\dagger_q a_r a_s\}+\frac{1}{36}\sum_{pqrstu}W_{pqrstu}\{a^\dagger_p a^\dagger_q a^\dagger_r a_u a_t a_s\}\,. \tag{2.25}$$

Here, "in-medium" vertices are determined by Wick's theorem:

$$E_0=\sum_i T_{ii}n_i+\frac{1}{2}\sum_{ij}V^{(2)}_{ijij}n_i n_j+\frac{1}{6}V^{(3)}_{ijkijk}n_i n_j n_k, \tag{2.26}$$

$$f_{pq}=T_{pq}+\sum_i V^{(2)}_{piqi}n_i+\frac{1}{2}\sum_{ij}V^{(3)}_{pijqij}n_i n_j, \tag{2.27}$$

$$\Gamma_{pqrs}=V^{(2)}_{pqrs}+\sum_i V^{(3)}_{pqirsi}n_i, \tag{2.28}$$

$$W_{pqrstu}=V^{(3)}_{pqrstu}. \tag{2.29}$$

Here n_i is the integer occupation number for the reference state ($n_i=\Theta(\varepsilon_F-\varepsilon_i)$). All normal-ordered vertices include in-medium contributions from higher order many-body forces. For example, the zero-body term E_0 contains hole index summations over all of the free-space operators, and corresponds to the energy of the reference state, which has become the in-medium vacuum state.

Normal ordering of the Hamiltonian is injective, and thus exact solution of the many-body Schrödinger equation requires the same amount of work in either representation. However, in the in-medium formulation, one may truncate away the residual three-body force W, and still retain in-medium components of the free-space three-body force in the zero, one and two-body terms. This constitutes the normal-ordered two-body (NO2B) approximation, where three-body physics can be incorporated in a computationally practical two-body framework. With these tools, we have a foundation on which to build a many-body method. However, we will return briefly to the IPM in the context of Hartree-Fock theory, which we use to systematically construct a single-particle basis.

2.4 Hartree-Fock Theory

The mean-field picture of the IPM can be put on a microscopic foundation through use of Hartree-Fock (HF) theory. This method again seeks to describe the ground state with only a single Slater determinant, but here we work with the full inter-nucleon interaction, constructing the mean-field through minimization of the energy functional

$$E[\Phi] = \langle \Phi | H | \Phi \rangle \,, \tag{2.30}$$

where the ground state is taken to be a single Slater determinant. Using NN and 3N forces, the energy functional becomes

$$E[\Phi] = \sum_i \langle i|T|i\rangle + \frac{1}{2}\sum_{ij}\langle ij|V^{(2)}|ij\rangle + \frac{1}{6}\sum_{ijk}\langle ijk|V^{(3)}|ijk\rangle \,, \tag{2.31}$$

where the choice of indices indicates summation over hole states. We vary the single particle orbitals via Thouless' theorem [103], which states that any two Slater determinants are related by an exponentiated one-body excitation operator,

$$|\Phi'\rangle = e^{C_1}|\Phi\rangle \,. \tag{2.32}$$

Taking the amplitudes of C_1 to be small, we arrive at

$$|\Phi'\rangle = (1 + \sum_{ia} \delta C_{ai} a_a^\dagger a_i)|\Phi\rangle\,, \tag{2.33}$$

and

$$\delta E[\Phi] = \sum_{ai} \delta C_{ai} \langle \Phi | H a_a^\dagger a_i | \Phi \rangle\,. \tag{2.34}$$

Setting $\delta E[\Phi]$ to zero yields the condition

$$\langle \Phi | H a_a^\dagger a_i | \Phi \rangle = 0 \quad \forall\ a, i \text{ such that } \varepsilon_i \leq \varepsilon_F \text{ and } \varepsilon_a > \varepsilon_F\,. \tag{2.35}$$

Expanding in terms of the single-particle basis, we arrive at

$$\langle \Phi | H a_a^\dagger a_i | \Phi \rangle = \langle i|T|a\rangle + \sum_k \langle ik|V^{(2)}|ak\rangle + \frac{1}{2}\sum_{kl} \langle ikl|V^{(3)}|akl\rangle = 0\,. \tag{2.36}$$

this condition is known as the Brillouin condition, and is clearly satisfied by the eigenbasis of the operator

$$F = \sum_{pq} a_p^\dagger a_q \left[T_{pq} + \sum_k V^{(2)}_{pkqk} + \frac{1}{2}\sum_{kl} V^{(3)}_{pklqkl} \right]. \tag{2.37}$$

F is called the Fock operator. Its eigenfunctions correspond to the HF orbitals, and eigenvalues to the HF single-particle energies. F is the one-body piece of the normal-ordered Hamiltonian in eq. 2.25, highlighting the fact that in-medium operators contain mean-field components of higher-order free-space operators.

Here we have computed the HF mean-field,

$$V^{HF}_{pq} = \sum_k V^{(2)}_{pkqk} + \frac{1}{2}\sum_{kl} V^{(3)}_{pklqkl}\,, \tag{2.38}$$

a one-body potential constructed by summing over the hole orbitals in the reference state. This is the microscopic analog to the phenomenological construction of the IPM in sec. 2.2. The HF reference state $|\Phi_{HF}\rangle$ is a Slater-determinant filled up to ε_F, and thus it is the energetically optimized reference state for a many-body calculation. The reference energy corresponds to the Hartree-Fock energy $E_{HF} = E[\Phi_{HF}]$.

One does not know the form of the HF basis a priori, so in practice, we start with a HO basis, and solve the eigenvalue problem self-consistently, as the construction of the mean-field requires knowledge of the HF orbitals. We construct F using the HO orbitals, diagonalize F, and use the new orbitals to restart the procedure. We iterate until convergence is obtained in the single particle energies and the HF basis has been established. As the HO basis is truncated to a finite single-particle energy $e_{\max}$, the HF orbitals will be dependent on the frequency of the HO basis $\hbar\omega$. However, for large enough $e_{\max}$, we see convergence where $\hbar\omega$ dependence of computed quantities is negligible over a wide range.

2.5 The Configuration Interaction Method

As previously stated, the principle task facing *ab initio* nuclear structure theorists is to solve for the coefficients C_α of the configuration expansion

$$|\Psi_\nu\rangle = C_0|\Phi_0\rangle + \sum_{N=1}^{A} \frac{1}{N!} \sum_{\substack{i_1,\ldots,i_N \\ a_1,\ldots,a_N}} C_{i_1,\ldots,i_N}^{a_1,\ldots,a_N} a_{a_1}^\dagger \cdots a_{a_N}^\dagger a_{i_N} \cdots a_{i_1} |\Phi_0\rangle \,. \tag{2.39}$$

If we have knowledge of the correlated wave function $|\Psi_\nu\rangle$, accurate observables such as energy, radii, and transition strengths follow from expectation values. The expansion of states in terms of the many-body basis suggests that the most straightforward way of doing this is to express the Hamiltonian as a matrix on the many-body Hilbert space. Solving the matrix eigenvalue problem yields the energies as eigenvalues and the coefficients C_α in the eigenvectors. Thus, for a given single-particle basis truncated at e_{max}, we wish to construct all possible configurations of A filled orbitals, written as Slater determinants, and then represent the matrix in the resulting basis by computing individual matrix elements, e.g.

$$\langle \Phi_{ij}^{ab} | H | \Phi_0 \rangle = \Gamma_{abij} \,. \tag{2.40}$$

Subsequent solution of the eigenvalue problem yields the correlated wave functions for the ground and excited states. This approach is appropriately named the full configuration interaction (FCI)

approach. Frequently, we will refer to FCI as the standard of "exactness" within a given model space.

It now appears that solving the many-body problem is a rather simplistic task, but of course, FCI is not practical for nuclear physics beyond the lightest nuclei, as construction of the full set of configurations scales factorially with the number of single particle orbitals. Nonetheless, a close relative of FCI has made a name for itself in *ab initio* nuclear structure, namely the no-core shell model (NCSM) [16–18]. Here COM factorization is ensured using a truncation on the excitation quanta allowed in the many-body basis rather than including the full set of configurations. In practice, the actual Slater determinants are never explicitly constructed in either of these approaches, as Krylov space approximate diagonalization methods [104, 105] can be used in place of conventional eigenvalue solvers, requiring only knowledge of the matrix-vector products, which may be computed fully in Fock-space with second quantization machinery. Regardless, computational demands grow rapidly with system size, so either of these exact methods are only applicable to light nuclei. Methods such as the FCI and NCSM belong to a class of *ab initio* approaches called "quasi-exact" methods, meaning that they are exact within the accessible model spaces. Other examples include quantum Monte Carlo [19–21] and lattice effective field theory [106, 107], which are exact up to statistical errors. A common feature of any quasi-exact method is limited applicability, as the complex nature of the many-body problem demands significant computational power for an exact solution.

While no *ab initio* method can proclaim universal applicability, vast improvements can be made here if we sacrifice the quasi-exact moniker by applying some systematically improvable many-body truncation. This can be accomplished by limiting the number of Slater determinants included in the expansion of the correlated state functions. The most obvious way to do this is to truncate the FCI expansion of eq. 2.39 up to a certain excitation rank from the reference state. The resultant configuration interaction (CI) method is specified by what remains. In this manner, we define the

configuration interaction with singles and doubles (CISD) [108]:

$$|\Psi_{\nu}^{CISD}\rangle = C_0|\Phi_0\rangle + \sum_{i,a} C_i^a a_a^\dagger a_i|\Phi_0\rangle + \frac{1}{4}\sum_{ijab} C_{ij}^{ab} a_a^\dagger a_b^\dagger a_j a_i|\Phi_0\rangle\,. \tag{2.41}$$

This method is approximate of course, as the many-body Hamiltonian directly couples the reference state to single, double, and triple excitations, and indirectly to all excitation ranks. Any results expressed with such a method are then subject to so-called "many-body truncation errors". We say this method is systematically improvable, as we can make things better by going to the next level of CISDT, or further to CISDTQ if we have the patience to implement such a method. The many-body truncation of the configuration interaction sheds some light on the importance of Hartree-Fock theory. As the CI expansion is limited to the reference state and a finite number of excitations built on top of that reference, it is critical that we use the best possible reference state. For most systems, the HF reference is a sufficient choice, as it minimizes the energy functional for Slater determinants.

Truncated CI, despite having a desirable simplicity in its formulation, suffers from a fatal shortcoming; the method violates size-extensivity, a principle that states that a uniformly distributed system's energy should be proportional to system size [11].

2.6 Many-Body Perturbation Theory

The lack of size-extensivity observed in truncated CI can be understood using many-body perturbation theory (MBPT), which is itself a method for constructing the correlated ground state wave function [11, 109, 110]. MBPT treats the non-interacting reference state as the order zero wave function, and the corresponding reference energy as the order zero energy. Generically, the Hamiltonian is partitioned into a diagonal and interaction piece

$$H|\Psi_0\rangle = (H_0 + H_I)|\Psi_0\rangle = E_0|\Psi_0\rangle\,, \tag{2.42}$$

with the known order zero solution

$$H_0|\Phi_0\rangle = E_0^{(0)}|\Phi_0\rangle\,. \tag{2.43}$$

Left multiplying eq. 2.42 by $\langle\Phi_0|$ gives

$$\langle\Phi_0|H_I|\Psi_0\rangle = E_0 - E_0^{(0)} \equiv \Delta E\,, \tag{2.44}$$

where we have invoked the intermediate normalization $\langle\Phi_0|\Psi_0\rangle = 1$. Treating this problem in Rayleigh-Schrödinger perturbation theory yields MBPT to infinite order

$$|\Psi_0\rangle = \sum_{m=0}^{\infty} [R_0(H_I - \Delta E)]^m |\Phi_0\rangle\,, \tag{2.45}$$

with the resolvent operator

$$R_0 = \frac{Q}{E_0^{(0)} - H_0}\,, \tag{2.46}$$

where the complement space projector is given by $Q = 1 - |\Phi_0\rangle\langle\Phi_0|$. Thus, MBPT can be computed up to a specified order m, and at each order, a finite number of terms contribute. For example, the first order wave-function is given by

$$|\Psi_0^{(1)}\rangle = |\Phi_0\rangle + R_0 H_I |\Phi_0\rangle\,, \tag{2.47}$$

and the corresponding second-order energy correction is

$$\Delta E^{(2)} = \langle\Phi_0|H_I R_0 H_I|\Phi_0\rangle\,. \tag{2.48}$$

The energy and wave functions are often evaluated using Goldstone diagrams (for details, see [11]), and it can be shown that any unlinked diagrams arising from the $H_I[R_0 H_I]^m$ term in eq. 2.45 are canceled exactly at each order by so-called renormalization terms proportional to ΔE. This is a restatement of the famous linked-cluster theorem [111–114], and it results in a simplified expression for the MBPT energy corrections

$$\Delta E^{(m+1)} = \langle\Phi_0|\{H_I[R_0 H_I]^m\}_C|\Phi_0\rangle\,, \tag{2.49}$$

where the subscript C denotes connected diagrams. By the linked-cluster theorem, a method is size-extensive if the ground state energy can be expressed diagrammatically using only connected diagrams, hence MBPT is size-extensive at each order.

Starting from the NO2B approximation, we partition the Hamiltonian as

$$H_0 = E_0 + \sum_p f_{pp}\{a_p^\dagger a_p\} \qquad H_I = \sum_{pq} f_{pq}(1-\delta_{pq})\{a_p^\dagger a_q\} + \frac{1}{4}\sum_{pqrs}\Gamma_{pqrs}\{a_p^\dagger a_q^\dagger a_s a_r\}\,. \quad (2.50)$$

This is simplified in the HF basis, as the Brillouin condition sets the one-body piece of H_I to zero. Employing this partitioning in the HF basis, the first-order energy correction vanishes and the second-order correction (MBPT(2)) is

$$E_0^{(2)} = \sum_\alpha \frac{|\langle\Phi_\alpha|H_I|\Phi_0\rangle|^2}{E_0 - E_\alpha} = \frac{1}{4}\sum_{ijab}\frac{|\Gamma_{ijab}|^2}{\Delta_{ab}^{ij}}\,, \quad (2.51)$$

where $\Delta_{ab}^{ij} = f_{ii} + f_{jj} - f_{aa} - f_{bb}$ is the Møller-Plesset energy denominator. This energy correction scales as $\mathscr{O}(N_p^2 N_h^2)$, where N_p and N_h are the number of particle and hole orbitals in the single particle basis. The method is systematically improvable, with the MBPT(3) correction scaling as $\mathscr{O}(N_p^4 N_h^2)$.

In principle, truncated CI and MBPT are different routes to solving the same problem. In fact, CISD includes energy contributions from all orders of MBPT at a computational cost similar to MBPT(3). The resummation is incomplete however, in particular the renormalization terms which violate size-extensivity are not cancelled out at each order of CI. This manifests diagrammatically with the observation that the CI excitation operators

$$\mathscr{C}_1 \equiv \sum_{ia} C_i^a a_a^\dagger a_i \qquad \mathscr{C}_2 \equiv \frac{1}{4}\sum_{ijab} C_{ij}^{ab} a_a^\dagger a_b^\dagger a_j a_i\,, \quad (2.52)$$

which are constructed by solving the CISD eigenvalue problem

$$H|\Psi_0^{CISD}\rangle = E_{CISD}|\Psi_0^{CISD}\rangle\,, \quad (2.53)$$

contain unlinked diagrams composed of the bare interaction vertices.

2.7 Coupled Cluster Theory

The resummation of perturbation theory exhibited by CI motivates a size-extensive counterpart, called coupled cluster (CC) theory [11, 25]. CC theory reorganizes the CI expansion into an expo-

nential expansion of cluster operators,

$$exp[T_1 + T_2 + T_3 + \cdots + T_A] \equiv 1 + \mathscr{C}_1 + \mathscr{C}_2 + \mathscr{C}_3 + \cdots + \mathscr{C}_A \,, \tag{2.54}$$

where T_N are the N-body cluster operators defined by

$$T_N = \sum_{m=1}^{\infty} \{R_0 H_I\}^m_{C,N} \,, \tag{2.55}$$

where the subscript (C,N) denotes connected terms with $2N$ external lines. Rewriting the expansion in this way allows us to make a size-extensive many-body truncation on the cluster operators, denoted as CCSD, CCSDT, and so on. Thus the CCSD ground state is

$$|\Psi_0^{CCSD}\rangle = exp[\sum_{ai} t_i^a \{a_a^\dagger a_i\} + \frac{1}{4} \sum_{abij} t_{ij}^{ab} \{a_a^\dagger a_b^\dagger a_j a_i\}]|\Phi_0\rangle \,. \tag{2.56}$$

In coupled-cluster calculations, the exponential operator e^T is a similarity transformation,

$$H|\Psi_0\rangle = E_0|\Psi_0\rangle \rightarrow e^{-T} H e^T |\Phi_0\rangle = E_0|\Phi_0\rangle \rightarrow \bar{H}|\Phi_0\rangle = E_0|\Phi_0\rangle \,, \tag{2.57}$$

which is applied to the Hamiltonian and used to derive a system of algebraic equations in the intermediate normalization,

$$\langle\Phi_0|\bar{H}|\Phi_0\rangle = E_0 \qquad \langle\Phi_{\alpha\neq 0}|\bar{H}|\Phi_0\rangle = 0 \,. \tag{2.58}$$

Thus, CCSD calculations are carried out by solving eqs. 2.58 for the cluster amplitudes t_i^a, t_{ij}^{ab} and the energy E_0, with α ranging over all singly- and doubly-excited Slater determinants. Here it is possible to show that the MBPT energy through third-order is included completely in the CCSD energy, with incomplete but size-extensive contributions from all orders of perturbation theory included in addition to MBPT(3). This is a marked improvement over MBPT, as the time complexity is the same, yet significantly more components of the infinite MBPT energy expansion are included in the ground state energy and wave function.

The many-body truncations used here lead to large errors when confronted with hard core potentials where HF is often unbound, but these methods have become popular in nuclear physics in

the past decade, as the number of soft perturbative potentials such as those from chiral EFT has been rapidly increasing. CCSD and perturbative approximations to CCSDT, such as Λ-CCSD(T) and completely renormalized CCSD(T) (CR-CC(2,3)), have ushered in a new era of *ab initio* calculations in nuclei, providing access to nuclei in the vicinity of closed shells throughout the medium-mass region [41, 49, 50, 57, 58, 115, 116].

Along with CC theory, additional methods such as the self-consistent Green's function (SCGF) method [53–55] and the in-medium similarity renormalization group (IMSRG) [43, 44, 46] offer alternative tactics to resum MBPT in a size-extensive framework. The IMSRG, which is of principle interest in this work, uses a modified exponential ansatz to produce a similar resummation to CC theory in a Hermitian framework,

$$|\Psi_0^{IMSRG}(s)\rangle = e^{-\Omega(s)}|\Phi_0\rangle\,. \tag{2.59}$$

Here $\Omega(s)$ is an anti-Hermitian operator and consequently the similarity transformation is unitary. The Hermitian framework is extremely desirable as it allows for simplistic extensions of the method, such as the multireference IMSRG (MR-IMSRG) [45, 47], which targets open shell nuclei. The IMSRG offers Hermitian calculations at comparable computational cost to CC theory, but a consequence of this Hermiticity is that the IMSRG cannot construct the intuitive system of equations in 2.58. Instead, the IMSRG transformation is applied as a differential flow equation,

$$\frac{d\bar{H}(s)}{ds} = [\eta(s), \bar{H}(s)]\,, \tag{2.60}$$

where $\eta(s)$ is the arbitrary anti-Hermitian generator of the transformation. Alternatively, one can solve for $\Omega(s)$ directly using the Magnus expansion [117]. This method will be explored in detail in chapter 3, and extended to the calculation of excited states and general observables in chapters 4 and 5, respectively.

CHAPTER 3

IN-MEDIUM SIMILARITY RENORMALIZATION GROUP

As mentioned in previous chapters, much progress has recently been made in *ab initio* nuclear structure, largely due to the development of renormalization group methods to produce soft "low-momentum" interactions from underlying "hard" interactions while preserving observables. Such potentials greatly facilitate many-body methods which expand wave functions in a finite basis of localized single-particle orbitals, as convergence is achieved with much smaller bases using softened potentials. Because softened interactions reduce the effects of short-range correlations, Hartree-Fock becomes a reasonable starting point for methods like many-body perturbation theory and coupled cluster theory, and consequently these methods have flourished in the presence of these innovations.

In this chapter, we will flesh out the fundamentals of the IMSRG approach, which extends the RG concept of decoupling low- and high-momentum degrees of freedom to the decoupling of states in the many-body Hilbert space. Here we formulate "in-medium" flow equations; the solution of which is tantamount to the block-diagonalization of the many-body Hamiltonian [43–48]. The IMSRG offers the ability to target ground and excited states in both closed- and open-shell nuclei, and as it exhibits polynomial scaling with system size, the method is a powerful *ab initio* approach for medium-mass nuclei. We discuss recent results, as well as some advances in the implementation of the method. We review the Magnus expansion variant of the IMSRG, which enables the explicit construction of the unitary transformation. We also briefly review the perturbative resummation of the IMSRG(2), and discuss corrections to this resummation which are motivated by the availability of the unitary transformation via the Magnus generator.

3.1 The Similarity Renormalization Group

The similarity renormalization group (SRG) can be viewed as a continuous sequence of unitary transformations,

$$U^\dagger U = U U^\dagger = \mathbb{1}\,, \tag{3.1}$$

which by construction preserves the inner product of two vectors, and consequently the eigenvalues of all operators. Renormalization groups (RGs) are designed to exploit separation of scales in physical problems. The SRG was developed independently by Wegner [118], for the solution of many-body problems in condensed matter physics, and Głazek and Wilson [119], who developed the procedure for Hamiltonians in light-front quantum field theory. The SRG was subsequently ported to nuclear physics, where it was used to decouple low- and high-momentum modes in the input inter-nucleon interactions [9,39,120–124]. This was motivated by the fact that realistic interactions which give a good description of low energy nuclear observables tend to feature strongly repulsive cores and strong tensor forces [21, 39, 125]. Both of these features produce strong couplings between low- and high-momentum states in the many-body Hamiltonian, which in turn leads to computationally demanding matrix diagonalizations due to the large couplings between energetically well-separated basis states. The SRG can be used as a means to soften this core, and thus reduce the off-diagonal couplings in momentum-space via a suitably chosen unitary transformation.

3.1.1 Formalism

If we parameterize the SRG transformation by some arbitrary flow variable s, we can then take the derivative of eq. 3.1,

$$\frac{dU(s)}{ds} U^\dagger(s) + U(s) \frac{dU^\dagger(s)}{ds} = 0\,, \tag{3.2}$$

which yields a differential equation for the explicit form of the unitary transformation,

$$\frac{dU(s)}{ds} = -\eta(s) U(s)\,. \tag{3.3}$$

Here $\eta(s)$ is the so-called generator of the unitary transformation

$$\eta(s) \equiv \frac{dU(s)}{ds}U^\dagger(s) = -U(s)\frac{dU^\dagger(s)}{ds} = -\eta^\dagger(s)\,, \tag{3.4}$$

where the constraint of anti-Hermiticity immediately follows from eq. 3.2. The solution of eq. 3.3 is the s-ordered exponential,

$$U(s) = \mathscr{S}exp(-\int_0^s ds'\eta(s')) \equiv \lim_{N\to\infty}\left(e^{\eta(s_N)\delta s}e^{\eta(s_{N-1})\delta s}\ldots e^{\eta(s_1)\delta s}e^{\eta(s_0)\delta s}\right). \tag{3.5}$$

The s-ordering assures that the sequence of infinitesimal transformations, which are in general non-commutative, will be applied in the correct order. In practice, using this form of the transformation requires storage of the generator at each step in the s-evolution. One may circumvent the complications of ordered exponential operators by use of flow equations to determine the form of SRG evolved operators. For any operator O, the similarity transformation takes the form

$$\bar{O}(s) = U(s)OU^\dagger(s)\,. \tag{3.6}$$

Taking the derivative,

$$\frac{d\bar{O}(s)}{ds} = \frac{d}{ds}[U(s)OU^\dagger(s)] = \frac{dU(s)}{ds}OU^\dagger(s) + U(s)O\frac{dU^\dagger(s)}{ds} = [\eta(s), U(s)OU^\dagger(s)]\,, \tag{3.7}$$

we arrive at the SRG differential flow equation

$$\frac{d\bar{O}(s)}{ds} = [\eta(s), \bar{O}(s)]\,. \tag{3.8}$$

The power of eq. 3.8 is the ability to apply the SRG transformation numerically without retaining knowledge of η for all values of s. As the only constraint on η is that the operator must be anti-Hermitian, it can be chosen to construct Hamiltonians tailored for particular many-body methods.

A general prescription for choosing an SRG generator was proposed by Wegner [118],

$$\eta(s) \equiv [H^d(s), H^{od}(s)]\,, \tag{3.9}$$

where H^d and H^{od} are arbitrarily defined diagonal and off-diagonal components of the Hamiltonian. H^d need not be limited to the literal diagonal of the matrix, but rather describes the desired form of the rotated operator, which may be band- or block-diagonal. Such a choice of generator clearly produces a fixed point in the flow equation 3.8 if H^{od} becomes zero for some value of s. If such a condition arises, the flow equation can be evolved to $s \to \infty$, and the desired decoupling will be achieved. Coincidental commutation of H^d and H^{od} will also create a fixed point, but such an incidence has not been observed in practice.

3.1.2 A Practical Example

As a pedagogical example, it is instructive to consider a two-body system in momentum-space, where we can express the problem in relative coordinates. The flowing Hamiltonian is

$$H(s) = T_{rel} + V(s)\,, \tag{3.10}$$

where the kinetic energy T_{rel} is independent of s by construction, and is diagonal in momentum space. The residual s-dependence is absorbed into the potential $V(s)$ and equation 3.9 becomes

$$\eta(s) = [T_{rel}, V(s)]\,. \tag{3.11}$$

Plugging eq. 3.11 into eq. 3.8, we can show that for a given partial wave in momentum space [121],

$$\frac{dV(k_1,k_2,s)}{ds} = -(k_1^2 - k_2^2)^2 V(k_1,k_2,s) + \frac{2}{\pi}\int_0^\infty q^2 dq (k_1^2 + k_2^2 - 2q^2) V(k_1,q) V(q,k_2)\,. \tag{3.12}$$

The solution of eq. 3.12 for strongly off-diagonal terms is dominated by the linear term,

$$V(k_1,k_2,s) \approx V(k_1,k_2,0) exp(-(k_1^2 - k_2^2)^2 s)\,. \tag{3.13}$$

Eq. 3.13 demonstrates proper RG behavior, where farther off-diagonal matrix elements decay at an increased rate, quantified by the lifetime

$$\lambda(k_1,k_2) = \frac{1}{(k_1^2 - k_2^2)^2}\,. \tag{3.14}$$

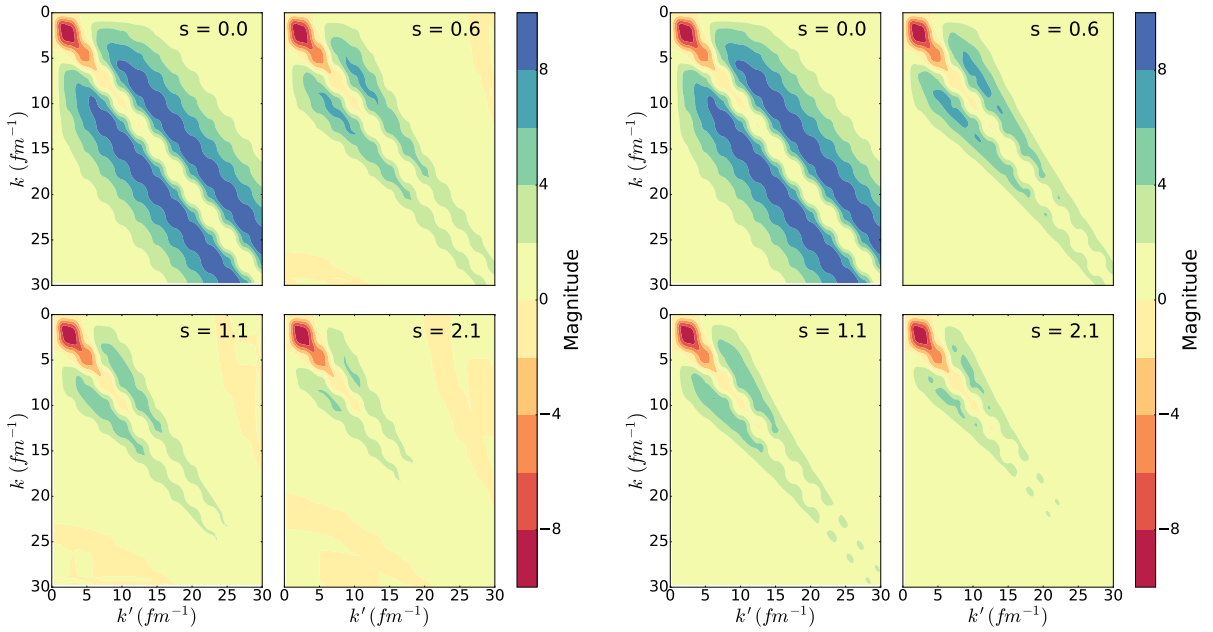

Figure 3.1 SRG evolution of the two-body Hamiltonian in momentum space. In the left panel, we show solution of eq. 3.8 for select values of s. In the right panel we show the non-unitary decay of matrix elements when given a half-life corresponding to eq. 3.14.

A simple example is provided by the 1d mock-up of a local nuclear interaction suggested by Negele and Orland [126]:

$$V(k_1,k_2) = V_1(e^{(-\alpha_1(k1-k2)^2)} - e^{(-\alpha_1(k1+k2)^2)}) \\ - V_2(e^{(-\alpha_2(k1-k2)^2)} - e^{(-\alpha_2(k1+k2)^2)}). \tag{3.15}$$

Here $V_1 = V_2$=12.0 fm^{-2}, α_1 = 0.01 fm^2 and α_2 = 0.16 fm^2. We analyze this potential for the case of two particles, where constructing the many-body Hamiltonian is as simple as discretizing the relative momentum and evaluating V at each point. For purposes of demonstration, we use a modest 120 relative momentum states, building a momentum grid with spacing 0.25 fm^{-1}. Here we may demonstrate the SRG's properties exactly, as at most two-body forces are needed.

This potential does not induce extreme scattering from low to high momentum, but those modes are coupled through the band diagonal structure, shown in the $s = 0.0$ panels of fig. 3.1. While one could easily diagonalize this small matrix using a packaged solver, much insight is to be gained

by performing the SRG exactly. For reference, the right panel of fig. 3.1 shows the decay pattern if eq. 3.13 were the only contribution to the SRG evolution. The left panel demonstrates the exact SRG flow, where additional features are present. It is evident that the broad features of the flow are very similar in either case, but fine details are present in the SRG flow which account for unitary equivalence.

This SRG softening allows for a significant reduction in storage requirements with minimal loss of accuracy in the ground state energy. For this system, diagonalization of the unevolved operator gives a ground state energy of -0.473 fm^{-2}. If the diagonalization is instead performed with only the first 90 basis states, the result is 46.000 fm^{-2}, clearly an unsuitable result. However, after SRG softening to s=2.1$\times 10^{-4}$ fm^4, both the 90 and full 120 state diagonalizations yield -0.473 fm^{-2}. Additional softening further reduces the number of basis states needed for a converged ground state energy.

For notational purposes, we note that SRG softened forces are often specified by a momentum-cutoff $\lambda_{SRG} = s^{-1/4}$, in natural units. We can think of λ_{SRG} as a scale for the maximum size of momentum transfer between nucleons allowed after SRG softening [39, 121].

3.1.3 SRG Softening of Interactions

The primary use of the SRG is to pre-process nuclear interactions, making them more amenable to many-body calculations [18, 40, 45, 47, 48, 53–55, 63, 89, 102, 116, 124, 127–129]. NN and 3N interactions from χ-EFT are applied to many-body calculations using the second-quantized Hamiltonian:

$$H = \sum_{\mathbf{k}} \frac{k^2}{2} a^\dagger_{\mathbf{k}} a_{\mathbf{k}} + \frac{1}{4} \sum_{\mathbf{k}_1\mathbf{k}_2\mathbf{k}_3\mathbf{k}_4} \langle \mathbf{k}_1\mathbf{k}_2|V^{(2)}|\mathbf{k}_3\mathbf{k}_4\rangle a^\dagger_{\mathbf{k}_1} a^\dagger_{\mathbf{k}_2} a_{\mathbf{k}_4} a_{\mathbf{k}_3} + \frac{1}{36} \sum_{\substack{\mathbf{k}_1\mathbf{k}_2\mathbf{k}_3 \\ \mathbf{k}_4\mathbf{k}_5\mathbf{k}_6}} \langle \mathbf{k}_1\mathbf{k}_2\mathbf{k}_3|V^{(3)}|\mathbf{k}_4\mathbf{k}_5\mathbf{k}_6\rangle a^\dagger_{\mathbf{k}_1} a^\dagger_{\mathbf{k}_2} a^\dagger_{\mathbf{k}_3} a_{\mathbf{k}_6} a_{\mathbf{k}_5} a_{\mathbf{k}_4} \,. \tag{3.16}$$

Here $V^{(2)}$ and $V^{(3)}$ in general connect two- and three-body kets with bras containing elements with drastically different momentum components, which is a hallmark of a hard-core interaction, and is

largely responsible for convergence difficulties in many-body methods based on diagonalization.

Starting from unevolved quantities, the Wegner generator (eq. 3.9) is

$$\eta = \sum_{\text{all } \mathbf{k}} \frac{k_7^2}{2} \Bigg(\langle \mathbf{k}_1 \mathbf{k}_2 | V^{(2)} | \mathbf{k}_3 \mathbf{k}_4 \rangle [a^\dagger_{\mathbf{k}_7} a_{\mathbf{k}_7}, a^\dagger_{\mathbf{k}_1} a^\dagger_{\mathbf{k}_2} a_{\mathbf{k}_4} a_{\mathbf{k}_3}] + \langle \mathbf{k}_1 \mathbf{k}_2 \mathbf{k}_3 | V^{(3)} | \mathbf{k}_4 \mathbf{k}_5 \mathbf{k}_6 \rangle [a^\dagger_{\mathbf{k}_7} a_{\mathbf{k}_7}, a^\dagger_{\mathbf{k}_1} a^\dagger_{\mathbf{k}_2} a^\dagger_{\mathbf{k}_3} a_{\mathbf{k}_6} a_{\mathbf{k}_5} a_{\mathbf{k}_4}] \Bigg), \tag{3.17}$$

where the commutators of the first and second terms yield two and three-body operators respectively. Thus, $\eta(s)$ is in principle a many-body operator. Solution of eq. 3.8 will necessarily induce higher order operators, as the commutator of two three-body operators includes up to five-body operators. It is apparent that to retain an exact unitary transformation, the A-body nucleus will require up to A-body induced forces. Of course, this is intractable computationally, and in fact, including three-body forces is a demanding challenge which has only recently become feasible [9, 123, 124, 130, 131]. Nonetheless, it has been shown that inclusion of the three-body force is absolutely imperative [130], as truncation to two-body operators has been linked to strong s-dependence in many-body observables. The errors introduced by truncating four-body forces and higher are ostensibly smaller than those of missing three-body forces, provided we do not make absurd demands of our SRG transformation. Softening beyond a certain point will almost certainly induce large many-body forces, so one must take care to stop at a reasonable value of λ_{srg}. Typical choices are between $\lambda_{srg} = 1.8$ and 4.0 fm^{-1}.

3.2 The In-Medium Similarity Renormalization Group

The free-space SRG formalism has had great success as a method to soften input nuclear interactions for few- and many-body calculations, but the general SRG concept can be extended to serve as an *ab initio* method in and of itself when the evolution is performed directly in the A-body system. The in-medium similarity renormalization group (IMSRG) applies eq. 3.8 to the many-body Hamiltonian after normal-ordering with respect to an A-body reference state. In this context, the

application of the SRG seeks to renormalize couplings between A-body basis states, i.e. Slater determinants (SD).

3.2.1 The In-Medium Similarity Renormalization Group Equations

With the power of normal-ordering, which was discussed in sec. 2.3, we may derive the in-medium variant of the SRG, by normal-ordering the generators and operators with respect to the A-body reference state, and evaluating eq. 3.8 using Wick's theorem. The critical component of this derivation is the computation of the commutator of two normal-ordered two-body operators,

$$[A,B]^{(0b)} = \sum_{ab}(n_a - n_b)A_{ab}B_{ba} + \frac{1}{4}\sum_{abcd}(A_{abcd}B_{cdab} - B_{abcd}A_{cdab})n_a n_b \bar{n}_c \bar{n}_d \,, \tag{3.18}$$

$$\begin{aligned}[A,B]^{(1b)}_{qr} = &\sum_{a}(A_{qa}B_{ar} - B_{qa}A_{ar}) + \sum_{ab}(n_a - n_b)(A_{ab}B_{bqar} - B_{ab}A_{bqar}) \\ &+ \frac{1}{2}\sum_{abc}(n_a n_b \bar{n}_c + \bar{n}_a \bar{n}_b n_c)(A_{cqab}B_{abcr} - B_{cqab}A_{abcr}) \,,\end{aligned} \tag{3.19}$$

$$\begin{aligned}[A,B]^{(2b)}_{qrst} = &\sum_{a}((A_{qa}B_{arst} + A_{ra}B_{qast} - B_{qa}A_{arst} - B_{ra}A_{qast}) \\ &- (A_{as}B_{qrat} + A_{at}B_{qrsa} - B_{as}A_{qrat} - B_{at}A_{qrsa})) \\ &+ \frac{1}{2}\sum_{ab}(1 - n_a - n_b)(A_{qrab}B_{abst} - A_{qrab}B_{abst}) \\ &- \sum_{ab}(n_a - n_b)(1 - P_{qr})(1 - P_{st})A_{brat}B_{aqbs} \,.\end{aligned} \tag{3.20}$$

Here n_i is the reference state occupation number for the ith orbital, and $\bar{n}_i = (1 - n_i)$ and P_{qr} exchanges the indices q and r. The commutator of two-body operators will also have three-body components, but we will only concern ourselves with the two-body components, anticipating that this truncation will cause minimal error in the final results of computations in the NO2B approximation. Plugging these expressions into eq. 3.8, we arrive at the IMSRG(2) flow equations

$$\frac{dE_0}{ds} = \sum_{ab}(n_a - n_b)\eta_{ab}f_{ba} + \frac{1}{2}\sum_{abcd}\eta_{abcd}\Gamma_{cdab}n_a n_b \bar{n}_c \bar{n}_d \,, \tag{3.21}$$

$$\frac{df_{qr}}{ds} = \sum_a (1+P_{qr})\eta_{qa}f_{ar} + \sum_{ab}(n_a - n_b)(\eta_{ab}\Gamma_{bqar} - f_{ab}\eta_{bqar}) + \frac{1}{2}\sum_{abc}(n_a n_b \bar{n}_c + \bar{n}_a \bar{n}_b n_c)(1+P_{qr})\eta_{cqab}\Gamma_{abcr}\,, \tag{3.22}$$

$$\begin{aligned}\frac{d\Gamma_{qrst}}{ds} = &\sum_a ((1-P_{qr})(\eta_{qa}\Gamma_{arst} - f_{qa}\eta_{arst}) \\ &- (1-P_{st})(\eta_{as}\Gamma_{qrat} - f_{as}\eta_{qrat})) \\ &+ \frac{1}{2}\sum_{ab}(1-n_a-n_b)(\eta_{12ab}\Gamma_{ab34} - \Gamma_{12ab}\eta_{ab34}) \\ &- \sum_{ab}(n_a - n_b)(1-P_{12})(1-P_{34})\eta_{b2a4}\Gamma_{a1b3}\,.\end{aligned} \tag{3.23}$$

The name IMSRG(2) refers to the truncation of the commutators to two-body operators. While here we have only included two-body operators, taking the commutator of an N- and M-body operator results in an $(N+M-1)$-body operator, thus an exact solution of the IMSRG equations will produce up to A-body forces for an A-body nucleus. IMSRG(A), where up to A-body operators are included in the commutator expressions and IMSRG equations, would then produce the same result as FCI, making it an exact method within a given model-space. Naturally, any implementation of this exact method would pose the same computational difficulties as the FCI calculation itself. The utility of the IMSRG lies in the ability to make systematically improvable, size-extensive truncations on the CI expansion, such as IMSRG(2) or the next level of IMSRG(3), which keep normal-ordered three-body operators in the flowing Hamiltonian and generator. In practice, the commutator expressions are often implemented in JJ-coupled scheme (see appendix), where spherical symmetry is exploited by summing magnetic substates out of the single-particle and many-body bases using the Wigner-Eckart theorem.

3.2.2 Choice of Generator

A variety of generator choices have been explored for IMSRG calculations [3, 48]. As in the free-space SRG, the specific choice of generator reflects the desired decoupling scheme. For ground-state calculations, one seeks to decouple the reference state from the block of particle-hole excited

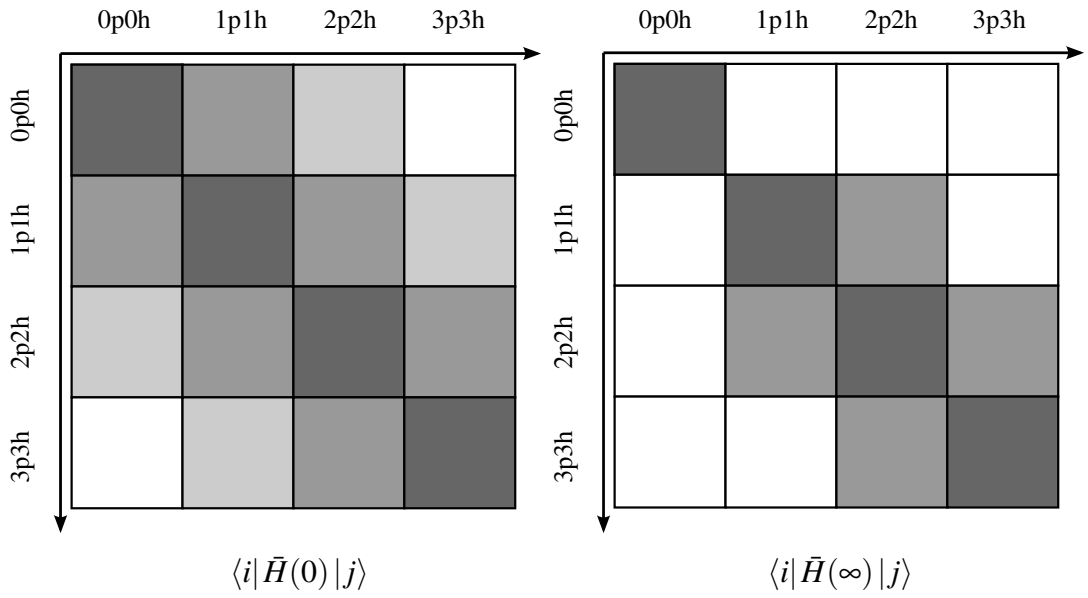

Figure 3.2 Schematic representation of the initial and ground-state-decoupled Hamiltonians, $\bar{H}(0)$ and $\bar{H}(\infty)$, in the many-body Hilbert space spanned by particle-hole excitations of the reference state.

Slater determinants. Fig. 3.2 demonstrates this schematically, where we have included up to 3p3h states in the visualization. In the left panel we see that the reference state is coupled to particle-hole excitations through the 1p1h and 2p2h channels. These matrix elements are induced by the f_{ph} and $\Gamma_{pp'hh'}$ terms in eq. 2.25,

$$\langle \Phi_h^p | H | \Phi_0 \rangle = f_{ph}\,, \tag{3.24}$$

$$\langle \Phi_{hh'}^{pp'} | H | \Phi_0 \rangle = \Gamma_{pp'hh'}\,, \tag{3.25}$$

as well as their Hermitian conjugates. Here p and h denote particle and hole indices respectively. The generator of the IMSRG unitary transformation thus should be designed to suppress

$$H^{od} = \sum_{ij} f_{ij}(\bar{n}_i n_j + \bar{n}_j n_i)\{a_i^\dagger a_j\} + \frac{1}{4}\sum_{ijkl}\Gamma_{ijkl}(\bar{n}_i\bar{n}_j n_k n_l - \bar{n}_k\bar{n}_l n_i n_j)\{a_i^\dagger a_j^\dagger a_l a_k\}\,. \tag{3.26}$$

With this definition, the Wegner choice can be computed using eq. 3.9, and the desired decoupling is achieved with leading off-diagonal behavior

$$\Gamma(s)_{pp'hh'} \approx \Gamma(0)_{pp'hh'} e^{-(\Delta_{hh'}^{pp'})^2 s}\,. \tag{3.27}$$

Here $\Delta^{pp'}_{hh'} = (f_{pp} + f_{p'p'} - f_{hh} - f_{h'h'})$ is the Møller-Plesset (MP) energy difference. Analogous to the free-space variant, the decay rate of off-diagonals is mediated by this energy difference. As a result, the differential flow equations are moderately stiff when solved with this generator. This means that at different points in the flow, different terms will be emphasized for suppression in the differential equation, and thus numerical complications can arise. Under these circumstances, calculations will have difficulty converging, and often a more sophisticated and memory intensive ordinary differential equation solver will be required to solve the flow equations.

More numerically practical generators can be devised to mitigate the stiffness by making the lifetimes of off-diagonal matrix elements less dependent on the single particle energy spectrum. An example is proposed by White, following from the theory of Jacobi canonical diagonalization [43, 132],

$$\eta^{(1)}_{ij} = \frac{f^{od}_{ij}}{\Delta^{i}_{j}} \qquad \eta^{(2)}_{ijkl} = \frac{\Gamma^{od}_{ijkl}}{\Delta^{ij}_{kl}}\,, \tag{3.28}$$

where the Δ may be either MP or Epstein-Nesbet (EN) denominators. The definition is chosen to conceptually match the IMSRG rotation to a Jacobi rotation, by scaling individual off-diagonal matrix elements by the angle with which they must be rotated in order for suppression. At leading order, off-diagonals are suppressed like

$$\Gamma(s)_{pp'hh'} \approx \Gamma(0)_{pp'hh'} e^{-s}\,, \tag{3.29}$$

which means all elements decay at a similar rate, and thus stiffness is relieved.

The cost of this drastic reduction in stiffness is the presence of explicit energy denominators in eq. 3.28, which may potentially become small during the course of IMSRG decoupling. Such an event would certainly create pathological behavior in the flow and derail the computation. A reasonable compromise between the Wegner and White generators can be inferred by starting from the general form

$$\eta_\alpha = (\Delta_\alpha)^\gamma H^{od}_\alpha\,. \tag{3.30}$$

Here α denotes a general set of indices, and γ an integer power. For the White generator, γ=-1, and for Wegner's choice γ=1 at leading order in the interaction vertices. The compromise, known

as the imaginary-time generator [47], is found at γ=0,

$$\eta^{(1)}_{ij} = f^{od}_{ij} g(\Delta^i_j) \qquad \eta^{(2)}_{ijkl} = \Gamma^{od}_{ijkl} g(\Delta^{ij}_{kl}), \tag{3.31}$$

where $g(x)$ is some odd regulator function which ensures an anti-Hermitian η. Here we get an off-diagonal decay of

$$\Gamma(s)_{pp'hh'} \approx \Gamma(0)_{pp'hh'} e^{-\Delta^{pp'}_{hh'} s}, \tag{3.32}$$

which is more stiff than the White generator, but less so than Wegner.

In practical applications of the IMSRG, the White generator is often sufficient. However, in decouplings which strongly renormalize the single-particle spectra, it is useful to employ the imaginary-time generator to avoid vanishing energy denominators. For the remainder of this dissertation, it should be assumed that the White generator is applied, and use of any other generator will be specified explicitly.

3.2.3 Solving the IMSRG Equations

We can analyze the IMSRG equations by writing them in terms of Hugenholtz diagrams. Diagrammatically, eq. 3.21 becomes

$\frac{d}{ds}E =$ 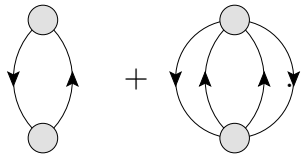 (3.33)

Figure 3.3 Schematic zero-body flow.

where $\eta(s)$ is proportional to $H(s)$, and MBPT energy denominators are included within the definition of η. The gray circles represent renormalized or *dressed* vertices, which have s-dependence. If we discretize the flow and take light gray circles to be $\Gamma(2\delta s)$, dark gray as $\Gamma(\delta s)$, and a small black circle as the bare vertex $\Gamma(0)$, we may represent the integration step of eq. 3.23 for $\Gamma(2\delta s)$ in terms of the vertex of the previous step, and again in terms of the bare vertex:

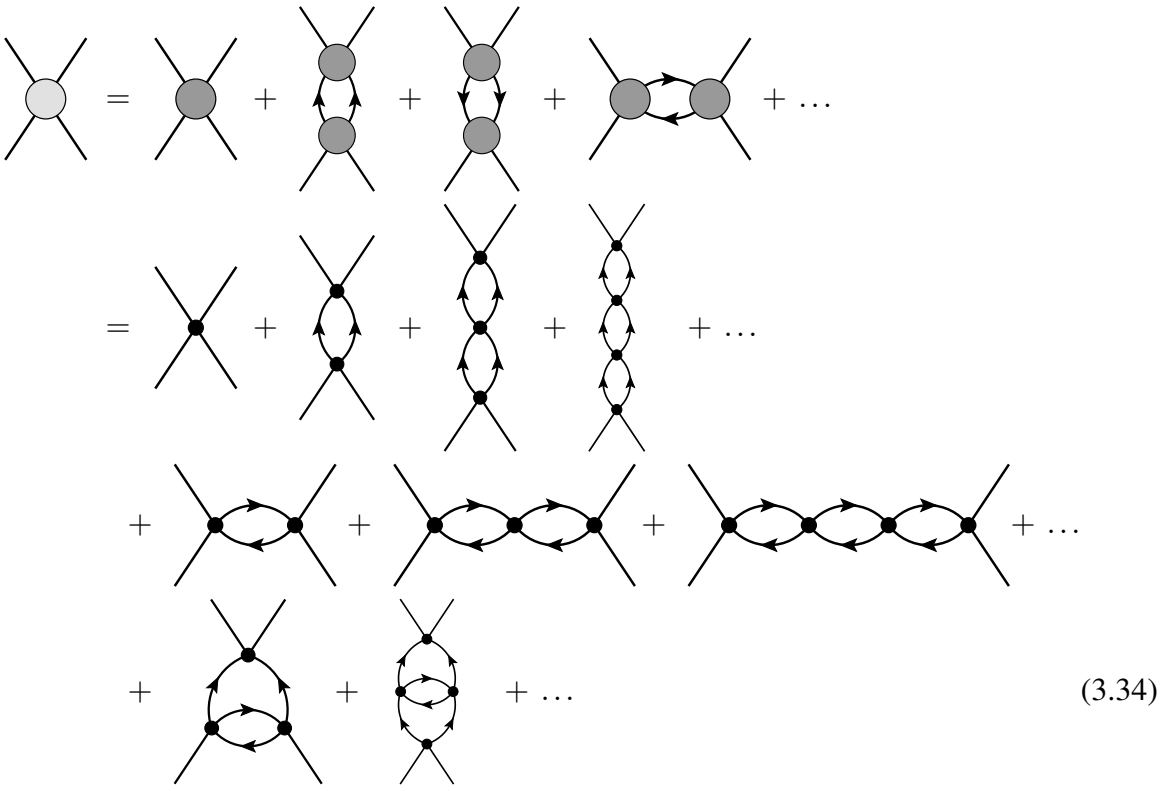

(3.34)

Figure 3.4 Schematic resummation of MBPT diagrams.

This representation illustrates an important feature of the IMSRG equations; solving them sums higher-orders of MBPT into the flowing vertices. In the first row, we see that IMSRG renormalizes short-range physics with the resummation of all particle-particle and hole-hole ladders into the dressed vertex, similar to Brueckner G-matrix approaches [112, 114, 133–136]. Additionally, long-range physics is consistently included with the resummation of particle-hole chains, which is a feature of the random phase approximation (RPA) [100,114,136]. On top of incorporating the resummations of both of these well known methods, the IMSRG incorporates interference diagrams between ladder and chain components. In the limit of IMSRG(A), an exact solution of the IMSRG equations would result in a complete infinite resummation of MBPT. As the IMSRG is truncated to two-body operators in practice, this resummation is only approximate, but can be shown to be exact up to third-order, while also containing extensive, but incomplete, content from all orders of perturbation theory [3].

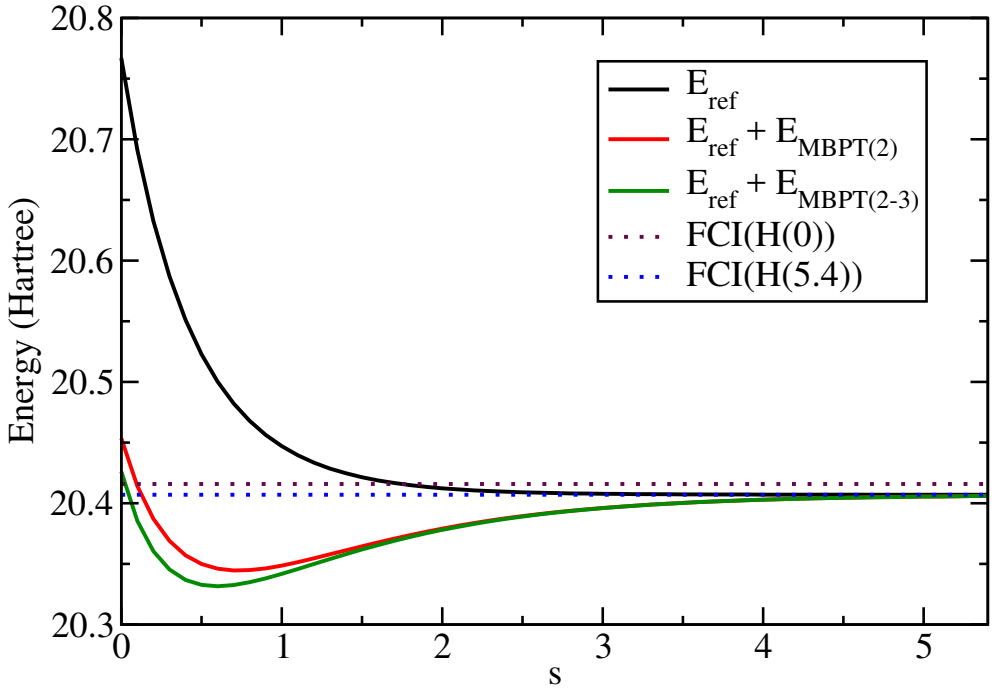

Figure 3.5 IMSRG ground-state-decoupling for a 6-electron quantum dot, with $\omega = 1.0$ and four major oscillator shells. Hartree-Fock energy, second-, and third-order MBPT energies are plotted as function of flow parameter s. Exact energies for the *bare* and *dressed* Hamiltonians are given for reference.

This point is illustrated in practice by fig. 3.5, which demonstrates a typical IMSRG ground-state-decoupling for a 6-electron parabolic quantum dot in two dimensions. Parabolic quantum dots consist of A electrons confined by a harmonic oscillator potential in two dimensions. In atomic units, the Hamiltonian is given by:

$$H = \sum_{i=1}^{A} [\frac{1}{2} p_i^2 + \frac{1}{2}\omega^2 r_i^2] + \frac{1}{2} \sum_{i \neq j}^{A} \frac{1}{|\mathbf{r}_i - \mathbf{r}_j|} . \tag{3.35}$$

Quantum dots provide an excellent testing ground for approximate many-body methods, as the strength of many-body correlations can be controlled by varying ω, with smaller values corresponding to stronger correlations, and comparisons can be made to exact full configuration in-

teraction (FCI) calculations in sufficiently small bases. In the present work, all calculations are performed for the 6-electron system. The IMSRG(2) equations are solved here using a high-order adaptive step solver (see below), so numerical errors in the solution of the ODE should be negligible here. At s=0, the solid lines correspond to so-called *bare* quantities, which are yet to be renormalized. Thus the reference energy corresponds to the Hartree-Fock (HF) energy and the perturbative corrections represent standard MBPT. For reference, the dotted purple line gives the exact energy, $E_{gs}(0)$ = 20.4158 Hartree, computed with FCI using the bare Hamiltonian. The IMSRG equations are propagated forward to s=5.4, where numerical convergence has been obtained. At this point, some truncation errors due to the neglect of induced higher-body forces have accumulated; for reference the exact result using the dressed Hamiltonian, $E_{gs}(5.4)$ = 20.4070 Hartree, is given by the dotted blue line. The truncation error amounts to less than 10 mH, which is on the order of chemical precision.

Note that as the IMSRG(2) equations are solved, the HF energy becomes equivalent to the correlated ground state energy of the dressed Hamiltonian. This is due to complete decoupling of the reference state from excitations, as illustrated in fig. 3.2. As the flow converges, the second- and third-order energy corrections are diminished to zero, consistent with the expectation of a resummation of MBPT. Note that the perturbative corrections have strong s-dependence, indicating that higher-order corrections are also being summed into the reference energy during the flow. While the MBPT(3) appears to capture the vast majority of the correlation energy here, this will not be the case for more strongly correlated systems such as nuclei. This indicates a clear preference for IMSRG, as the dominant contribution to the scaling of the IMSRG(2) equations goes as $\mathcal{O}(N_p^4 N_h^2)$, which is the same as MBPT(3), while including higher-order terms such as ladder summations and bubble chains.

The previous calculation, as well as the original implementation of the IMSRG [43–45], employed a high-order ordinary differential equation (ODE) solver to solve eqs. 3.21-3.23 directly. High-order predictor/corrector methods such as the Shampine and Gordan implementation of Adams-Bashforth [137] are necessary to solve the IMSRG equations accurately, as accumulated

numerical errors in low-order solvers rapidly degrade the unitarity of the IMSRG transformation to the point where computed eigenvalues can have sizable errors. High-order adaptive step solvers require anywhere from 10-25 copies of the ODE, and thus memory requirements can be extraordinary for computations with large model spaces. Additionally, the flow equation (eq. 3.8) must be solved individually for every operator of interest in order to compute observables consistently. This means that the memory requirements, which are already demanding for a single operator, scale linearly with the number of observables requested.

Many of these complications were mitigated by the development of the Magnus expansion variant of the IMSRG [6]. The Magnus expansion [117] provides an expression for ordered-exponentials in the form of a true exponential,

$$U(s) \equiv exp(-\Omega(s)) = \mathscr{S} exp(-\int_0^s ds' \eta(s'))\,, \tag{3.36}$$

where the components of the Magnus generator $\Omega(s)$ follow from the differential equation

$$\frac{d\Omega}{ds} = \sum_{j=0}^{\infty} \frac{B_j}{j!} ad_\Omega^j \eta(s)\,, \tag{3.37}$$

where B_j are Bernoulli numbers ($B_0 = 1, B_1 = -1/2\,, B_2 = 1/6, \ldots$) and

$$ad_\Omega^0 \eta(s) = \eta(s)\,, \quad ad_\Omega^j \eta(s) = [\Omega(s), ad_\Omega^{j-1} \eta(s)]\,. \tag{3.38}$$

This method is an exact reformulation of the IMSRG, provided that no truncations are made. Of course, the flow equation approach is truncated to two-body operators, and any practical implementation of the Magnus variant requires a similar truncation, as well as numerical termination of the expansion at a reasonable number of terms. As evaluation of eq. 3.37 depends on the same generator as eq. 3.8 and requires computation of only one commutator at at time, it can be solved with the same machinery that one might use in the flow equation method. The expressions 3.18-3.20 can be used for the evaluation of $ad_\Omega^j \eta(s)$, where the only difference from the flow equation approach is that both operators are anti-Hermitian.

The Magnus formalism avoids the complications of using a sophisticated ODE solver, as numerical step-size errors in the exponential operator do not degrade the unitary transformation,

because even if time-step errors are significant, upon exponentiation of the anti-Hermitian $\Omega(s)$, a unitary transformation is still realized. However, numerical errors will still accumulate in the exponentiation procedure, (i.e. applying the transformation to an operator), so care must be taken to assure that the desired transformation is achieved as quickly as possible. If we do not retain a reasonable amount of numerical accuracy in the solution of eq. 3.37, we will not achieve the desired decoupling and eventually errors from applying the transformation will destabilize the calculation. Consequently, the Magnus variant of the IMSRG may be solved with a rudimentary forward Euler step, but we cannot take arbitrarily large steps in s without changing the nature of the unitary transformation so far as to increase off-diagonal pieces rather than suppress them. The most useful property of the Magnus formalism is that eq. 3.37 need only be solved once, and all other observables follow from application of the explicitly constructed unitary transformation using the well known Baker-Campbell-Hausdorff expansion,

$$\bar{O}(s) = \sum_{j=0}^{\infty} \frac{1}{j!} ad_{\Omega}^{j} O \,. \tag{3.39}$$

Fig. 3.6 displays results for the ^{16}O ground-state energy for both approaches using a forward Euler step to solve the respective differential equations. For this system, we compute the ground state energies using both the direct ODE solver approach and the Magnus expansion method. Additionally the Adams-Bashforth method is used as a high-precision point of reference. Here we see that the IMSRG flow equation is subject to large errors when solved using a forward Euler step method, with the converged result strongly dependent on the step size δs. The Magnus approach, on the other hand, does not exhibit dependence on δs, but rather converges to approximately the same result as the Adams-Bashforth ODE solver, regardless of step-size. This is confirmation that the Magnus expansion minimizes the effect of step-size errors, and thus reduces the immense storage requirements of IMSRG which originate from the use of high-order ODE solvers.

As mentioned above, the efficacy of the Magnus approach is contingent upon a reasonable numerical termination point for both the Magnus and the BCH expansions. For the kth term in

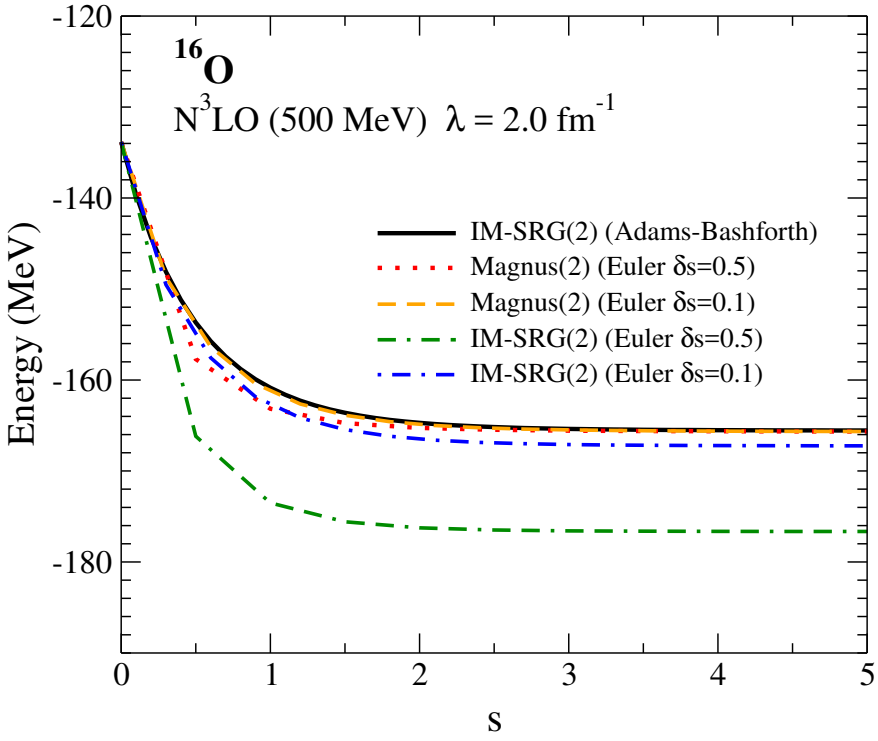

Figure 3.6 Flowing reference energy $E_0(s)$ for ^{16}O at with the EM input NN potential, N3LO(500) [5] at $\lambda_{SRG} = 2.0$ fm^{-1}, $e_{max} = 8$ and $\hbar\omega = 24$ MeV. Computed with Magnus and flow equation methods using forward Euler step. Results are benchmarked against flow equation solved by high-order adaptive step solver [6].

eq. 3.37, we adjudicate numerical termination by the convergence criterion

$$\left| \frac{B_k || ad^k_\Omega \eta ||}{k! ||\Omega||} \right| < \varepsilon_{deriv} , \tag{3.40}$$

where double bars refer to the Frobenius norm. The convergence of eq. 3.39 is determined by

$$\left| \frac{\{ad^k_\Omega H\}_{0b}}{k!} \right| < \varepsilon_{BCH} . \tag{3.41}$$

This criterion is not as strict as the one used for the Magnus expansion, as the BCH expansion is used only to determine the ground state energy in this application. If one wishes to analyze the full content of the dressed Hamiltonian post-IMSRG decoupling, a more stringent criterion analogous to eq. 3.40 should be used. Fig. 3.7 displays the relative magnitude of each nested commutator term as a function of the flow parameter, in either expansion, computed for ^{16}O with a sample

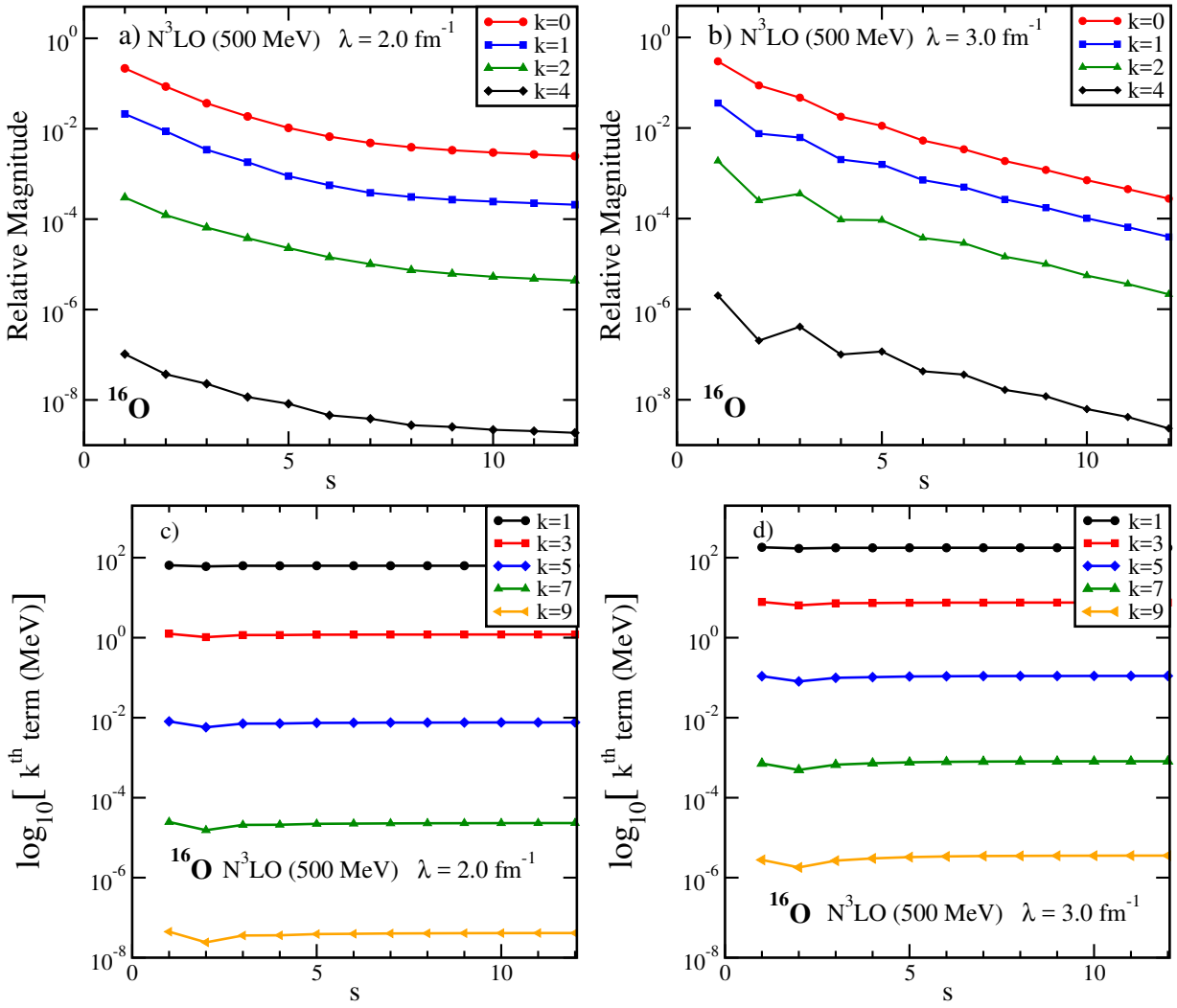

Figure 3.7 The top panels show the relative magnitude of each term in the Magnus expansion, eq. 3.37, computed for ^{16}O with the EM input NN potential, N3LO(500) [5] at $e_{max} = 8$ and $\hbar\omega = 24$ MeV. The potential is SRG evolved to (a) $\lambda_{SRG} = 2.0$ fm^{-1}, and (b) $\lambda_{SRG} = 3.0$ fm^{-1}. The bottom panels show similar plots for the BCH expansion of eq. 3.39 [6].

NN interaction SRG evolved to either λ_{SRG}= 2.0 or 3.0 fm^{-1}. We see monotonic weakening of the magnitude of each successive term, indicating that these expansions numerically terminate at a manageable number of terms. In the Magnus expansion (top), the fourth nested commutator is sufficient for a numerical convergence criteria of 10^{-6}. The individual terms are larger for the harder $\lambda = 3.0$ fm^{-1} interaction since the system is more strongly correlated, but they systematically decrease with increasing order k. The convergence criteria for the BCH expansion (bottom)

is met at about nine nested commutators, with more commutators needed for harder interactions. Reassuringly, we find that the final results in our calculations are essentially independent of the convergence criteria provided $\varepsilon_{deriv} \lesssim 10^{-4}$ and $\varepsilon_{BCH} \lesssim 10^{-4}$, where the latter is in units of MeV. For instance, raising both convergence criteria from 10^{-8} to 10^{-4} changes the ground state energy at the 1 eV level.

3.2.4 Center-of-Mass Factorization in the IMSRG

The Magnus expansion offers a straightforward means to compute effective operators via the BCH expansion, and thus we can investigate the center-of-mass (COM) factorization using an effective operator $H_{cm}(s)$. This problem is of critical importance in nuclear structure, as the structure of self bound nuclei is governed by a translationally invariant Hamiltonian, and thus we require factorization of the intrinsic and COM components of the wave function

$$|\Psi\rangle = |\psi\rangle_{in} \otimes |\psi\rangle_{cm} \,. \tag{3.42}$$

The many-body problem is often formulated in a spherical basis, as intrinsic conservation of angular momentum appears naturally here. A consequence of this is the loss of translational invariance due to localization of the center of mass. This is not a problem if the wave function factorizes properly, as we would only expect a degeneracy in the intrinsic spectra corresponding to each of the COM excitations. The expression of the problem in a truncated HO basis results in an artificial oscillatory behavior of the center of mass, which is often characterized by a harmonic trap with characteristic frequency $\tilde{\omega}$. Thus, COM excitations are evenly spaced by $\hbar\tilde{\omega}$, and offsetting the COM Hamiltonian (H_{cm}) by $(3/2)\hbar\tilde{\omega}$ guarantees that the COM ground state will have E_{cm} = 0 MeV. The COM excitations with $E_{cm} \neq 0$ MeV are considered spurious states, as we are only interested in the intrinsic structure of the nucleus, and the harmonic spectrum of the COM is an artifact of the truncated model space.

There are two popular methods for preserving COM factorization with a spherical basis. The first is to formulate the problem in Jacobi coordinates, which are translationally invariant [138–

140]. This approach is limited in applicability due to factorial scaling of the antisymmetrization procedure. A second approach is to use the HO single particle basis with a truncation on the many-body basis which includes all excitations from the reference up to and including $N\hbar\omega$. For this truncation, called the N_{max} truncation, the model-space projection operator commutes with the COM Hamiltonian, and thus factorization is ensured. Again, this approach is not particularly useful for heavier nuclei, as the construction of the basis scales exponentially with the number of active nucleons. Thus, for medium-mass nuclei and beyond, we must be content with approximate center of mass factorization.

The form of the COM Hamiltonian is taken to be that of a harmonic trap,

$$H_{cm}(\tilde{\omega}) = \frac{\mathbf{P}^2}{2mA} + \frac{1}{2}mA\tilde{\omega}^2\mathbf{R}^2 - \frac{3}{2}\hbar\tilde{\omega}. \tag{3.43}$$

For methods where factorization is analytically guaranteed, such as the NCSM, $\tilde{\omega}$ is an arbitrary quantity. Here it can be shown that the model-space projection operator commutes with $H_{cm}(\tilde{\omega})$ regardless of the choice for $\tilde{\omega}$. The IMSRG and similar methods are formulated in a general basis with truncation on the single particle energies ($e_{max} = 2n + l$), and as a result we cannot ensure rigorous factorization of the COM and intrinsic wave functions. Nevertheless, we often see oscillatory COM behavior if we probe the intrinsic wave functions with COM coordinate space operators. From these observations we may extract an optimized $\tilde{\omega}$, where approximate COM factorization is typically observed.

H_{cm} is evolved consistently with the intrinsic Hamiltonian in the IMSRG unitary transformation [6]. Calculation of $\tilde{\omega}$ demonstrates that equation 3.43 is indeed the approximate form of H_{cm}, as the observed trapping frequency is approximately independent of the underlying frequency of the single particle basis. This is demonstrated in fig. 3.8, where results are shown for ^{14}C at two frequencies, $\tilde{\omega}_{\pm}$, which are solutions of a quadratic equation [141].

$$\hbar\tilde{\omega} = \hbar\omega + \frac{2}{3}E_{\mathrm{cm}}(\omega) \pm \sqrt{\frac{4}{9}(E_{\mathrm{cm}}(\omega))^2 + \frac{4}{3}\hbar\omega E_{\mathrm{cm}}(\omega)}\,. \tag{3.44}$$

In the top panel of figure 3.8, $E_{cm}(\omega)$ is the center of mass energy calculated for trapping frequencies equal to that of the underlying basis. It is apparent that $E_{cm}(\omega)$ exhibits quadratic dependence

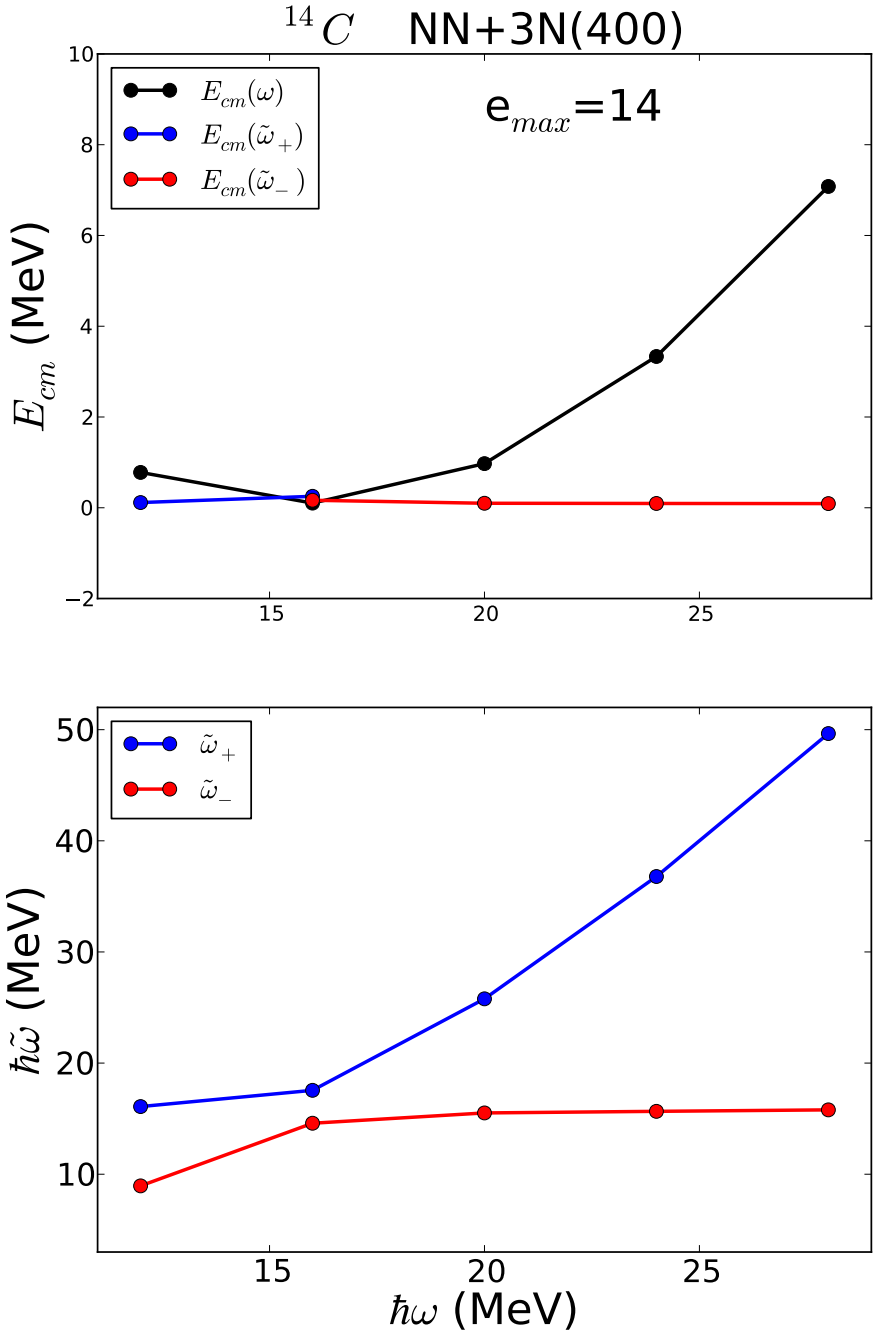

Figure 3.8 Center-of-mass diagnostics for IMSRG(2) calculations of ^{14}C starting from the NN+3N(400) interaction, SRG evolved to λ_{SRG} = 2.0 fm^{-1}. See the text for details. The calculations were done in an $e_{\max}$=14 model space.

on ω, indicating that the center of mass behaves approximately as an isotropic harmonic oscillator of frequency $\tilde{\omega}$, which corresponds to the vertex of the parabola.

The lower panel displays the calculated frequencies from eq. 3.44, which show approximate independence of ω, with an approximate value of 15.7 MeV/$\hbar$, consistent with the vertex of E_{cm}. Returning to the top panel, we see that $E_{cm}(\tilde{\omega})$ is approximately independent of ω, at an energy of 0 MeV, which indicates that our wave function is properly factorized, and in the ground state of the COM trap. Verification of factorization must be performed for every computed state, but the full frequency sweep and computation of $\tilde{\omega}$ is often unneeded. $\tilde{\omega}$ is obtained using the intrinsic ground state wave function, and as we expect all non-spurious states to have the same COM ground state, it suffices to demonstrate that $E_{cm} \approx 0$ for each excited state. States which exhibit $E_{cm} = N\hbar\tilde{\omega}$ for non-zero N are clearly spurious excitations of the center of mass.

Difficulty arises when E_{cm} is non-zero, nor a multiple of $\hbar\tilde{\omega}$. This is an indicator of strong COM contamination of an intrinsic state. In other words, the wave function does not factorize for these states. For such states, it is best to augment the intrinsic Hamiltonian with a scaled variant of eq. 3.43, constituting the Lawson-Gloeckner method [142],

$$H_{in} \to H_{in} + \beta H_{cm}(\tilde{\omega})\,. \tag{3.45}$$

Here the energy from COM excitations is explicitly included, but as the ground-state is defined to have $E_{cm} = 0$ MeV, this should only scale spurious states. Thus, β can be taken to arbitrarily large values, which will scale spurious states from the spectrum and increase the perturbative energy denominators for contaminated states, improving their factorization.

3.2.5 Results for Ground States of Closed Shell Nuclei

This dissertation focuses primarily on the single reference IMSRG, which is most appropriate for the description of nuclei in the vicinity of shell closures, which are subject to correlations of primarily dynamic nature. The IMSRG(2) exhibits computational scaling $\mathcal{O}(N_p^4 N_h^2)$ and is thus able to work with very large single particle bases, on the order of 15 major harmonic oscillator

shells. In these model spaces, even bare chiral NN interactions will show reasonably converged results for doubly magic nuclei. Fig. 3.9 demonstrates the convergence properties for the three doubly-magic nuclei ^{4}He, ^{16}O, and ^{40}Ca. In the left column, results are shown for the bare ($\lambda_{srg} = \infty$) Entem and Machleidt (EM) NN interaction at N^{3}LO with cutoff Λ = 500 MeV [5]. In the right column are results for the same potential softened with the free-space SRG to λ_{srg} = 2.0 fm^{-1}. These calculations were originally published in the review by Hergert et. al. [3]. They use a Hartree Fock reference state, and the White generator for IMSRG(2) ground-state-decoupling in the flow equation approach.

The exhibited convergence properties are desirable in either case, where for each nucleus, independence from basis frequency has begun to appear by $e_{\max} = 14$. For each case an extrapolated result is given by the dashed line, using the prescription described in [3]. For the bare interaction, the extrapolated result is matched nicely by actual calculations for ^{4}He and ^{16}O at optimal basis frequencies $\hbar\omega \approx 32$ MeV. For ^{40}Ca, convergence in $e_{\max}$ is not quite obtained, but the difference between actual calculations and extrapolation is minimal.

SRG softening clearly improves the convergence properties of ^{16}O and ^{40}Ca, which are essentially converged outside of the high-frequency infrared regime. The convergence of ^{4}He with the soft interaction does not show much improvement from the bare interaction, as this system is small enough to have significantly converged calculations in either case. Some non-variational convergence patterns are evident in the softened interaction, which is a result of the IMSRG(2) truncation having invalidated the variational principle. The accelerated convergence in heavier nuclei is indicative of the fact that SRG softened potentials can be used with IMSRG to describe much heavier nuclei and also more strongly correlated open shell nuclei with multi-reference approaches.

An important point is that the SRG softened interaction produces a significantly stronger binding than that of the bare interaction. As alluded to in section 3.1.3, this is because using the SRG to soften interactions shifts significant repulsive content into the induced three-body force, which is ignored here. In order to properly describe binding in these nuclei, we must at least keep the three-body forces induced from the free-space SRG. The results of doing so are shown in fig. 3.10,

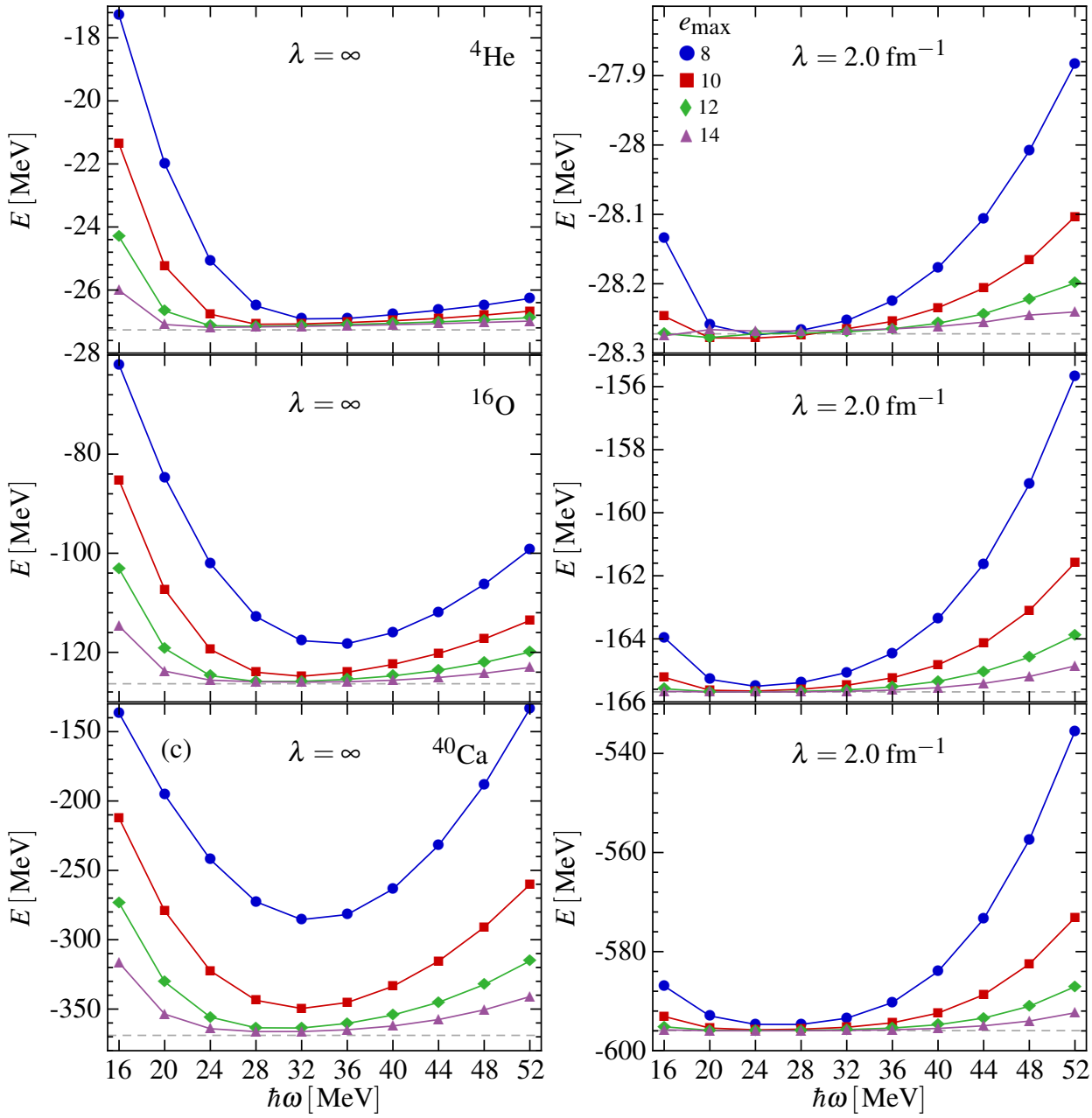

Figure 3.9 Convergence of ^{4}He, ^{16}O, and ^{40}Ca IMSRG(2) ground-state energies w.r.t. single-particle basis size $e_{\max}$, for a chiral N^{3}LO NN interaction with $\lambda = \infty$ (left panels) and $\lambda = 2.0$ fm^{-1} (right panels). Notice the significant differences in the energy scales between the left and right panels. Gray dashed lines indicate energies from extrapolation the $e_{\max} \geq 10$ data sets to infinite basis size (see text and Refs. [7, 8]).

which was taken from the work of Hergert et. al., [64]. For the time being, we will focus only on the IMSRG(2) results, shown in blue. In the left column, two nucleon forces plus 3N forces induced by SRG softening are included. In the right column, both induced and SRG softened forces from a local chiral 3N potential [13] are included. While including induced forces significantly corrects for the errors in binding energy introduced by SRG evolving the NN potential, significant dependence on λ_{srg} is still present, and for reliable binding energies, one must use large values of λ_{srg}, which do not exhibit the pleasant convergence properties of more softened potentials (e.g. λ_{srg} = 2.00, 1.88 fm^{-1}). Inclusion of the full 3N force mostly rectifies this difficulty, where the difference between λ_{srg} = 2.24 and 1.88 fm^{-1} has been reduced to roughly 1-10% of the total binding energy.

Returning to the additional methods plotted in fig. 3.10, we see that IMSRG(2) is compared with coupled-cluster (CC) theory. Two variants of CC theory are shown. CC with singles and doubles (CCSD) [11, 58, 116, 143] is a truncation analogous to IMSRG(2), where correlations are included through exponential cluster operators, truncated at two-body operators,

$$|\Psi_0\rangle = exp[T^{1b} + T^{2b}]|\Phi_0\rangle\,. \tag{3.46}$$

Here cluster amplitudes are solved for by applying the exponential operator to the Hamiltonian and exploiting the intermediate normalization of the ground-state (see sec. 2.7). Λ-CCSD(T) [116,144] includes an additional perturbative step to correct for the missing three-body cluster operator T^{3b}. For reference, quasi-exact importance-truncated no-core shell model (IT-NCSM) [145, 146] calculations are included where available. We note that IT-NCSM includes the full 3N force, where in IMSRG and CC theory, the 3N force is included in the NO2B approximation. Interestingly, IMSRG(2) tracks closer to Λ-CCSD(T) than CCSD. This point will be discussed in the next section.

It's evident that all of these approximate approaches produce overbinding in comparison with IT-NCSM. This is largely attributable to three components, which are the many-body truncation, the NO2B approximation and the E_{3max} truncation, which does not contribute to the error in IT-NCSM as the model-space truncation incorporates this. The NO2B approximation has been shown

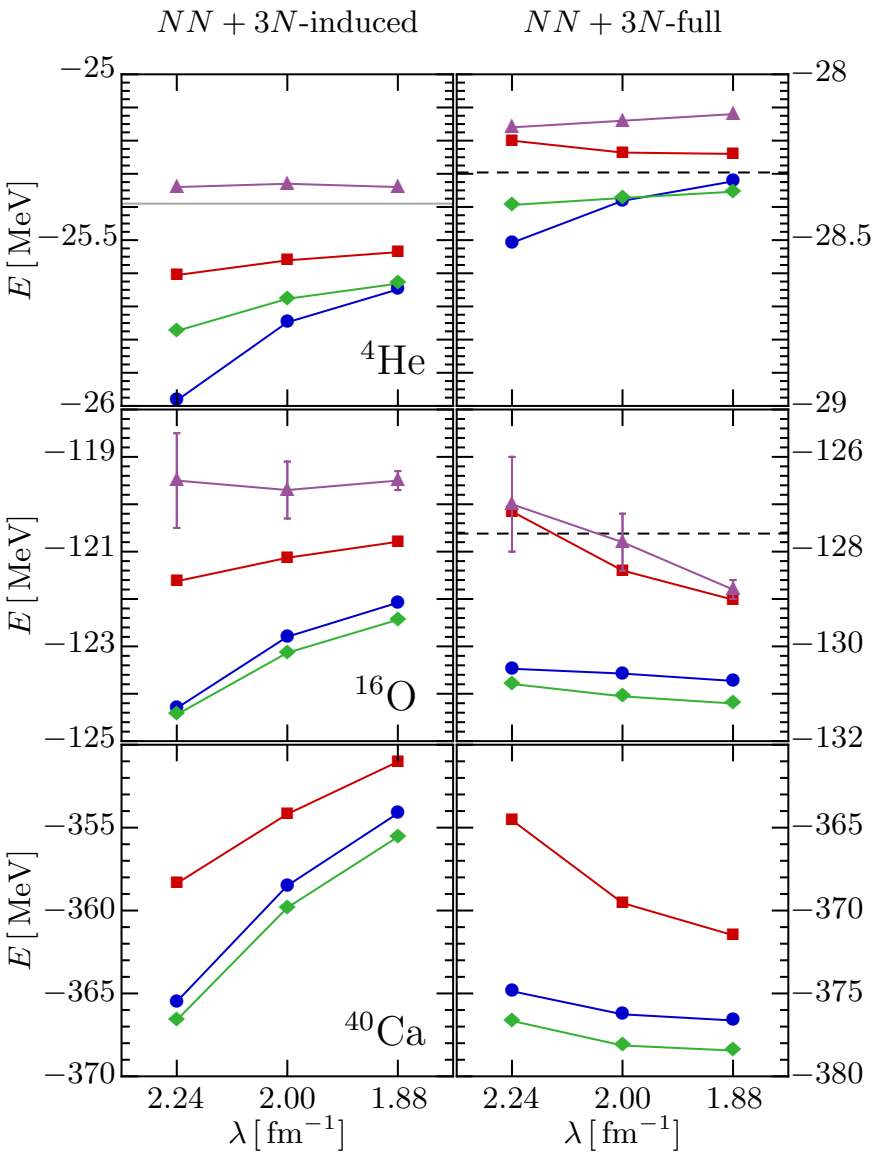

Figure 3.10 Ground-state energies of stable closed-shell nuclei as a function of the resolution scale λ for the SRG-evolved $NN+3N$-induced (left column) and $NN+3N$-full Hamiltonians (right column), using different many-body methods: IMSRG(2) (●), CCSD (■), Λ-CCSD(T) (♦), and IT-NCSM (▲). IMSRG and CC results are obtained with $e_{max}=14$, and the IT-NCSM results have been extrapolated to infinite model space, with error bars indicating the uncertainties of the importance truncation and the model space extrapolation (for ^{4}He, the error bars are smaller than the symbols). The gray solid line for ^{4}He in the top left panel is the result of a converged NCSM calculation with the bare NN Hamiltonian, $E=-25.39$ MeV (see e.g. [9]). Dashed black lines are experimental values from [10].

to add about 1.0-2.5% additional binding, and is likely responsible for the bulk of the error in the approximate methods shown here.

3.2.6 Perturbative Corrections

As mentioned in section 3.2.5, IMSRG(2) ground state results, despite having a more restrictive many-body truncation, track with the many-body method Λ-CCSD(T). IMSRG(2) is third-order exact in MBPT, meaning that the resummation of MBPT into the reference state energy includes all terms up to MBPT(3), along with additional incomplete resummations of all orders of MBPT [3]. The same is true of CCSD. The difference comes from the fact that the missing terms at fourth order and above are different between the two methods. Fig. 3.11 shows all fourth order Hugenholtz energy diagrams, grouped by intermediate states. CCSD contains all fourth order energy diagrams except those with intermediate triples states, whereas IMSRG(2) lacks all intermediate triples and also undercounts a class of asymmetric intermediate quadruples diagrams (Q_1, Q_2, Q_6, Q_7) by a factor of two [3, 147, 148]. The different counting of these quadruples diagrams is responsible for the bulk of the difference between the CCSD and IMSRG(2) ground state energies. Λ-CCSD(T), on the other hand, is fourth-order exact, and thus includes all energy diagrams from MBPT(4). Errors from the undercounting of repulsive asymmetric quadruples in the IMSRG(2) apparently cancel those from missing attractive triples diagrams, as IMSRG(2) has been observed to reproduce Λ-CCSD(T) results robustly for a variety of single-reference systems.

The Magnus variant of the IMSRG offers a convenient framework to formulate perturbative corrections to the IMSRG(2) [147], as the unitary transformation is explicitly constructed and then applied via the BCH expansion. Explicitly writing the first several terms of eq. 3.39

$$\bar{H}(s) = H + [\Omega(s), H] + \frac{1}{2}[\Omega(s), [\Omega(s), H]] + \frac{1}{6}[\Omega(s), [\Omega(s), [\Omega(s), H]]] + \cdots , \tag{3.47}$$

we see that the induced three-body forces in this case may be approximated by

$$W_{pqrstu} = [\Omega(s), Y(s)]_{pqrstu} , \tag{3.48}$$

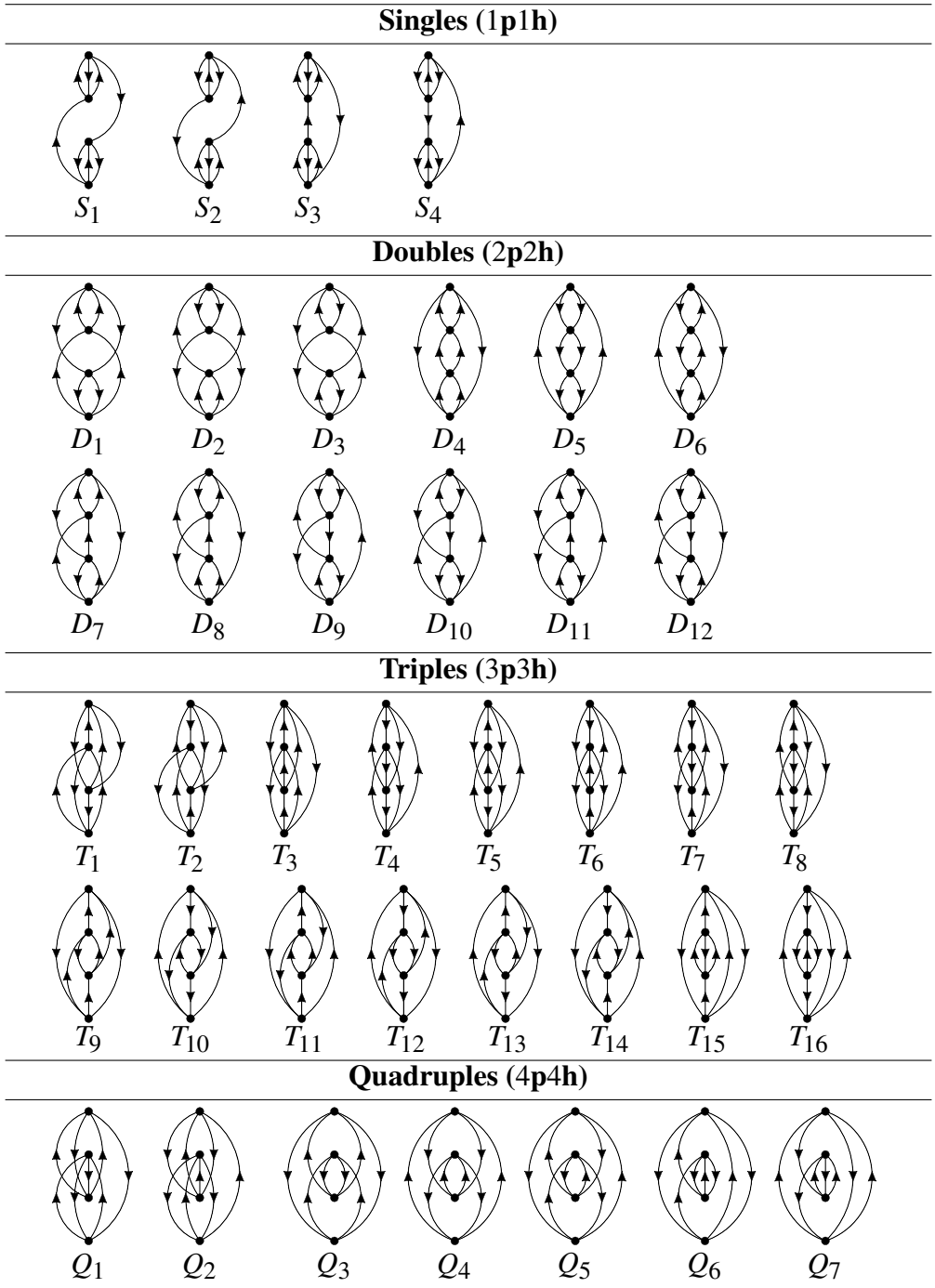

Figure 3.11 Connected Hugenholtz diagrams for the fourth-order energy correction $E^{(4)}$ (cf. [11]).

where Y(s) can be as limited as $Y(s) = H$ or as sophisticated as

$$Y(s) = H + \frac{1}{2}[\Omega(s), H] + \frac{1}{6}[\Omega(s), [\Omega(s), H]]] + \cdots, \tag{3.49}$$

where the commutators in expansion of eq. 3.49 are limited to two-body operators, similar to the BCH expansion used in the Magnus implementation of the IMSRG(2). $Y(s)$ and $\Omega(s)$ appear at first order in MBPT, and thus the leading order component of eq. 3.48 is second-order in MBPT. From this we may immediately construct a fourth order triples correction, using Rayleigh-Schrödinger perturbation theory. The induced three-body forces from eq. 3.48 can be treated as a perturbation on the IMSRG(2) ground-state-decoupled Hamiltonian, and the first non-zero correction to the energy is

$$\delta E_{\{3\}} = \frac{1}{36} \sum_{abcijk} \frac{|W_{abcijk}|^2}{\Delta_{abc}^{ijk}}, \tag{3.50}$$

where Δ are EN energy denominators. This correction is just an MBPT(2) correction in the dressed vertices, but constitutes a fourth order correction in the bare vertices. Diagrammatically, one can show that this expression encapsulates all fourth-order triples expressions, in the approximation that W is the full three-body force. We will refer to the IMSRG(2) with this triples correction as IMSRG($\{3\}$), where brackets indicate the approximate nature of the triples inclusion.

The undercounting of antisymmetric fourth-order quadruples diagrams in IMSRG(2) originates from the neglect of induced three-body forces which feed into renormalized two-body forces later in the flow. Fig. 3.12 shows the relevant dressed two-body forces which contribute to the asymmetric quadruples diagrams. Looking at the portion of the diagrams above the dashed blue line, we see two two-body vertices which are singly contracted and thus form an intermediate three-body force at second-order in MBPT. The intermediate force is triply contracted with an another two-body vertex, which creates a dressed two-body force at third-order in MBPT. The diagram can be closed at fourth order to form an asymmetric quadruples energy diagram.

These diagrams are included in CCSD due to the presence of $(T_2)^2$ in the exponential expansion. Inclusion of these terms in the IMSRG would require the IMSRG(3) formalism, but their effect can be approximated in the spirit of eq. 3.48. In CCSD, these diagrams would first appear in

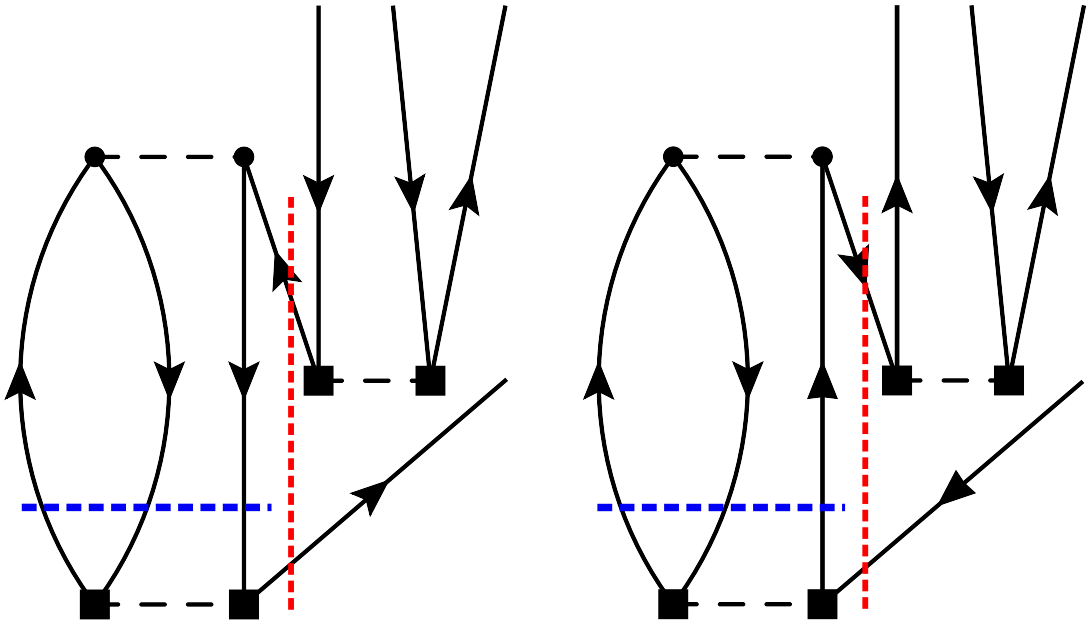

Figure 3.12 Induced two-body force with intermediate three-body force. Above the dashed blue line is the intermediate three-body force. The portion to the left of the dashed red line is an effective one-body insertion term.

the third term ($k = 2$ or two nested commutators) of the BCH expansion. We can add a correction for the missing fourth order quadruples by adding them to the $k \geq 2$ terms in eq. 3.39,

$$X_k \rightarrow X_k + X_k^* \,, \tag{3.51}$$

where $X_k = k[ad_\Omega^k(H)]$ and X_k^* contains the missing quadruples contributions. In this context, the square vertices in fig. 3.12 refer to $\Omega(s)$ and the black circle vertex to the Hermitian intermediate, or previous $(k-1)$ nested commutator. We note here that there are two additional diagrams which must be computed, where the black circles and squares are exchanged in the intermediate three-body term. These additional terms are the result of the commutators in the BCH expansion. While one might think that a three-body vertex must be computed in this case, this is not actually required, because the vertices on the left side of the dashed red line constitute a one-body operator at second order in MBPT, and can be computed as an intermediate state, and then contracted with the remaining two-body vertex in the form of a one-body insertion.

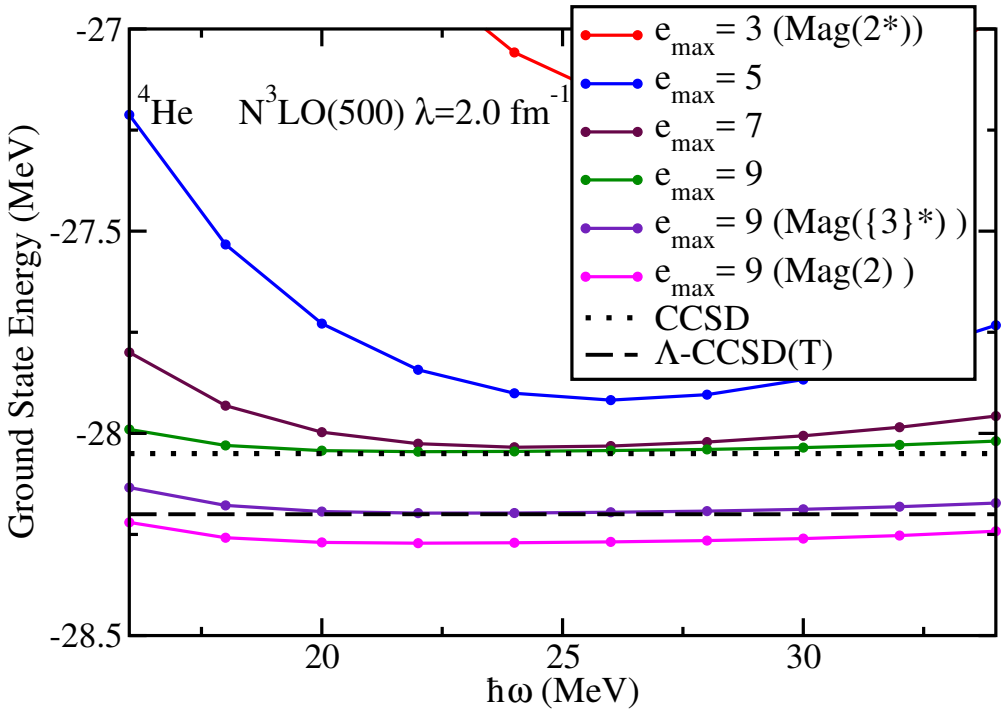

Figure 3.13 Convergence of IMSRG(2*) ground state energy for ^{4}He with the input EM N^{3}LO NN potential, SRG evolved to λ_{SRG} = 2.0 fm^{-1}. IMSRG ground state energies are computed to $e_{\max}$=9 for IMSRG(2), IMSRG(2*), and IMSRG({3}*). Results from CCSD and Λ-CCSD(T) are also shown.

The problem becomes the evaluation of

$$(X_k^*)_{abij} = \frac{1}{4}(1-P_{ij})\sum_k n_k \left([X_{(k-1)}]_{abkj} G_{ki} - \Omega_{abkj} D_{ki} \right) - \frac{1}{4}(1-P_{ab})\sum_c \bar{n}_c \left(G_{ac}[X_{(k-1)}]_{cbij} D_{ac} - \Omega_{cbij} \right), \tag{3.52}$$

where the intermediate one-body operators are given by

$$G_{pq} = \frac{1}{2}\sum_{rst} \Omega_{tprs}\Omega_{rstq}(\bar{n}_r\bar{n}_s n_t - n_r n_s \bar{n}_t) \tag{3.53}$$

and

$$D_{pq} = \frac{1}{2}\sum_{rst} \left([X_{(k-1)}]_{tprs}\Omega_{rstq}\bar{n}_r\bar{n}_s n_t - \Omega_{tprs}[X_{(k-1)}]_{rstq} n_r n_s \bar{n}_t \right). \tag{3.54}$$

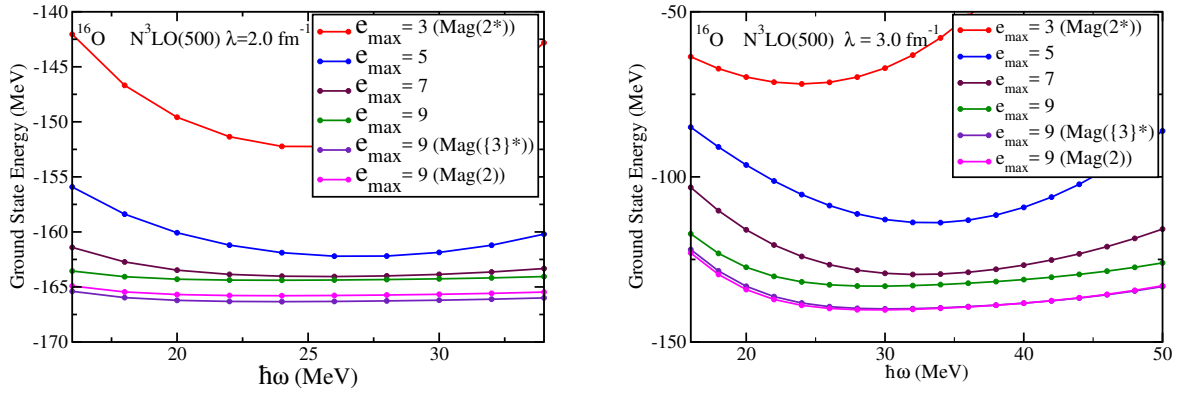

Figure 3.14 Convergence of IMSRG(2*) ground state energy for ^{16}O with the input EM N^{3}LO NN potential, SRG evolved to λ_{SRG} = 2.0 (3.0) fm^{-1} in the left (right) panel. IMSRG ground state energies are computed to $e_{\max}$=9 for IMSRG(2), IMSRG(2*), and IMSRG({3}*).

This method is denoted as IMSRG(2*) or IMSRG({3}*) in the case where it accompanies the perturbative triples correction.

Fig. 3.13 shows the convergence of the IMSRG(2*) method as a function of $e_{\max}$ and $\hbar\omega$ for ^{4}He using the E.M. N^{3}LO NN potential. The calculation uses up to $e_{\max}$=9, where convergence is satisfactory for purposes of demonstration. The IMSRG({3}*) and IMSRG(2) curves for $e_{\max}$=9 are also included. For reference, converged CCSD and Λ-CCSD(T) calculations are provided [43]. Consistent with our expectations, IMSRG(2) falls nearer to Λ-CCSD(T) than CCSD. IMSRG(2*) closely reproduces CCSD and IMSRG({3}*) closely reproduces Λ-CCSD(T). Thus, we conclude that for this case, IMSRG(2*) and IMSRG({3}*) capture much of the same perturbative content as CCSD and Λ-CCSD(T), respectively.

In fig. 3.14, the same calculation is shown for ^{16}O with the E.M. N^{3}LO interaction softened to 2.0 and 3.0 fm^{-1} in the left and right panels respectively. Here we do not have CC results for comparison, but the same pattern is evident. With the softer interaction, the IMSRG(2*) correction removes about 2 MeV of binding energy, which is promptly reintroduced by the triples correction. For the harder interaction, convergence is not as clear, but nonetheless the same trend is observed,

albeit at a somewhat larger scale.

CHAPTER 4

EXCITED STATE EXTENSIONS

After ground-state-decoupling, the IMSRG rotated Hamiltonian is block diagonal, where the reference state has been completely decoupled from all excitations. Ground state properties can then be extracted using the reference expectation value of any consistently transformed effective operators. However, if we wish to explore excited states, we must further process the remaining block of the Hamiltonian matrix, which still exhibits correlations between all levels of excitation, despite complete isolation from the reference state. While the couplings between various excitation ranks have been softened in the ground-state-decoupling, 1p1h excitations are still indirectly coupled to as much as ApAh excitations, and thus the problem of solving for excited states requires essentially the same effort as an FCI calculation using the bare Hamiltonian.

There are two different strategies for the computation of excited states in the IMSRG formalism. One approach is to devise a secondary transformation to decouple blocks of different particle-hole excitation rank. If such a transformation is possible with the IMSRG(2) truncation, then diagonalizations of the particle-hole sub-blocks would provide tractable access to low lying excited states. We will show that this method is viable for a limited set of physical systems, which includes doubly magic nuclei. For these nuclei, the method performs exceedingly well for low lying 1p1h dominant odd-parity states, but poorly for states with higher-order content in their wave functions. As such, the method is often formulated in a valence 1p1h space, and is hence named the valence Tamm-Dancoff approximation IMSRG (vTDA-IMSRG).

A more robust, but less elegant approach may be formulated without a second decoupling. Here we work with the ground-state-decoupled Hamiltonian, where softened couplings between the various excitation ranks facilitates the use of approximate diagonalization methods such as the second-RPA [149, 150]. The general method, named the equations-of-motion IMSRG (EOM-IMSRG), is introduced in this chapter. We show that this method provides more consistent access to 1p1h states, with slightly diminished accuracy due to the approximate nature of the diagonaliza-

tion. However, the EOM-IMSRG is systematically improvable through the many-body truncations of both the IMSRG and EOM stages. The implementation of EOM-IMSRG is similar to what is done in CC theory [68, 69]. While the EOM-IMSRG potentially offers some technical simplifications due to the Hermiticity of the transformed Hamiltonian (e.g., no need to solve a separate left-eigenvalue problem when calculating properties other than energy), the practical limitations of the single-reference formulation should be comparable to the analogous EOM-CC calculations, limiting the method to nuclei within 1 or 2 nucleons of a closed shell.

To remove these limitations, one possibility is to merge EOM techniques with the multireference IMSRG (MR-IMSRG) formulation recently developed for ground-state calculations of open-shell even-even nuclei [45, 47]. In principle, spectroscopy for the target nucleus and its even-odd, odd-even, and odd-odd neighbors could then be accessed using suitably generalized EOM excitation operators. Since the full implementation of the MR-EOM-IMSRG is a significant undertaking, we first develop the single-reference EOM-IMSRG to calculate excited states in closed-shell systems as a "proof-of-principle", before taking on the much more challenging multireference formulation. In the following we will show that the EOM-IMSRG is indeed a viable approach to target excited states, giving good agreement with analogous EOM-CC calculations for the ^{16}O and ^{22}O nuclei considered, and exhibiting systematic improvement towards the exact full configuration interaction (FCI) results in 2d quantum dots when perturbative triple-excitation corrections are included in our EOM calculations. We demonstrate improvement in nuclear spectra when computed with the perturbative triples correction. We also introduce extensions to the EOM-IMSRG in the form of particle removed and attached variants for neighboring isotopes and isotones, and a charge-exchange variant to compute properties of neighboring isobars.

4.1 Sequential Decoupling

4.1.1 TDA-IMSRG

At the end of the IMSRG ground-state decoupling, Hartree-Fock is made exact for the ground state of the evolved Hamiltonian. One might propose a similar treatment for excited states, supposing that a decoupling can be designed to make some simple approximation for excited states exact at the end of the evolution. We start with the Tamm-Dancoff approximation (TDA), where excited states are approximated as linear combinations of 1p1h excitations of a reference Slater determinant [95],

$$|\Psi_\nu^{TDA}\rangle = \sum_{ai} X_i^a a_a^\dagger a_i |\Phi_0\rangle \,. \tag{4.1}$$

With this excitation operator, the Schrödinger equation becomes:

$$\sum_{bj} (f_{ab}\delta_{ij} - f_{ji}\delta_{ab} + \Gamma_{ajib}) X_j^b = \omega_\nu^{TDA} X_i^a \tag{4.2}$$

where $\omega_\nu^{TDA} = (E_\nu^{TDA} - E_{ref})$. For a Hartree-Fock reference state, the TDA is equivalent to diagonalizing H on the subspace spanned by $|\Phi_0\rangle$ and the singly-excited $|\Phi_i^a\rangle$ Slater determinants. The TDA neglects all ground-state correlations and higher-rank particle-hole excitations in the excited states, making it a poor approximation for Hamiltonians that feature significant coupling between the reference state and the higher particle-hole sectors, or between the 1p1h and higher excitation blocks. The initial nuclear Hamiltonian (treated in the NO2B approximation) certainly falls into this class, as indicated by the left panel in Fig. 3.2.

For the ground-state-decoupled Hamiltonian in the right panel of Fig. 3.2, we note a block-diagonal form, where couplings between individual particle-hole excitation ranks have been considerably weakened. The ground-state is completely decoupled from the excited states, and direct couplings between the 1p1h and 3p3h blocks have been suppressed to zero. Thus, we expect a TDA calculation using $\bar{H}(\infty)$ to be more accurate than an analogous calculation for the initial Hamiltonian $\bar{H}(0) \equiv H$. In fact, as ground-state decoupling removes all correlations between the reference state and 1p1h excitations, the TDA becomes equivalent to the random phase approx-

imation (RPA) [95] in this reference frame, as the only difference between the methods is the incorporation of ground-state correlations in the RPA.

A secondary transformation can be devised to make the TDA *exact*, up to IMSRG(2) truncation errors, for a subset of excited states. Such a transformation necessarily decouples the 1p1h block from all higher rank particle-hole excitations, while leaving the decoupling from the ground state intact. In fact, such a transformation would bring the Hamiltonian to the block diagonal form seen in the left panel of Fig. 4.1. As the transformations are applied sequentially, we label the ground-state decoupling as U_1, and the secondary transformation to decouple the different particle-hole sectors as U_2. We seek to construct

$$\begin{aligned}\bar{H}_{21}(s) &\equiv U_2(s)\bar{H}_1(\infty)U_2^\dagger(s) \\ &= U_2(s)U_1(\infty)HU_1^\dagger(\infty)U_2^\dagger(s)\,,\end{aligned} \tag{4.3}$$

with the relevant off-diagonal terms for U_2 given in the NO2B approximation by

$$\bar{H}^{od} : \langle \Phi^{bc}_{jk}|\bar{H}_{21}(s)|\Phi^{a}_{i}\rangle \sim \Gamma_{icjk}\,, \Gamma_{bcak} \tag{4.4}$$

and their Hermitian conjugates. Assuming the second IMSRG evolution converges, the transformed Hamiltonian becomes block-diagonal in particle-hole excitations

$$\langle \Phi^{a_1\ldots a_n}_{i_1\ldots i_n}|\bar{H}_{21}(\infty)|\Phi^{a'_1\ldots a'_m}_{i'_1\ldots i'_m}\rangle = 0 \quad (n \neq m)\,, \tag{4.5}$$

taking the schematic form shown in the left panel of Fig. 4.1. It is often useful to use the imaginary-time generator for the sequential decoupling, as the secondary stage strongly renormalizes the single particle spectra. Hereafter, we refer to this sequential decoupling as TDA-IMSRG, since the TDA is exact when applied to $\bar{H}_{21}(\infty)$.

4.1.2 vTDA-IMSRG

The simple block-diagonal structure of $\bar{H}_{21}(\infty)$ enables the exact calculation of eigenvalues by diagonalization of each *npn*h block separately, with the TDA being the simplest case. However, in

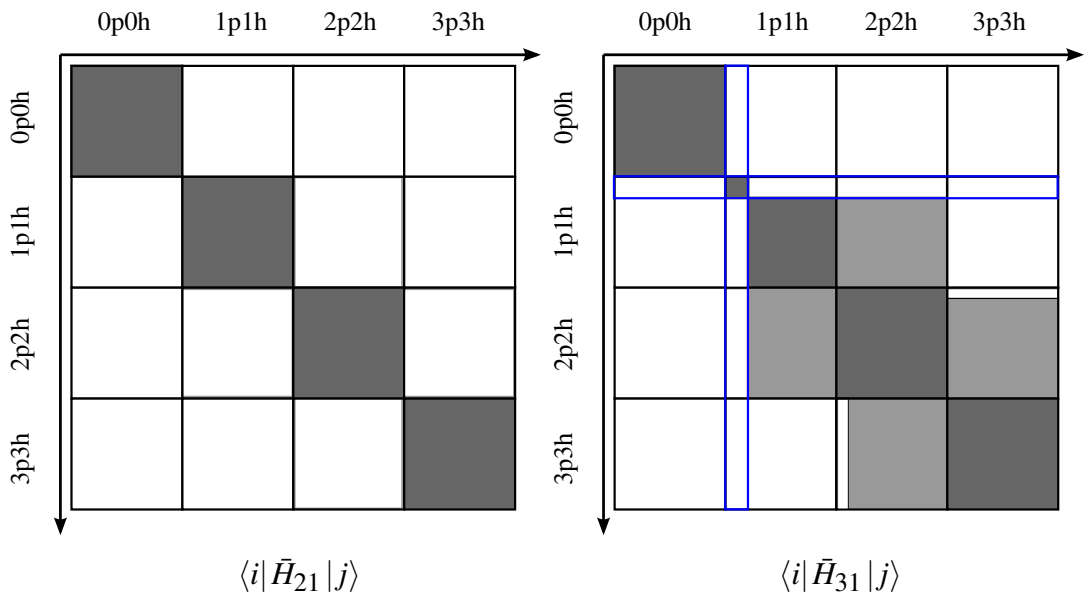

Figure 4.1 Schematic representation of the sequentially-decoupled Hamiltonians in the many-body Hilbert space spanned by particle-hole excitations of the reference state. The left panel corresponds to the use of Eq. 4.4 where the entire 1p1h sector is decoupled, and the right panel corresponds to Eq. 4.10 where just the valence 1v1h excitations are decoupled. The latter corresponds to the small block in the upper left corner of the full 1p1h-block.

practice we find that the second U_2 transformation does not always converge with respect to the flow parameter s. Even if the U_2 evolution converges, the IMSRG(2) truncation errors are typically found to degrade the unitary equivalence between the initial H and $\bar{H}_{21}(\infty)$ beyond acceptable tolerances. The breakdown of unitarity is a result of the large number of off-diagonal terms driven to zero in the second transformation, which can lead to large induced three- and higher-body terms which are neglected in the IMSRG(2).

We can mitigate the effects of truncation errors in the second transformation by decoupling a smaller portion of the 1p1h configuration space in which the particle orbital is restricted to the lowest valence shell, as shown in the right panel of Fig. 4.1. This valence-space approach is denoted vTDA-IMSRG, and we denote the new transformation by U_3 with

$$\begin{aligned}\bar{H}_{31}(s) &\equiv U_3(s)\bar{H}_1(\infty)U_3^\dagger(s) \\ &= U_3(s)U_1(\infty)HU_1^\dagger(\infty)U_3^\dagger(s)\,. \end{aligned} \tag{4.6}$$

To determine the form of $\bar{H}^{od}$ for the U_3 transformation, let us denote low-lying valence particle states as $a_v, b_v, c_v, \ldots$ and high-lying non-valence particle states as $a_q, b_q, c_q, \ldots$. If we don't distinguish between valence and non-valence particle states, we use the labels $a, b, c, \ldots$ as before. Performing TDA in the valence space alone modifies Eq. 4.1 to

$$|\Psi_\nu^{VTDA}\rangle = \sum_{a_v i} X_i^{a_v} a_{a_v}^\dagger a_i |\Phi_0\rangle\,, \tag{4.7}$$

and hence condition 4.5 is reduced to

$$\langle \Phi_{jk}^{bc} | \bar{H}_{31} | \Phi_i^{a_v} \rangle = 0\,, \tag{4.8}$$

with the additional requirement

$$\langle \Phi_j^{a_q} | \bar{H}_{31} | \Phi_i^{a_v} \rangle = 0\,. \tag{4.9}$$

These two conditions are met if we choose

$$\bar{H}^{od} : \Gamma_{a_q i j a_v}, \Gamma_{ic jk}, \Gamma_{bc a_v k}, f_{a_q a_v}\,. \tag{4.10}$$

This definition of the off-diagonal terms is significantly reduced in scope from that of Eq. 4.4, so we expect that the loss of unitarity caused by the IMSRG(2) truncation should be less severe. The right panel of Fig. 4.1 shows the schematic form of a successful vTDA-IMSRG(2) decoupling. A vTDA-IMSRG(2) calculation will not leave the Hamiltonian block diagonal for all excitation ranks, and will limit the number of states accessible to the calculation. However, if we are interested in only low-lying states, this calculation is much more stable than the full TDA-IMSRG(2). We note here that both TDA-IMSRG(2) and vTDA-IMSRG(2) are conceptually similar to the similarity-transformed EOM-CC method, reviewed recently in [151].

4.1.3 Full Configuration Interaction Analysis of TDA-IMSRG(2) and vTDA-IMSRG(2)

The sequential TDA-IMSRG decoupling is designed so that FCI in the space of 1p1h configurations is exact for a set of low lying eigenvalues. As both IMSRG decouplings are carried out using

the IMSRG(2) truncation, we expect some deterioration of the unitary equivalence between the initial, ground-state-decoupled, and sequentially-decoupled Hamiltonians due to the neglect of induced three- and higher-body forces. The breakdown of unitarity can be understood and quantified by performing FCI calculations at various values of s during the flow. In the limit of an IMSRG(A) calculation with no truncations, we expect energies computed with FCI to be s-independent. Thus, in an IMSRG(2) calculation, we can measure the truncation errors by analyzing the s-dependence of each energy level as computed by FCI.

In the left panel of fig. 4.2, FCI behavior is demonstrated as a function of s for a few low-lying energy levels of a 6-electron quantum dot, with single-particle basis truncated to four major oscillator shells. The FCI calculations use the evolved Hamiltonian at intermediate steps in the sequential decoupling, defined by eq. 4.3. The first stage of the IMSRG evolution is the ground-state-decoupling, and the second stage decouples the particle-hole blocks. The vertical black line in Fig. 4.2 indicates the endpoint of the ground-state decoupling U_1, and the beginning of the secondary 1p1h decoupling U_2. The ground state and first $(M_L, M_S) = (1,0)$ excited state show weak dependence on s in either transformation, indicating that the loss of unitarity from the IMSRG(2) is small.

A more pathological behavior is uncovered by zooming in on the second and third excited states, as seen in the right panel of Fig. 4.2. For reference, FCI results computed with the initial Hamiltonian are indicated by horizontal dotted lines. In the second stage, dashed lines show FCI results for the flowing $\bar{H}_{21}(s)$ during TDA-IMSRG(2), and solid lines correspond to the analogous vTDA-IMSRG(2) calculations using $\bar{H}_{31}(s)$ where the valence-space used for the vTDA-IMSRG calculation includes all 1p1h excitations into the third oscillator shell. The U_3 evolution shows limited s-dependence, with small errors induced at the beginning of the flow. The calculation is converged numerically around $s \approx 11.5$. Conversely, the U_2 evolution induces larger errors from the outset, and continues to show s-dependence as the flow continues, exhibiting undesirable features such as erratic convergence patterns and level crossings. These results are consistent with our intuition that IMSRG(2) truncation errors should be smaller for the valence 1p1h decoupling,

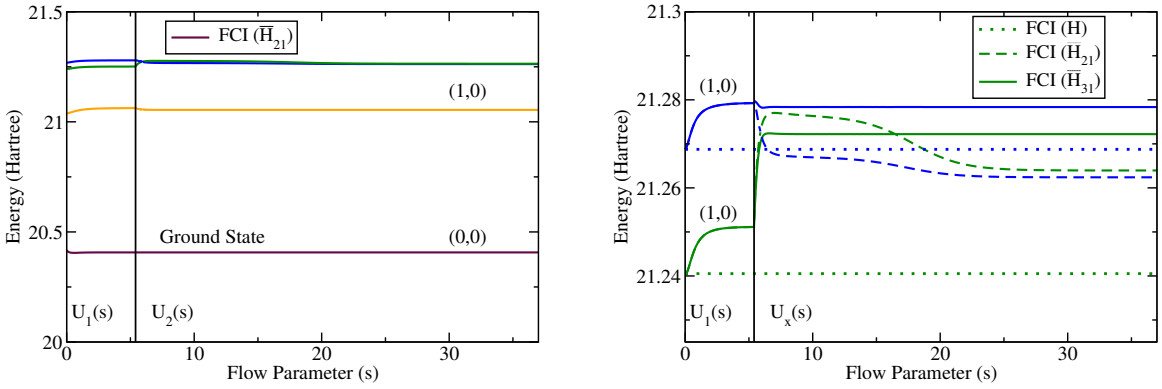

Figure 4.2 $(M_L, M_S) = (1,0)$ excited states of a 6-electron quantum dot in an $\omega = 1.0$ trap model space composed of four major oscillator shells. Three FCI calculations are shown; two using the flowing TDA-IMSRG(2) and vTDA-IMSRG(2) Hamiltonians corresponding to each choice of the secondary decoupling $U_x(s)$ (where $x = 2$ or 3), and one using the bare Hamiltonian.

as fewer matrix elements are driven to zero in this framework. In fact, the behavior of the U_2 transformation in this specific case is relatively pleasant; we find that in larger systems, the pathological behavior of the TDA-IMSRG(2) decoupling typically leads to numerical instabilities and thus non-convergent energies. It is for this reason that we consider the vTDA-IMSRG(2) to be the preferred sequential decoupling method.

In fig. 4.3, we show the practical benefits of the vTDA-IMSRG(2), where sequential decoupling is used to make TDA *exact* in the rotated frame. This calculation is performed for the first $(1,0)$ state of the 6-electron quantum dot. For comparison, we have plotted the flowing and bare FCI calculations for both the ground and first excited state, as well as the 0-body component of the Hamiltonian $E_{ref}(s)$. At $s = 0$, $E_{ref}(0)$ corresponds to the Hartree-Fock energy and $E_{TDA}(0)$ to a traditional TDA calculation limited to the third oscillator shell. These are rather poor approximations to reality, as they fail to incorporate couplings to higher order configurations, which are critical in correlated systems such as quantum-dots and nuclei. As s increases, successively more many-body correlations are resummed into the relevant pieces of the flowing Hamiltonian, and thus the corresponding $E_{ref}(s)$ and $E_{TDA}(s)$ become better approximations to exact results. At

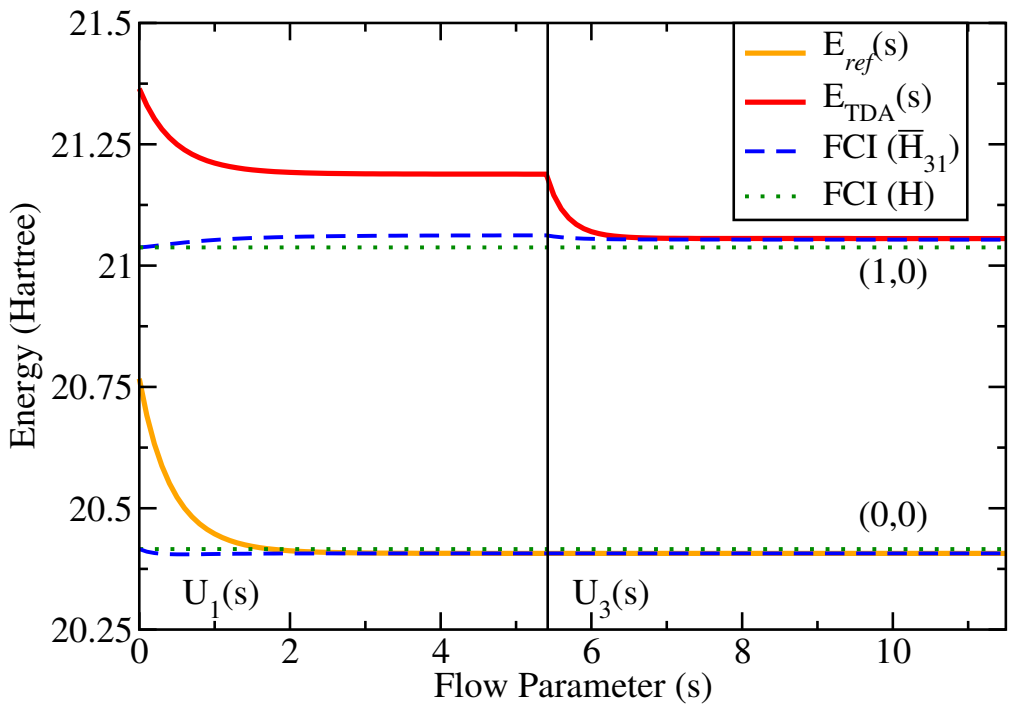

Figure 4.3 FCI and TDA calculations of the first $(M_L, M_S) = (1,0)$ excited state using the flowing vTDA-IMSRG(2) Hamiltonian for a 6-electron quantum dot with $N = 3$ and $\omega = 1.0$. For reference, the flowing 0-body part of the Hamiltonian $E_{ref}(s)$ and the FCI results for the bare Hamiltonian are also shown.

the completion of ground-state-decoupling, $E_{ref}(s \approx 5.4)$ is in excellent agreement with the exact ground state, while $E_{TDA}(s \approx 5.4)$ is significantly improved compared with its initial counterpart. As the secondary decoupling progresses, $E_{TDA}(s)$ approaches the flowing FCI calculation, which at this point has deviated little from the bare result. Thus $E_{TDA}(s)$ is now a very good approximation of the exact ground state, with a much more modest computational demand. This method is powerful because of its scalability. The time-complexity of vTDA-IMSRG(2) is dominated by the IMSRG(2) equation, and thus behaves as $\mathcal{O}(N_p^4 N_v N_h)$, which is far more manageable than the factorial scaling of FCI. Another important feature of this sequential decoupling is that $E_{ref}(s)$ is independent of s during the second stage, indicating that the secondary decoupling does not re-

introduce couplings between the reference state and particle-hole excitations. The computational benefits of this approach come at a cost, as the valence space severely limits the number of excited states which one may describe with this method. Thus we turn to the equations-of-motion method for a less elegant but more general approach to excited states.

4.2 Equations-of-Motion Method

The sequential decoupling seeks to make simple methods exact, by suppressing the matrix elements which are responsible for the errors in these methods. While this strategy is intuitively pleasing, methods such as the TDA- and vTDA-IMSRG(2) cannot circumvent the problems associated with maintaining unitary equivalence, particularly when they are tasked with decoupling a large space of excited states from the rest of the Hamiltonian. We showed that one can decrease the number of matrix elements we must suppress by defining a valence space for vTDA-IMSRG, but if we want to describe higher energy excited states, vTDA-IMSRG(2) quickly becomes unpractical because of the increased size of the valence space required to encapsulate these states.

These limitations can be avoided if we pursue a third strategy where we apply higher-order equations-of-motion techniques to approximately diagonalize the ground-state-decoupled Hamiltonian without the need for a second transformation. Equations-of-motion (EOM) methods [71] describe a class of systematically improvable methods, which include the TDA and RPA. The key observation in the formulation of EOM is that any excited state can be exactly rewritten in terms of a ladder-operator $X_\nu^\dagger$ and the correlated ground state

$$|\Psi_\nu\rangle = X_\nu^\dagger |\Psi_0\rangle \,. \tag{4.11}$$

$X_\nu^\dagger$ is formally given by the dyad $|\Psi_\nu\rangle\langle\Psi_0|$, and can be written as a linear combination of 1- to A-body excitation and deexcitation operators. The energy eigenvalue problem can then be expressed in terms of the commutator of H and $X_\nu^\dagger$:

$$[H, X_\nu^\dagger]|\Psi_0\rangle = \omega_\nu X_\nu^\dagger |\Psi_0\rangle \,, \tag{4.12}$$

where $\omega_\nu = E_\nu - E_0$ is the excitation energy. The strength of EOM methods, when applied to the bare Hamiltonian, lies in the ability to make controlled, computationally feasible approximations on the form of $X_\nu^\dagger$. Given some approximation of the correlated ground state, the amplitudes of $X_\nu^\dagger$ can be solved for in a generalized eigenvalue problem [95]. In principle, the approximate ground state can then be improved iteratively using the $X_\nu^\dagger$ and its Hermitian conjugate, which can then be used to get an improved $X_\nu^\dagger$, and so on.

We can eliminate the need to solve the equations-of-motion self-consistently with the IMSRG. After ground-state-decoupling, the reference state $|\Phi_0\rangle$ corresponds to the true ground state of $\bar{H}_1 \equiv U_1(\infty) H U_1^\dagger(\infty)$, and thus need not be improved. Multiplying Eq. 4.12 by $U_1(\infty)$ and using the rotated ground state $U_1(\infty)|\Psi_0\rangle = |\Phi_0\rangle$ gives

$$[\bar{H}_1, \bar{X}_\nu^\dagger]|\Phi_0\rangle = \omega_\nu \bar{X}_\nu^\dagger |\Phi_0\rangle\,, \tag{4.13}$$

where $\bar{X}_\nu^\dagger \equiv U_1(\infty) X_\nu^\dagger U_1^\dagger(\infty)$ only contains excitation operators since the reference state is annihilated by deexcitation operators. We recover the TDA equations for the ground-state-decoupled Hamiltonian if we choose

$$\bar{X}_\nu^\dagger = \sum_{ai} \bar{X}_i^a a_a^\dagger a_i\,. \tag{4.14}$$

Alternatively, we may use a more complete ladder operator which includes up to 2p2h excitations,

$$\bar{X}_\nu^\dagger = \sum_{ai} \bar{X}_i^a a_a^\dagger a_i + \frac{1}{4} \sum_{abij} \bar{X}_{ij}^{ab} a_a^\dagger a_b^\dagger a_j a_i\,. \tag{4.15}$$

The consequence of the increased precision introduced with eq. 4.15 is a more complicated eigenvalue problem than that of the TDA, but it significantly reduces the need for a second transformation as it includes a large portion of the correlations which are suppressed by U_2 or U_3. If we return to fig. 3.2, we see that in addition to the complete decoupling of the reference state, IMSRG(2) ground-state-decoupling also achieves a significant softening of the excited state block, and thus an EOM method such as that specified by eq. 4.15 will be much more successful here than with the bare operator, which includes direct couplings between the 1p1h and 3p3h channels. Note that the EOM calculation with this ladder operator is equivalent to diagonalizing $\bar{H}_1$ on the

space of singly- and doubly-excited Slater determinants. This is a configuration interaction calculation with singles and doubles (CISD) in disguise. However, this is only due to the fact that the true ground state is a simple Slater determinant in this rotated frame.

In general, the EOM ladder operator may have any excitation rank up to ApAh, which would constitute an exact diagonalization of $\bar{H}_1$. Similarly, the truncation rank of the IMSRG equations can in principle be increased to the IMSRG(A) level, where the unitary equivalence of $\bar{H}_1$ and H is exact. Therefore, EOM-IMSRG approximations are systematically improvable, allowing for EOM(m)-IMSRG(n) calculations, which will simply be referred to as EOM-IMSRG(m,n). The calculations in the present work are carried out in the EOM-IMSRG(2,2) approximation.

As a result of the vanishing de-excitation piece of $\bar{X}^\dagger_\nu$, Eq. 4.13 has the advantage that it may be solved as a traditional eigenvalue problem using power-iteration methods such as the Lanczos algorithm. Such methods only require knowledge of matrix-vector products. If $\bar{X}^\dagger_\nu$ is taken to be an eigenvector, the corresponding matrix-vector product is given by

$$[\bar{H}_1, \bar{X}^\dagger_\nu] = \{\bar{H}_1 \bar{X}^\dagger_\nu\}_C \tag{4.16}$$

where the subscript C denotes connected terms. Thus, pre-packaged Lanczos algorithm solvers can be used with the EOM-IMSRG, where the matrix-vector product is just the evaluation of the commutator expressions, and thus the method scales the same as IMSRG(2) ground-state-decoupling: $\mathcal{O}(N_p^4 N_h^2)$. Note that for nuclei, ladder operators are spherical tensors of rank J with definite parity, as they must connect the ground state to excited states of any desired spin J^π. For this reason, EOM-IMSRG calculations are more computationally demanding than TDA-IMSRG and vTDA-IMSRG calculations. However, the relatively small rotation of the ground-state decoupling U_1 makes the EOM-IMSRG equations far more numerically stable in comparison to the sequential decoupling approaches, which require a large secondary rotation $U_{2,3}$.

4.2.1 Improving the EOM-IMSRG(2,2)

By the nature of the ground-state-decoupled Hamiltonian, we expect some coupling between the 1p1h and 3p3h channels simply because those blocks are transitively related through the 2p2h block. Thus, description of 1p1h dominant states can be largely improved by going to the next truncation level in EOM, the EOM-IMSRG(3,2). Additionally, inclusion of triples excitations will be imperative for the description of 2p2h dominant states, which are still directly coupled to the 3p3h block in the ground-state-decoupled frame. The appropriate ladder operator is

$$\bar{X}^{\dagger}_{\nu} = \sum_{ai} \bar{x}^{a}_{i} a^{\dagger}_{a} a_{i} + \frac{1}{4} \sum_{abij} \bar{x}^{ab}_{ij} a^{\dagger}_{a} a^{\dagger}_{b} a_{j} a_{i} + \frac{1}{36} \sum_{abcijk} \bar{x}^{abc}_{ijk} a^{\dagger}_{a} a^{\dagger}_{b} a^{\dagger}_{c} a_{k} a_{j} a_{i} \,. \tag{4.17}$$

The solution of eq. 4.13 using eq. 4.17 can be achieved with a modest increase in computational scaling, $\mathcal{O}(N_p^5 N_h^3)$, but doing so requires the storage of a three-body operator for each desired excited state. This is not practical computationally, particularly in the case of nuclear excited states with large total angular momentum, where a significant number of matrix elements can be non-zero. We can instead treat the problem with Rayleigh-Schrödinger perturbation theory. The order zero wave function is taken to be the solution of the EOM-IMSRG(2,2),

$$|\tilde{\Psi}^{(0)}_{\nu}\rangle = |\bar{\Psi}_{\nu}\rangle = \bar{X}^{\dagger}_{\nu} |\Phi_0\rangle \,. \tag{4.18}$$

Using Epstein-Nesbet partitioning of the Hamiltonian, the zero order energy is

$$E^{(0)}_{\nu} = E_0 + \omega_{\nu} \,, \tag{4.19}$$

and the first order energy correction is zero by definition. The second order energy correction is then given by

$$E^{(2)}_{\nu} = \langle \tilde{\Psi}^{(0)}_{\nu} | \bar{H}_1 \frac{\hat{Q}}{E^{(0)}_{\nu} - \bar{H}^{(0)}} \bar{H}_1 | \tilde{\Psi}^{(0)}_{\nu} \rangle \,, \tag{4.20}$$

where $\hat{Q}$ is the complement space projector

$$\hat{Q} = |\Phi_0\rangle\langle\Phi_0| + \sum_{\mu \neq \nu} |\bar{\Psi}_{\mu}\rangle\langle\bar{\Psi}_{\mu}| + \frac{1}{36} \sum_{ijkabc} |\Phi^{abc}_{ijk}\rangle\langle\Phi^{abc}_{ijk}| + \cdots \tag{4.21}$$

Note that $\hat{Q} = 1 - \hat{P}$, where $\hat{P} = |\bar{\Psi}_\nu\rangle\langle\bar{\Psi}_\nu|$ projects onto the particular solution of the EOM-IMSRG(2,2) for which we are calculating the perturbative correction. Since couplings between $|\bar{\Psi}_\nu\rangle$ and the reference state or $npnh$ excitations with $n \geq 4$ are zero in a ground-state-decoupled framework, and since couplings with $|\bar{\Psi}_{\mu\neq\nu}\rangle$ vanish due to the approximate diagonalization performed in the EOM-IMSRG(2,2) calculation, the triply-excited terms of Eq. 4.21 give the only non-vanishing contribution and Eq. 4.20 becomes

$$E_\nu^{(2)} = \frac{1}{36} \sum_{ijkabc} \frac{\langle\Phi_0|\bar{X}_\nu \bar{H}_1|\Phi_{ijk}^{abc}\rangle\langle\Phi_{ijk}^{abc}|\bar{H}_1\bar{X}_\nu^\dagger|\Phi_0\rangle}{E_\nu^{(0)} - \langle\Phi_{ijk}^{abc}|\bar{H}_1|\Phi_{ijk}^{abc}\rangle}. \tag{4.22}$$

Eq. 4.22 gives a perturbative energy correction that approximates the full EOM-IMSRG(3,2) energy. In practice, we write Eq. 4.22 as:

$$E_\nu^{(2)} = \frac{1}{36} \sum_{ijkabc} \frac{|W_{abcijk}|^2}{D_{abc}^{ijk}}, \tag{4.23}$$

where

$$D_{abc}^{ijk} = \omega_\nu - \langle\Phi_{ijk}^{abc}|\bar{H}|\Phi_{ijk}^{abc}\rangle, \tag{4.24}$$

and

$$W_{abcijk} = [\bar{H}, \bar{X}_\nu^\dagger]_{abcijk}. \tag{4.25}$$

Storage of three-body matrix elements is not needed as Eqs. 4.23-4.25 need only be calculated once for each excited state with manageable $N_p^4 N_h^3$ scaling. In the following, the inclusion of perturbative triples on top of EOM-IMSRG(2,2) will be referred to as the EOM-IMSRG({3},2) approximation.

4.2.2 Comparison of the EOM-IMSRG and vTDA-IMSRG via Quantum Dots

Fig. 4.4 shows vTDA-IMSRG(2), EOM-IMSRG(2,2) and EOM-IMSRG({3},2) (labeled TDA_{31}, EOM_1, $\text{EOM}\{3\}_1$, respectively) spectra for two different quantum dots, along with FCI calculations performed for the bare Hamiltonian (FCI_0) and FCI calculations using the ground-state-decoupled Hamiltonian $\bar{H}_1$ (FCI_1). The length of the lines indicate the 1p1h content of a given

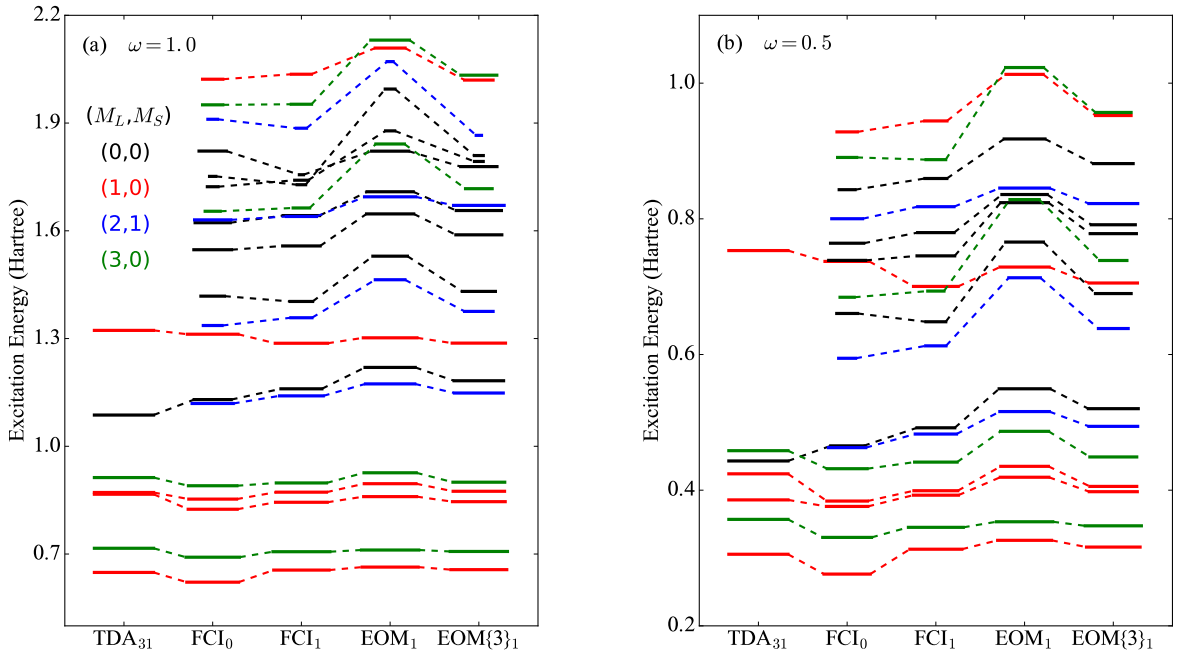

Figure 4.4 Selected excitation spectra of 6-electron quantum dots for $\omega = 1.0$ (left) and $\omega = 0.5$ (right) performed in an $N = 3$ single-particle basis. The quantum numbers of the various states are color-coded as (M_L, M_S) = (0,0), (1,0), (2,1), (3,0). The calculated spectra are displayed for five different many-body approaches, where the subscript indicates which Hamiltonian the respective method is applied to. For example FCI_0 and FCI_1 denote FCI calculations on the bare and ground-state-decoupled Hamiltonians respectively, TDA_{31} denotes a TDA calculation on the vTDA-decoupled Hamiltonian, etc. The lengths of the plotted energy levels indicate the 1p1h content of the state as defined in Eqs. 4.26-4.29.

state which we define as

$$n(1p1h)_{FCI_0} = \sum_{ph} |C_h^p|^2 \tag{4.26}$$

$$n(1p1h)_{FCI_1} = \sum_{ph} |(\bar{C}_1)_h^p|^2 \tag{4.27}$$

$$n(1p1h)_{EOM_1} = \sum_{ph} |(\bar{X}_1)_h^p|^2 \tag{4.28}$$

$$n(1p1h)_{TDA_{31}} = \sum_{vh} |(\bar{X}_{31})_h^v|^2 = 1\,. \tag{4.29}$$

Note that this quantity is defined differently depending on the particular unitary transformation, so a direct 1-to-1 comparison can be misleading. For instance, in the vTDA-IMSRG calculations, the excited states are completely 1p1h in the unitarily-transformed frame, hence all of the lines in the TDA_{31} column are the maximum possible length. Since FCI_1 and EOM_1 are performed for the same operator $\bar{H}_1$, a direct comparison of Eq. 4.28 and 4.27 is consistent. We note that EOM-IMSRG({3},2) partial norms are corrected by normalizing with the wave function corrected to first order in perturbation theory, resulting in a slight decrease.

In Fig. 4.4 we show four sets of states with the indicated quantum numbers chosen to demonstrate the robustness of the EOM-IMSRG method. For odd parity states such as $(M_L,M_S) = (1,0)$ and (3,0), we see that those which are strongly of 1p1h nature are well-described by both vTDA-IMSRG and EOM-IMSRG methods. We also note that the EOM-IMSRG reproduces the FCI_1 partial norms nicely for these states, indicating that the EOM-IMSRG(2,2) is a good approximation to the full diagonalization of $\bar{H}_1$. The EOM-IMSRG spectra degrades somewhat for even parity states, since the sizable shell gap at the Fermi level tends to suppress the 1p1h dominance for such states, and at higher excitation energies. However, it bears repeating that the EOM-IMSRG is significantly more flexible than the vTDA-IMSRG, as the latter is intrinsically unable to access even parity and/or higher excited states without expanding the model space to include the entire 1p1h configuration space, which often leads to numerical instabilities and/or erratic convergence.

While the EOM-IMSRG is only an approximate diagonalization of the evolved Hamiltonian, it can be systematically improved. EOM-IMSRG({3},2) corrections significantly reduce the errors in the EOM-IMSRG(2,2) approximation at a manageable computational cost. Excitation energies, which are consistently overestimated by the EOM-IMSRG(2,2) calculation, are consistently reduced by the perturbative triples correction, bringing results into better agreement with the FCI_1 and FCI_0 spectra. The quality of EOM-IMSRG({3},2) energies is still dependent on higher excitation rank content, but 1p1h states are described quite sufficiently by this approximation. The error in 2p2h dominant states is significantly reduced, but this block couples directly to the 3p3h block, so a perturbative treatment may be uncontrolled here.

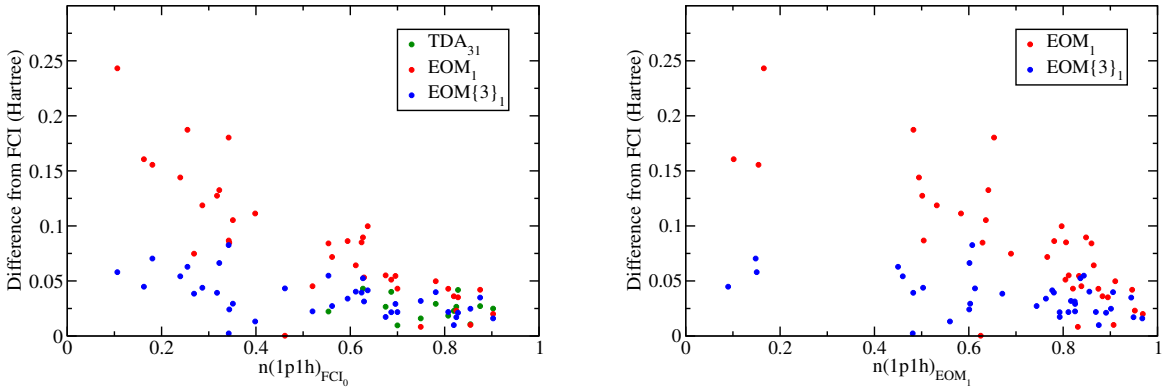

Figure 4.5 Absolute difference between quantum dot excitation energies calculated via IMSRG methods and those calculated with FCI on the bare Hamiltonian. Each point corresponds to an EOM or TDA energy level in Figure 4.4. The left panel is plotted against FCI 1p1h content, while the right is plotted against the EOM 1p1h amplitudes.

The quality of IMSRG results degrades as the importance of correlation in the system increases. This is seen clearly in the right panel of Fig. 4.4 for the smaller trap frequency $\omega = 0.5$. Nevertheless, the perturbative triples correction still gives substantial improvement. A strong correlation between the errors of either method and the bare FCI 1p1h amplitudes is apparent. The right panel of fig. 4.5 shows the absolute difference between the FCI_0 excitation energy and those calculated via EOM-IMSRG(2,2) or vTDA-IMSRG(2), plotted against the bare FCI partial norm for each state. A clear inverse proportional relationship can be seen. Accessible vTDA-IMSRG(2) results are generally more accurate than EOM-IMSRG(2,2). While a successful vTDA-IMSRG calculation should fully decouple the relevant excited states from truncated terms in the configuration expansion, where EOM-IMSRG(2,2) ignores some non-zero couplings by definition. Despite full decoupling, the vTDA-IMSRG(2) should induce additional errors due to the secondary transformation. Evidently, the errors from the EOM(2) truncation are typically greater than those of the vTDA-IMSRG(2) secondary transformation. However, this difference is for the most part erased by the EOM-IMSRG({3},2) triples correction. The root-mean square deviations from the FCI results are 0.095 Hartree for EOM-IMSRG(2,2) and 0.031 Hartree for EOM-IMSRG({3},2).

In larger spaces, FCI calculations are not feasible, so we should also consider the relationship between the error and the EOM_1 partial norm of Eq. 4.28. The right panel of fig. 4.5 demonstrates this relationship, using the same states displayed in Fig. 4.5. Here it is evident that EOM-IMSRG overestimates the 1p1h content of calculated states, however there is a modestly linear relationship between the error and the EOM partial norm. This is a useful tool to gauge the reliability of EOM-IMSRG calculations in larger spaces, as EOM amplitudes are immediately available after solution of Eq. 4.12.

4.2.3 Results in Finite Nuclei

Applying both the vTDA-IMSRG(2) and EOM-IMSRG(2,2) to finite nuclei, we find a clear preference for the latter method. Unfortunately, the promising results of vTDA-IMSRG(2) calculations in quantum dots do not carry over to nuclei, as uncontrolled numerical instabilities in the secondary transformation render the vTDA-IMSRG unusable for systems with strong correlations. Until these instabilities are better understood and overcome, sequential decoupling appears to be appropriate only for computations in doubly-magic nuclei. Figure 4.6 depicts the lowest excitation energies of ^{16}O calculated at several different angular momenta and parities. We find that the vTDA-IMSRG(2) tracks well with EOM-IMSRG(2,2) for low-lying 1p1h dominant states, but is non convergent for all others. In the left column, the 1p1h partial norm (Eq. 4.28) of the EOM wave function is listed above the corresponding energy for that state. While the 0^+ state has strong 1p1h content in the EOM calculation, the vTDA-IMSRG(2) fails to converge beyond the three lowest excited states[1]. Strongly 1p1h even parity states in doubly-magic nuclei require the valence space to contain two-major shells above the Fermi level, hence the convergence difficulties. In nuclei with sub-shell closures such as ^{22}O, the vTDA-IMSRG(2) fails to converge even for most low-lying 1p1h dominant states. This is most likely due to the presence of stronger correlations,

[1]We are not attaching any physical meaning to states at such unphysical high excitation energies. Rather, our point is to illustrate that obtaining converged, stable calculations in the EOM-IMSRG is relatively foolproof for a wide range of states, whereas the vTDA-IMSRG calculations are fraught with numerical difficulties.

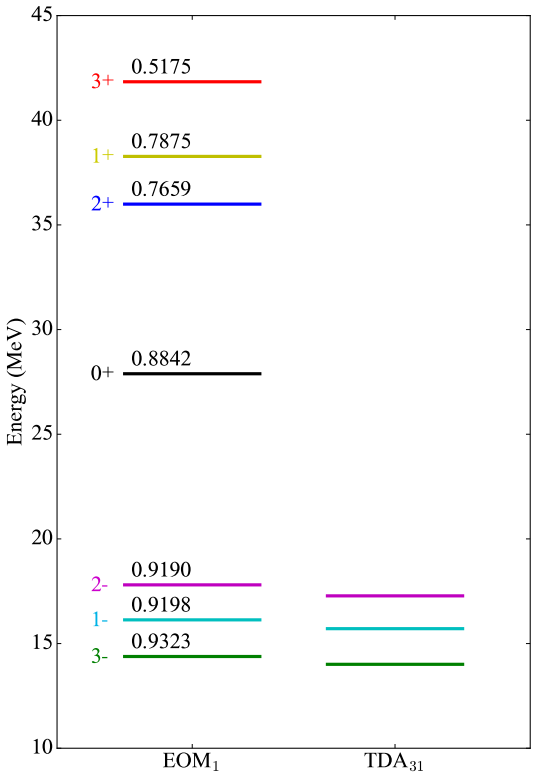

Figure 4.6 Lowest ^{16}O excitation energies plotted for various quantum numbers, calculated with EOM-IMSRG(2,2) and vTDA-IMSRG(2) starting from the N^{3}LO (500 MeV) NN interaction of EM [5], softened by free-space SRG evolution to $\lambda = 2.0$ fm^{-1}. The single-particle basis is given by $\hbar\omega$ = 24.0 MeV and $e_{max} = 8$. Above each plotted energy level from the EOM-IMSRG(2,2) calculation is the 1p1h partial norm of Eq. 4.28.

which exacerbate the issue of unitary breakdown. For this reason, we will restrict ourselves to the EOM-IMSRG(2,2) formalism in the remainder of this chapter.

As we restrict the single-particle basis by orbital energy rather than excitation quanta, there is no a priori factorization of center of mass components of the wave function for self-bound systems such as nuclei. Nonetheless, we expect approximate factorization and thus spurious COM excitations are treated via the Lawson-Gloeckner method [142], with an augmented intrinsic Hamiltonian

$$H = H_{int} + \beta H_{CM}(\tilde{\omega}), \tag{4.30}$$

where $\tilde{\omega}$ is determined with the method of Hagen et. al. [6, 152]. Assuming that the intrinsic and COM wave functions factorize, the use of the Lawson term in Eq. 4.30 should remove spurious excitations from the low-lying spectrum as β is increased. An example is shown in Figure 4.7 for the 1^- spurious state in ^{22}O, which gets shifted rapidly out of the spectrum for non-zero values of β. The weak residual β dependence of the remaining states indicates that the COM factorization

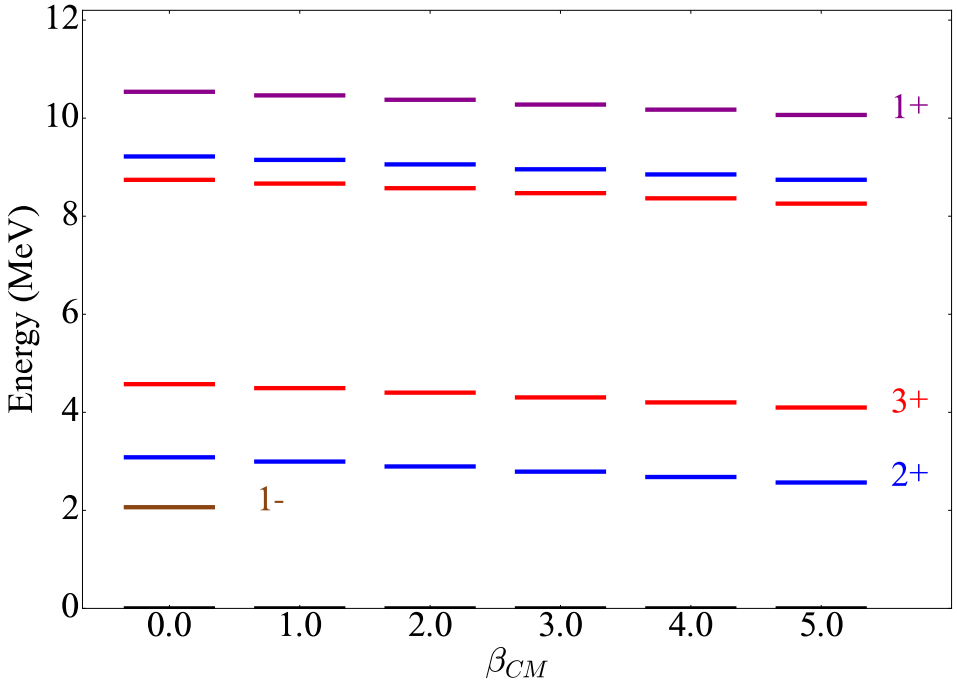

Figure 4.7 Low lying states of ^{22}O at $\hbar\omega = 28.0$ MeV and $e_{max} = 11$ for several values of the Lawson parameter β, using the N^{3}LO (500 MeV) NN interaction of EM [5], softened by free-space SRG evolution to $\lambda = 3.0$ fm^{-1}. The COM frequency $\hbar\tilde{\omega} = 17.28$ MeV.

is approximately satisfied for these states. We expect this factorization to improve (weaker β dependence) as we go to higher excitation levels and larger bases, as has been empirically observed in [152, 153].

An important litmus test for the EOM-IMSRG(2,2) method is the ability to produce results that are comparable to analogous EOM-CC calculations. As with ground-state coupled cluster theory, EOM-CC methods originated in nuclear physics [73, 74, 154], but were largely ignored for many years due to convergence issues arising from the "hard cores" found in most NN potential models,

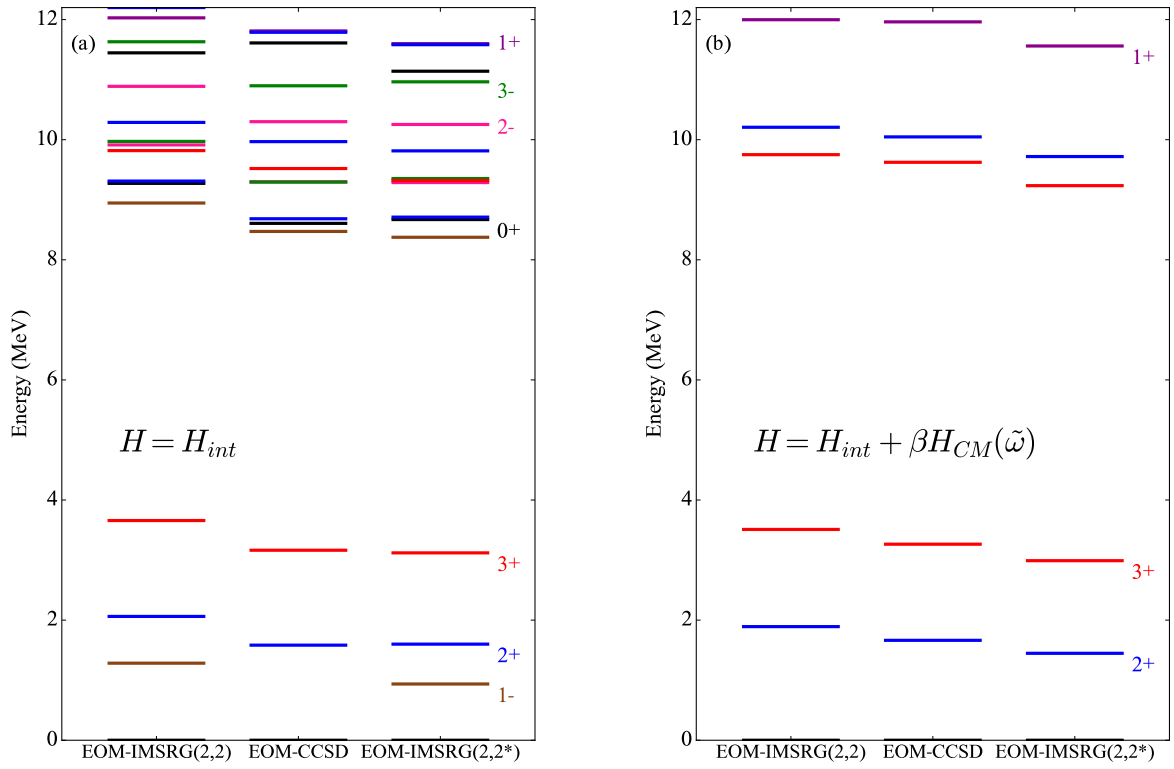

Figure 4.8 Selected excitation spectra of ^{22}O at $\hbar\omega = 20.0$ MeV and $e_{max} = 11$ using the N^{3}LO (500 MeV) NN interaction of EM [5], softened by free-space SRG evolution to $\lambda = 2.0$ fm^{-1}. The left frame shows the excitation energies calculated with the intrinsic Hamiltonian, and the right frame shows the result of adding a Lawson center-of-mass term $H = H_{int} + \beta H_{CM}(\tilde{\omega})$, with β = 5.0. Different colors indicate different J$^{\Pi}$.

while going on to enjoy great success in quantum chemistry [11, 76]. In recent years, EOM-CC methods have had a resurgence in nuclear physics due to the development of softer chiral EFT interactions and RG methods to soften them further, providing unprecedented access to *ab initio* calculations of ground and excited state properties for medium-mass nuclei in the vicinity of closed shells [42, 59, 68, 69, 93, 144].

Due to similar truncations being made, we expect the EOM-IMSRG(2,2) to produce results that are comparable to EOM-CCSD calculations. As mentioned in section 3.2.6, IMSRG(2) ground state calculations tend to more closely reproduce the more sophisticated CCSD(T), due to an

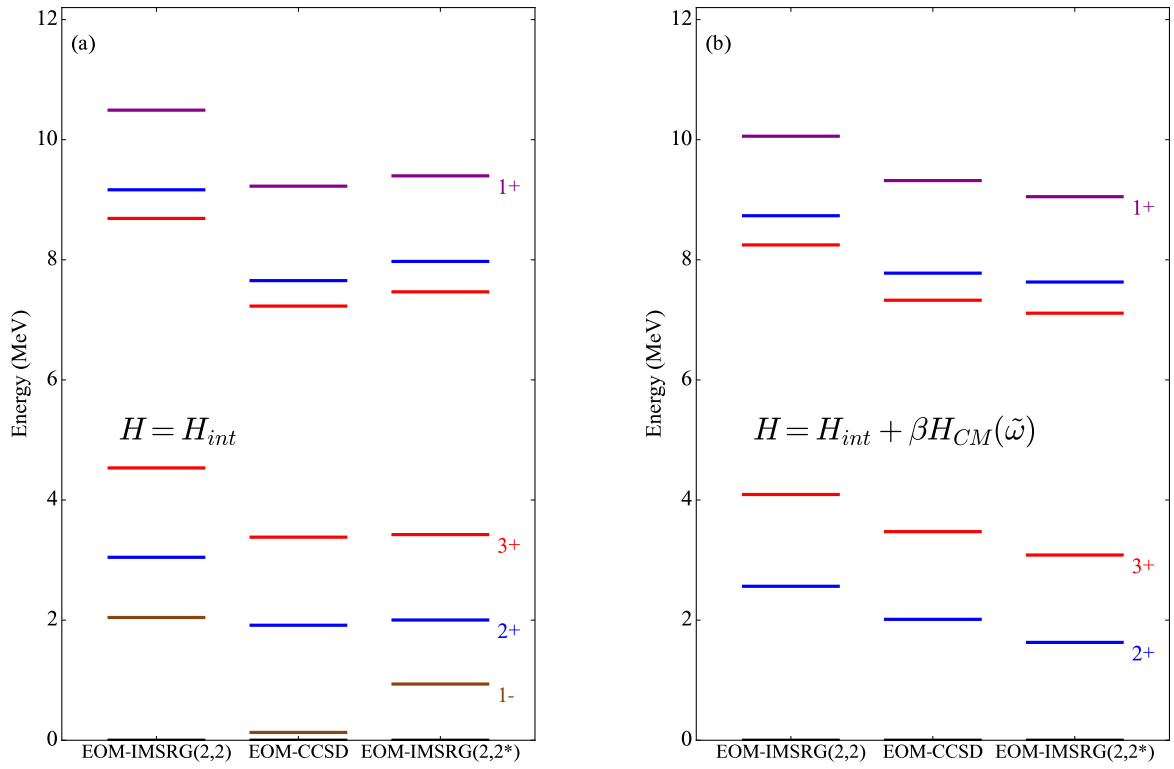

Figure 4.9 Selected excitation spectra of ^{22}O at $\hbar\omega = 28.0$ MeV and e_{max}=11 using the N^{3}LO (500 MeV) NN interaction of EM [5], softened by free-space SRG evolution to $\lambda = 3.0$ fm^{-1}. The left frame shows the excitation energies calculated with the intrinsic Hamiltonian, and the right frame shows the result of adding a Lawson center-of-mass term $H = H_{int} + \beta H_{CM}$, with β = 5.0. Different colors indicate different J$^{\Pi}$.

undercounting of asymmetric quadruple diagrams at MBPT(4). Understanding how each specific resummation of MBPT affects excited states would require an analytical treatment in quasi-degenerate perturbation theory, which is beyond the scope of this work. We will content ourselves with empirical investigations, using both the IMSRG(2) and IMSRG(2*) ground-state-decoupled Hamiltonians in our exploration. In Figure 4.8 we show calculations of the low-lying spectra of ^{22}O performed on the intrinsic Hamiltonian, as well as the Lawson Hamiltonian with β=5.0. In each panel, the left column shows the excited states calculated in the standard EOM-IMSRG(2,2) approximation, while the right column shows the quadruples corrected EOM-IMSRG(2,2*).

On a technical note, COM frequencies $\tilde{\omega}$ are calculated independently for the IMSRG(2) and IMSRG(2*) methods, and corresponding Lawson terms are constructed. The Lawson term is constructed in the CCSD calculations using the frequencies calculated in the IMSRG(2*) formalism, which we expect to be a good approximation given the similar perturbative content of both methods. The relevant frequencies are given in table 4.2.3. The observed removal of spurious center-of-mass excitations is consistent in all three approaches.

Figure 4.9 displays a similar comparison for a "harder" interaction at $\lambda = 3.0$ fm^{-1}. Differences between the EOM-IMSRG(2,2*) and CCSD are more notable here, but qualitative agreement is still intact. The EOM-IMSRG(2,2) excitation energies are generally shifted up from their CCSD counterparts. This is indicative of the increasing effect of missing 4th-order quadruples for harder interactions and is consistent with observations of increasing differences between IMSRG(2) and CCSD ground-state energies for interactions with larger λ values [3].

To reproduce experimental spectra, we include an N^{2}LO 3N force fit at $\Lambda = 400$ MeV [13], which has had some success in the *ab initio* description of excited states [46, 51, 155]. Fig. 4.10 shows the computed spectra for closed shell nuclei ^{14}C and ^{22}O, using the above interaction. Results are compared with experiment. Here spurious states have been identified and removed from the spectra.

Here much of the experimental spectrum is poorly reproduced by EOM-IMSRG(2,2). We see many of the states in ^{14}C are missed, and the calculated 2_1^+ state appears to align with the experimental 2_2^+ state. We are unable to rule out the possibility that we miss the first experimental 2^+ state entirely due to low 1p1h content, as we only have energetics to draw comparisons with. This

Method	$\lambda = 2.0$ fm^{-1}	$\lambda = 3.0$ fm^{-1}
IMSRG(2)	18.19	17.28
IMSRG(2*)	18.05	17.50
CCSD	18.05	17.50

Table 4.1 Values of $\hbar\tilde{\omega}$ in MeV, used in center-of-mass Hamiltonian for Lawson calculations of ^{22}O energy spectra.

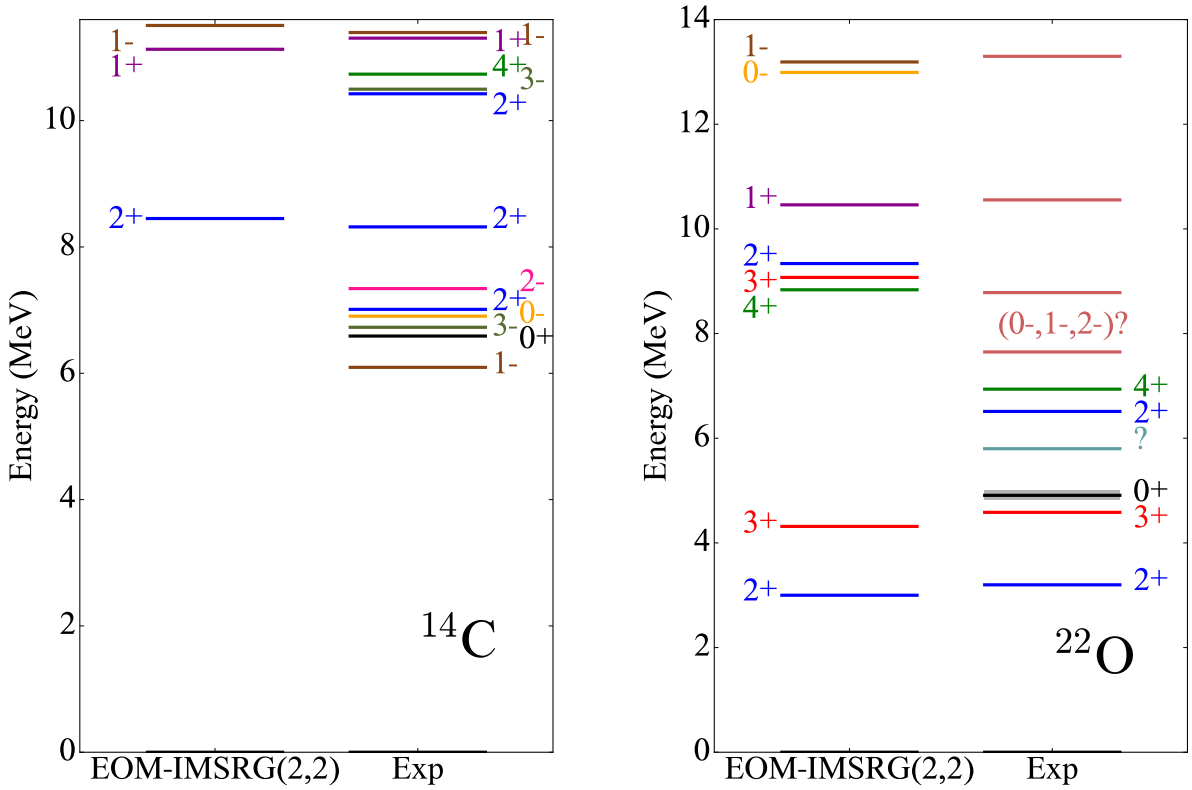

Figure 4.10 Low lying spectra of ^{14}C and ^{22}O at $\hbar\omega = 20.0$ MeV and e_{max}=14 using the standard input NN+3N(400) interaction, softened by free-space SRG evolution to $\lambda = 2.0$ fm^{-1}. Results are compared with experiment [12].

calculation can surely benefit from the inclusion of a triples correction and analysis of observables. Matching with experimental states will be discussed in more detail in chapter 5.

The picture is less obscure in ^{22}O, where given the assumption that the nucleus is appropriately described by a single-reference state, parity arguments give us confidence that the low-lying 2^+_1 and 3^+_1 are largely composed of single excitations within the *sd*-shell. Accordingly, EOM-IMSRG(2,2) reproduces experiment for these states fairly well. Higher energy spectra are not produced particularly well, which is expected as the higher energy states certainly contain more 2p2h and higher content than the first two excited states. Again, this study can be greatly facilitated by inclusion of a triples correction, which we would expect to be small for the first two excited states.

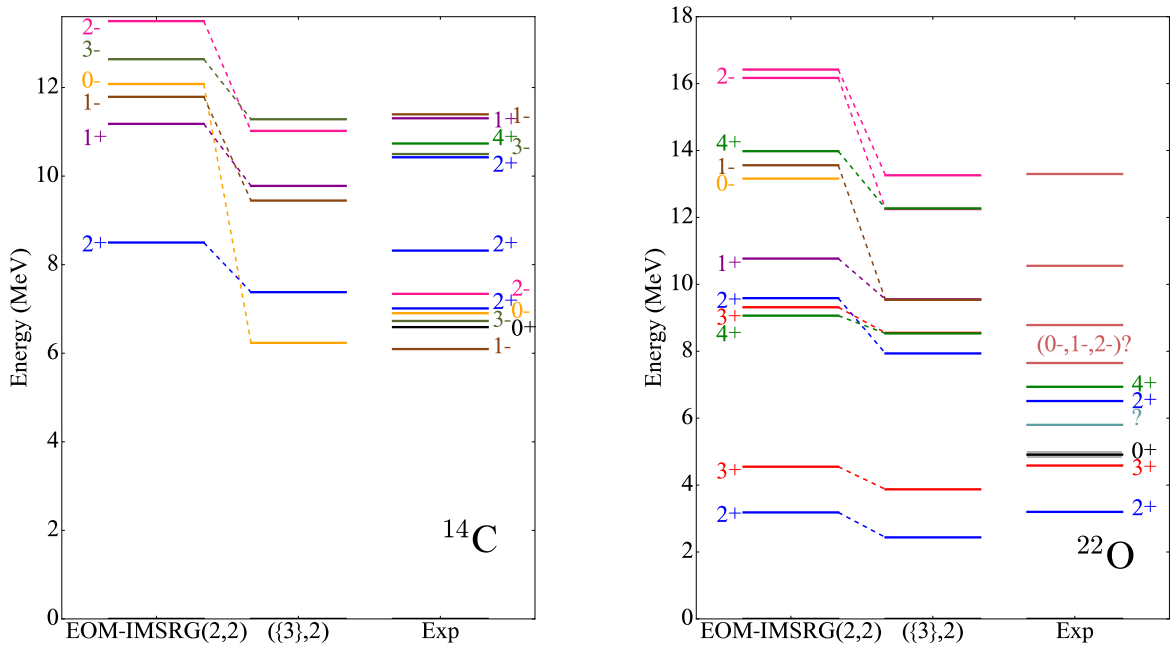

Figure 4.11 Triples correction for low lying spectra of ^{14}C and ^{22}O at $\hbar\omega = 20.0$ MeV and e_{max}=8 using the N^{3}LO (500 MeV) NN interaction of EM [5] with N^{2}LO 3N force (400 MeV) [13], softened by free-space SRG evolution to $\lambda = 2.0$ fm^{-1}. Results are compared with experiment [12].

4.2.4 Perturbative Corrections for Nuclei

While the EOM-IMSRG({3},2) correction is a rather straightforward computation for manageable systems such as parabolic quantum dots, the correction is much more computationally challenging for a strongly correlated nucleus. The correction must be implemented in J-scheme (see appendix), and thus requires numerous sums over intermediate couplings to total angular momentum quantum number, along with the already taxing $\mathcal{O}(N_p^4 N_h^3)$ scaling. For this reason we are unable to perform extensive EOM-IMSRG({3},2) calculations with the large model spaces used in the previous calculations. However, as a demonstration of the method, results for an $e_{\max}$=8 model space are shown in Fig. 4.11. Here we compute the same states as in fig. 4.10, but we use a smaller model space for the purposes of computational feasibility. As calculations are performed at the

optimal basis frequency ($\hbar\omega$ = 20 MeV) for these systems, EOM-IMSRG(2,2) calculations are reasonably converged despite the small model space. The EOM-IMSRG({3},2) correction shifts all of the states down, as constituents of the excluded-space of triply excited Slater-determinants do not exhibit any near degeneracies with the low-lying EOM-IMSRG(2,2) spectra. Strongly 1p1h states such as the 2_1^+ and 3_1^+ states in ^{22}O undergo smaller corrections than higher energy states, which couple more strongly to the 3p3h block through their higher-order many-body content. The computed 2_1^+ state in ^{14}C experiences a shift which moves it closer to its experimental counterpart, whereas previously it aligned more closely with the experimental 2_2^+ state. Likewise, numerous states which appear at high energy are moved down significantly by the inclusion of the triples correction, in better correspondence with the experimental spectra. The larger shifts seen in odd-parity states indicate significant content beyond 1p1h, and thus it is likely that for a perturbative triples treatment, additional IMSRG evolution will be needed to soften couplings to higher-order content.

A curious case is presented by the 0^- state for both nuclei. The shift is quite large compared with the other odd-parity states, and in ^{22}O, the triples result (not shown to reduce clutter) gives a negative excitation energy for the 0^- state. Another issue is the observation that in ^{22}O, the EOM-IMSRG(2,2) results for the two lowest states, seemingly consistent with experiment, are shifted further from experiment by their triples corrections. At the moment, these results are not thoroughly understood, but the discrepancy may be attributable to several sources. The interaction may contribute to the overbinding in these states, leading to slightly lower energies. Work is in progress to understand the nature of these errors.

Overall, the EOM-IMSRG({3},2) is inconsistent in that it treats the IMSRG calculation with a two-body truncation and the EOM portion at an approximate three-body level. We could certainly construct the EOM-IMSRG({3},{3}) by shifting all of the absolute energies by the triples correction of eq. 3.50, however a full inclusion of correlations with the triples-corrected ground state would require additional perturbative terms involving the first-order wave functions of the ground and excited states, which we will denote EOM-IMSRG({3,3}) when it comes to fruition.

4.2.5 Extensions of EOM-IMSRG

The EOM-IMSRG formalism presented is sufficient to describe the excited states of closed shell nuclei only. This stems from the fact that the flowing vertices in eqs. 3.21-3.23 are normal-ordered with respect to a single Slater determinant reference state. The most obvious solution to this limitation would be to merge multireference IMSRG (MR-IMSRG) [45,47] with EOM techniques. This method uses generalized normal-ordering to include static correlations in the reference state [77], and as a result augments the IMSRG(2) equations with terms proportional to one-, two- and higher-body irreducible density matrices. Ultimately the full MR-EOM-IMSRG will allow for the description of many additional open-shell nuclei, but the current formulation of the MR-IMSRG with scalar operators in J-scheme limits the description to spherical even-even nuclei.

Single reference EOM-IMSRG can be extended to open shell nuclei using particle attached (PA) and removed (PR) operators,

$$Y_\nu^\dagger = \sum_a y^a a_a^\dagger + \frac{1}{2}\sum_{abi} y_i^{ab} a_a^\dagger a_b^\dagger a_i \tag{4.31}$$

$$Z_\nu^\dagger = \sum_i z_i a_i + \frac{1}{2}\sum_{aij} z_{ij}^a a_a^\dagger a_j a_i \,, \tag{4.32}$$

where particle number breaking operators are used to connect that A-body reference state to the $(A \pm 1)$-body spectra. Solving eq. 4.13 using eq. 4.31 or eq. 4.32 in place of $X^\dagger$ constitutes the PA-EOM-IMSRG(2,2) or PR-EOM-IMSRG(2,2) respectively, where the first "2" now refers to the truncation to 2p1h or 2h1p operators. Analogously, we can construct methods for two-particle attachment or removal. It's not foolhardy to think that the MR-IMSRG precludes the practical use of PA-EOM-IMSRG, as it provides direct access to open-shell nuclei. However, the particle number conserving formalism will only be able to describe even-even nuclei, as the MR-IMSRG can only provide a 0^+ reference state. Here the PA and PR formalism will be needed to fill in the gaps. At the moment, no MR-EOM-IMSRG implementation exists, but we have performed PA/PR-EOM-IMSRG for cylindrical quantum dots, as a proof of efficacy.

The left panel of Fig. 4.12 shows results of particle addition energies for the six particle quan-

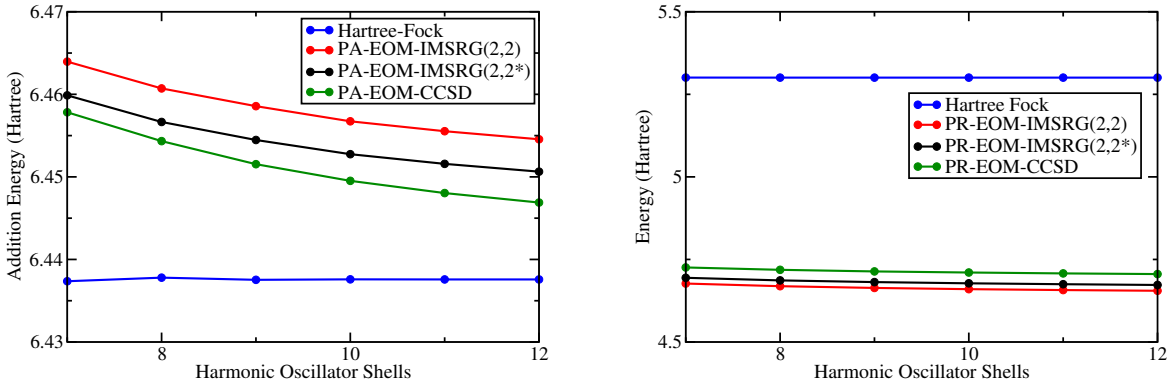

Figure 4.12 Calculated $(M_L, M_S) = (0,1)$ particle addition and removal energies for a 6-electron quantum dot with $\omega = 1.0$ state with EOM-IMSRG, EOM-CCSD and Hartree-Fock theory. Results are plotted as a function of oscillator shells used for the single-particle basis.

tum dot system. Results are computed using the IMSRG(2), IMSRG(2*), and CCSD as a base for EOM methods, and the HF single particle energy is given for reference. The effect of correlations here is rather small, but this system offers an excellent testing ground to compare methods. The IMSRG and CCSD methods show similar convergence properties. The discrepancy between PA-EOM-IMSRG(2) and PA-EOM-CCSD accounts for less that 0.01% of the total addition energy, with that discrepancy being reduced by roughly a factor of two when the IMSRG(2*) approximation is used. In the right panel, removal energies are computed for the same system. Despite showcasing a larger overall discrepancy than the addition energies, the difference between EOM-IMSRG and EOM-CCSD (1% of the removal energy) is much smaller than the effect of correlations (10%). This stands in contrast to the addition energies, where the discrepancy is only about a factor of two smaller than the discrepancy caused by correlations.

In nuclear systems, an additional extension of the single-reference EOM-IMSRG(2,2) can be made through use of isospin breaking charge-exchange operators, which can be used to describe isobaric neighbor nuclei to closed shells. The formalism is exactly the same as the particle-number conserving EOM-IMSRG derived from eq. 4.15, with the only difference being that neutrons are converted to protons or vice versa. For example, we may construct a ladder operator for the 1^+

ground state of ^{14}N , using the ^{14}C reference state,

$$|\Psi_0(^{14}N)\rangle = X^\dagger(\Delta Tz = -1)|\Phi_0(^{14}C)\rangle \tag{4.33}$$

$$X^\dagger(\Delta Tz = -1) = \sum_{ia} x_i^a p_a^\dagger n_i + \frac{1}{4}\sum_{ijab} x_{ij}^{ab}\delta_{t_{z_b}t_{z_j}} p_a^\dagger a_b^\dagger a_j n_i \tag{4.34}$$

where $p^\dagger$ and n are proton creation and neutron annihilation operators, respectively.

Results for ^{14}N are shown in fig. 4.13. Similar to the charge conserving EOM-IMSRG(2,2), the 1p1h-dominant low-lying 0_1^+ state is described well by this method. The remaining states have excitation energies which are too high, indicating some admixture of 2p2h and higher-order content. We have not implemented a triples correction here, but again we expect that such a correction would have a noticeable effect on the odd-parity states, which likely have more balanced compositions of 1p1h excitations into the *sd*-shell and 2p2h excitations where only one particle crosses the major shell-gap. We also consider the accuracy of ground state energy, as the wave function is built here upon the ^{14}C reference state. Its binding energy is calculated to be 7.430 MeV/nucleon, while the experimental value is 7.475614 MeV/nucleon [156]. We will use the charge-exchange formalism for both energetics and electromagnetic observables in chapter 5.

We have seen that with a single reference EOM-IMSRG(2,2) code, closed shell nuclei and their four nearest isobaric, isotonic and isotopic neighbors should be within reach. However, we caution that next-nearest neighbors will be described rather poorly in this way, as EOM-IMSRG(2,2) is a fairly limited approximation for nuclei which have no 1p(1h) components with respect to the closed-shell reference state.

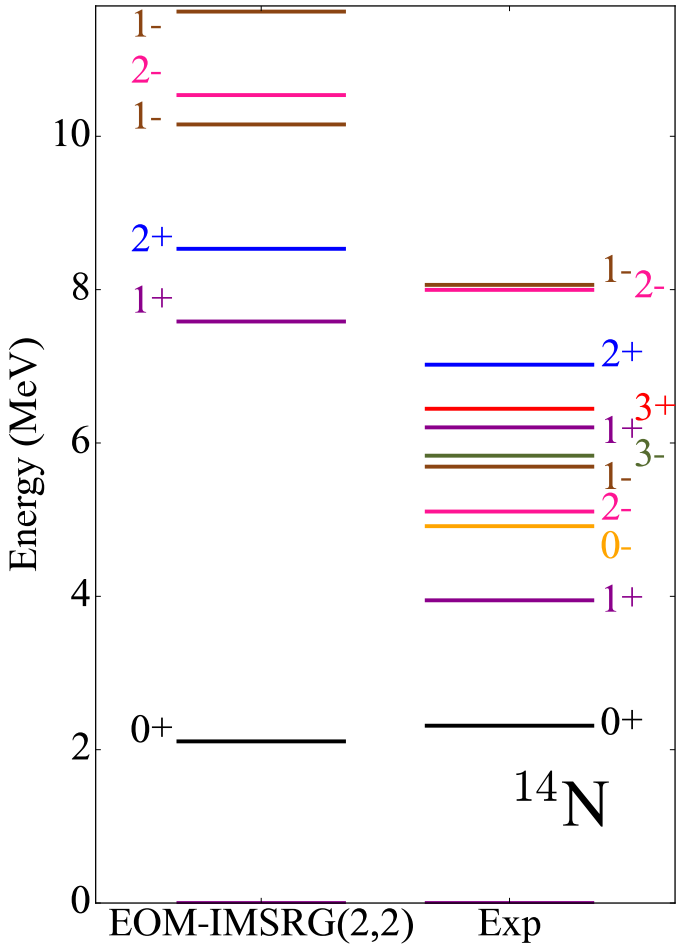

Figure 4.13 Low lying spectra of ^{14}N at $\hbar\omega = 20.0$ MeV and e_{max}=14 using the standard NN+3N(400) softened by free-space SRG evolution to $\lambda = 2.0$ fm^{-1}. Results are compared with experiment [12]. Experimental spectra beyond the 1_2^- state are omitted for clarity.

CHAPTER 5

CONSISTENT COMPUTATION OF OBSERVABLES

In the previous chapters, we have discussed the computation of both ground and excited state energies within the IMSRG framework. A complete theory, capable of guiding and analyzing experiment, should also be able to describe general observables which are of interest in experiment such as electromagnetic transition strengths and moments. A general and consistent framework for observables in *ab initio* methods will help address longstanding problems in nuclear physics, such as the nature of the observed quenching of the axial vector coupling constant g_A, or the source of effective charges in medium.

A critical property of physical observables is that they are invariant under unitary transformation. In other words, when a change of resolution scale is implemented through some renormalization group transformation or otherwise, the effects of the scale change should be applied consistently to the operators of interest. The consistently transformed operators,

$$\bar{O}(s) = U(s) O U^\dagger(s) \,, \tag{5.1}$$

are called "effective" operators. This highlights the fact that interactions and operators themselves are not observables [39], but rather tools used to probe observables. These tools are most useful when tuned to the proper degrees of freedom. In this chapter, we will introduce a general effective operator formalism for the IMSRG, where the bare operators are transformed consistently alongside the Hamiltonian. Non-scalar effective operators have been implemented in both the EOM-IMSRG and the recently developed valence-space IMSRG (VS-IMSRG). We explore the effects of consistent operator evolution and convergence properties for both methods, benchmarking with no-core shell model (NCSM) and experiment when available.

5.1 Effective Operators in the IMSRG

The IMSRG transformation may be straightforwardly applied to any operator using eq. 3.8 where the generator η is defined in terms of the flowing Hamiltonian. Prior to the Magnus formulation, large scale effective operator calculations were unpractical. As discussed in section 3.2.3, the traditional IMSRG approach is computationally unfeasible because of the many copies of each operator needed for a high-order ODE solver.

In the Magnus formulation, we may solve first for the Magnus generator Ω, and subsequently apply the transformation to each additional operator via the Baker-Campbell-Hausdorff expansion of eq. 3.39. Until recently, these calculations were limited to scalar observables such as radii and monopole moments. *Ab initio* calculations of non-scalar observables have been possible in the NCSM and QMC, where no renormalization of the operators is needed [157–160], but these explorations are limited to light nuclei and often lack sufficient convergence due to the restricted model spaces necessary for quasi-exact approaches. The present work extends IMSRG calculations in the medium-mass region to transitions and moments, through the derivation and efficient implementation of commutator expressions involving arbitrary rank spherical tensor operators. The relevant equations are given in the appendix. As a result, consistent calculation of all tensor observables such as electromagnetic strengths, moments, and Gamow-Teller strengths are now accessible. In principle, this formalism also paves the way for consistent predictions of quantities on the cutting edge of physics, such as the nuclear matrix elements for neutrinoless double β-decay [67] and structure factors of weakly interacting massive particles (WIMPs) scattering from nuclei, which are relevant in searches for dark matter [161, 162].

5.1.1 Transition Operators

In this work, we will consider three electromagnetic multipole operators, the M1, E2, and E3 operators. The latter, known as the electric octupole operator, allows for odd-parity transitions up to $\Delta J = 3$, which are relevant to the low lying 3^-_1 states observed in doubly magic nuclei. The M1

and E2 operators are responsible for the even-parity transitions which are most prolific in nuclear physics, namely the magnetic dipole and electric quadrupole transitions. Observables discussed here include transition strengths, given by

$$B(\sigma\lambda;\Psi_i J_i \to \Psi_j J_f) = \frac{1}{2J_i+1}|M_{fi}|^2, \tag{5.2}$$

where M_{fi} is the reduced transition matrix-element

$$M_{fi} = \langle \Psi_i J_i || O^{\sigma\lambda} || \Psi_f J_f \rangle, \tag{5.3}$$

and $O^{\sigma\lambda}$ are the transition operators (σ is a dummy variable for M or E, and λ is the tensor rank).

We also compute moments of the M1 and E2 operators,

$$\mathscr{M}^{\sigma\lambda} = \langle \Psi JM = J | O_0^{\sigma\lambda} | \Psi JM = J \rangle, \tag{5.4}$$

where the transition matrix element is no longer reduced, and we take the $M = J$ projection of the state Ψ. We take the bare operators as our starting point, using only the leading-order one-body piece for each operator, written in the lab frame. The operators are derived from the electric and magnetic multipole expansions [163],

$$O_\mu^{E\lambda} = \sum_{j=1}^{A} e(j) r_j^\lambda Y_\mu^\lambda(\Omega_j), \tag{5.5}$$

$$O_\mu^{M\lambda} = \mu_N \sum_{j=1}^{A} \left[\frac{2}{\lambda+1} g_l^{(j)} \mathbf{l}(j) + g_s^{(j)} \mathbf{s}(j) \right] \cdot \nabla_j [r_j^\lambda Y_\mu^\lambda(\Omega_j)], \tag{5.6}$$

where μ_N is the nuclear magneton. The electric charge $e(j)$ and gyromagnetic ratios $g_s^{(j)}$ and $g_l^{(j)}$ are given by their bare values

$$e(p) = 1 \qquad g_s^{(p)} = 5.586 \qquad g_l^{(p)} = 1 \tag{5.7}$$

for protons, and

$$e(n) = 0 \qquad g_s^{(n)} = -3.826 \qquad g_l^{(n)} = 0 \tag{5.8}$$

for neutrons. Phenomenological computations of electromagnetic observables typically require effective values for these parameters to account for in-medium effects, which can be thought of as

arising from the polarization of the core by valence nucleons through the inter-nucleon interactions. As the valence nucleons change their state, the polarized core produces a motion of charge beyond that of only the valence protons [95, 164–167]. In the spirit of *ab initio* nuclear structure, we start with the bare nucleon values for e, g_s and g_l, and expect them to be dressed appropriately by renormalization from consistent operator evolution.

While a detailed analysis is beyond the scope of this dissertation, the IMSRG provides an excellent environment to study the renormalization of these parameters in-medium. Of critical importance is the axial-vector coupling constant g_A, which mediates the Gamow-Teller strength of nuclear β-decay; a strong quenching of g_A is observed in medium [168, 169]. While some attempts to describe this effect have been made in an *ab initio* framework [170], the origin of this quenching is very much an open question in nuclear physics. Theoretical explanations attribute the quenching either to configurations missing from the model spaces used in the computations, or to non-nucleonic degrees of freedom. The former explanation pertains to phenomena such as short-range correlations or multi-phonon states [171–173], where the latter refers to missing physics such as Δ-isobar excitations [172, 174]. The effective operator formalism present here, coupled with the versatility of a Hermitian method such as the IMSRG, offers a promising framework to investigate such ideas for a wide range of nuclei.

5.1.2 General Observables in the IMSRG

At present, two distinct flavors of the IMSRG offer viable frameworks to study transitions and moments in nuclear structure. The EOM-IMSRG is a capable vessel, but observables may also be accessed by the valence-space (VS)-IMSRG [46, 52].

In the EOM-IMSRG, reduced matrix elements between excited-states and the ground state must be computed by the coupled product of spherical tensor operators,

$$M_{0\nu} = \langle \Phi_0 || \{ O^\lambda \otimes X^\dagger_\nu(J^\Pi_\nu, \Delta T_z) \}^0 || \Phi_0 \rangle \tag{5.9}$$

$$= \delta_{\lambda J_\nu}(-1)^{J_\nu}\left[\sum_{ai}\frac{X_{ai}}{\sqrt{2J+1}}O_{ai} + \frac{1}{4}\sum_{abij}\sum_{J_1J_2}\frac{\tilde{X}^{J_1J_2}_{abij}}{\sqrt{2J+1}}\tilde{O}^{J_1J_2}_{abij}\right]. \tag{5.10}$$

Here O^λ represents an operator of rank λ, and $X^\dagger_\nu(J^\Pi_\nu, \Delta T_z)$ is an EOM ladder operator whose tensorial rank is given by the total angular momentum J_ν, with parity Π and charge-exchange character given by ΔT_z.

For moments or transitions between two EOM excited states, a more involved calculation is needed:

$$M_{\mu\nu} = \langle\Phi_0||\{X_\mu(J^{\Pi'}_\mu, \Delta T_z{}')\otimes\{O^\lambda\otimes X^\dagger_\nu(J^\Pi_\nu, \Delta T_z)\}^{J_\mu}\}^0||\Phi_0\rangle\,. \tag{5.11}$$

Knowledge of the full tensor product

$$Y^J_M \equiv \{O^\lambda\otimes X^\dagger_\nu(J^\Pi_\nu, \Delta T_z)\}^J_M = \sum_{M_\nu\mu} C^{\lambda J_\nu J}_{\mu M_\nu M} O^\lambda_\mu X^\dagger_\nu(J_\nu M_\nu)\,, \tag{5.12}$$

is required for computation of eq. 5.11. The expressions for this are given by eqs. 108 and A.6.2 in the appendix.

The VS-IMSRG is not the focus of this dissertation, but nonetheless we include results for the sake of benchmarking and for a more complete interpretation of effective operator evolution in the IMSRG. The VS-IMSRG approaches spectroscopy and related observables via a different paradigm in which a valence space is decoupled for use with existing shell-model machinery. In this context, the IMSRG serves as a means to construct nonperturbative effective valence space interactions and corresponding effective operators. After decoupling the shell-model core by the ground-state IMSRG, a secondary decoupling, similar to the vTDA-IMSRG decoupling of section 4.1.2, is used to suppress dynamic correlations between the two valence particle-attached space and the core and non-valence orbitals. The relevant off-diagonal is given by

$$H^{od} : f_{ph}, f_{pp'}, f_{pp'}, \Gamma_{pp'hh'}, \Gamma_{pp'vh}, \Gamma_{pq'vv'} \tag{5.13}$$

and their Hermitian conjugates [46]. Here p and h are particle and hole indices, respectively, v are valence space orbitals, and q non-valence particle orbitals. In typical calculations, the Hamiltonian

is normal ordered with respect to an ensemble reference state specified by the density matrix

$$\rho = \sum_{\alpha} C_{\alpha} |\Phi_{\alpha}\rangle\langle\Phi_{\alpha}|, \tag{5.14}$$

where $|\Phi_{\alpha}\rangle$ are Slater determinants of varying particle number A_{α}, and the C_{α} are chosen so that the ensemble-averaged particle number is equal to the mass of the target nucleus. This alters the Wick contractions (see sec 2.3) such that they are proportional to a fractional occupation number, rather than an integer occupation. Ensemble normal ordering (ENO) has the effect of properly including valence three-body forces in the NO2B approximation, and is crucial for the reproduction of binding energies far from shell-closures. With these improvements in normal-ordering, the method has had great success in the reproduction of binding energies and spectra throughout the *sd*- and pf-shells [51, 52]. Despite this progress, the VS-IMSRG has heretofore been limited to scalar operators. However, the same machinery required for effective operator evolution in the EOM-IMSRG can be used for the VS-IMSRG. The actual computation of observables is accomplished in a shell model framework using the consistently transformed operator together with the wave functions that result from diagonalizing the valence Hamiltonian.

5.2 Results

5.2.1 Center-of-Mass Treatment

Spurious center-of-mass-excited states manifest as nearly degenerate intrinsic states in nuclear spectra. As discussed in sec. 3.2.4, these states are removed via the Lawson-Gloeckner method [175], where the intrinsic Hamiltonian is augmented with a scaled center of mass trap of the form of eq. 3.43,

$$H = H_{in} + \beta H_{cm}. \tag{5.15}$$

Here, the scale factor β can be taken to arbitrarily large values if sufficient factorization is achieved in calculations using H_{in} only. This process effectively scales spurious states out of the spectrum by adding a large COM excitation energy.

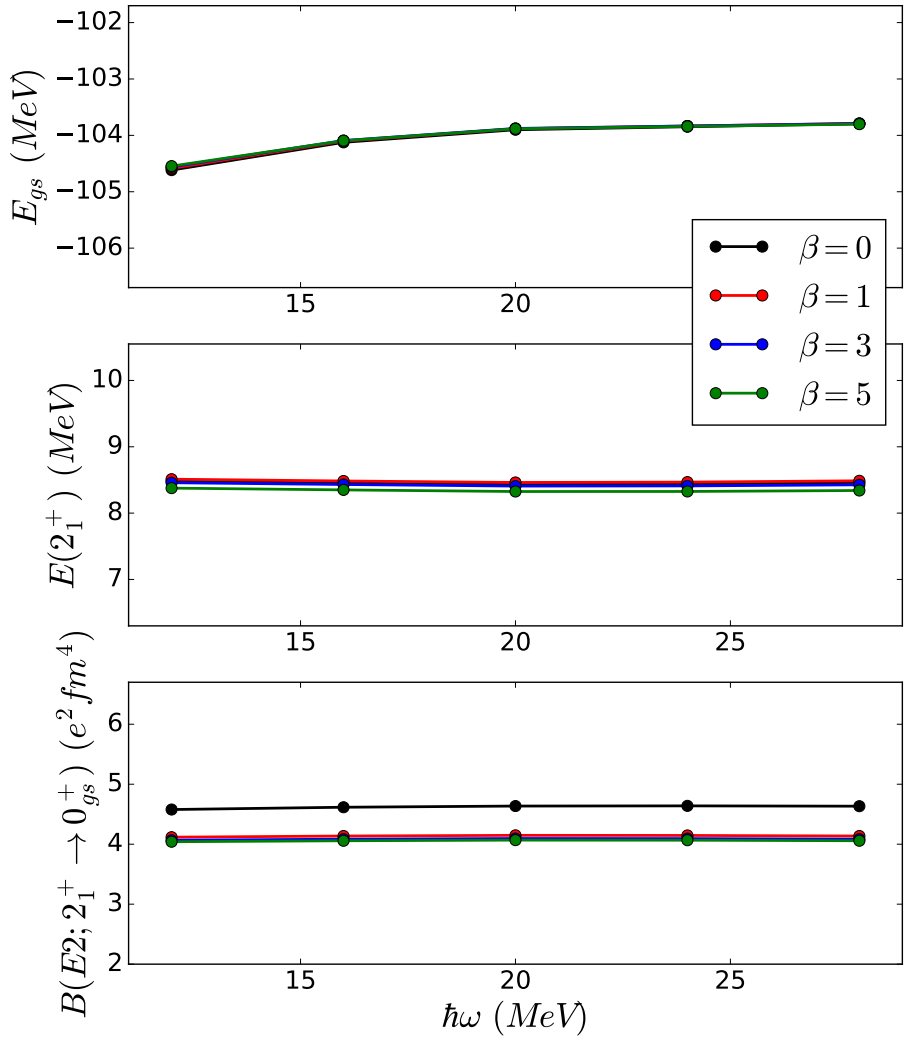

Figure 5.1 Observables calculated at several values of the Lawson scaling parameter β, for ^{14}C, using the standard input NN+3N(400) interaction softened by the SRG to $\lambda_{SRG} = 2.0$ fm^{-1}, at $e_{\max} = 14$.

β	$E_{cm}(0^+_{gs})$ (MeV)	$E_{cm}(2^+_1)$ (MeV)
0	0.099	1.298
1	0.068	0.046

Table 5.1 E_{cm} for intrinsic ground state and first 2^+ state of ^{14}C, computed at e_{max}=14 and $\hbar\omega$ = 20 MeV using the standard input NN+3N(400) interaction softened by the SRG to $\lambda_{SRG} = 2.0$ fm^{-1} with EOM-IMSRG(2,2). Values are given for calculations using H_{in} (β=0), and $H_{in} + H_{cm}$ (β=1).

Figure 5.1 demonstrates this procedure with ^{14}C, for the ground state, first 2^+ excited state, and corresponding B(E2) value. Quantities are calculated with the EOM-IMSRG(2,2) method. The energies are approximately independent of β; this may be taken naively as evidence of factorization for these states. However, the B(E2) value undergoes a sudden downward shift as the Lawson term is introduced. The value saturates and displays factorization as we go to higher β. This shift indicates that the approximate factorization observed in the energies is not sufficient to describe observables whose operators are not expressed in a translationally-invariant manner, such as the electric quadrupole operator discussed here.

A common resolution for this problem is the inclusion of a cumbersome recoil correction for the transition operator [164]. This is a two-body operator which may require approximate or exact IMSRG(3) machinery to minimize truncation errors. A more elegant solution is to force the COM wave function into the ground state via explicit trapping with the Lawson-Gloeckner method discussed above. Table 5.2.1 gives the computed E_{cm} for calculations with and without explicit inclusion of a center of mass trap via the Lawson term. We expect a perfectly factorized wave-function to have E_{cm}=0 MeV, as H_{cm} is written so that the COM ground state has zero energy. For either case, the ground state wave function demonstrates limited contamination from spurious COM excitations, with $E_{cm} < 100$ keV. The 2^+_1 state of H_{in} does not exhibit this level of factorization, with E_{cm}=1.298 MeV, indicating a relatively small admixture of spurious states, as the first spurious excited state has energy $\hbar\tilde{\omega} = 15.7$ MeV. This level of contamination is evidently negligent for excitation energies, but has important effects when the state is probed by the quadrupole operator. When the COM trap is explicitly added this issue is rectified, and as a result, we see a shift in the

B(E2) strength, which corresponds to a recoil correction.

5.2.2 The Deuteron

As a first illustration, we consider some ground state properties of the deuteron. This is useful for a few reasons. First, the system consists of only two particles and so induced three body forces are irrelevant. Further, the reference is taken to be the true vacuum, so the neglected three body forces do not feed back into the two body terms. We should therefore expect the IMSRG(2) to be exact. Second, full configuration interaction (FCI) calculations are easily performed for modest model spaces, allowing a direct evaluation of the precision of the IMSRG calculation. Finally, we may treat the deuteron in the $0s$ valence space where the bare quadrupole moment is identically zero. In this case, the calculated quadrupole moment is entirely due to effects of the IMSRG decoupling. Fig. 5.2 shows the ground-state energy, root-mean-square charge radius, quadrupole moment and magnetic moment of the deuteron, computed both with FCI and using IMSRG to decouple the $0s$ valence space, followed by a trivial diagonalization. We can see that the IMSRG calculation indeed reproduces the FCI.

Here again we see the effect of COM spuriosities in the deuteron wave function. While the energy and dipole moment converge to the exact values with little alteration from COM contamination, the charge radius overshoots it drastically. Although we have not reached convergence for the charge radius, it is evident that Lawson scaling significantly reduces its value. Furthermore, the quadrupole moment, which is also non converged at e_{max}=12, shows a more agreeable convergence pattern when treated with the Lawson scaling. We note that the convergence properties and COM sensitivity of the charge radius and quadrupole moment are quite different, despite the latter being proportional to the square of the radius. These discrepancies are not fully understood at the moment.

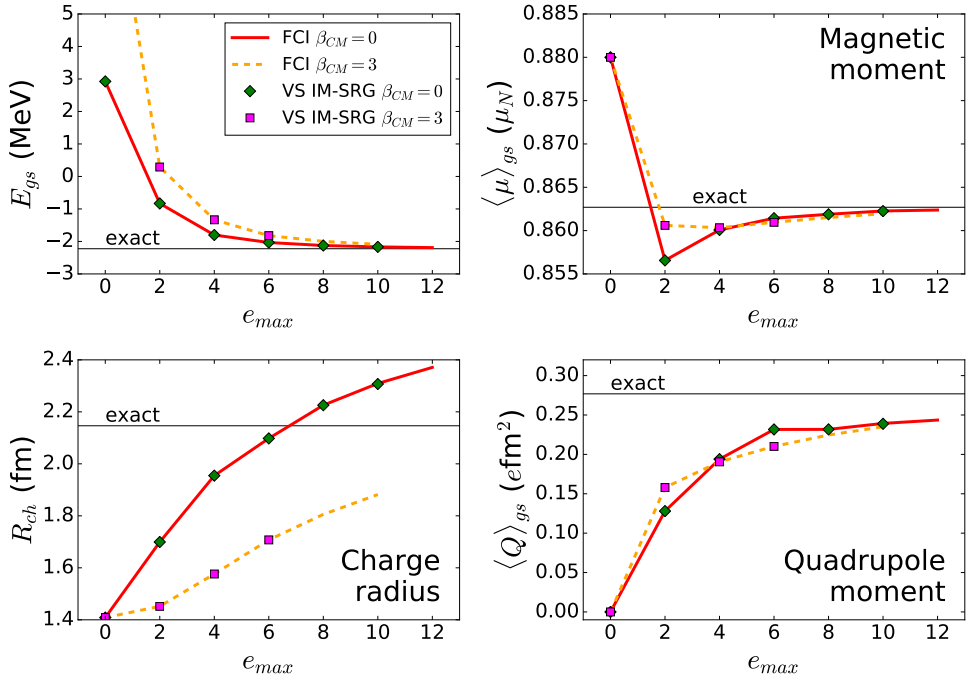

Figure 5.2 Ground state properties of the deuteron calculated with a full diagonalization (labeled FCI), compared to the same properties calculated in the 0s valence space using operators transformed with the IMSRG. The line labeled "exact" is obtained by diagonalizing in the Jacobi basis with $e_{max} = 200$. Here we use the EM input N^{3}LO nucleon-nucleon interaction SRG evolved to $\lambda_{SRG} = 2.0$ fm^{-1}.

5.2.3 p shell Nuclei: Comparison to NCSM and Small-Space FCI

The deuteron is, of course, an exceptionally simple case, due to the fact that there is not really a "medium", and so the IMSRG is really a free-space SRG. Once additional particles are considered, the normal-ordered two-body approximation is used, and the IMSRG(2) should no longer be exact. To test this approximation, we consider p-shell nuclei which may also be treated exactly in the no-core shell model (NCSM).

As a test in the p shell, we consider ^{14}C. Because this is a closed-shell nucleus, we may employ the EOM-IMSRG as well as the VS-IMSRG, while 14 particles is still feasible with the NCSM. Fig. 5.3 displays results for the 2_1^+ excitation energy and $B(E2;2_1^+ \to 0_0^+)$ for ^{14}C. Here, we find excellent agreement between NCSM and both variants of the IMSRG. We remind the reader that the EOM-IMSRG calculation is performed with an explicit center-of-mass trap, as in eq. 5.15,

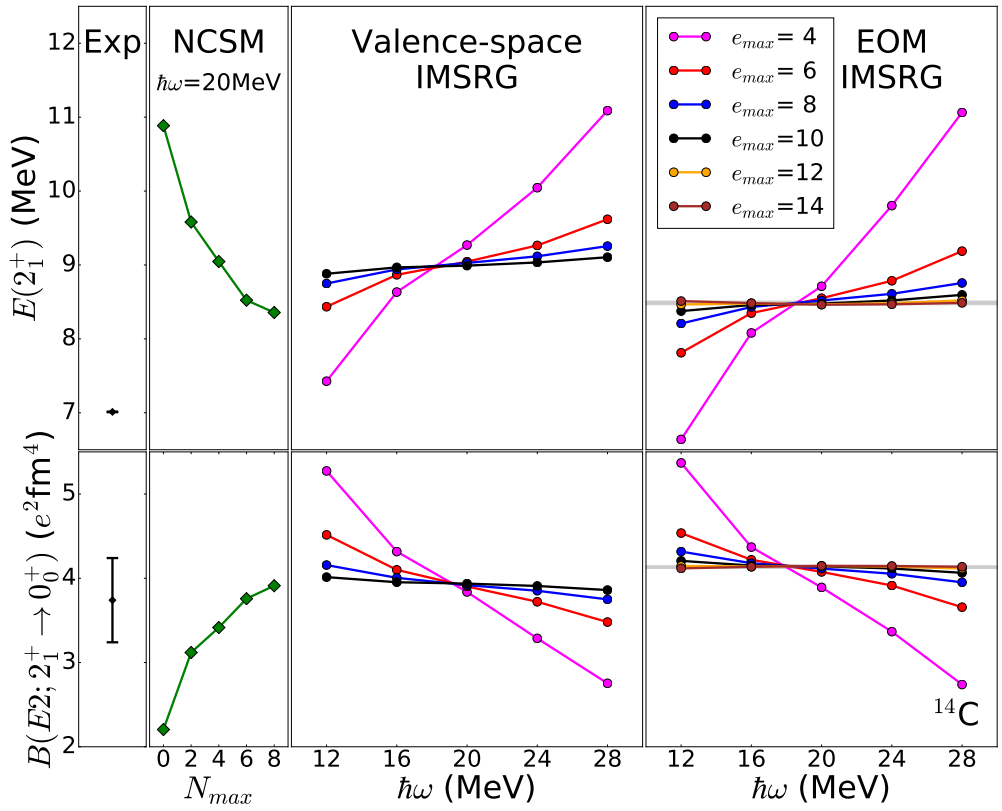

Figure 5.3 Convergence of the 2_1^+ excitation energy and B(E2) to ground state of ^{14}C with the VS- and EOM-IMSRG methods, using the standard input NN+3N(400) interaction softened by the SRG to $\lambda_{SRG} = 2.0$ fm^{-1}. Experimental values are taken from [1].

where $\beta = 1.0$. This treatment only serves to remove spurious COM contamination of the 2_1^+ state.

Of note are the excellent convergence properties of the IMSRG calculations. For the EOM-IMSRG, observables are nearly independent of the specified $\hbar\omega$ for the single-particle basis. VS-IMSRG calculations have not used the exhaustive model spaces of the EOM-IMSRG, but they too demonstrate desirable convergence features. The NCSM has begun to show convergence at N_{max}=8, but extrapolation methods must be used to reveal fully converged values. Hence the utility of the IMSRG; for light mass nuclei such as ^{14}C, convergence is obtainable without extrapolation because the IMSRG cannot only reach higher model-spaces, but also indirectly treats the full configuration space within the e_{max} truncation on the single-particle basis. On the other hand, the quasi-exact NCSM is restricted to the subset of Slater determinants with total excitation quanta

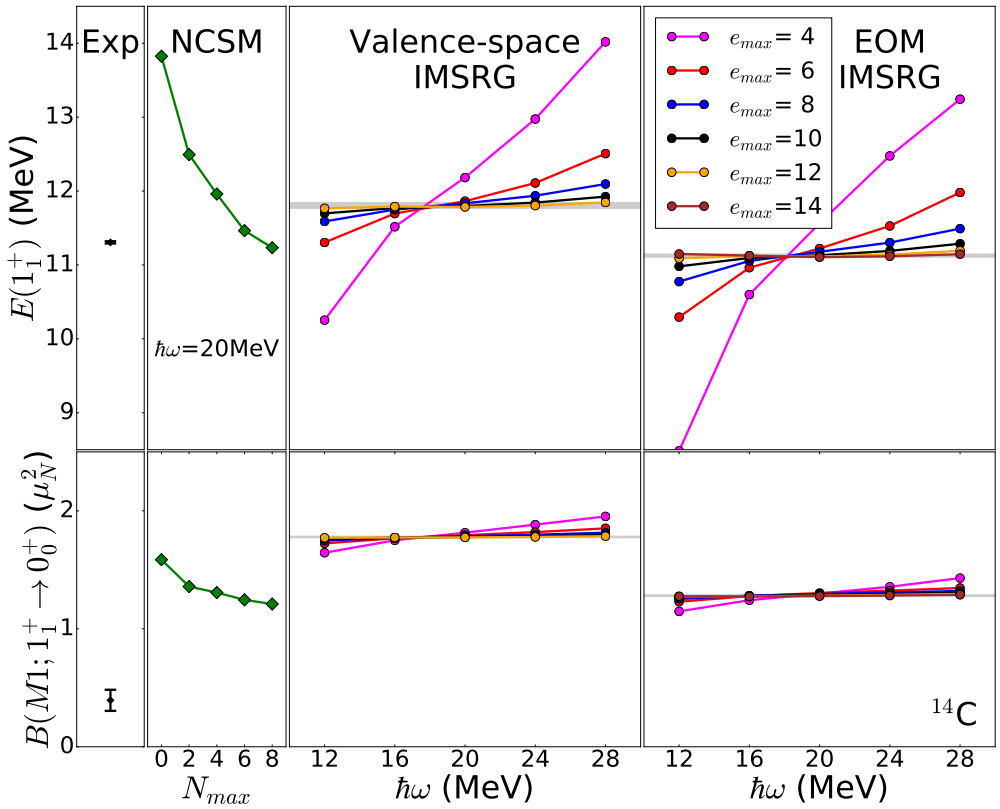

Figure 5.4 Convergence of the 1_1^+ excitation energy and B(M1) to ground state of ^{14}C with the VS- and EOM-IMSRG methods, using the standard input NN+3N(400) interaction softened by the SRG to $\lambda_{SRG} = 2.0$ fm^{-1}. Experimental values are taken from [14].

up to and including N_{max}. Correspondingly, we expect extrapolation procedures in heavier nuclei to be relatively painless in the IMSRG, compared with exact methods such as NCSM.

As a further test in ^{14}C, we analyze the first 1^+ state and corresponding $M1$ transition to the ground state in figure 5.4. Again, fantastic convergence properties are exhibited by both IMSRG methods, and consistency with NCSM is observed. The 1_1^+ excitation energy is consistent between methods and shows reasonable reproduction of experiment. While B(M1) values computed by the many-body methods are in excellent agreement, these overestimate experiment by a significant amount. A possible source of this discrepancy are contributions from two-body currents which originate from chiral-EFT. These currents can in principle be incorporated in our calculations, but the normal-ordered current operators have yet to be implemented in this formalism.

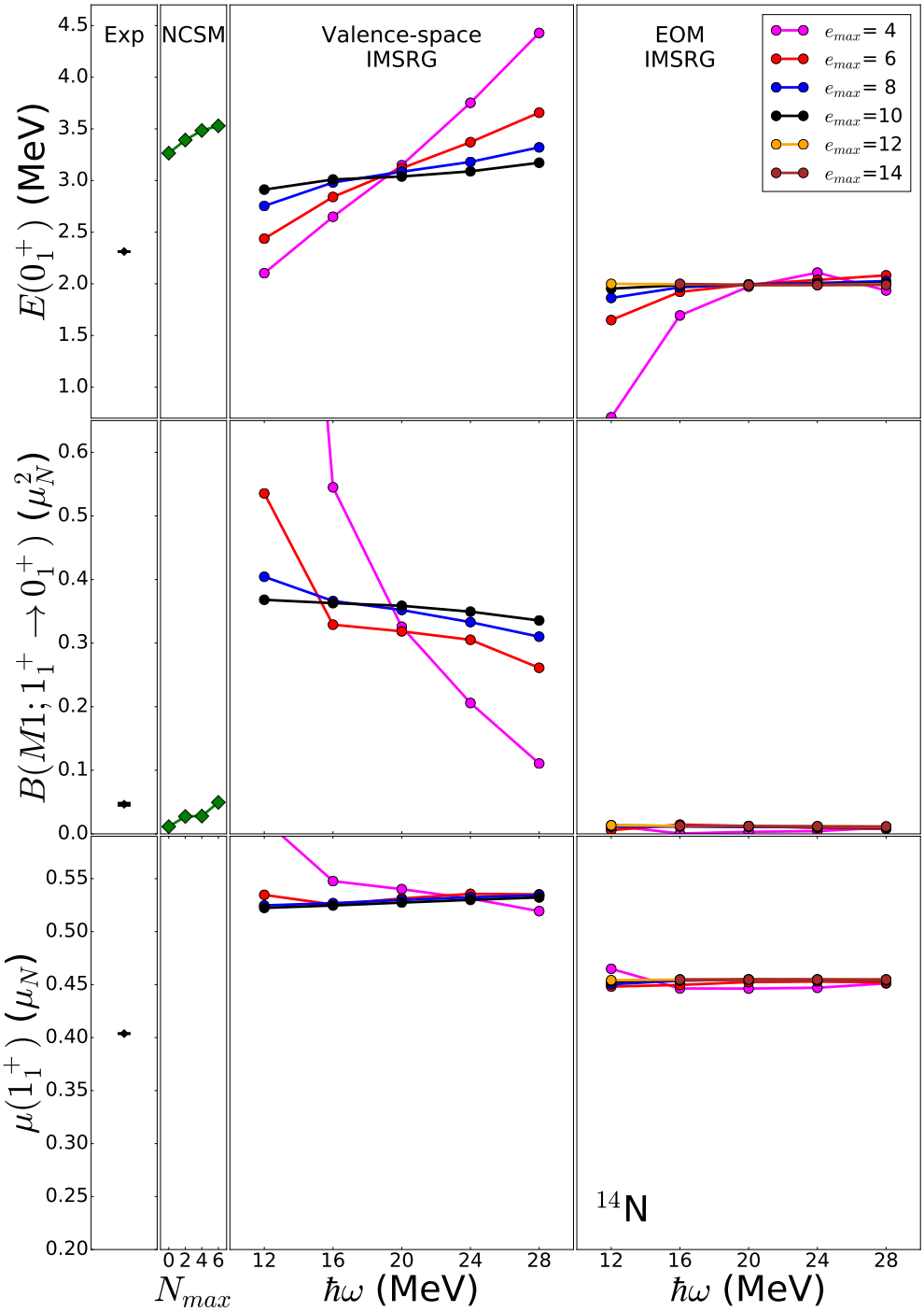

Figure 5.5 Convergence of 0_1^+ excitation energy, B(M1) to ground state, and magnetic dipole moment of ^{14}N with the VS- and EOM-IMSRG methods, using the standard input NN+3N(400) interaction softened by the SRG to $\lambda_{SRG} = 2.0$ fm^{-1}. Experimental values are taken from [14].

Additionally, we analyze the isobaric neighbor nucleus ^{14}N. Here the EOM-IMSRG requires charge-exchange formalism discussed in sec. 4.2.5, i.e. ladder operators which exchange one neutron for a proton. Figure 5.5 displays the 0_1^+ excitation energy for ^{14}N, the strength of the dipole transition to the 1_0^+ ground state and the ground state magnetic dipole moment. Here we see a trend of VS-IMSRG overpredicting observables. The EOM-IMSRG(2,2) underpredicts experiment for the energy and B(M1) value, while slightly overpredicting the magnetic moment. The VS-IMSRG(2) drastically overpredicts both experiment and NCSM for the B(M1) value. We do not yet understand the source of this discrepancy, but the EOM-IMSRG(2,2) also struggles here, underpredicting the B(M1) value by roughly an order of magnitude. While the lack of discernible convergence for the B(M1) value in the NCSM calculation seems to demonstrate that this nucleus is challenging for *ab initio* theory, the IMSRG methods certainly should share a fair portion of the blame; in sec. 5.2.7, we will discuss potential sources of error in the VS- and EOM-IMSRG approaches.

Ultimately, the power of IMSRG approaches for excited states and effective operators will be the ability to describe these properties in medium- to heavy-mass regions where exact methods are not computationally tractable. In the next sections, we investigate the quality of these calculations for several medium-mass nuclei, again using the electric quadrupole and magnetic dipole operators as case studies.

5.2.4 Electric Quadrupole Observables in *sd* and *fp* shell Systems

Figure 5.6 displays the first 2^+ energy and B(E2) strength for transitions to the ground state of ^{22}O. While we see excellent convergence and agreement with experiment for the excitation energy, the transition strength is underpredicted by an order of magnitude. These results are strikingly consistent between the two methods. A tentative explanation is provided by the lack of valence protons in the *sd*-shell. The VS-IMSRG treats this nucleus as six neutrons sitting above an ^{16}O core; the low-lying 2_1^+ state is composed solely of excitations within the *sd*-shell, and thus the wave func-

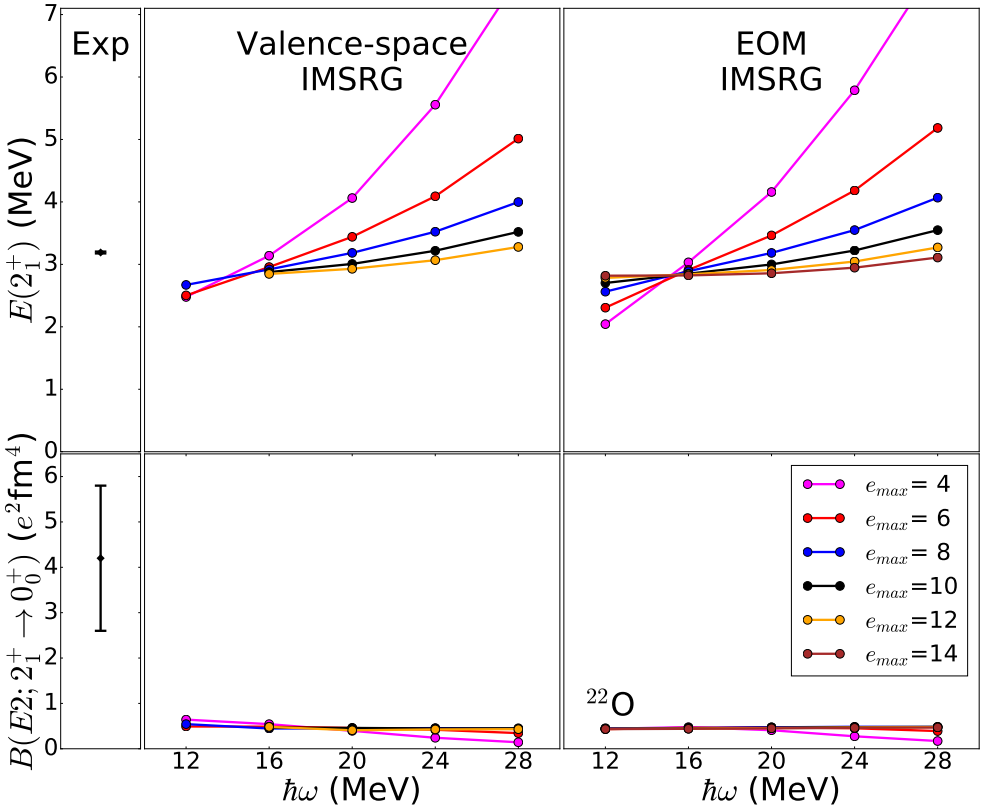

Figure 5.6 Convergence of the 2_1^+ excitation energy and B(E2) to ground state of ^{22}O with the VS- and EOM-IMSRG methods, using the standard input NN+3N(400) interaction softened by the SRG to $\lambda_{SRG} = 2.0$ fm^{-1}. Experimental values are taken from [1].

tion is is composed purely of neutron excitations. As a result, valence neutrons must be dressed consistently as quasi-neutrons possessing an effective charge in order to properly produce transition strengths. A similar situation manifests in the EOM-IMSRG(2,2), where by conservation of parity, the only proton excitations allowed across the major shell gap are 2p2h, and these are of significantly higher energy than the 1p1h neutron excitations within the *sd*-shell. The absence of any appreciable strength in the two IMSRG calculations is a somewhat convincing argument that IMSRG decoupling does not appropriately renormalize the neutron charges. However, this discrepancy is evident in many other nuclei, regardless of whether the protons are semi-magic or not. Figure 5.7 shows a similar situation for ^{32}S, which has numerous valence protons to account for the transition strength. Here we see reasonable reproduction of the 2_1^+ experimental excita-

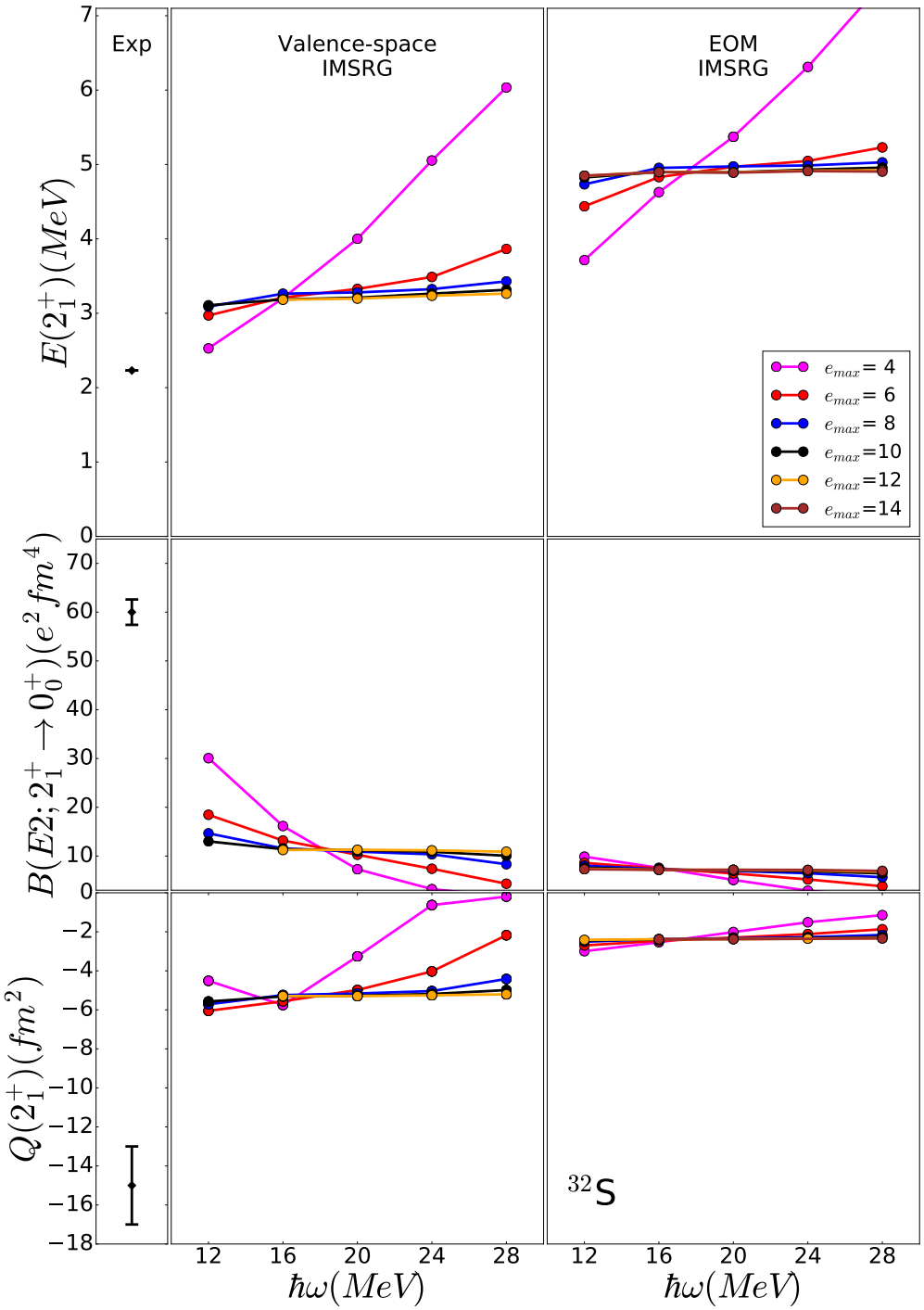

Figure 5.7 Convergence of the 2_1^+ excitation energy, corresponding B(E2) to ground state and quadrupole moment of ^{32}S with the VS- and EOM-IMSRG methods, using the standard input NN+3N(400) interaction softened by the SRG to $\lambda_{SRG} = 2.0$ fm^{-1}. Experimental values are taken from [1].

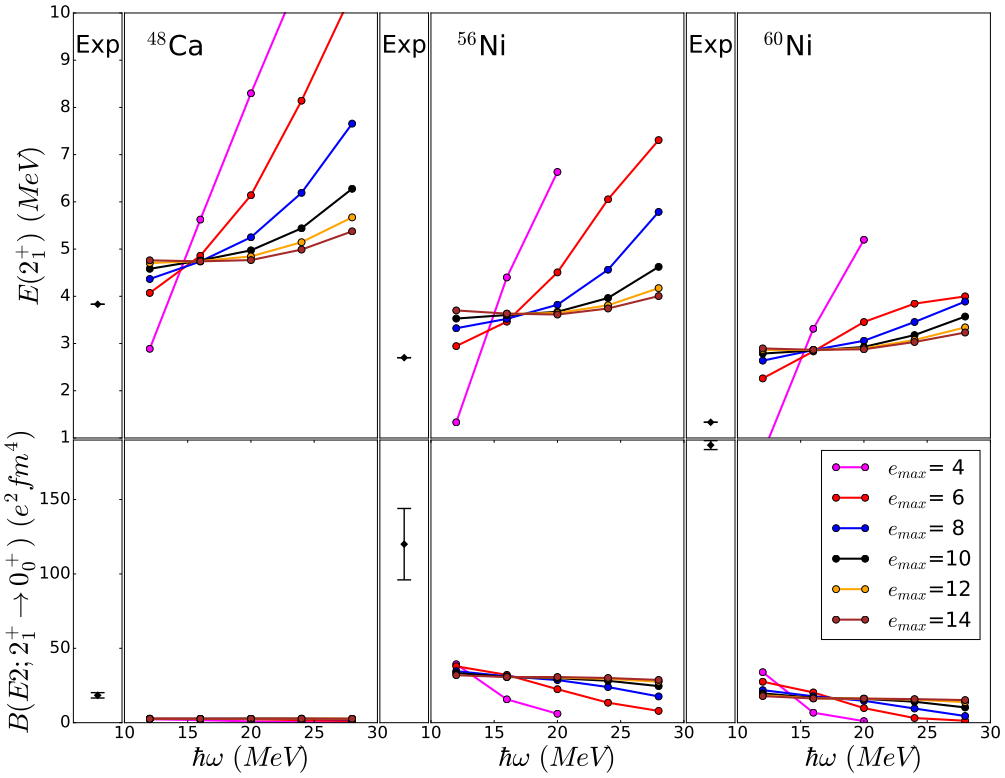

Figure 5.8 First excited 2^+ states and corresponding B(E2) transition strengths for ^{48}Ca and ^{56,60}Ni, using the standard input NN+3N(400) interaction softened by the SRG to $\lambda_{SRG} = 2.0$ fm^{-1}. Convergence patterns are shown, computed with EOM-IMSRG(2,2). Results are compared with experimental points in the left panel [1].

tion energy, but the B(E2) value is drastically underpredicted by roughly an order of magnitude. Correspondingly, the quadrupole moment's magnitude is underpredicted by a factor of about 3.5 for the valence-space IMSRG and about 6 for EOM-IMSRG. Much like ^{14}N, this nucleus exhibits marked disagreement between the two IMSRG approaches. We will forego discussion here and discuss this in detail in section 5.2.7.

As we investigate heavier nuclei, we find that underprediction of B(E2) values is far more common than the stunning success seen with ^{14}C. Figure 5.8 shows convergence of 2_1^+ energies and E2 transition strengths in ^{48}Ca and ^{56,60}Ni. Again, calculated strengths are roughly an order of magnitude smaller than experiment, while energies are reasonably consistent with observed values. Table 5.2.4 compiles the results from several of the calculations presented here, where

Nucleus	B(E2↓)$_{exp}$	B(E2↓)$_{EOM}$	B(E2↓)$_{VS}$	B$_W$(E2↓)
^{14}C	3.6(6)	4.1	3.9	2.0
^{22}O	4.2(1.6)	0.5	0.4	3.7
^{32}S	59(1)	7.2	11.3	6.0
^{48}Ca	17(2)	2.6		10.4
^{56}Ni	$1.2(3)\times10^2$	30.7		12.7
^{60}Ni	186(3)	16.2		14.0

Table 5.2 Computed E2 transition strengths from first excited 2^+ state to 0^+ ground state for even-even nuclei, using the standard input NN+3N(400) interaction softened by the SRG to $\lambda_{SRG} = 2.0$ fm^{-1}. Experiment [1] and Weisskopf [2] single particle estimates are compared with IMSRG calculations.

B(E2↓) corresponds to B(E2;$2_1^+ \rightarrow 0_0^+$) value. In the far right column, the Weisskopf units (W.U.) for the transition are included [2]. Weisskopf units, given by

$$B_W(E2) = \frac{9r_0^4}{100\pi}A^{4/3}e^2fm^4, \tag{5.16}$$

take the transition to be a single proton excitation from a hard-core with the empirical nuclear radius $r_0A^{1/3}$, where $r_0 = 1.2$ fm. Strongly 1p1h transitions will yield experimental B(E2) values near the Weisskopf estimate. This picture certainly falls short of describing those nuclei with magic proton numbers, such as ^{22}O, but it is instructive to consider what the single particle estimates are for this nucleus nonetheless, as they describe neutrons with an effective charge in this case.

We find that computed B(E2) values track with Weisskopf estimates rather than actual experimental values, except in the case of a magic proton shell closure, where computations are significantly smaller than the Weisskopf units, suggesting that indeed, the renormalization of neutron effective charges may not be sufficient in our IMSRG calculations. Importantly, the fact that many of the experimental B(E2) values are significantly larger than the single particle estimates indicates that collectivity which is neglected by IMSRG(2) calculations may be more critical to $E2$ transition strengths than it is to excitation energies.

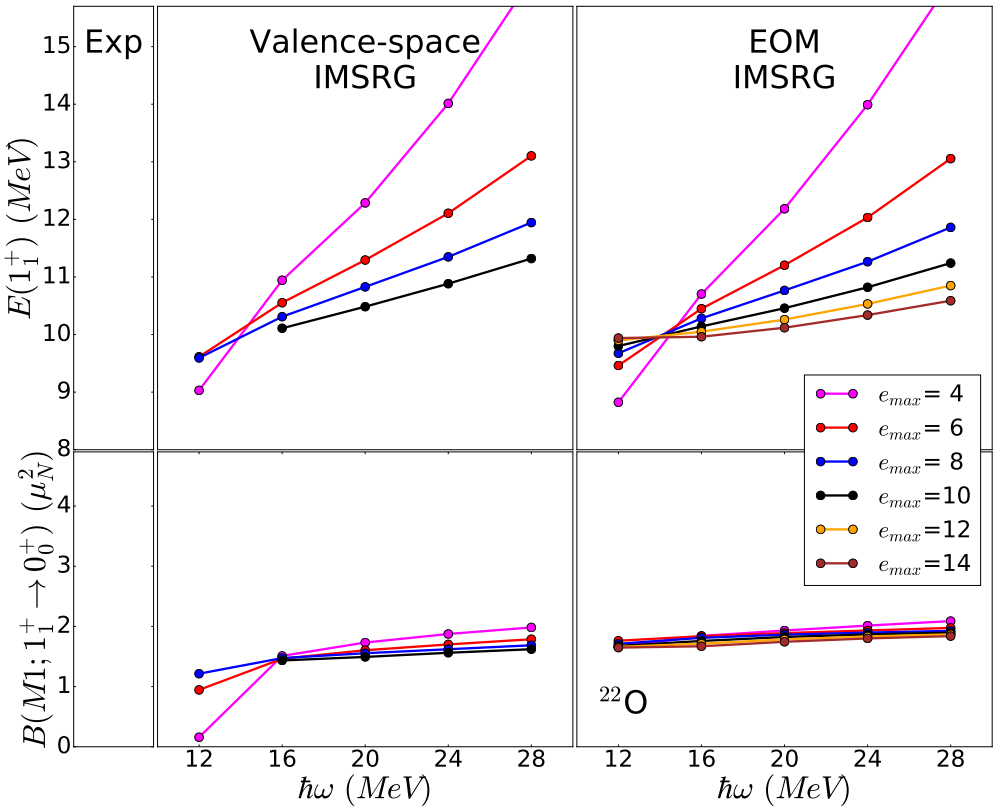

Figure 5.9 Convergence of the 1_1^+ excitation energy, B(M1) to ground state of ^{22}O with the VS- and EOM-IMSRG methods, using the standard input NN+3N(400) interaction softened by the SRG to $\lambda_{SRG} = 2.0$ fm^{-1}.

5.2.5 Magnetic Dipole Observables in *sd* and *fp* shell Systems

We turn to M1 observables, where the Weisskopf unit has no dependence on A and thus we expect the transition to have similar properties from nucleus to nucleus, unlike E2 observables. As an analog to the E2 observables, we first investigate ^{22}O. Here we do not have a measurement of the 1_1^+ state, so this analysis serves only to compare EOM- and VS-IMSRG. Here we see excellent consistency between the two methods, with convergence patterns for the energy being nearly identical, and those for the M1 transition very similar in character. This matches expectations derived from the agreement we saw for the E2 transition. As expected from the mass independence of the Weisskopf estimates, the B(M1) for this nucleus is predicted around 1 μ_N^2, which is similar to that of ^{14}C.

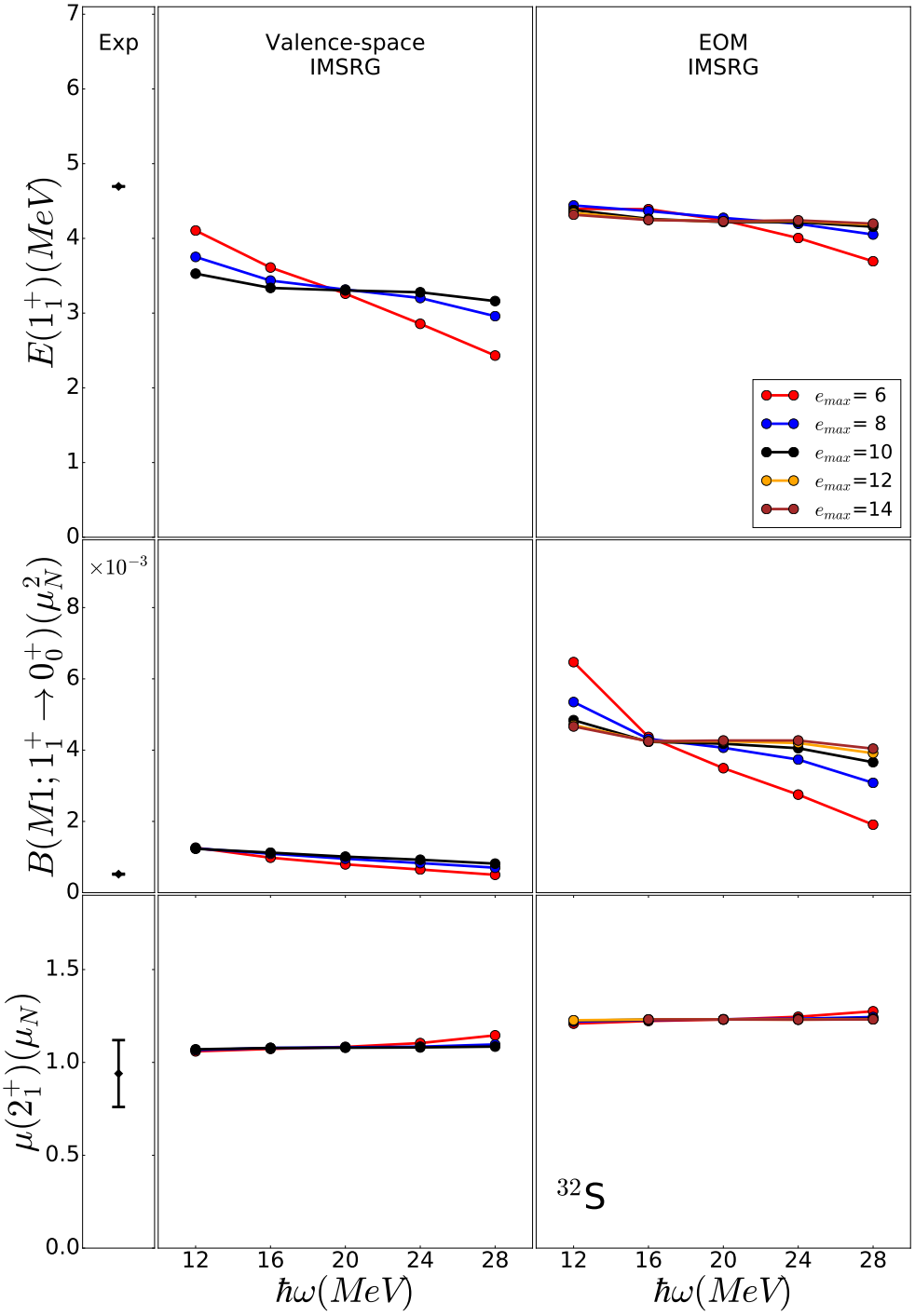

Figure 5.10 Convergence of 1_1^+ excitation energy, B(M1) to ground state and 2_1^+ magnetic dipole moment of ^{32}S with the VS- and EOM-IMSRG methods, using the standard input NN+3N(400) interaction softened by the SRG to $\lambda_{SRG} = 2.0$ fm^{-1}. Experimental values are taken from [14].

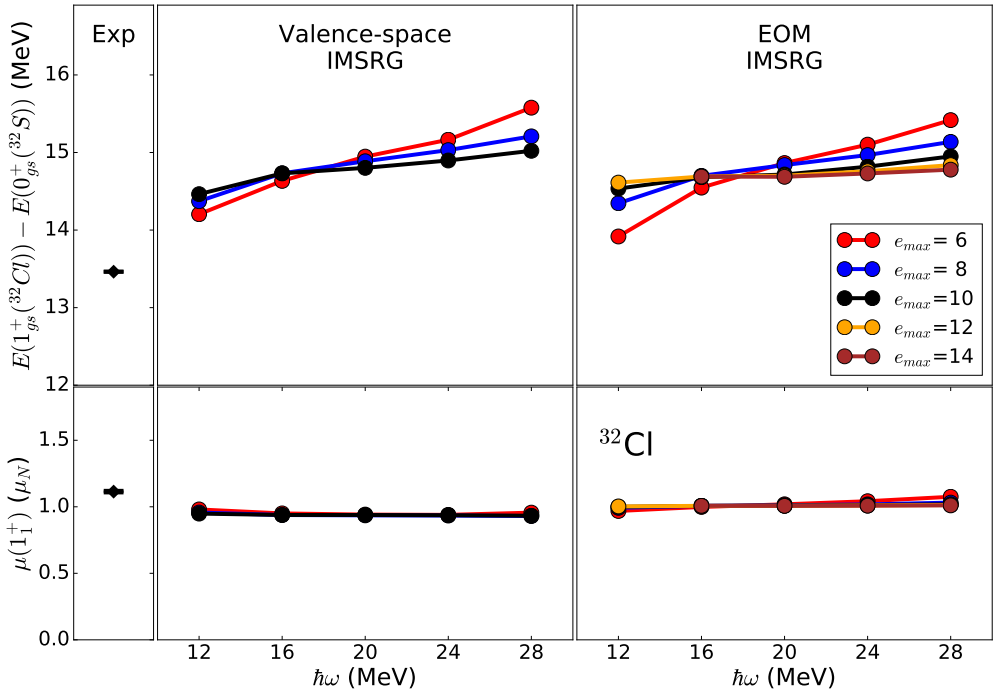

Figure 5.11 Computed ground state energy and magnetic dipole moment of ^{32}Cl with the VS- and EOM-IMSRG methods, using the standard input NN+3N(400) interaction softened by the SRG to $\lambda_{SRG} = 2.0$ fm^{-1}. Experimental values are taken from [14].

We also compute M1 observables for the 1^+_1 and 2^+_1 states in ^{32}S. Figure 5.10 shows results for these calculations. Here we see that IMSRG calculations are within an order of magnitude of experiment for all observables considered. Again, some notable discrepancies between VS- and EOM-IMSRG are evident, stemming from the fact that the VS-IMSRG uses a full valence space diagonalization, and the EOM-IMSRG uses an approximate diagonalization in the full active space. Nonetheless, some consistency is observed, particularly for the dipole moment of the 2^+_1 state. We don't expect agreement with experiment for the M1 observables, as we neglect meson-exchange currents, which are understood to be important to reproducing experiment [95, 176]. However, as the leading order effects are included in our calculation, it is promising to see qualitative agreement within an order of magnitude.

A more pleasant picture surfaces in fig. 5.11, where we have computed ground state properties of ^{32}Cl. The ground state energy is given here as an excitation energy from the ^{32}S ground state,

as it is calculated in the EOM-IMSRG as an excited state of ^{32}S with a charge-exchange excitation operator. Disagreement between EOM- and VS-IMSRG is far less prominent here than in the isobaric neighbor ^{32}S, and the methods again show qualitative agreement with experiment. This agreement is somewhat surprising considering that ^{32}Cl is situated near the center of the *sd*-shell. The observed consistency indicates strong 1p1h character in the ground state.

We have computed the magnetic dipole properties of five nuclei: ^{32}S, ^{32}Cl, ^{22}O, ^{14}C and ^{14}N, with reasonable consistency between VS-IMSRG and EOM-IMSRG achieved for ^{14}C, ^{22}O, and ^{32}Cl. Considering the closed shell cases only, this corresponds to what is seen for E2 observables. In order to compare with experiment, we would need to add higher-order mesonic currents which occur within the nucleus during the transition. Computationally, these manifest as a two body correction to the M1 transition operator. This is beyond the scope of this work, as normal-ordering has yet to be implemented for two-body tensor operators (normal-ordering is trivial for one-body tensor operators). IMSRG truncation errors are more important for two-body operators than one-body, so additional considerations must be made before exploring the addition of mesonic currents.

5.2.6 Electric Octupole Transitions

The electric octupole transition offers an additional test of the EOM-IMSRG. We investigate the transition strengths from the first 3^- state to ground state for the doubly magic nuclei ^{16}O and ^{40}Ca. The left panel of figure 5.12 shows the convergence of this calculation for ^{16}O. This is an interesting case study, as the 3^-_1 excitation energy has been shown to correlate with the ^{16}O charge radius and thus depends on saturation properties of the interaction [177]. For this reason, we compare calculations with the NN+3N(400) interaction to those using N^{2}LO$_{sat}$, which is fit to the ^{16}O charge radius [177]. We see an improvement of the excitation energy when using N^{2}LO$_{sat}$, moving from 9.03 MeV with the NN+3N(400) interaction to 6.90 MeV, in significantly better agreement with the experimental value at 6.13 MeV. Regardless, the gains from switching to the saturating interaction are not seen in the B(E3) value, as both interactions underpredict experiment

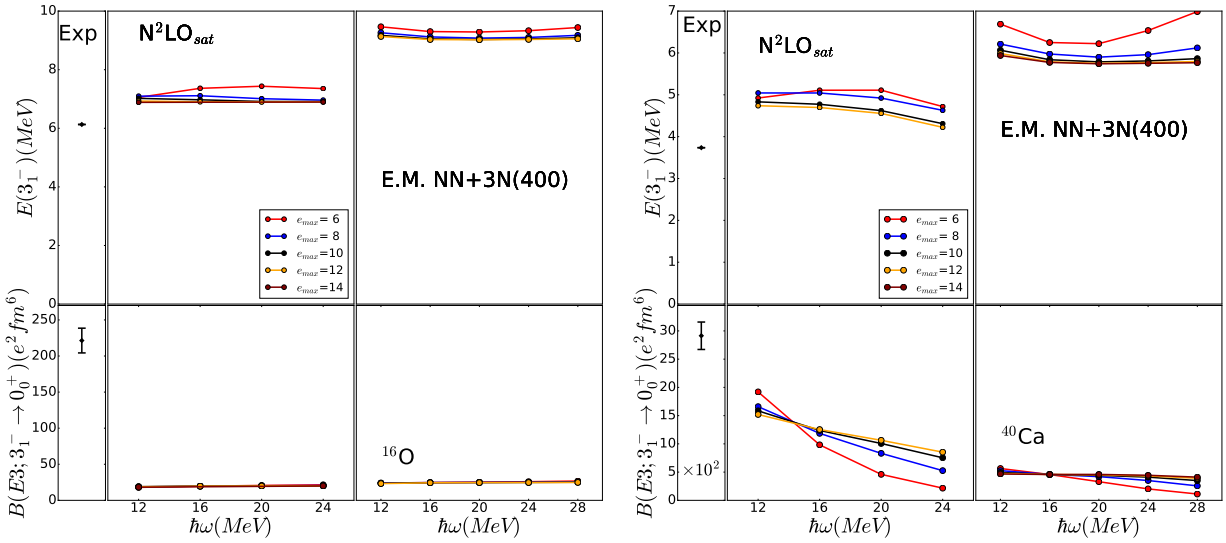

Figure 5.12 Excitation energies of the first 3^- state of ^{16}O and ^{40}Ca, along with corresponding B(E3) strength for transition to ground state. These values are computed using the EOM-IMSRG(2,2) with N^{2}LO$_{sat}$ and the standard NN+3N(400) interaction softened by the SRG to $\lambda_{SRG} = 2.0$ fm^{-1}.. Results are compared with experiment [15].

by roughly an order of magnitude. Despite EOM partial norms indicating 90% 1p1h content in the 3^- wave-function, higher order correlations may play a significant role in the structure pertinent to the E3 transition, as α-clustering may be important to the structure of the 3^-_1 state [178].

A similar picture presents itself for ^{40}Ca in the right panel of figure 5.12, where again, N^{2}LO$_{sat}$ improves excitation energy but underpredicts the B(E3) strength. For either interaction, the discrepancy is less striking than that seen in ^{16}O, but the deviation is significant nonetheless. Notable is the poor convergence features exhibited by N^{2}LO$_{sat}$, where results are seemingly dependent on the basis frequency $\hbar\omega$ for both energy and B(E3) value. At the moment we are working to understand these issues.

Computed E3 strengths suffer from largely the same shortcomings as E2 strengths, where we see a significant reduction of the strength from that of experiment. The Weisskopf single-particle estimates for ^{16}O and ^{40}Ca are 15.21 and 95.04 e^2fm^6 respectively. The immense size of the experimental values compared with these estimates indicates a strong level of collectivity in these 3^-_1 states, which is apparently missed by our calculations, though computed E3 strengths are indeed

larger than the single-particle estimates.

5.2.7 Comparing and Contrasting Methods

We return now to ^{32}S, where noticeable differences between the EOM- and valence-space variants of IMSRG were demonstrated. This discrepancy is the result of some combination of two sources of error. The VS-IMSRG(2) introduces a second decoupling, and as such, unitarity is degraded beyond truncation errors from ground-state-decoupling. On the other hand, the EOM-IMSRG(2,2) lacks the ability to describe higher-order correlations in states with minimal 1p1h character. This underscores the fact that the two methods are complimentary, and a different class of states fall into the set that is best described by either method.

The VS-IMSRG takes into account all possible valence-particle configurations within the specified valence space. States that are described well by phenomenological shell-model approaches should then be described appropriately by the VS-IMSRG. However, states with significant contributions from multiple major shells, in particular unnatural parity states, are unreachable by this method in its current state. Methods to decouple a multi-shell valence space are still under investigation.

EOM-IMSRG is not restricted by any valence space, but rather derives its computational simplicity from a restriction of the configurations included in the diagonalization. Thus, unnatural parity states are treated on the same footing as natural. However, any state will be poorly described if the dominant configurations of particle-hole excitation are left out of the definition of the ladder operators. For the EOM-IMSRG(2,2), we work with a space of 1p1h and 2p2h configurations. In this case, states with strong 1p1h content are best described by the method. States with 2p2h dominant wave functions are described reasonably well, but the ground-state-decoupled Hamiltonian still introduces strong correlations between these states and 3p3h excitations. For these states, additional IMSRG softening may be needed to make a perturbative treatment valid.

For the specific case of ^{32}S, the differences between the two IMSRG methods appear in calculations of both the energy and transition strength. The 1p1h partial norms for the 2_1^+ state are

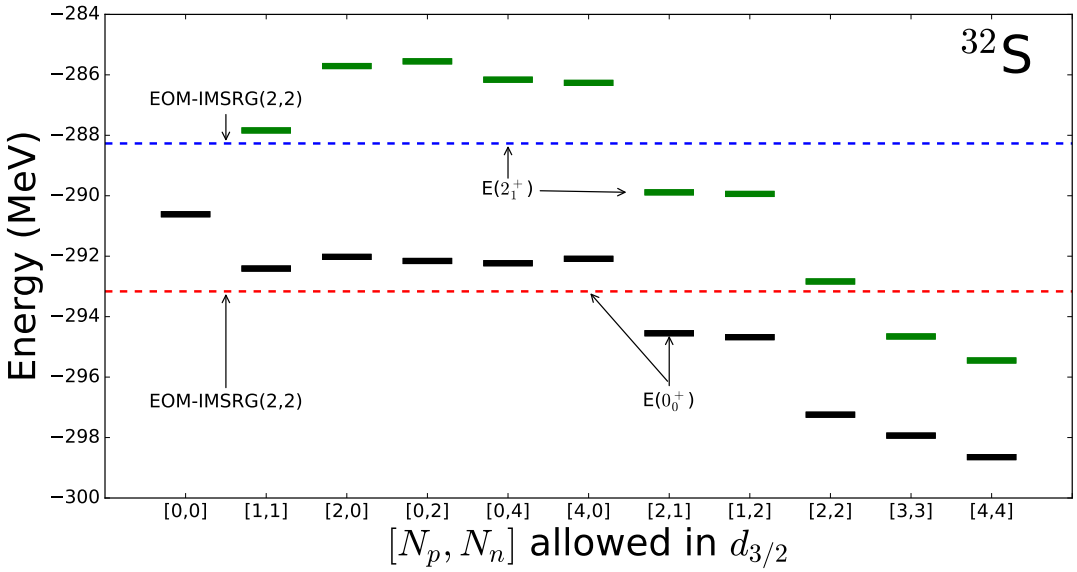

Figure 5.13 Computed ground-state and 2_1^+ energies for ^{32}S, using the standard input NN+3N(400) interaction softened by the SRG to $\lambda_{SRG} = 2.0$ fm^{-1}. Here we use VS-IMSRG with a variety of truncations on particles allowed into the $0d_{3/2}$ shell. Results are compared with EOM-IMSRG values.

around 0.87 for ^{32}S, while they are at 0.92 for the analogous state in ^{22}O. This difference, while small, could be responsible for the noticeable discrepancy between EOM and VS-IMSRG. In the *sd*-shell diagonalization, ^{32}S has eight active protons and an equal amount of active neutrons. This allows for the inclusion of many *sd*-shell configurations not accounted for by EOM-IMSRG(2,2), which at most examines two particle excitations from the ^{32}S core. On the other hand, EOM-IMSRG includes excitations of nucleons into much higher shells, and from lower lying shells. While VS-IMSRG compensates for this through decoupling of the valence space, this additional decoupling introduces IMSRG truncation errors beyond those inflicted by the EOM-IMSRG.

Figure 5.13 demonstrates the effect of restricting various particles from entering the $0d_{3/2}$ shell during the VS-IMSRG diagonalization. The ground and 2_1^+ state are computed at various $[N_p,N_n]$, which corresponds to the number of protons and neutrons allowed in the $0d_{3/2}$ shell. EOM-IMSRG(2,2) energies are given for reference. The EOM-IMSRG(2,2) treats the ground state as a Slater determinant which is filled through the $1s$ and $0d_{5/2}$ shells. Any excited states are

constructed of at most 2p2h excitations into the $0d_{3/2}$ shell and higher. The comparison made here is not rigorous, as the two methods use different decoupling schemes, but nonetheless it sheds light on some of the differences between these methods.

It is evident from fig. 5.13 that the full active valence-space is needed to describe the absolute energies with VS-IMSRG, which are similar to that of the single-reference EOM-IMSRG(2,2) for lower truncations, and have shifted downward by 4-5 MeV once the full valence-space becomes active. The discrepancy between the single-reference ground state and VS-IMSRG is due to IMSRG(2) truncation errors related to the differing decoupling schemes. EOM-IMSRG(2,2) allows for all one- and two-particle excitations of neutrons or protons. While limitations of the shell-model code [179] used here do not allow for an analogous truncation in the VS-IMSRG, we can compare to truncations which include a portion of the EOM-IMSRG(2,2) content; these are [1,1], [2,0], and [0,2]. We can also analyze truncations which contain EOM-IMSRG(2,2) content as well as extra valence-space configurations, namely [1,2], [2,1], and [2,2].

We see that the 2_1^+ excitation energy of EOM-IMSRG(2,2) is produced reasonably well by the [1,1] truncation, using just one proton and neutron in the $0d_{3/2}$ shell. For the [0,2] and [2,0] truncations, we find that the VS-IMSRG produces a larger excitation energy than EOM-IMSRG(2,2). The [1,2], [2,1] and [2,2] truncations allow for significantly more configuration mixing relevant to the EOM-IMSRG(2,2), but also introduce 3p3h and 4p4h content that EOM-IMSRG(2,2) neglects. Nonetheless, we see that the EOM-IMSRG(2,2) excitation energy is still closely mirrored by the VS-IMSRG(2) for these truncations, with a shift in the absolute energies. As one adds more active particles in the [3,3] and [4,4] truncations, the excitation energy reduces to the result shown in fig. 5.7. It is apparent from these results that the full valence space needs to be active here to produce the smaller excitation energy of VS-IMSRG(2), which is somewhat illuminating when considering the noticeably larger excitation energy of EOM-IMSRG(2,2), where configurations of more than two $0d_{3/2}$ nucleons are ignored.

The discrepancies exhibited in ^{32}S are ostensibly the result of its midshell character, where for nuclei with fewer valence nucleons, such as ^{22}O, discrepancies are minimized. While this analysis

has certainly clarified some of the differences between EOM- and VS-IMSRG, it is generally difficult to clearly determine which method performs best for any given state because, at present, there is no prescription to assign accurate theoretical error bars to these calculations. However, one can make inferences about which method will perform best based on the 1p1h partial norms, the number of valence nucleons, and the size of the valence-space decoupling. Here it will be important to develop a reliable measure of unitarity to quantify IMSRG(2) truncation errors associated with additional decoupling.

5.2.8 The Effects of Consistent Operator Evolution

We now seek to understand the effects of consistently applying the IMSRG unitary transformation to the operators we've discussed thus far. Bare operators are expressed in the Hartree Fock basis, and have not been consistently evolved along with free-space SRG softening. As a result, the operator evolution cannot be exactly consistent, but free-space softening transformations are understood to have little effect on long-range operators such as the electromagnetic multipole operators discussed here. The principle effect of SRG softening is to renormalize short-range physics. Nonetheless, the problem is currently being given ample attention in the nuclear physics community [180, 181].

The IMSRG transformation is expected to have a noticeable effect on transition operators, as it renormalizes dynamic correlations in the nucleus which are crucial to transition behavior. Table 5.2.8 contains a few examples of transition matrix elements computed with and without consistent evolution of the operator. M^{1b}_{bare} refers to the matrix element computed without consistent evolution, (the wave functions are computed in the evolved frame however), and $M^{1b,2b}_{dressed}$ refer to the same calculation with consistently evolved operators. It is evident from those values included in the table that IMSRG evolution transforms a one-body operator into a many-body operator. Here we truncate this operator to two-body terms, consistent with the IMSRG(2) truncation.

For EOM-IMSRG(2,2) calculations, The induced two-body term generally contributes less than 10% of the total magnitude. This indicates that the current level of truncation is sufficient.

Nucleus	operator	method	$M^{1b}_{dressed}$	$M^{2b}_{dressed}$	$M^{1b+2b}_{dressed}$	M^{1b}_{bare}
^{14}C	M1	EOM	1.816	0.155	1.931	2.396
		VS	1.724	0.051	1.775	1.889
^{14}C	E2	EOM	4.257	0.297	4.554	3.870
		VS	4.345	0.094	4.439	4.933
^{22}O	M1	EOM	2.154	0.134	2.288	2.620
		VS	2.124	-0.025	2.099	2.351
^{22}O	E2	EOM	1.383	0.117	1.500	0.845
		VS	1.499	-0.071	1.428	0.000
^{32}S	M1	EOM	0.110	0.004	0.114	0.126
		VS	0.049	0.004	0.053	0.063
^{32}S	E2	EOM	5.403	0.594	5.997	4.990
		VS	7.688	-0.174	7.514	5.773

Table 5.3 Operator matrix elements computed for select nuclei with the EOM-IMSRG(2,2), using the standard input NN+3N(400) interaction softened by the SRG to $\lambda_{SRG} = 2.0$ fm^{-1}. Calculations are performed for *bare* operators and operators *dressed* by consistent IMSRG evolution. Values are expressed in efm^2 and μ_N for E2 and M1 operators respectively.

In regards to the total magnitude, consistently evolved M1 transition matrix elements exhibit a 10-20% decrease in magnitude compared with the bare operator, and the equivalent comparison for E2 transitions show an increase in magnitude of 20%, except in the case of ^{22}O, where the magnitude increases by 77.5%. Regardless of consistency with experiment, these results demonstrate that the use of effective operators is crucial in IMSRG calculations of electromagnetic observables.

As the decoupling schemes of the VS- and EOM-IMSRG are different, we include results for both methods. We note that the VS-IMSRG(2), despite having a two-stage decoupling, produces a smaller two-body contribution to the matrix elements for all cases studied here. The patterns demonstrated by the EOM-IMSRG are not observed for the VS-IMSRG, where the one- and two-body terms do not have consistent signs, and the E2 matrix element is reduced rather than increased by consistent evolution. This suggests that the renormalization of operators in the EOM-IMSRG is more predictable than it is in the VS-IMSRG. This is naively expected, as the EOM-IMSRG uses a more intuitive decoupling of the reference state for the specific nucleus of interest, where for the VS-IMSRG, the reference state used for normal ordering is not typically decoupled from excitations. The VS-IMSRG results demonstrate the critical effect of charge renormalization in

^{22}O, which has no *sd*-shell protons, and thus vanishing strength when using the bare operator.

From the results shown here, it is evident that consistent operator evolution is of integral importance to *ab initio* nuclear structure calculations, as it is responsible for dressing the effective parameters of the transition, such as e, g_l and g_s. Furthermore, even when the relevant nucleons are protons, renormalization effects are important for an accurate description of transition matrix elements.

CHAPTER 6

SUMMARY AND CONCLUSIONS

The present thesis focused on novel extensions and applications of the IMSRG to excited states and observables related to excited states. The particular vehicle chosen for this task was the newly formulated equations-of-motion IMSRG (EOM-IMSRG), which was demonstrated to be successful for describing low-lying, single excitation dominant excited states. The results here were focused on closed-shell nuclei and isobaric neighbors, which were accessed by generalized charge-exchange ladder operators.

In our quest to describe excited states with the IMSRG, we also have introduced the vTDA-IMSRG, which is a special case of the EOM-IMSRG, where explicit decoupling of the valence 1p1h block can in principle be achieved to make the method exact up to IMSRG(2) truncation errors. While this latter method has shown some promise in doubly magic nuclei as a means to describe odd-parity 1p1h states, the nature of the secondary valence space decoupling renders it impractical for more correlated systems. Thus, the generic EOM-IMSRG, which exchanges errors from the secondary decoupling for errors in approximate diagonalization, is championed as the preferred and more robust approach for excited states computed directly in the IMSRG. We demonstrated that EOM-IMSRG(2,2) produces results comparable to the well established EOM-CCSD, and also that the method can be systematically improved using perturbative corrections to include triple-excitation components in the wave functions. With these corrections we demonstrated general improvements in spectra when compared with experiment, but we note that these corrections have yet to be analyzed rigorously.

We have also introduced an effective operator formalism for the IMSRG, where now it is possible to consistently evolve operators of arbitrary spherical tensor rank. Thus, this work has introduced to the IMSRG the capability to handle electromagnetic transitions and moments, and in principle, we can also tackle Gamow-Teller strengths and various form factors. We benchmarked results for energies and electromagnetic observables using the EOM-IMSRG, the recently estab-

lished VS-IMSRG, and NCSM. General agreement between all three methods was observed for energies, $B(E2)$, and $B(M1)$ values in ^{14}C. As we go to heavier nuclei where NCSM is not applicable, we see a varied picture of consistency between the VS- and EOM-IMSRG. Here the VS-IMSRG is presumably more accurate for midshell nuclei such as ^{32}S, where the EOM-IMSRG neglects many-particle configurations within the valence space. For nuclei nearer to the extrema of the shell, such as ^{22}O, excellent agreement is exhibited. Despite this agreement, we note striking disagreement with experiment for $B(E2)$ values in all but ^{14}C, which is ostensibly due to significant many-particle collectivity which is neglected by the truncation to two-body operators in both the IMSRG and EOM calculations. The EOM-IMSRG offers a path forward here, as the triples corrections are straightforward, and their wave function components can be used to add collectivity to the calculations of observables.

The broad conclusion from this work is that EOM-IMSRG is a viable framework for which to compute nuclear excited states and observables, despite some notable limitations. The method is straightforwardly extended to a multireference formalism which will make it applicable to open-shells. The MR-EOM-IMSRG, which we anticipate to arrive within a year, will be a powerful method to compute spectra, transitions, and response in open-shell nuclei. Response functions follow directly from the Lanczos method used to evaluate the equations of motion. We note that this is not straightforward in the shell-model formalism which has become popular in the *ab initio* community, as the required method of moments will certainly excite states outside of the valence space. The MR-EOM-IMSRG will derive the bulk of its utility from its lightweight computational requirements, as even in the multireference formalism, polynomial scaling will be observed. This will provide a simple tool to perform large computational sweeps, crossing the nuclear landscape in an attempt to analyze generic issues in nuclear physics, such as the quenching of g_A and the enigma of neutrinoless double β-decay, which is tied intimately with the former point.

Moreover, the methods discussed here are important to the nuclear community because it is desirable to have numerous approaches to *ab initio* nuclear structure problems, where we can make predictions and benchmark them against methods starting from the exact same fundamental

assumptions. For example, multiple *ab initio* methods producing consistent results for the neutrinoless double β-decay matrix element would mark a triumph for nuclear theory. Consistency is not the only goal for our methods however; here we return to the oft repeated distinguishment between precision and accuracy. As alluded to in this work, we have achieved precise predictions for observables and energies which are reproduced from method to method. However, we lack accuracy with experiment. It is crucial that we use these precise methods to facilitate the quest to achieve accuracy through improved interactions and currents, and for this, intricate understanding of the strengths and weaknesses of each method is paramount.

APPENDIX

A.1 Definitions for J-scheme Formulation

Shorthand:

$$(am_a) \equiv (\xi_a, j_a, m_a)\,, \tag{1}$$

$$(a) \equiv (\xi_a, j_a)\,, \tag{2}$$

$$\hat{J} \equiv \sqrt{2J+1}\,, \tag{3}$$

$$P_{rs}A_{\ldots r\ldots s\ldots} \equiv A_{\ldots s\ldots r\ldots} \tag{4}$$

$$P_{rs}(J) \equiv (-1)^{(j_r+j_s-J)}P_{rs}\,, \tag{5}$$

$$\sum_{\{m\}} : \text{sum over all } m\,, \tag{6}$$

m-scheme antisymmetrized matrix elements:

$$A^{\lambda\mu}_{pq} \equiv \langle pm_p|A^{\lambda}_{\mu}|qm_q\rangle\,, \tag{7}$$

$$A^{\lambda\mu}_{pqrs} \equiv \langle pm_p, qm_q|A^{\lambda}_{\mu}|rm_r sm_s\rangle\,, \tag{8}$$

Clebsch-Gordan coefficients:

$$C^{j_p j_q J}_{m_p m_q M} \equiv \langle j_p m_p; j_q m_q|(j_p j_q)JM\rangle \tag{9}$$

$$C^{j_p \bar{j}_q J}_{m_p \bar{m}_q M} \equiv (-1)^{(j_q-m_q)}\langle j_p m_p; j_q - m_q|(j_p j_q)JM\rangle\,, \tag{10}$$

J-scheme matrix elements:

$$A^{\lambda}_{pq} \equiv \langle p||A^{\lambda}||q\rangle\,, \tag{11}$$

$$A^{(J_1J_2)\lambda}_{pqrs} \equiv \langle (pq)J_1||A^{\lambda}||(rs)J_2\rangle\,, \tag{12}$$

Unnormalized matrix elements for practical use:

$$\tilde{A}^{(J_1J_2)\lambda}_{pqrs} \equiv (N_{pq(J_1)})^{-1}(N_{rs(J_2)})^{-1}\langle (pq)J_1||A^{\lambda}||(rs)J_2\rangle\,, \tag{13}$$

$$\tilde{A}^{J}_{pqrs} \equiv (N_{pq(J)})^{-1}(N_{rs(J)})^{-1}\langle (pq)J0|A^{0}|(rs)J0\rangle\,, \tag{14}$$

$$(N_{pq(J)})^{-1} \equiv \frac{(1+\delta_{\xi_p\xi_q}\delta_{j_p j_q})}{\sqrt{1+(-1)^J\delta_{\xi_p\xi_q}\delta_{j_p j_q}}} \tag{15}$$

Pandya transformed matrix elements:

$$\bar{A}^{(J_1J_2)\lambda}_{p\bar{s}r\bar{q}} = -\sum_{J_3J_3}(-1)^{(J_2+J_4+jq+js)}\hat{J}_1\hat{J}_2\hat{J}_3\hat{J}_4\begin{Bmatrix} j_p & j_s & J_1 \\ j_q & j_r & J_2 \\ J_3 & J_4 & \lambda \end{Bmatrix}\tilde{V}^{(J_3J_4)\lambda}_{pqrs} \tag{16}$$

Spherical tensor product:

$$[A^{\lambda_1}B^{\lambda_2}]^{\lambda}_{\mu} = \sum_{\mu_1\mu_2} C^{\lambda_1\lambda_2\lambda}_{\mu_1\mu_2\mu}A^{\lambda_1}_{\mu_1}B^{\lambda_2}_{\mu_2} \tag{17}$$

A.2 Spherical tensor operators

The definition of a spherical tensor T^J_M is:

$$[J_z, T^J_M] = M\hbar T^J_M\,, \tag{18}$$

$$[J_\pm, T^J_M] = \hbar\sqrt{(J\pm M+1)(J\mp M)}T_{J,M\pm1}\,, \tag{19}$$

where

$$J_z = \hbar\sum_{pm_p} m_p a^\dagger_{pm_p}a_{pm_p}\,, \tag{20}$$

$$J_\pm = \hbar\sum_{pm_p} m^\mp_p a^\dagger_{pm_p}a_{pm_p\mp1}\,, \tag{21}$$

and

$$m^\pm_p = \sqrt{(j_p\pm m_p+1)(j_p\mp m_p)}\,. \tag{22}$$

One can very quickly show that a particle creation operator transforms as a tensor:

$$[j_z, a^\dagger_{jm}] = \sum_{m'} m'[a^\dagger_{jm'}a_{jm'}, a^\dagger_{jm}] = ma^\dagger_{jm}\,, \tag{23}$$

$$[j_\pm, a^\dagger_{jm}] = \sum_{m'} m^{\mp\prime}[a^\dagger_{jm'}a_{jm'\mp1}, a^\dagger_{jm}] = m^\pm a^\dagger_{jm\pm1}\,. \tag{24}$$

Attempts to show this for the particle annihilation operator fail:

$$[j_z, a_{jm}] = \sum_{m'} m'[a^\dagger_{jm'}a_{jm'}, a_{jm}] = -ma_{jm}\,, \tag{25}$$

$$[j_\pm, a_{jm}] = \sum_{m'} m^{\mp\prime}[a^\dagger_{jm'}a_{jm'\mp1}, a_{jm}] = -m^\mp a_{jm\mp1}\,. \tag{26}$$

An operator which does in fact transform as a tensor is

$$\tilde{a}_{jm} = (-1)^{(j+m)} a_{j,-m}\,, \tag{27}$$

as is demonstrated here:

$$[j_z, \tilde{a}_{jm}] = \sum_{m'} m' [a^{\dagger}_{jm'} a_{jm'}, a_{j,-m}](-1)^{(j+m)} = m a_{j,-m}(-1)^{(j+m)} = m\tilde{a}_{jm}\,, \tag{28}$$

$$[j_{\pm}, \tilde{a}_{jm}] = \sum_{m'} m^{\mp\prime} [a^{\dagger}_{jm'} a_{jm'\mp 1}, a_{j,-m}](-1)^{(j+m)} = -m^{\pm}(-1)^{(j+m)} a_{j,-m\mp 1} = m^{\pm}\tilde{a}_{j,(m\pm 1)}\,. \tag{29}$$

Consider now the tensor product of two spherical tensor operators $A^{jp}_{m_p}$ and $B^{jq}_{m_q}$ coupled to total angular momentum J:

$$[A^{jp} B^{jq}]^J_M = \sum_{m_p, m_q} C^{jp\,jq\,J}_{m_p m_q M} A^{jp}_{m_p} B^{jq}_{m_q} \tag{30}$$

It can be shown that this product is a spherical tensor of rank J:

$$\begin{aligned}
[J_z, [A^{jp} B^{jq}]^J_M] &= \sum_{m_p, m_q} [(j_p)_z + (j_q)_z, C^{jp\,jq\,J}_{m_p m_q M} A^{jp}_{m_p} B^{jq}_{m_q}] \\
&= \sum_{m_p, m_q} (m_p + m_q) C^{jp\,jq\,J}_{m_p m_q M} A^{jp}_{m_p} B^{jq}_{m_q} = M [A^{jp} B^{jq}]^J_M
\end{aligned} \tag{31}$$

$$\begin{aligned}
[J_{\pm}, [A^{jp} B^{jq}]^J_M] &= \sum_{m_p, m_q} [(j_p)_{\pm} + (j_q)_{\pm}, C^{jp\,jq\,J}_{m_p m_q M} A^{jp}_{m_p} B^{jq}_{m_q}] \\
&= \sum_{m_p, m_q} (m^{\pm}_p C^{jp\,jq\,J}_{m_p m_q M} A^{jp}_{m_p \pm 1} B^{jq}_{m_q} + m^{\pm}_q C^{jp\,jq\,J}_{m_p m_q M} A^{jp}_{m_p} B^{jq}_{m_q \pm 1}) \\
&= \sum_{m_p, m_q} (m^{\mp}_a C^{jp\,jq\,J}_{m_p \mp 1 m_q M} + m^{\mp}_b C^{jp\,jq\,J}_{m_p m_q \mp 1 M}) A^{jp}_{m_p} B^{jq}_{m_q} \\
&= M^{\pm} C^{jp\,jq\,J}_{m_p m_q M \pm 1} A^{jp}_{m_p} B^{jq}_{m_q} = M^{\pm} [A^{jp} B^{jq}]^J_{M\pm 1}
\end{aligned} \tag{32}$$

where the identity used to arrive at the third line comes from acting with $J_{\pm}$ on both M-scheme and J-scheme versions of a two body ket and equating the two expressions.

A.2.1 J-scheme operators in second quantization

We can use the Wigner-Eckart theorem

$$\langle p j_p m_p | T_{\lambda\mu} | q j_q m_q \rangle = \hat{j}_p^{-1} T^{\lambda}_{pq} C^{j_q \lambda j_p}_{m_q \mu m_p} \tag{33}$$

to write a one-body operator in J-scheme:

$$\begin{aligned}
\sum_{pq} \langle p j_p m_p | T_{\lambda\mu} | q j_q m_q \rangle a^{\dagger}_{pm_p} a_{qm_q} &= \sum_{pq} \hat{j_p}^{-1} T^{\lambda}_{pq} C^{j_q \lambda j_p}_{m_q \mu m_p} a^{\dagger}_{pm_p} a_{qm_q} \\
&= \sum_{pq} \hat{\lambda}^{-1} T^{\lambda}_{pq} C^{j_p j_q \lambda}_{m_p -m_q \mu} (-1)^{(j_q - m_q)} a^{\dagger}_{pm_p} a_{qm_q} \\
&= \sum_{pq} \hat{\lambda}^{-1} T^{\lambda}_{pq} C^{j_p \bar{j}_q \lambda}_{m_p \bar{m}_q \mu} a^{\dagger}_{pm_p} a_{qm_q} \\
&= \sum_{pq} \hat{\lambda}^{-1} T^{\lambda}_{pq} [a^{\dagger}_p \tilde{a}_q]^{\lambda}_{\mu}
\end{aligned} \tag{34}$$

Consider now two particle excitations on the fermi-vacuum:

$$[a^{\dagger}_p a^{\dagger}_q]^J_M |\Phi_0\rangle = N_{pq} \sum_{m_p m_q} C^{j_p j_q J}_{m_p m_q M} a^{\dagger}_{pm_p} a^{\dagger}_{qm_q} |\Phi_0\rangle \tag{35}$$

The excitation operator transforms as a spherical tensor. In order for the de-excitation operator to transform in this way, we take the Hermitian conjugate

$$\begin{aligned}
(N_{pq} [a^{\dagger}_p a^{\dagger}_q]^J_M |\Phi_0\rangle)^{\dagger} &= N_{pq} \sum_{m_p m_q} C^{j_p j_q J}_{m_p m_q M} \langle \Phi_0 | a_{qm_q} a_{pm_p} \\
&= N_{pq} \sum_{m_p m_q} C^{j_p j_q J}_{-m_p -m_q -M} (-1)^{(j_p + j_q - J)} \langle \Phi_0 | a_{qm_q} a_{pm_p} \\
&= -N_{pq} \sum_{m_p m_q} C^{j_p j_q J}_{m_p m_q -M} (-1)^{(J-M)} \langle \Phi_0 | \tilde{a}_{pm_p} \tilde{a}_{qm_q} \\
&= -N_{pq} \langle \Phi_0 | [\tilde{a}_p \tilde{a}_q]^J_{-M} (-1)^{(J-M)}
\end{aligned} \tag{36}$$

The normalization constant is obtained by calculating the overlap of the two wavefunctions. We tend to use un-normalized matrix elements to avoid this issue however. We can from here construct

a two-body operator:

$$
\begin{aligned}
&\frac{1}{4}\sum_{pqrs}\langle pm_p,qm_q|V^{\lambda}_{\mu}|rm_r,sm_s\rangle a^{\dagger}_{pm_p}a^{\dagger}_{qm_q}a_{sm_s}a_{rm_r}\\
&\quad=\frac{1}{4}\sum_{\substack{J_1J_2\\M_1M_2}}\sum_{pqrs}N^{-1}_{pq}N^{-1}_{rs}C^{jpjqJ_1}_{m_pm_qM_1}C^{jrjsJ_2}_{m_rm_sM_2}\langle(pq)J_1M_1|V^{\lambda}_{\mu}|(rs)J_2M_2\rangle a^{\dagger}_{pm_p}a^{\dagger}_{qm_q}a_{sm_s}a_{rm_r}\\
&\quad=\frac{1}{4}\sum_{\substack{J_1J_2\\M_1M_2}}\sum_{pqrs}\frac{1}{\hat{J}_1}C^{jpjqJ_1}_{m_pm_qM_1}C^{jrjsJ_2}_{m_rm_sM_2}C^{J_2\lambda J_1}_{M_2\mu M_1}\tilde{V}^{(J_1J_2)\lambda}_{pqrs}a^{\dagger}_{pm_p}a^{\dagger}_{qm_q}a_{sm_s}a_{rm_r}\\
&\quad=\frac{1}{4}\sum_{\substack{J_1J_2\\M_1M_2}}\sum_{pqrs}\frac{1}{\hat{\lambda}}C^{jpjqJ_1}_{m_pm_qM_1}C^{jrjsJ_2}_{m_rm_sM_2}C^{J_1J_2\lambda}_{M_1-M_2\mu}(-1)^{(J_2-M_2)}\tilde{V}^{(J_1J_2)\lambda}_{pqrs}a^{\dagger}_{pm_p}a^{\dagger}_{qm_q}a_{sm_s}a_{rm_r}\\
&\quad=-\frac{1}{4}\sum_{\substack{J_1J_2\\M_1M_2}}\sum_{pqrs}\frac{1}{\hat{\lambda}}C^{jrjsJ_2}_{-m_r-m_sM_2}C^{J_1J_2\lambda}_{M_1-M_2\mu}(-1)^{(J_2-M_2)}\tilde{V}^{(J_1J_2)\lambda}_{pqrs}[a^{\dagger}_pa^{\dagger}_q]^{J_1}_{M_1}a_{r-m_r}a_{s-m_s}\\
&\quad=-\frac{1}{4}\sum_{\substack{J_1J_2\\M_1M_2}}\sum_{pqrs}\frac{1}{\hat{\lambda}}C^{jrjsJ_2}_{m_rm_s-M_2}C^{J_1J_2\lambda}_{M_1-M_2\mu}(-1)^{(j_r+j_s+m_r+m_s)}\tilde{V}^{(J_1J_2)\lambda}_{pqrs}[a^{\dagger}_pa^{\dagger}_q]^{J_1}_{M_1}a_{r-m_r}a_{s-m_s}\\
&\quad=-\frac{1}{4}\sum_{\substack{J_1J_2\\M_1M_2}}\sum_{pqrs}\frac{1}{\hat{\lambda}}C^{J_1J_2\lambda}_{M_1-M_2\mu}\tilde{V}^{(J_1J_2)\lambda}_{pqrs}[a^{\dagger}_pa^{\dagger}_q]^{J_1}_{M_1}[\tilde{a}_r\tilde{a}_s]^{J_2}_{-M_2}\\
&\quad=-\frac{1}{4}\sum_{J_1J_2}\sum_{pqrs}\frac{1}{\hat{\lambda}}\tilde{V}^{(J_1J_2)\lambda}_{pqrs}[[a^{\dagger}_pa^{\dagger}_q]^{J_1}[\tilde{a}_r\tilde{a}_s]^{J_2}]^{\lambda}_{\mu}
\end{aligned}
\tag{37}
$$

A.2.2 Normal-ordered spherical tensor operators

If we normal order these operators, we find:

$$
\begin{aligned}
&\sum_{pq}\sum_{m_pm_q}\langle pm_p|T_{\lambda\mu}|qm_q\rangle a^{\dagger}_{pm_p}a_{qm_q}\\
&\qquad=\sum_{pq}\hat{\lambda}^{-1}T^{\lambda}_{pq}\{a^{\dagger}_p\tilde{a}_q\}^{\lambda}_{\mu}+\sum_{im_i}T^{\lambda}_{ii}n_i\frac{(-1)^{(j_i-m_i)}}{\hat{\lambda}}C^{j_ij_i\lambda}_{m_i-m_i\mu}\\
&\qquad=\sum_{pq}\hat{\lambda}^{-1}T^{\lambda}_{pq}\{a^{\dagger}_{j_p}\tilde{a}_{j_q}\}^{\lambda}_{\mu}+\sum_i\hat{j}_iT^{\lambda}_{ii}n_i\delta_{\lambda0}
\end{aligned}
\tag{38}
$$

We find a similar zero body piece when we normal order the two-body operator:

$$
\frac{1}{2}\sum_{ij}\sum_J\hat{J}\tilde{V}^{(JJ)\lambda}_{ijij}n_in_j\delta_{\lambda0}
\tag{39}
$$

The in-medium one-body piece from the free-space two-body operator is:

$$\sum_{J_1 J_2} \sum_{pqi} \frac{\hat{J}_1 \hat{J}_2}{\hat{\lambda}} \tilde{V}^{(J_1 J_2)\lambda}_{piqi} n_i (-1)^{(j_i + j_p + J_2 + \lambda)} \begin{Bmatrix} J_1 & j_i & j_p \\ j_q & \lambda & J_2 \end{Bmatrix} \{a_p^\dagger \tilde{a}_q\}^\lambda_\mu \tag{40}$$

For scalar operators, this reduces to

$$\sum_J \sum_{pqi} \frac{\hat{J}^2}{\hat{j}_p^2} \tilde{V}^J_{pibi} n_i \{a_p^\dagger a_q\} \tag{41}$$

In summary, a spherical tensor operator A^λ_μ can be expressed in normal ordered form:

$$\begin{aligned} \{V^\lambda_\mu\} = \delta_{\lambda 0}\delta_{\mu 0}[&\sum_i \hat{j}_i V^0_{ii} n_i + \frac{1}{2}\sum_{ij}\sum_J \hat{J} \tilde{V}^{(JJ)0}_{ijij} n_i n_j] \\ &+ \frac{1}{\hat{\lambda}} \sum_{pq} \{a_p^\dagger \tilde{a}_q\}^\lambda_\mu (V^\lambda_{pq} + \sum_i \sum_{J_1 J_2} \hat{J}_1 \hat{J}_2 \begin{Bmatrix} J_1 & J_2 & \lambda \\ j_q & j_p & j_i \end{Bmatrix} (-1)^{(\lambda + J_2 + j_p + j_i)} \tilde{V}^{\lambda J_1 J_2}_{piqi} n_k) \\ &- \frac{1}{4\hat{\lambda}} \sum_{pqrs} \sum_{J_1 J_2} \{[a_p^\dagger a_q^\dagger]^{J_1} [\tilde{a}_r \tilde{a}_s]^{J_2}\}^\lambda_\mu \tilde{V}^{\lambda J_1 J_2}_{pqrs} \end{aligned} \tag{42}$$

Typically, we use non-reduced matrix elements for the scalar operators, i.e.:

$$\langle p|X|q\rangle = \frac{1}{\hat{j}_p} \langle p||X^0||q\rangle \,. \tag{43}$$

This is possible because the non-reduced matrix elements are independent of M just as the reduced ones are. So in a typical IMSRG code you might calculate the zero body piece of a scalar operator as:

$$E_0 = \sum_i \hat{j}_i^2 V_{ii} n_i + \frac{1}{2}\sum_{ij}\sum_J \hat{J}^2 \tilde{V}^J_{ijij} n_i n_j \tag{44}$$

A.3 Jucys diagrams

In the following sections it becomes necessary to use a diagrammatic strategy to execute the required angular momentum coupling. Without immense digression into the theory of Jucys angular momentum diagrams, we introduce some relevant definitions and identities for this work. We implore the reader to learn more about these fantastic diagrams in Ref. [182].

A.3.1 Basic Components and Symmetries

First we introduce the basic diagrams for Clebsch-Gordan coefficients,

$$C^{j_1 j_2 j_3}_{m_1 m_2 m_3} = \hat{j}_3 (-1)^{2j_2}$$ 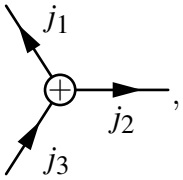

, (45)

$$C^{j_1 \bar{j}_2 j_3}_{m_1 \bar{m}_2 m_3} \equiv C^{j_1 j_2 j_3}_{m_1 -m_2 m_3} (-1)^{j_2 - m_2} = \hat{j}_3$$ 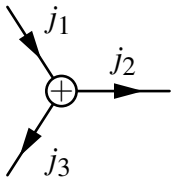

. (46)

Figure A.1 Diagrammatic representation of Clebsch-Gordan coefficients

The diagrams consist of three oriented lines and an oriented vertex. The diagrams are based on $3j$-symbols, hence the phase and scale factors that pop out when you equate them to Clebsch-Gordan coefficients. The orientation of the lines indicates whether or not the specific angular momenta is time-reversed, and the orientation of the vertex indicates the direction you would read off a $3j$-symbol from these diagrams, with $+$ indicating clockwise.

Some diagrammatic represenations of the symmetries of the $3j$-symbol:

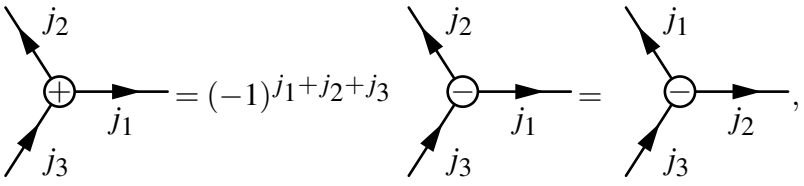

, (47)

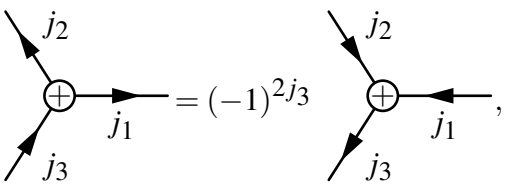

, (48)

Figure A.2 Symmetries of Jucys diagrams.

Figure A.2 (cont'd)

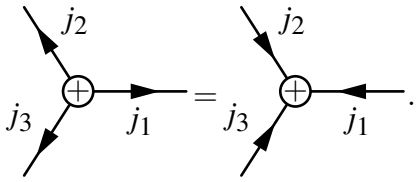

(49)

Here we see diagrammatic rules for permutation of columns and time reversal of all angular momenta.

A.3.2 Diagram manipulation

The utility of Jucys diagrams comes from contracting the lines, which corresponds to summing out an angular-momentum substate,

$$\sum_{m_1} C^{j_1 j_2 j_3}_{m_1 m_2 m_3} C^{j_4 j_5 j_1}_{m_4 m_5 m_1} = \hat{j}_1 \hat{j}_3 (-1)^{2(j_2+j_5)}$$

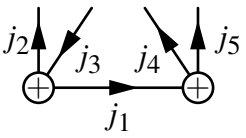

(50)

Figure A.3 Jucys contraction.

Now we have arrived at the concept of external and internal lines. For computation of J-scheme expressions (where all m-dependence has been summed out of the problem), our goal is to construct diagrams consisting only of internal lines.

We need to be able to change the orientation of a line. For internal lines labeled j, this is as simple as multiplying by $(-1)^{2j}$. You get a sign change if you flip the orientation of a half-integer angular momenta. For external lines, time reversal still has an explicit effect, as the line still has m-dependence. Thus for an external line labeled j, you must multiply by $(-1)^{j-m}$ in order to flip the line orientation.

Once all lines are connected, we must be able to factorize large diagrams. There are only two rules that are important for our purposes,

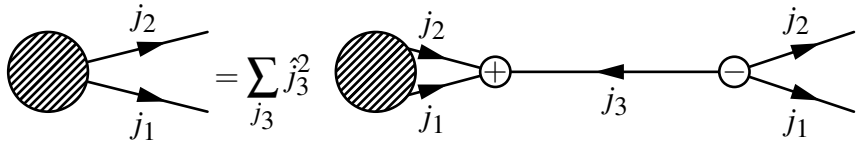

, (51)

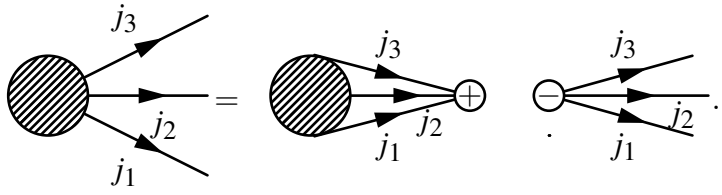

. (52)

Figure A.4 Jucys factorization rules.

With these two rules, we can factorize pretty much everything we encounter into $6j$ and $9j$ symbols,

$$\begin{Bmatrix} j_1 & j_2 & j_3 \\ j_4 & j_5 & j_6 \end{Bmatrix} =$$

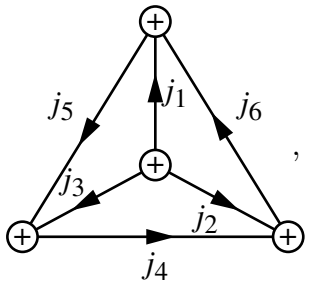

, (53)

$$\begin{Bmatrix} j_1 & j_2 & j_3 \\ j_4 & j_5 & j_6 \\ j_7 & j_8 & j_9 \end{Bmatrix} =$$

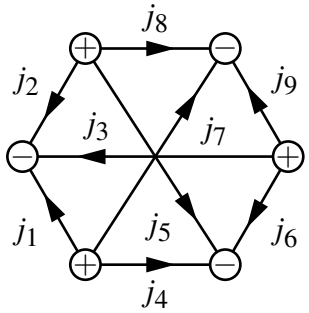

(54)

Figure A.5 Jucys diagrams for $6j$- and $9j$-symbols.

A.4 Particle-hole picture

For certain derivations, it is convenient to formulate angular momentum coupling in terms of particle-hole creation and annihilation operators. The hole creation operator, which creates a time reversed particle, is given by

$$\bar{a}^\dagger_{m_p} = \tilde{a}_{m_p} = (-1)^{p+m_p} a_{-m_p}\,, \tag{55}$$

and the corresponding annihilation operator by

$$\bar{a}_{m_p} = \tilde{a}^\dagger_{m_p} = (-1)^{p-m_p} a^\dagger_{-m_p}\,. \tag{56}$$

Again we must alter the form of the annihilation operator to ensure that it is a spherical tensor.

$$\tilde{\bar{a}}_{m_p} = -a^\dagger_{m_p}\,. \tag{57}$$

With these definitions, we can construct particle-hole creators

$$\begin{aligned}
|\Phi^p_q(JM)\rangle &= \sum_{m_p m_q} C^{j_p j_q J}_{m_p m_q M} a^\dagger_{pm_p} \bar{a}^\dagger_{qm_q} |\Phi_0\rangle\,, \\
&\equiv \sum_{m_p m_q} C^{j_p \bar{j}_q J}_{m_p \bar{m}_q M} a^\dagger_{pm_p} a_{qm_q} |\Phi_0\rangle\,, \\
&= [a^\dagger_p \bar{a}^\dagger_q]^J_M |\Phi_0\rangle\,,
\end{aligned} \tag{58}$$

and corresponding annihilators

$$\begin{aligned}
\langle\Phi^p_q(JM)| &= \sum_{m_q m_p} C^{j_q j_p J}_{m_q m_p -M} (-1)^{(j_q + j_p + M)} \langle\Phi_0| \tilde{\bar{a}}_{qm_q} \tilde{a}_{pm_p} \\
\langle\Phi^p_q(JM)| &= \sum_{m_q m_p} C^{\bar{j}_p j_q \bar{J}}_{\bar{m}_p m_q \bar{M}} \langle\Phi_0| a_{pm_p} a^\dagger_{qm_q} \\
&= (-1)^{J-M} \langle\Phi_0| [\tilde{a}_p \tilde{\bar{a}}_q]^J_{-M}\,.
\end{aligned} \tag{59}$$

Now we may construct a two-body operator in the particle-hole picture.

$$\begin{aligned}
&-\frac{1}{4\hat{\lambda}} \sum_{\substack{pqrs \\ J_1 J_2}} \tilde{V}^{(J_1 J_2)\lambda}_{pqrs} [[a^\dagger_p a^\dagger_q]^{J_1} [\tilde{a}_r \tilde{a}_s]^{J_2}]^\lambda_\mu \\
&\quad = \frac{1}{4\hat{\lambda}} \sum_{\substack{pqrs \\ J_1 J_2}} \tilde{V}^{(J_1 J_2)\lambda}_{pqrs} \sum_{\substack{m_p m_q m_r m_s \\ M_1 M_2}} C^{j_p j_q J_1}_{m_p m_q M_1} C^{j_r j_s J_2}_{m_r m_s M_2} C^{J_1 \bar{J}_2 \lambda}_{M_1 \bar{M}_2 \mu} a^\dagger_{m_p} a^\dagger_{m_q} a_{m_s} a_{m_r}
\end{aligned} \tag{60}$$

$$= \frac{1}{4} \sum_{\substack{pqrs \\ J_1 J_2}} \tilde{V}^{(J_1 J_2)\lambda}_{pqrs} \sum_{m_p m_q m_r m_s} a^\dagger_{m_p} a^\dagger_{m_q} a_{m_s} a_{m_r} (-1)^{(J_1+J_2+\lambda)} \hat{J}_1 \hat{J}_2$$ 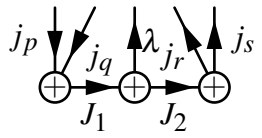 (61)

Figure A.6 Jucys diagram for a two-body operator.

The sum over the Clebsch-Gordan coefficients, represented as a Jucys diagram, can be recoupled using Jucys factorization rules,

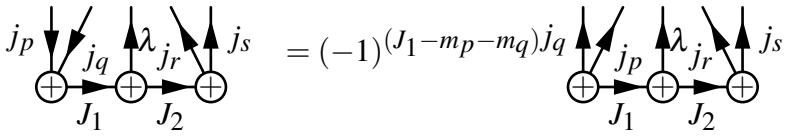

$= (-1)^{(J_1-m_p-m_q)}$

$$= \sum_{J_3 J_4} (\hat{J}_3 \hat{J}_4)^2$$ 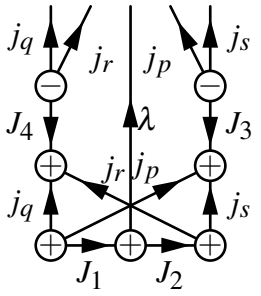

$(-1)^{(J_1-m_p-m_q)}$

$$= \sum_{J_3 J_4} (-1)^{(J_2+\lambda-m_p-m_q)} (\hat{J}_3 \hat{J}_4)^2$$ 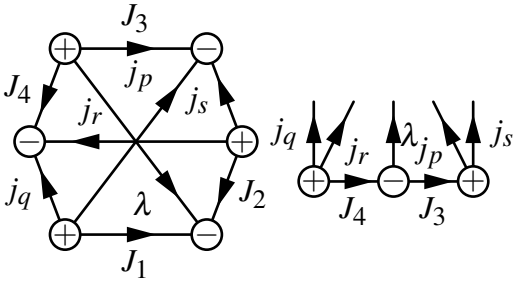

$$= \sum_{J_3 J_4} (-1)^{(J_1-m_p-m_q)} (\hat{J}_3 \hat{J}_4)^2 \begin{Bmatrix} j_p & j_s & J_3 \\ j_q & j_r & J_4 \\ J_1 & J_2 & \lambda \end{Bmatrix}$$ 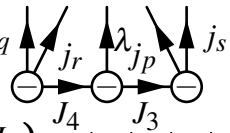

$$= \sum_{J_3 J_4} (-1)^{(J_1+J_4+\lambda+j_q-j_s)} (\hat{J}_3 \hat{J}_4)^2 \begin{Bmatrix} j_p & j_s & J_3 \\ j_q & j_r & J_4 \\ J_1 & J_2 & \lambda \end{Bmatrix}$$ 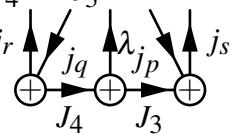

$$= \sum_{J_3 J_4} (-1)^{(J_1+J_4+\lambda+j_q+j_s)} \hat{J}_4 \begin{Bmatrix} j_p & j_s & J_3 \\ j_q & j_r & J_4 \\ J_1 & J_2 & \lambda \end{Bmatrix} \sum_{M_3 M_4} C^{j_r \bar{j}_q J_4}_{m_r \bar{m}_q M_4} C^{j_p \bar{j}_s J_3}_{m_s \bar{m}_p M_3} C^{J_4 \lambda J_3}_{M_4 \mu M_3} . \quad (62)$$

Figure A.7 Diagrammatic derivation of the Pandya transform.

Thus,

$$
\begin{aligned}
&-\frac{1}{4\hat{\lambda}}\sum_{\substack{pqrs\\J_1J_2}}\tilde{V}^{(J_1J_2)\lambda}_{pqrs}[[a^\dagger_p a^\dagger_q]^{J_1}[\tilde{a}_r\tilde{a}_s]^{J_2}]^\lambda_\mu \\
&=\frac{1}{4}\sum_{\substack{pqrs\\J_1J_2J_3J_4}}\tilde{V}^{(J_1J_2)\lambda}_{pqrs}(-1)^{(J_2+J_4+jq+js)}\hat{J}_1\hat{J}_2\hat{J}_4\begin{Bmatrix} j_p & j_s & J_3\\ j_q & j_r & J_4\\ J_1 & J_2 & \lambda\end{Bmatrix} \\
&\qquad\times\sum_{\substack{m_pm_qm_rm_s\\M_3M_4}}C^{j_pj_s\bar{J}_3}_{m_pm_sM_3}C^{j_rj_q\bar{J}_4}_{m_rm_qM_4}C^{J_4\lambda J_3}_{M_4\mu M_3}a^\dagger_{m_p}a_{m_s}a_{m_r}a^\dagger_{m_q} \\
&=\frac{1}{4}\sum_{\substack{pqrs\\J_1J_2J_3J_4}}\tilde{V}^{(J_1J_2)\lambda}_{pqrs}(-1)^{(J_2+J_4+jq+js)}\hat{J}_1\hat{J}_2\hat{J}_4\begin{Bmatrix} j_p & j_s & J_3\\ j_q & j_r & J_4\\ J_1 & J_2 & \lambda\end{Bmatrix} \\
&\qquad\times\sum_{\substack{m_pm_qm_rm_s\\M_3M_4}}C^{j_pj_s\bar{J}_3}_{m_pm_sM_3}a^\dagger_{m_p}a_{m_s}C^{\bar{j}_rj_q\bar{J}_4}_{\bar{m}_rm_q\bar{M}_4}a_{m_r}a^\dagger_{m_q}\frac{\hat{J}_3}{\hat{\lambda}}C^{J_3\bar{J}_4\lambda}_{M_3\bar{M}_4\mu} \\
&\qquad=\frac{1}{4\hat{\lambda}}\sum_{\substack{pqrs\\J_1J_2J_3J_4}}\tilde{V}^{(J_1J_2)\lambda}_{pqrs}(-1)^{(J_2+J_4+jq+js)}\hat{J}_1\hat{J}_2\hat{J}_3\hat{J}_4\begin{Bmatrix} j_p & j_s & J_3\\ j_q & j_r & J_4\\ J_1 & J_2 & \lambda\end{Bmatrix}[[a^\dagger_p\bar{a}^\dagger_s]^{J_3}[\tilde{a}_r\tilde{\bar{a}}_q]^{J_4}]^\lambda_\mu
\end{aligned}
\tag{63}
$$

The particle-hole formalism two-body operator has been "Pandya transformed",

$$
-\frac{1}{4\hat{\lambda}}\sum_{\substack{pqrs\\J_1J_2}}\tilde{V}^{(J_1J_2)\lambda}_{pqrs}[[a^\dagger_p a^\dagger_q]^{J_1}[\tilde{a}_r\tilde{a}_s]^{J_2}]^\lambda_\mu \equiv -\frac{1}{4\hat{\lambda}}\sum_{\substack{p\bar{q}r\bar{s}\\J_3J_4}}\bar{V}^{(J_3J_4)\lambda}_{p\bar{s}r\bar{q}}[[a^\dagger_p\bar{a}^\dagger_s]^{J_3}[\tilde{a}_r\tilde{\bar{a}}_q]^{J_4}]^\lambda_\mu \tag{64}
$$

where

$$
\bar{V}^{(J_3J_4)\lambda}_{p\bar{s}r\bar{q}} = -\sum_{J_1J_2}(-1)^{(J_2+J_4+jq+js)}\hat{J}_1\hat{J}_2\hat{J}_3\hat{J}_4\begin{Bmatrix} j_p & j_s & J_3\\ j_q & j_r & J_4\\ J_1 & J_2 & \lambda\end{Bmatrix}\tilde{V}^{(J_1J_2)\lambda}_{pqrs} \tag{65}
$$

Pandya transformed matrix elements are very useful for computing terms with multiple Wick contractions acting on particle and hole states.

A.5 Derivation of the general tensor product

In order to calculate moments and certain transitions in the EOM-IMSRG(2,2), the spherical tensor product

$$[A^{\lambda_1}B^{\lambda_2}]^{\lambda}_{\mu} = \sum_{\mu_1\mu_2\mu} C^{\lambda_1\lambda_2\lambda}_{\mu_1\mu_2\mu} A^{\lambda_1}_{\mu_1} B^{\lambda_2}_{\mu_2} \tag{66}$$

must be computed. We will include up to two-body operators in accordance with the truncations of both the EOM and IMSRG calculations. The tensor product of A and B is named Z, for which we may compute reduced matrix-elements

$$\langle XJ_X||Z^{\lambda}||YJ_Y\rangle = \frac{1}{\hat{J}_X}\sum_{\mu M_X M_Y}\sum_{\mu_1\mu_2} C^{J_Y\lambda J_X}_{M_Y\mu M_X} C^{\lambda_1\lambda_2\lambda}_{\mu_1\mu_2\mu}\langle XJ_XM_X|A^{\lambda_1}_{\mu_1}B^{\lambda_2}_{\mu_2}|YJ_YM_Y\rangle\,, \tag{67}$$

or equivalently

$$\langle XJ_X||Z^{\lambda}||YJ_Y\rangle = \frac{1}{\hat{\lambda}}\sum_{\mu M_X M_Y}\sum_{\mu_1\mu_2} C^{J_X\bar{J}_Y\lambda}_{M_x\bar{M}_Y\mu} C^{\lambda_1\lambda_2\lambda}_{\mu_1\mu_2\mu}\langle XJ_XM_X|A^{\lambda_1}_{\mu_1}B^{\lambda_2}_{\mu_2}|YJ_YM_Y\rangle\,. \tag{68}$$

This calculation proceeds in two steps:

1. Expand A and B in m-scheme and perform all possible Wick contractions.

2. Return full expression to J-scheme by summing out remaining angular momentum substates.

A.5.1 Step one: Wick Contractions

We write out the relevant multiplications of two normal-ordered operator strings,

$$\Big[\{a_p^\dagger a_q\}\{a_r^\dagger a_s\}\Big]_{0b} = \delta_{qr}\delta_{ps}n_p\bar{n}_q \tag{69}$$

$$\Big[\{a_p^\dagger a_q\}\{a_r^\dagger a_s\}\Big]_{1b} = \delta_{qr}\bar{n}_q\{a_p^\dagger a_s\} - \delta_{ps}n_p\{a_q^\dagger a_r\} \tag{70}$$

$$\Big[\{a_p^\dagger a_q\}\{a_r^\dagger a_s\}\Big]_{2b} = \{a_p^\dagger a_r^\dagger a_s a_q\} \tag{71}$$

$$\Big[\{a_p^\dagger a_q^\dagger a_s a_r\}\{a_t^\dagger a_u\}\Big]_{1b} = (1-P_{pq})(1-P_{rs})\delta_{pu}\delta_{rt}n_p\bar{n}_r\{a_q^\dagger a_s\} \tag{72}$$

$$\Big[\{a_p^\dagger a_q^\dagger a_s a_r\}\{a_t^\dagger a_u\}\Big]_{2b} = (1-P_{rs})\delta_{tr}\bar{n}_r\{a_p^\dagger a_q^\dagger a_s a_u\} + (1-P_{pq})\delta_{pu}n_p\{a_q^\dagger a_t^\dagger a_s a_r\} \tag{73}$$

$$\Big[\{a_p^\dagger a_q^\dagger a_s a_r\}\{a_t^\dagger a_u^\dagger a_w a_v\}\Big]_{0b} = (1-P_{rs})(1-P_{pq})\delta_{pv}\delta_{qw}\delta_{su}\delta_{rt}n_p n_q \bar{n}_s \bar{n}_r \tag{74}$$

$$\begin{aligned}\Big[\{a_p^\dagger a_q^\dagger a_s a_r\}\{a_t^\dagger a_u^\dagger a_w a_v\}\Big]_{1b} &= (1-P_{pq})(1-P_{rs})(1-P_{wv})\delta_{qw}\delta_{su}\delta_{rt}n_q\bar{n}_r\bar{n}_s\{a_p^\dagger a_v\} \\ &\quad -(1-P_{pq})(1-P_{rs})(1-P_{tu})\delta_{pv}\delta_{qw}\delta_{su}n_p n_q\bar{n}_s\{a_t^\dagger a_r\}\end{aligned} \tag{75}$$

$$\begin{aligned}\Big[\{a_p^\dagger a_q^\dagger a_s a_r\}\{a_t^\dagger a_u^\dagger a_w a_v\}\Big]_{2b} &= (1-P_{rs})\delta_{rt}\delta_{su}\bar{n}_r\bar{n}_s\{a_p^\dagger a_q^\dagger a_w a_v\} \\ &\quad +(1-P_{pq})\delta_{pv}\delta_{qw}n_p n_q\{a_t^\dagger a_u^\dagger a_s a_r\} \\ &\quad -(1-P_{pq})(1-P_{rs})(1-P_{tu})(1-P_{vw})\delta_{rt}\delta_{qw}n_q\bar{n}_q\{a_p^\dagger a_t^\dagger a_s a_v\}\,.\end{aligned} \tag{76}$$

With these expressions, we can perform step one for all terms up to and including two-body operators. We will do this for one example only. For simplicity, we denote the R-body product of an N and M body operator as Z($NM \to R$).

$$\begin{aligned}Z_{pq}^{\lambda}(11\to 1) &\sim \frac{1}{\hat{\lambda}_1\hat{\lambda}_2}\sum_{\{m\}}\sum_{rstu}A_{rs}^{\lambda_1}B_{tu}^{\lambda_2}C_{m_r\bar{m}_s\mu_1}^{jr\bar{j}s\lambda_1}C_{m_t\bar{m}_u\mu_2}^{jt\bar{j}u\lambda_2}C_{\mu_1\mu_2\mu}^{\lambda_1\lambda_2\lambda}C_{m_p\bar{m}_q\mu}^{jp\bar{j}q\lambda}\Big[\{a_r^\dagger a_s\}\{a_t^\dagger a_u\}\Big]_{1b} \\ &= \frac{1}{\hat{\lambda}_1\hat{\lambda}_2}\sum_{\{m\}}\sum_{rstu}A_{rs}^{\lambda_1}B_{tu}^{\lambda_2}C_{m_r\bar{m}_s\mu_1}^{jr\bar{j}s\lambda_1}C_{m_t\bar{m}_u\mu_2}^{jt\bar{j}u\lambda_2}C_{\mu_1\mu_2\mu}^{\lambda_1\lambda_2\lambda}C_{m_p\bar{m}_q\mu}^{jp\bar{j}q\lambda}\Big[\delta_{st}\bar{n}_s\{a_r^\dagger a_u\}-\delta_{ru}n_r\{a_t^\dagger a_s\}\Big]\,.\end{aligned} \tag{77}$$

$$\begin{aligned}Z_{pq}^{\lambda}(11\to 1) &= \frac{1}{\hat{\lambda}_1\hat{\lambda}_2}\sum_{\{m\}}\sum_{rs}A_{pr}^{\lambda_1}B_{sq}^{\lambda_2}C_{m_p\bar{m}_r\mu_1}^{jp\bar{j}r\lambda_1}C_{m_s\bar{m}_q\mu_2}^{js\bar{j}q\lambda_2}C_{\mu_1\mu_2\mu}^{\lambda_1\lambda_2\lambda}C_{m_p\bar{m}_q\mu}^{jp\bar{j}q\lambda}\bar{n}_r\delta_{rs} \\ &\quad -\frac{1}{\hat{\lambda}_1\hat{\lambda}_2}\sum_{\{m\}}\sum_{rs}B_{pr}^{\lambda_2}A_{sq}^{\lambda_1}C_{m_p\bar{m}_r\mu_2}^{jp\bar{j}r\lambda_2}C_{m_s\bar{m}_q\mu_1}^{js\bar{j}q\lambda_1}C_{\mu_1\mu_2\mu}^{\lambda_1\lambda_2\lambda}C_{m_p\bar{m}_q\mu}^{jp\bar{j}q\lambda}n_r\delta_{rs} \\ &= \frac{1}{\hat{\lambda}_1\hat{\lambda}_2}\sum_{r}A_{pr}^{\lambda_1}B_{rq}^{\lambda_2}\sum_{\{m\}}C_{m_p\bar{m}_r\mu_1}^{jp\bar{j}r\lambda_1}C_{m_r\bar{m}_q\mu_2}^{jr\bar{j}q\lambda_2}C_{\mu_1\mu_2\mu}^{\lambda_1\lambda_2\lambda}C_{m_p\bar{m}_q\mu}^{jp\bar{j}q\lambda}\bar{n}_r \\ &\quad -\frac{1}{\hat{\lambda}_1\hat{\lambda}_2}\sum_{r}B_{pr}^{\lambda_2}A_{rq}^{\lambda_1}\sum_{\{m\}}C_{m_p\bar{m}_r\mu_2}^{jp\bar{j}r\lambda_2}C_{m_r\bar{m}_q\mu_1}^{jr\bar{j}q\lambda_1}C_{\mu_1\mu_2\mu}^{\lambda_1\lambda_2\lambda}C_{m_p\bar{m}_q\mu}^{jp\bar{j}q\lambda}n_r\end{aligned} \tag{78}$$

From here, we may proceed with step two and sum out all of the m-dependence remaining in the expression. While we will explicitly demonstrate step two for each term in the multiplication, we will skip the demonstration of step one for all except $Z(11\to 1)$, and immediately jump to step

two.

A.5.2 Step two: angular momentum coupling

To verify the final expressions, we have derived them using both the angular-momentum relations of [183] and the Jucys diagrammatic formalism summarized in [182]. As the latter method is more transparent (after an admittedly steep learning curve has been surmounted), we will use this strategy here.

A.5.2.1 Zero-body terms

$$\begin{aligned} Z_0(11\to 0) &= \frac{1}{\hat{\lambda}_1\hat{\lambda}_2}\sum_{\{m\}} C^{\lambda_1\lambda_2\lambda}_{\mu_1\mu_2\mu}\sum_{pq} C^{j_p\bar{j}_q\lambda_1}_{m_p\bar{m}_q\mu_1} C^{j_q\bar{j}_p\lambda_2}_{m_q\bar{m}_p\mu_2} A^{\lambda_1}_{pq} B^{\lambda_2}_{qp} n_q\bar{n}_p \\ &= \frac{1}{\hat{\lambda}_1\hat{\lambda}_2}\sum_{\mu_1\mu_2\mu} C^{\lambda_1\lambda_2\lambda}_{\mu_1\mu_2\mu}\sum_{pq}\delta_{\lambda_1\lambda_2}\delta_{\mu_1-\mu_2} A^{\lambda_1}_{pq} B^{\lambda_2}_{qp}(-1)^{(j_p-j_q-\mu_1)} n_q\bar{n}_p \\ &= \frac{1}{\hat{\lambda}_1}\delta_{\lambda 0}\delta_{\lambda_1\lambda_2}\sum_{pq} A^{\lambda_1}_{pq} B^{\lambda_2}_{qp}(-1)^{(j_p-j_q+\lambda_1)} n_q\bar{n}_p \end{aligned} \tag{79}$$

Analogously,

$$Z_0(22\to 0) = \frac{1}{\hat{\lambda}_1}\delta_{\lambda 0}\delta_{\lambda_1\lambda_2}\sum_{\substack{pqrs\\ J_1J_2}} A^{(J_1J_2)\lambda_1}_{pqrs} B^{(J_2J_1)\lambda_2}_{rspq}(-1)^{(J_1-J_2+\lambda_1)} n_p n_q\bar{n}_r\bar{n}_s \tag{80}$$

A.5.2.2 One-body terms

$$\begin{aligned} Z^{\lambda}_{pq}(11\to 1) &= \frac{1}{\hat{j}_p\hat{\lambda}_1\hat{\lambda}_2} C^{j_q\lambda j_p}_{m_q\mu m_p} C^{\lambda_1\lambda_2\lambda}_{\mu_1\mu_2\mu} \\ &\times \sum_{r\{m\}}\left[\bar{n}_r C^{j_p\bar{j}_r\lambda_1}_{m_p\bar{m}_r\mu_1} C^{j_r\bar{j}_q\lambda_2}_{m_r\bar{m}_q\mu_2} A^{\lambda_1}_{pr} B^{\lambda_2}_{rq} - n_r C^{j_p\bar{j}_r\lambda_2}_{m_p\bar{m}_r\mu_2} C^{j_r\bar{j}_q\lambda_1}_{m_r\bar{m}_q\mu_1} B^{\lambda_2}_{pr} A^{\lambda_1}_{rq}\right]. \end{aligned} \tag{81}$$

We will look at only the first term, as the second follows analogously.

$$\frac{1}{\hat{j}_p\hat{\lambda}_1\hat{\lambda}_2}\sum_{\{m\}} C^{j_q\lambda\, j_p}_{m_q\mu m_p} C^{\lambda_1\lambda_2\lambda}_{\mu_1\mu_2\mu} C^{j_p\bar{j}_r\lambda_1}_{m_p\bar{m}_r\mu_1} C^{j_r\bar{j}_q\lambda_2}_{m_r\bar{m}_q\mu_2}$$

$$= \sum \hat{\lambda}$$

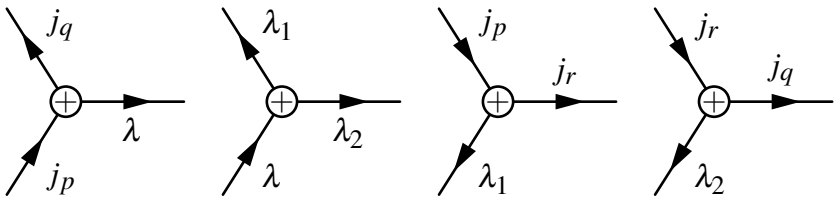

(82)

Figure A.8 Expression of the first term of eq. 81 with Jucys Diagrams.

Here we see that each external line can be contracted if we reverse time for the two leftmost diagrams and permute the indices of all but the first.

$$\frac{1}{\hat{j}_p\hat{\lambda}_1\hat{\lambda}_2}\sum_{\{m\}} C^{j_q\lambda\, j_p}_{m_q\mu m_p} C^{\lambda_1\lambda_2\lambda}_{\mu_1\mu_2\mu} C^{j_p\bar{j}_r\lambda_1}_{m_p\bar{m}_r\mu_1} C^{j_r\bar{j}_q\lambda_2}_{m_r\bar{m}_q\mu_2} = \hat{\lambda}$$

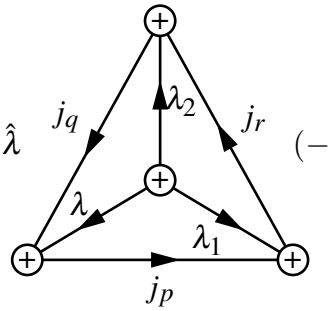

$$(-1)^{(j_p+j_q+\lambda)},$$

$$= \hat{\lambda} \begin{Bmatrix} \lambda_1 & \lambda_2 & \lambda \\ j_q & j_p & j_r \end{Bmatrix} (-1)^{(j_p+j_q+\lambda)}. \qquad (83)$$

Figure A.9 Contraction of all Jucys diagrams in eq. 82.

The second term is the same up to an index exchange and a phase. Hence,

$$Z^{\lambda}_{pq}(11 \to 1)$$

$$= \hat{\lambda}(-1)^{(j_p+j_q+\lambda)} \sum_{j_r} \left[\bar{n}_r \begin{Bmatrix} \lambda_1 & \lambda_2 & \lambda \\ j_q & j_p & j_r \end{Bmatrix} A^{\lambda_1}_{pr} B^{\lambda_2}_{rq} - n_r \begin{Bmatrix} \lambda_1 & \lambda_2 & \lambda \\ j_p & j_q & j_r \end{Bmatrix} (-1)^{(\lambda_1+\lambda_2+\lambda)} B^{\lambda_2}_{pr} A^{\lambda_1}_{rq} \right].$$

(84)

For the next term, we start from the Pandya two-body representation, which is more straightforward

for sums over particle and hole states,

$$
\begin{aligned}
&Z^{\lambda}_{pq}(21\to 1)\\
&=\frac{1}{\hat{j_p}\hat{\lambda}_1\hat{\lambda}_2}\sum_{\substack{rs\\ J_1J_2\{m\}}} C^{jq\lambda\, jp}_{mq\mu m_p}C^{\lambda_1\lambda_2\lambda}_{\mu_1\mu_2\mu}C^{jr\bar{j}_s\lambda_2}_{m_r\bar{m}_s\mu_2}C^{jp\bar{j}_qJ_1}_{m_p\bar{m}_qM_1}C^{jr\bar{j}_sJ_2}_{m_r\bar{m}_sM_2}C^{J_1\bar{J}_2\lambda_1}_{M_1\bar{M}_2\mu_1}\bar{A}^{(J_1J_2)\lambda_1}_{p\bar{q}r\bar{s}}B^{\lambda_2}_{rs}n_s\bar{n}_r\,,\\
&=\frac{1}{\hat{j_p}\hat{\lambda}_1\hat{\lambda}_2}\sum_{rs\{m\}J_1} C^{jq\lambda\, jp}_{mq\mu m_p}C^{\lambda_1\lambda_2\lambda}_{\mu_1\mu_2\mu}C^{jp\bar{j}_qJ_1}_{m_p\bar{m}_qM_1}C^{J_1\bar{\lambda}_2\lambda_1}_{M_1\bar{\mu}_2\mu_1}\bar{A}^{(J_1\lambda_2)\lambda_1}_{p\bar{q}r\bar{s}}B^{\lambda_2}_{rs}n_s\bar{n}_r\,,\\
&=\frac{1}{\hat{j_p}\hat{\lambda}\hat{\lambda}_2}\sum_{rs\{m\}} C^{jq\lambda\, jp}_{mq\mu m_p}C^{jp\bar{j}_q\lambda}_{m_p\bar{m}_q\mu}\bar{A}^{(\lambda\lambda_2)\lambda_1}_{p\bar{q}r\bar{s}}B^{\lambda_2}_{rs}n_s\bar{n}_r(-1)^{(\lambda_1+\lambda_2+\lambda)}\,,\\
&=\frac{1}{\hat{\lambda}^2\hat{\lambda}_2}\sum_{rs\mu}\bar{A}^{(\lambda\lambda_2)\lambda_1}_{p\bar{q}r\bar{s}}B^{\lambda_2}_{rs}n_s\bar{n}_r(-1)^{(\lambda_1+\lambda_2+\lambda)}\,,\\
&=\frac{1}{\hat{\lambda}_2}\sum_{rs}\bar{A}^{(\lambda\lambda_2)\lambda_1}_{p\bar{q}r\bar{s}}B^{\lambda_2}_{rs}n_s\bar{n}_r(-1)^{(\lambda_1+\lambda_2+\lambda)}\,.
\end{aligned}
\tag{85}
$$

Likewise,

$$
Z^{\lambda}_{pq}(12\to 1)=\frac{1}{\hat{\lambda}_1}\sum_{rs}A^{\lambda_1}_{rs}\bar{B}^{(\lambda_1\lambda)\lambda_2}_{r\bar{s}p\bar{q}}n_r\bar{n}_s\,.
\tag{86}
$$

The final contribution to Z_{pq} is from two two-body operators,

$$
\begin{aligned}
&Z^{\lambda}_{pq}(22\to 1)=\frac{1}{2}\frac{1}{\hat{j_p}\hat{\lambda}_1\hat{\lambda}_2}\sum_{\substack{rst\{m\}\\ J_1J_2J_3}}\\
&\Big[n_r\bar{n}_s\bar{n}_t\tilde{A}^{(J_1J_2)\lambda_1}_{prst}\tilde{B}^{(J_2J_3)\lambda_2}_{stqr}C^{jq\lambda\, jp}_{mq\mu m_p}C^{\lambda_1\lambda_2\lambda}_{\mu_1\mu_2\mu}C^{jp\, jr J_1}_{m_p m_r M_1}C^{J_1\bar{J}_2\lambda_1}_{M_1\bar{M}_2\mu_1}C^{jq\, jr J_3}_{m_q m_r M_3}C^{J_2\bar{J}_3\lambda_2}_{M_2\bar{M}_3\mu_2}\\
&-\bar{n}_r n_s n_t\tilde{B}^{(J_1J_2)\lambda_2}_{prst}\tilde{A}^{(J_2J_3)\lambda_1}_{stqr}C^{jq\lambda\, jp}_{mq\mu m_p}C^{\lambda_1\lambda_2\lambda}_{\mu_1\mu_2\mu}C^{jp\, jr J_1}_{m_p m_r M_1}C^{J_1\bar{J}_2\lambda_2}_{M_1\bar{M}_2\mu_2}C^{jq\, jr J_3}_{m_q m_r M_3}C^{J_2\bar{J}_3\lambda_1}_{M_2\bar{M}_3\mu_1}\Big]
\end{aligned}
\tag{87}
$$

The angular momentum coupling is achieved using Jucys diagrams,

$$
\frac{1}{\hat{j_p}\hat{\lambda}_1\hat{\lambda}_2}\sum_{\{m\}}C^{jq\lambda\, jp}_{mq\mu m_p}C^{\lambda_1\lambda_2\lambda}_{\mu_1\mu_2\mu}C^{jp\, jr J_1}_{m_p m_r M_1}C^{J_1\bar{J}_2\lambda_1}_{M_1\bar{M}_2\mu_1}C^{jq\, jr J_3}_{m_q m_r M_3}C^{J_2\bar{J}_3\lambda_2}_{M_2\bar{M}_3\mu_2}
$$

$$
=\hat{\lambda}\hat{J}_1\hat{J}_2\sum_{\{m\}}
$$

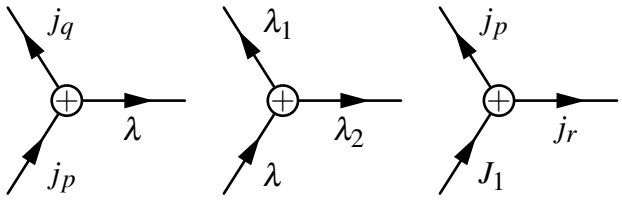

Figure A.10 Derivation of $Z^{\lambda}_{pq}(22\to 1)$ with Jucys diagrams.

Figure A.10 (cont'd)

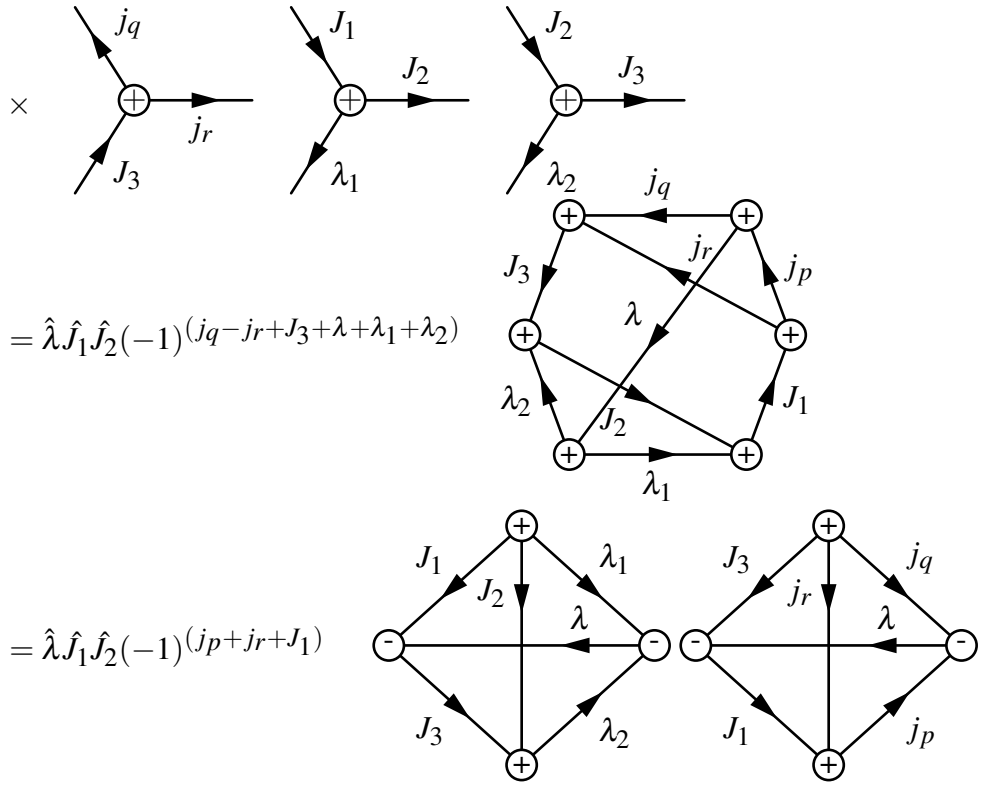

$$= \hat{\lambda}\hat{J}_1\hat{J}_2(-1)^{(j_q-j_r+J_3+\lambda+\lambda_1+\lambda_2)}$$

$$= \hat{\lambda}\hat{J}_1\hat{J}_2(-1)^{(j_p+j_r+J_1)}$$

$$= \hat{\lambda}\hat{J}_1\hat{J}_2(-1)^{(j_p+j_r+J_1)} \begin{Bmatrix} J_1 & J_2 & \lambda_1 \\ \lambda_2 & \lambda & J_3 \end{Bmatrix} \begin{Bmatrix} J_3 & j_r & j_q \\ j_p & \lambda & J_1 \end{Bmatrix}. \tag{88}$$

Applying this expression to eq. 87, we arrive at

$$Z^{\lambda}_{pq}(22 \to 1) = \frac{1}{2}\hat{\lambda} \sum_{\substack{rst \\ J_1J_2J_3}} \hat{J}_1\hat{J}_2 \begin{Bmatrix} j_p & j_q & \lambda \\ J_3 & J_1 & j_r \end{Bmatrix} \Bigg[\bar{n}_r n_s n_t \tilde{B}^{(J_1J_2)\lambda_2}_{rpst} \tilde{A}^{(J_2J_3)\lambda_1}_{stqr} \begin{Bmatrix} \lambda_1 & \lambda_2 & \lambda \\ J_1 & J_3 & J_2 \end{Bmatrix}$$
$$- n_r \bar{n}_s \bar{n}_t \tilde{A}^{(J_1J_2)\lambda_1}_{rpst} \tilde{B}^{(J_2J_3)\lambda_2}_{stqr} \begin{Bmatrix} \lambda_1 & \lambda_2 & \lambda \\ J_3 & J_1 & J_2 \end{Bmatrix} \Bigg] \tag{89}$$

A.5.2.3 Two-body terms

For two-body operators, we start with the disconnected term,

$$
\begin{aligned}
Z^{(J_1J_2)\lambda}_{pqrs}(11\to 2) &= \frac{1}{\hat{\lambda}\hat{\lambda}_1\hat{\lambda}_2}(1-P_{pq}(J_1))(1-P_{rs}(J_2))A^{\lambda_1}_{pr}B^{\lambda_2}_{qs} \\
&\times \sum_{\{m\}} C^{j_p j_q J_1}_{m_p m_q M_1} C^{j_r j_s J_2}_{m_r m_s M_2} C^{J_1 \bar{J}_2 \lambda}_{M_1 \bar{M}_2 \mu} C^{\lambda_1 \lambda_2 \lambda}_{\mu_1 \mu_2 \mu} C^{j_p \bar{j}_r \lambda_1}_{m_p \bar{m}_r \mu_1} C^{j_q \bar{j}_s \lambda_2}_{m_q \bar{m}_s \mu_2} \\
&= (1-P_{pq}(J_1))(1-P_{rs}(J_2))A^{\lambda_1}_{pr}B^{\lambda_2}_{qs}
\end{aligned}
$$

$$
\times \sum_{\{m\}} \hat{\lambda}\hat{J}_1\hat{J}_2
$$

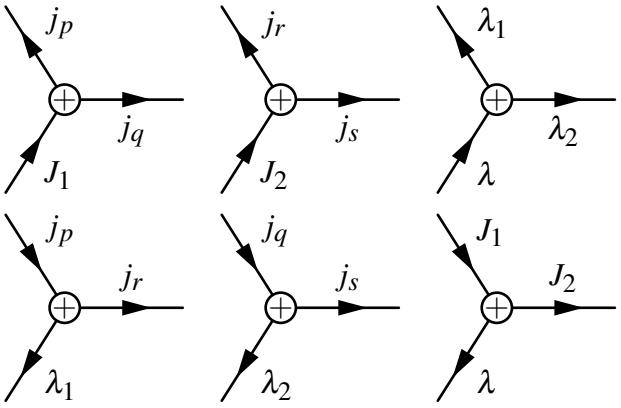

(90)

$$
= (1-P_{pq}(J_1))(1-P_{rs}(J_2))A^{\lambda_1}_{pr}B^{\lambda_2}_{qs} \sum_{\{m\}} \hat{\lambda}\hat{J}_1\hat{J}_2
$$

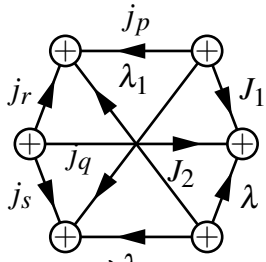

$$
= (1-P_{pq}(J_1))(1-P_{rs}(J_2))A^{\lambda_1}_{pr}B^{\lambda_2}_{qs}\hat{\lambda}\hat{J}_1\hat{J}_2 \begin{Bmatrix} j_p & j_r & \lambda_1 \\ j_q & j_s & \lambda_2 \\ J_1 & J_2 & \lambda \end{Bmatrix}. \tag{91}
$$

Figure A.11 Derivation of $Z^{(J_1J_2)\lambda}_{pqrs}(11\to 2)$ using Jucys diagrams.

Next, we couple the $(21\to 2)$ and $(12\to 2)$ multiplications. There are four unique terms here, which we will express in m-scheme first for clarity.

$$
Z_{pqrs}(21\to 2) = \sum_{tm_t}\Big[(1-P_{rs})A_{pqts}B_{tr}\bar{n}_t - (1-P_{pq})B_{pt}A_{tqrs}n_t\Big] \tag{92}
$$

$$
Z_{pqrs}(12\to 2) = \sum_{tm_t}\Big[(1-P_{pq})A_{pt}B_{tqrs}\bar{n}_t - (1-P_{rs})B_{pqts}A_{tr}n_t\Big] \tag{93}
$$

Now we will express the first term of eq. 92 in J-scheme,

$$Z_{pqrs}^{(J_1J_2)\lambda}(21\to 2a)=\frac{1}{\hat{\lambda}\hat{\lambda}_1\hat{\lambda}_2}\sum_{tJ_3}(1-P_{rs}(J_2))A_{pqts}^{(J_1J_3)\lambda_1}B_{tr}^{\lambda_2}$$
$$\times\sum_{\{m\}}C_{M_1\bar{M}_2\mu}^{J_1\bar{J}_2\lambda}C_{m_rm_sM_2}^{j_rj_sJ_2}C_{\mu_1\mu_2\mu}^{\lambda_1\lambda_2\lambda}C_{m_tm_sM_1}^{j_tj_sJ_3}C_{M_1\bar{M}_3\mu_1}^{J_1\bar{J}_3\lambda_1}C_{m_t\bar{m}_r\mu_2}^{j_t\bar{j}_r\lambda_2} \tag{94}$$

where

$$\frac{1}{\hat{\lambda}\hat{\lambda}_1\hat{\lambda}_2}\sum_{\{m\}}C_{M_1\bar{M}_2\mu}^{J_1\bar{J}_2\lambda}C_{m_rm_sM_2}^{j_rj_sJ_2}C_{\mu_1\mu_2\mu}^{\lambda_1\lambda_2\lambda}C_{m_tm_sM_1}^{j_tj_sJ_3}C_{M_1\bar{M}_3\mu_1}^{J_1\bar{J}_3\lambda_1}C_{m_t\bar{m}_r\mu_2}^{j_t\bar{j}_r\lambda_2}$$

$=\sum_{\{m\}}\hat{\lambda}\hat{J}_2\hat{J}_3$ 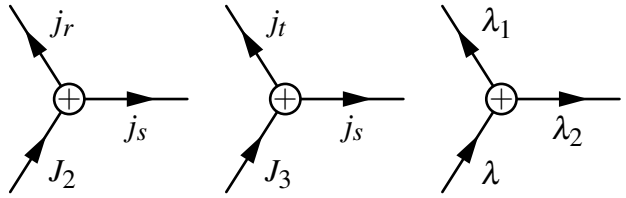

$\times$ 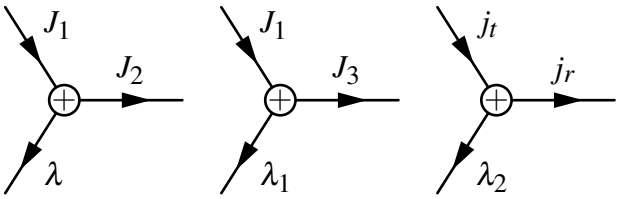

$=\hat{\lambda}\hat{J}_2\hat{J}_3(-1)^{(J_2+J_3+j_t-j_r)}$ 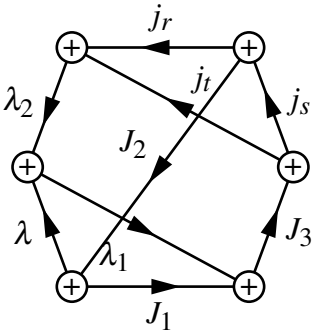

$=\hat{\lambda}\hat{J}_2\hat{J}_3(-1)^{(j_t+j_s+J_1+\lambda_2+\lambda)}$ 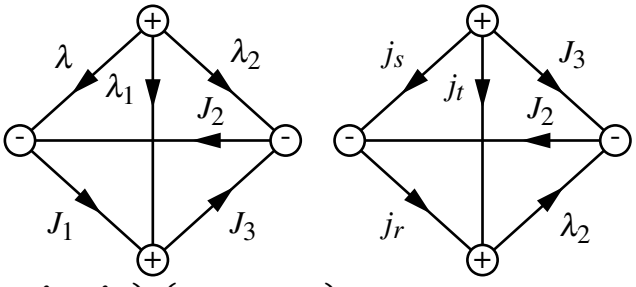

$$=\hat{\lambda}\hat{J}_2\hat{J}_3(-1)^{(j_t+j_s+J_1+\lambda_2+\lambda)}\begin{Bmatrix}\lambda & \lambda_1 & \lambda_2\\ J_3 & J_2 & J_1\end{Bmatrix}\begin{Bmatrix}j_s & j_t & J_3\\ \lambda_2 & J_2 & j_r\end{Bmatrix}. \tag{95}$$

Figure A.12 Derivation of $Z_{pqrs}^{(J_1J_2)\lambda}(21\to 1)$ using Jucys diagrams.

From this, and analagous derivations, we arrive at

$$
\begin{aligned}
&Z^{(J_1J_2)\lambda}_{pqrs}(12\to 2)\\
&\quad=(1-P_{pq}(J_1))\hat{\lambda}\hat{J}_1\sum_t\sum_{J_3}\hat{J}_3(-1)^{(jp+jq+J_1+J_2+J_3+\lambda_1+\lambda)}\\
&\qquad\qquad\times\begin{Bmatrix} j_p & j_q & J_1\\ J_3 & \lambda_1 & j_a\end{Bmatrix}\begin{Bmatrix}\lambda_1 & \lambda_2 & \lambda\\ J_2 & J_1 & J_3\end{Bmatrix}A^{\lambda_1}_{pt}\tilde{B}^{(J_3J_2)\lambda_2}_{tqrs}\bar{n}_t\\
&+(1-P_{rs}(J_2))\hat{\lambda}\hat{J}_2\sum_t\sum_{J_3}\hat{J}_3(-1)^{(J_1+J_3+\lambda_2)}\begin{Bmatrix} j_r & j_s & J_2\\ J_3 & \lambda_1 & j_i\end{Bmatrix}\begin{Bmatrix}\lambda_1 & \lambda_2 & \lambda\\ J_1 & J_2 & J_3\end{Bmatrix}A^{\lambda_1}_{tr}\tilde{B}^{(J_1J_3)\lambda_2}_{pqst}n_t \quad (96)
\end{aligned}
$$

and

$$
\begin{aligned}
&Z^{(J_1J_2)\lambda}_{pqrs}(21\to 2)\\
&=-(1-P_{rs}(J_2))\hat{\lambda}\hat{J}_2\sum_t\sum_{J_3}\hat{J}_3(-1)^{(J_1+J_3+\lambda_2+\lambda)}\begin{Bmatrix} j_r & j_s & J_2\\ J_3 & \lambda_2 & j_a\end{Bmatrix}\begin{Bmatrix}\lambda_1 & \lambda_2 & \lambda\\ J_2 & J_1 & J_3\end{Bmatrix}B^{\lambda_2}_{tr}\tilde{A}^{(J_1J_3)\lambda_1}_{pqst}\bar{n}_t\\
&\quad-(1-P_{pq}(J_1))\hat{\lambda}\hat{J}_1\sum_t\sum_{J_3}\hat{J}_3(-1)^{(jp+jq+J_1+J_2+J_3+\lambda_1)}\\
&\qquad\qquad\times\begin{Bmatrix} j_p & j_q & J_1\\ J_3 & \lambda_2 & j_i\end{Bmatrix}\begin{Bmatrix}\lambda_1 & \lambda_2 & \lambda\\ J_1 & J_2 & J_3\end{Bmatrix}B^{\lambda_2}_{pt}\tilde{A}^{(J_3J_2)\lambda_2}_{tqrs}n_t\,. \quad (97)
\end{aligned}
$$

The $(22\to 2)$ term has three unique types of contractions. As demonstrated in eq. 76, we have pp and hh ladder diagrams, and the ph chain diagrams. We will start with the ladder diagrams, which are quite simple compared with the chain.

$$
\begin{aligned}
Z^{(J_1J_2)\lambda}_{pqrs}(22\to 2(pp,hh)) &= \frac{1}{2\hat{\lambda}\hat{\lambda}_1\hat{\lambda}_2}\sum_{tuJ_3}\tilde{A}^{(J_1J_3)\lambda_1}_{pqtu}\tilde{B}^{(J_3J_2)\lambda_2}_{turs}\bar{n}_t\bar{n}_u\\
&\qquad\times\sum_{\{m\}}C^{J_1\bar{J}_2\lambda}_{M_1\bar{M}_2\mu}C^{\lambda_1\lambda_2\lambda}_{\mu_1\mu_2\mu}C^{J_1\bar{J}_3\lambda_1}_{M_1\bar{M}_3\mu_1}C^{J_3\bar{J}_2\lambda_2}_{M_3\bar{M}_2\mu_2}\\
&+\frac{1}{2\hat{\lambda}\hat{\lambda}_1\hat{\lambda}_2}\sum_{tuJ_3}\tilde{B}^{(J_1J_3)\lambda_2}_{pqtu}\tilde{A}^{(J_3J_2)\lambda_1}_{turs}n_tn_u\\
&\qquad\times\sum_{\{m\}}C^{J_1\bar{J}_2\lambda}_{M_1\bar{M}_2\mu}C^{\lambda_1\lambda_2\lambda}_{\mu_1\mu_2\mu}C^{J_1\bar{J}_3\lambda_2}_{M_1\bar{M}_3\mu_2}C^{J_3\bar{J}_2\lambda_1}_{M_3\bar{M}_2\mu_1} \quad (98)
\end{aligned}
$$

where

$$\frac{1}{\hat{\lambda}\hat{\lambda}_1\hat{\lambda}_2}\sum_{\{m\}} C^{J_1\bar{J}_2\lambda}_{M_1\bar{M}_2\mu} C^{\lambda_1\lambda_2\lambda}_{\mu_1\mu_2\mu} C^{J_1\bar{J}_3\lambda_1}_{M_1\bar{M}_3\mu_1} C^{J_3\bar{J}_2\lambda_2}_{M_3\bar{M}_2\mu_2}$$

$$= \sum_{\{m\}} \hat{\lambda}$$

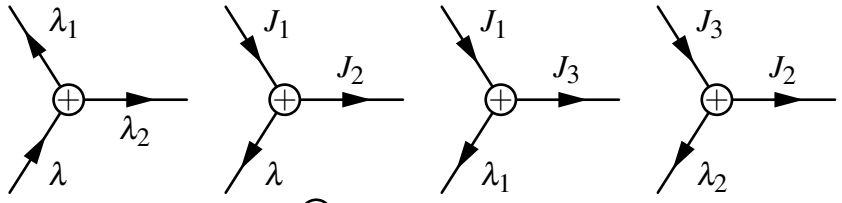

$$= \hat{\lambda}(-1)^{(J_1+J_2+\lambda)}$$

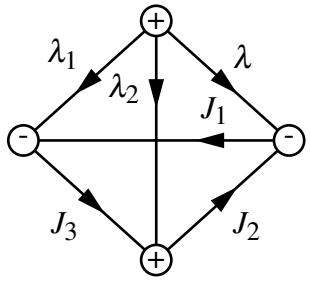

$$= \hat{\lambda}(-1)^{(J_1+J_2+\lambda)} \begin{Bmatrix} \lambda_1 & \lambda_2 & \lambda \\ J_2 & J_1 & J_3 \end{Bmatrix}, \tag{99}$$

Figure A.13 Derivation of $Z^{(J_1J_2)\lambda}_{pqrs}(22 \to 2(pp,hh))$ using Jucys diagrams.

hence,

$$\begin{aligned} &Z^{(J_1J_2)\lambda}_{pqrs}(22 \to 2(pp,hh) \\ &\quad = \frac{1}{2}\hat{\lambda}\sum_{tuJ_3}(-1)^{(J_1+J_2+\lambda)} \begin{Bmatrix} \lambda_1 & \lambda_2 & \lambda \\ J_2 & J_1 & J_3 \end{Bmatrix} \tilde{A}^{(J_1J_3)\lambda_1}_{pqtu} \tilde{B}^{(J_3J_2)\lambda_2}_{turs} \bar{n}_t \bar{n}_u \\ &\quad + \frac{1}{2}\hat{\lambda}\sum_{tuJ_3}(-1)^{(J_1+J_2+\lambda_1+\lambda_2)} \begin{Bmatrix} \lambda_1 & \lambda_2 & \lambda \\ J_1 & J_2 & J_3 \end{Bmatrix} \tilde{B}^{(J_1J_3)\lambda_2}_{pqtu} \tilde{A}^{(J_3J_2)\lambda_1}_{turs} n_t n_u \end{aligned} \tag{100}$$

For the final term, the *ph* chain, we use Pandya-transformed matrix elements,

$$\begin{aligned} \tilde{Z}^{(J_1J_2)\lambda}_{pqrs}(22 \to 2(ph)) =& \frac{1}{\hat{\lambda}\hat{\lambda}_1\hat{\lambda}_2}(1+P_{pq}(J_1))(1+P_{pq}(J_2)) \\ &\times \sum_{\substack{tu \\ J_3J_4J_5}} \hat{J}_1\hat{J}_2\hat{J}_3\hat{J}_4(-1)^{(jq+j_s+J_2+J_4)} \begin{Bmatrix} j_p & j_s & J_3 \\ j_q & j_r & J_4 \\ J_1 & J_2 & \lambda \end{Bmatrix} \bar{A}^{(J_3J_5)\lambda_1}_{p\bar{s}t\bar{u}} \bar{B}^{(J_5J_4)\lambda_2}_{t\bar{u}r\bar{q}} \bar{n}_t n_u \end{aligned}$$

$$\times \sum_{\{m\}} C^{J_3 \bar{J}_4 \lambda}_{M_3 \bar{M}_4 \mu} C^{\lambda_1 \lambda_2 \lambda}_{\mu_1 \mu_2 \mu} C^{J_3 \bar{J}_5 \lambda_1}_{M_3 \bar{M}_5 \mu_1} C^{J_5 \bar{J}_4 \lambda_2}_{M_5 \bar{M}_4 \mu_2} \tag{101}$$

Here we have applied the inverse pandya transform and anti-symmetrization operators to construct $Z^{(J_1 J_2)\lambda}_{pqrs}$. The angular momentum coupling is exactly the same as in the last case,

$$\tilde{Z}^{(J_1 J_2)\lambda}_{pqrs}(22 \to 2(ph)) = -\hat{\lambda}(1+P_{pq}(J_1))(1+P_{pq}(J_2))$$
$$\times \sum_{\substack{tu \\ J_3 J_4 J_5}} \hat{J}_1 \hat{J}_2 \hat{J}_3 \hat{J}_4 (-1)^{(j_q + j_s + J_2 + J_3 + \lambda)} \begin{Bmatrix} j_p & j_s & J_3 \\ j_q & j_r & J_4 \\ J_1 & J_2 & \lambda \end{Bmatrix} \begin{Bmatrix} \lambda_1 & \lambda_2 & \lambda \\ J_4 & J_3 & J_5 \end{Bmatrix} \bar{A}^{(J_3 J_5)\lambda_1}_{p\bar{s}t\bar{u}} \bar{B}^{(J_5 J_4)\lambda_2}_{t\bar{u}r\bar{q}} \bar{n}_t n_u \tag{102}$$

A.6 Compilation of the full tensor product

Here we compile the results of the previous section for use in the construction of transition matrix elements in the EOM-IMSRG(2,2). For nuclear physics applications, EOM-IMSRG(2,2) ladder operators are linear combinations of one- and two-body excitation operators coupled to desired spin J^Π

$$X^\dagger_\nu(J^\Pi M) = \sum_{pq} X^J_{pq}(\nu) \frac{[a^\dagger_p \tilde{a}_q]^J_M}{\sqrt{2J+1}} \bar{n}_p n_q + \frac{1}{4} \sum_{pqrs} \sum_{J_1 J_2} \tilde{X}^{(J_1 J_2)J}_{pqrs}(\nu) \frac{[[a^\dagger_p a^\dagger_q]^{J_1} [\tilde{a}_r \tilde{a}_s]^{J_2}]^J_M}{\sqrt{2J+1}}. \tag{103}$$

We suppress parity and isospin quantum numbers, as their selection rules do not affect the J-scheme expressions. However, ladder operators $X^\dagger$ do have definite parity and charge exchange characteristic, so commensurate selection rules apply. Note that we break from the convention that $a, b, c, \ldots$ denote particle states here. We will instead use $p, q, r, \ldots$ for non-contracted indices (external lines), and $a, b, c, \ldots$ for contracted or summed indices.

A.6.1 Transitions to the ground state

For transitions to the ground state, we compute

$$M_{0\nu} = \langle \Phi_0 || \bar{O}^\lambda || \bar{\Psi}_\nu \rangle = [\bar{O}^\lambda \bar{X}^\dagger_\nu(J_\nu)]^0. \tag{104}$$

Adding eqs. 79 and 80, we arrive at:

$$[A^{\lambda_1}B^{\lambda_2}]^0 = \frac{1}{\hat{\lambda}_2}\delta_{\lambda_1\lambda_2}\sum_{ab}A^{\lambda_1}_{ba}B^{\lambda_2}_{ab}(-1)^{(j_a-j_b+\lambda)}\bar{n}_a n_b + \frac{1}{\hat{\lambda}_2}\delta_{\lambda_1\lambda_2}\sum_{\substack{abcd\\J_1J_2}}A^{(J_1J_2)\lambda}_{cdab}B^{(J_2J_1)\lambda_2}_{abcd}(-1)^{(J_1-J_2+\lambda)}\bar{n}_a\bar{n}_b n_c n_d\,. \tag{105}$$

A.6.2 Transitions between excited states and moments

For transitions between states constructed via a ladder operator acting on the reference, or moments involving these states, we must compute the full tensor-product

$$Z^J_M \equiv [\bar{O}^{\lambda}\bar{X}^{\dagger}_{\nu}(J_\nu)]^J_M\,, \tag{106}$$

and then the zero-body product

$$M_{\mu\nu} = [X(J_\mu)Z^J]^0\,. \tag{107}$$

Here, we combine eqs. 84 through 89 to reveal

$$\begin{aligned}
Z^{\lambda}_{pq} = \hat{\lambda}(-1)^{(j_p+j_q)}\sum_a\Bigg[&A^{\lambda_1}_{pa}B^{\lambda_2}_{a\bar{q}}(-1)^{\lambda}\begin{Bmatrix}\lambda_1 & \lambda_2 & \lambda\\ j_q & j_p & j_a\end{Bmatrix}\bar{n}_a\\
&-B^{\lambda_2}_{p\bar{a}}A^{\lambda_1}_{aq}(-1)^{(\lambda_1+\lambda_2)}\begin{Bmatrix}\lambda_1 & \lambda_2 & \lambda\\ j_p & j_q & j_a\end{Bmatrix}n_a\Bigg]\\
+\sum_{ab}(&\frac{1}{\hat{\lambda_1}}A^{\lambda_1}_{ba}\bar{B}^{(\lambda\lambda_1)\lambda_2}_{p\bar{q}b\bar{a}} + \frac{(-1)^{(\lambda_1+\lambda_2+\lambda)}}{\hat{\lambda_2}}\bar{A}^{(\lambda\lambda_2)\lambda_1}_{p\bar{q}a\bar{b}}B^{\lambda_2}_{ab})n_b\bar{n}_a\\
-\frac{1}{2}\sum_{abc}\sum_{J_1J_2J_3}&\hat{\lambda}\hat{J}_1\hat{J}_3\begin{Bmatrix}j_p & j_q & \lambda\\ J_3 & J_1 & j_c\end{Bmatrix}\Bigg[\begin{Bmatrix}\lambda_1 & \lambda_2 & \lambda\\ J_3 & J_1 & J_2\end{Bmatrix}\tilde{A}^{(J_1J_2)\lambda_1}_{cpab}\tilde{B}^{(J_2J_3)\lambda_2}_{abqc}\bar{n}_a\bar{n}_b n_c\\
&-(-1)^{(\lambda_1+\lambda_2+\lambda)}\begin{Bmatrix}\lambda_2 & \lambda_1 & \lambda\\ J_3 & J_1 & J_2\end{Bmatrix}\tilde{B}^{(J_1J_2)\lambda_2}_{cpab}\tilde{A}^{(J_2J_3)\lambda_1}_{abqc}n_a n_b\bar{n}_c\Bigg]
\end{aligned} \tag{108}$$

and eqs. 91 through 102 to arrive at

$$\tilde{Z}^{(J_1J_2)\lambda}_{pqrs} = (1-P_{pq}(J_1))(1-P_{rs}(J_2))A^{\lambda_1}_{pr}B^{\lambda_2}_{qs}\hat{\lambda}\hat{J}_1\hat{J}_2 \begin{Bmatrix} j_p & j_r & \lambda_1 \\ j_q & j_s & \lambda_2 \\ J_1 & J_2 & \lambda \end{Bmatrix}$$

$$+(1-P_{pq}(J_1))\hat{\lambda}\hat{J}_1\sum_a\sum_{J_3}\hat{J}_3(-1)^{(j_p+j_q+J_1+J_2+J_3+\lambda_1+\lambda)} \begin{Bmatrix} j_p & j_q & J_1 \\ J_3 & \lambda_1 & j_a \end{Bmatrix} \begin{Bmatrix} \lambda_1 & \lambda_2 & \lambda \\ J_2 & J_1 & J_3 \end{Bmatrix} A^{\lambda_1}_{pa}\tilde{B}^{(J_3J_2)\lambda_2}_{aqrs}\bar{n}_a$$

$$+(1-P_{rs}(J_2))\hat{\lambda}\hat{J}_2\sum_a\sum_{J_3}\hat{J}_3(-1)^{(J_1+J_3+\lambda_2)} \begin{Bmatrix} j_r & j_s & J_2 \\ J_3 & \lambda_1 & j_a \end{Bmatrix} \begin{Bmatrix} \lambda_1 & \lambda_2 & \lambda \\ J_1 & J_2 & J_3 \end{Bmatrix} A^{\lambda_1}_{ar}\tilde{B}^{(J_1J_3)\lambda_2}_{pqsa}n_a$$

$$-(1-P_{rs}(J_2))\hat{\lambda}\hat{J}_2\sum_a\sum_{J_3}\hat{J}_3(-1)^{(J_1+J_3+\lambda_2+\lambda)} \begin{Bmatrix} j_r & j_s & J_2 \\ J_3 & \lambda_2 & j_a \end{Bmatrix} \begin{Bmatrix} \lambda_1 & \lambda_2 & \lambda \\ J_2 & J_1 & J_3 \end{Bmatrix} B^{\lambda_2}_{ar}\tilde{A}^{(J_1J_3)\lambda_1}_{pqsa}\bar{n}_a$$

$$-(1-P_{pq}(J_1))\hat{\lambda}\hat{J}_1\sum_a\sum_{J_3}\hat{J}_3(-1)^{(j_p+j_q+J_1+J_2+J_3+\lambda_1)} \begin{Bmatrix} j_p & j_q & J_1 \\ J_3 & \lambda_2 & j_a \end{Bmatrix} \begin{Bmatrix} \lambda_1 & \lambda_2 & \lambda \\ J_1 & J_2 & J_3 \end{Bmatrix} B^{\lambda_2}_{pa}\tilde{A}^{(J_3J_2)\lambda_2}_{aqrs}n_a$$

$$+\frac{1}{2}\hat{\lambda}\sum_{ab}\sum_{J_3}(-1)^{(J_1+J_2+\lambda)} \begin{Bmatrix} \lambda_1 & \lambda_2 & \lambda \\ J_2 & J_1 & J_3 \end{Bmatrix} \tilde{A}^{(J_1J_3)\lambda_1}_{pqab}\tilde{B}^{(J_3J_2)\lambda_2}_{abrs}\bar{n}_a\bar{n}_b$$

$$+\frac{1}{2}\hat{\lambda}\sum_{ab}\sum_{J_3}(-1)^{(J_1+J_2+\lambda_1+\lambda_2)} \begin{Bmatrix} \lambda_1 & \lambda_2 & \lambda \\ J_1 & J_2 & J_3 \end{Bmatrix} \tilde{B}^{(J_1J_3)\lambda_2}_{pqab}\tilde{A}^{(J_3J_2)\lambda_1}_{abrs}n_an_b$$

$$+(1-P_{pq}(J_1))(1-P_{rs}(J_2))\hat{\lambda}\hat{J}_1\hat{J}_2\sum_{J_3J_4J_5}\hat{J}_3\hat{J}_5(-1)^{(j_s-j_q+J_3+\lambda)}$$

$$\times \begin{Bmatrix} j_p & j_r & J_3 \\ j_q & j_s & J_5 \\ J_1 & J_2 & \lambda \end{Bmatrix} \begin{Bmatrix} \lambda_1 & \lambda_2 & \lambda \\ J_5 & J_3 & J_4 \end{Bmatrix} \sum_{ab} \bar{A}^{(J_3 J_4)\lambda_1}_{p\bar{r}a\bar{b}} \bar{B}^{(J_4 J_5)\lambda_2}_{a\bar{b}s\bar{q}} \bar{n}_a n_b \tag{109}$$

A.7 Tensor-scalar Commutators

The most frequently used result of the derivation of Sec. A.5 are the commutator expressions for a scalar operator (expressed in non-reduced matrix elements) and an arbitrary rank spherical tensor operator (expressed in reduced matrix elements). There are two uses for these expressions.

One use is the solution of the EOM-IMSRG(2,2) equations. Analogous to the m-scheme case, ladder the amplitudes $X^J_{ai}(\nu)$ and $\tilde{X}^{(J_{ab}J_{ij})J}_{abij}(\nu)$, as well as excitation energies, are obtained through application of the Lanczos algorithm to solve the eigenvalue problem in eq. 4.13. The commutator expression $[H, X^\dagger_\nu]$ requires the commutator of a scalar operator H, and the ladder operator, which is a spherical tensor.

A more general application is to compute effective operators in the IMSRG. For all IMSRG calculations, observables must be consistently evolved using eq. 3.8 in the flow-equation approach or eq. 3.39 in the Magnus formalism. If the operator is of tensor character, tensor-scalar commutators are required. Thus we must compute

$$Z^\lambda_\mu \equiv AB^\lambda_\mu - A^\lambda_\mu B\,, \tag{110}$$

which can be derived as a limiting case of the general tensor-product in eqs. 105 through A.6.2, A corresponds to the scalar operator, where $\lambda_1 \to 0$ and the Wigner-Eckart theorem has been used to revert to non-reduced matrix elements. B is a tensor operator of rank $\lambda_2 = \lambda$. The resultant

operator Z is also of rank λ.

$$
\begin{aligned}
Z^{\lambda}_{pq} = &\sum_a \Big(A_{pa}B^{\lambda}_{aq} - B^{\lambda}_{pa}A_{aq}\Big) - \sum_{ab}(n_a - n_b)\left(\bar{A}^{\lambda}_{p\bar{q}a\bar{b}}B^{\lambda}_{ab} - \hat{j}_a\bar{B}^{(\lambda 0)\lambda}_{p\bar{q}a\bar{b}}A_{ab}\right) \\
&+\frac{1}{2}\sum_{\substack{abc \\ J_1J_2}}(n_an_b\bar{n}_c + \bar{n}_a\bar{n}_bn_c)\hat{J}_1\hat{J}_2(-1)^{j_p+j_c+J_1+\lambda} \\
&\qquad\times\begin{Bmatrix} J_1 & J_2 & \lambda \\ j_q & j_p & j_c \end{Bmatrix}\Big(\tilde{A}^{J_1}_{cpab}\tilde{B}^{(J_1J_2)\lambda}_{abcq} - \tilde{B}^{(J_1J_2)\lambda}_{cpab}\tilde{A}^{J_2}_{abcq}\Big)
\end{aligned}
\tag{111}
$$

and

$$
\begin{aligned}
\tilde{Z}^{(J_1J_2)\lambda}_{pqrs} = &\sum_a\Big(A_{pa}\tilde{B}^{(J_1J_2)\lambda}_{aqrs} + A_{qa}\tilde{B}^{(J_1J_2)\lambda}_{pars} - \tilde{B}^{(J_1J_2)\lambda}_{pqas}A_{ar} - \tilde{B}^{(J_1J_2)\lambda}_{pqra}A_{as}\Big) \\
&-\hat{J}_1\hat{J}_2(-1)^{\lambda}\sum_a\Bigg[\ (1-P_{pq}(J_1))(-1)^{j_p+j_q+J_2}\begin{Bmatrix} J_2 & J_1 & \lambda \\ j_p & j_a & j_q \end{Bmatrix}B^{\lambda}_{pa}\tilde{A}^{J_2}_{aqrs} \\
&\qquad -(1-P_{rs}(J_2))(-1)^{j_r+j_s-J_1}\begin{Bmatrix} J_1 & J_2 & \lambda \\ j_s & j_a & j_r \end{Bmatrix}\tilde{A}^{J_1}_{pqra}B^{\lambda}_{as}\ \Bigg] \\
&+\frac{1}{2}\sum_{ab}(1-n_a-n_b)(\tilde{A}^{J_1}_{pqab}\tilde{B}^{(J_1J_2)\lambda}_{abrs} - \tilde{B}^{(J_1J_2)\lambda}_{pqab}\tilde{A}^{J_2}_{abrs}) + \sum_{abJ_3J_4}\hat{J}_1\hat{J}_2\hat{J}_3\hat{J}_4(n_a-n_b) \\
&\times\left[(1-P_{pq}(J_1))(1-P_{rs}(J_2))(-1)^{j_q+j_s+J_2+J_4}\begin{Bmatrix} j_p & j_s & J_3 \\ j_q & j_r & J_4 \\ J_1 & J_2 & \lambda \end{Bmatrix}\bar{A}^{J_3}_{p\bar{s}a\bar{b}}\bar{B}^{(J_3J_4)\lambda}_{a\bar{b}r\bar{q}}\right].
\end{aligned}
\tag{112}
$$

Here we have employed the scalar Pandya-transformed matrix elements defined by

$$
\bar{A}^{J_1}_{p\bar{q}r\bar{s}} = -\sum_{J_2}\hat{J}_2\begin{Bmatrix} j_p & j_q & J_1 \\ j_r & j_s & J_2 \end{Bmatrix}\tilde{A}^{J_2}_{psrq}
\tag{113}
$$

A.8 Scalar Commutators

Finally, taking $\lambda \to 0$ for both operators reveals the scalar limit, with non-reduced matrix elements.

$$Z_0 = \sum_{ab}(n_a - n_b)\hat{j}_a^2 A_{ab}B_{ba} + \frac{1}{4}\sum_{\substack{abcd \\ J}}(n_a n_b \bar{n}_c \bar{n}_d - n_c n_d \bar{n}_a \bar{n}_b)\hat{J}^2 \tilde{A}^J_{abcd}\tilde{B}^J_{cdab}\,, \tag{114}$$

$$\begin{aligned} Z_{pq} = &\sum_a (A_{pa}B_{aq} - B_{pa}A_{aq}) + \delta_{jpjq}\sum_{abJ}\frac{\hat{J}^2}{\hat{j}_p^2}(n_a - n_b)(A_{ab}\tilde{B}^J_{bpaq} - B_{ab}\tilde{A}^J_{bpaq}) \\ &+ \frac{1}{2}\delta_{jpjq}\sum_{abJ}\frac{\hat{J}^2}{\hat{j}_p^2}(n_a n_b \bar{n}_c + \bar{n}_a \bar{n}_b n_c)(\tilde{A}^J_{pcab}\tilde{B}^J_{abqc} - \tilde{B}^J_{pcab}\tilde{A}^J_{abqc})\,, \end{aligned} \tag{115}$$

$$\begin{aligned} \tilde{Z}^J_{pqrs} = &\sum_a (A_{pa}\tilde{B}^J_{aqrs} + A_{qa}\tilde{B}^J_{pars} - \tilde{B}^J_{pqas}A_{ar} - \tilde{B}^J_{aqra}A_{as}) \\ &- \sum_a (B_{pa}\tilde{A}^J_{aqrs} + B_{qa}\tilde{A}^J_{pars} - \tilde{A}^J_{pqas}B_{ar} - \tilde{A}^J_{aqra}B_{as}) \\ &+ \frac{1}{4}\sum_{ab}(1 - n_a - n_b)(\tilde{A}^J_{pqab}\tilde{B}^J_{abrs} - \tilde{B}^J_{pqab}\tilde{A}^J_{abrs}) \\ &+ (1 - P_{pq}(J))(1 - P_{rs}(J))\sum_{abJ_1}\hat{J}_1^2 \begin{Bmatrix} j_p & j_s & J_1 \\ j_r & j_q & J \end{Bmatrix} \bar{A}^{J_1}_{p\bar{s}a\bar{b}}\bar{B}^{J_1}_{a\bar{b}r\bar{q}}(n_a - n_b)\,. \end{aligned} \tag{116}$$

These expressions are used for the evaluation of the IMSRG unitary transformation involving the scalar operators η and H.

A.9 EOM-IMSRG({3},2) triples expression

For the computation of the EOM-IMSRG({3},2) triples correction in m-scheme, we must compute

$$\delta E^\nu_{\{3\}} = \frac{1}{36}\sum_{abcijk}\frac{|W_{abcijk}|^2}{D^{ijk}_{abc}} \tag{117}$$

where D^{ijk}_{abc} is the energy denominator, and

$$W_{abcijk} = [H, X^\dagger_\nu]_{abcijk} = (1 - P_{ab} - P_{ac})(1 - P_{ij} - P_{ik})\sum_{jq}(\Gamma_{bcqi}X_{aqjk} - X_{bcqi}\Gamma_{aqjk}) \tag{118}$$

In J-scheme, eq. 117 becomes

$$\frac{1}{36\hat{J}_\nu^2}\sum_{\substack{abc \\ ijk}}\sum_{\substack{j_1 j_2 \\ J_{ab}J_{ij}}}\frac{\hat{j}_1^2}{D^{ijk}_{abc}}|\langle[(ab)J_{ab}c]j_1||W^{J\nu}||[(ij)J_{ij}k]j_2\rangle|^2\,, \tag{119}$$

where the triples amplitudes are given by

$$\begin{aligned}
&\langle [(ab)J_{ab}c]j_1||W^{J\nu}||[(ij)J_{ij}k]j_2\rangle \\
&= \frac{1}{\hat{J}_\nu}\sum_{\{m\}} C^{j_a j_b J_{ab}}_{m_a m_b M_{ab}} C^{j_i j_j J_{ij}}_{m_i m_j M_{ij}} C^{J_{ab} j_c j_1}_{M_{ab} m_c m_1} C^{J_{ij} j_k j_2}_{M_{ij} m_k m_2} C^{j_1 \bar{j}_2 J\nu}_{m_1 \bar{m}_2 M\nu} \\
&\qquad \langle am_a, bm_b, cm_c|W^{J\nu}_{M\nu}|im_i, jm_j, km_k\rangle\,,
\end{aligned} \tag{120}$$

and the Epstein-Nesbet energy denominator D^{ijk}_{abc} is approximated with up to two-body monopole matrix elements,

$$\begin{aligned}
D^{ijk}_{abc} &= f_{ii} + f_{jj} + f_{kk} - f_{aa} - f_{bb} - f_{cc} + \urcorner_{abab} + \urcorner_{acac} + \urcorner_{bcbc} + \urcorner_{ijij} + \urcorner_{ikik} + \urcorner_{jkjk} \\
&\quad - \urcorner_{iaia} - \urcorner_{ibib} - \urcorner_{icic} - \urcorner_{jaja} - \urcorner_{jbjb} - \urcorner_{jcjc} - \urcorner_{kaka} - \urcorner_{kbkb} - \urcorner_{kckc}\,.
\end{aligned} \tag{121}$$

Where monopole matrix elements are given by

$$\urcorner_{pqrs} = \sum_J \tilde{\Gamma}^J_{pqrs}(2J+1)\,. \tag{122}$$

To compute the triples amplitudes, there are 18 terms to evaluate. We now derive the J-scheme expressions. We will only perform the derivation for the m-scheme term

$$T_{1A} = \sum_q \Gamma_{aqij} X_{bcqk}\,, \tag{123}$$

which is expressed in J-scheme as

$$\begin{aligned}
T_{1A} = \frac{1}{\hat{J}^2_\nu} \sum_{\substack{q\{m\} \\ J_1 J_2 J_3}} & C^{j_a j_b J_{ab}}_{m_a m_b M_{ab}} C^{J_{ab} j_c j_1}_{M_{ab} m_c m_1} C^{J_{ij} j_k j_2}_{M_{ij} m_k m_2} C^{j_1 \bar{j}_2 J\nu}_{m_1 \bar{m}_2 M\nu} \\
&\times C^{j_a j_q J_1}_{m_a m_q M_1} C^{j_b j_c J_2}_{m_b m_c M_2} C^{j_q j_k J_3}_{m_q m_k M_3} C^{J_2 \bar{J}_3 J\nu}_{M_2 \bar{M}_3 M\nu} \tilde{\Gamma}^{J_{ij}}_{aqij} \tilde{X}^{(J_2 J_3)J\nu}_{bcqk}\,.
\end{aligned} \tag{124}$$

We sum the angular momentum substates out,

$$\frac{1}{\hat{J}_\nu^2}\sum_{\{m\}} C^{j_a j_b J_{ab}}_{m_a m_b M_{ab}} C^{J_{ab} j_c j_1}_{M_{ab} m_c m_1} C^{J_{ij} j_k j_2}_{M_{ij} m_k m_2} C^{j_1 \bar{j}_2 J_\nu}_{m_1 \bar{m}_2 M_\nu}$$
$$\times C^{j_a j_q J_{ij}}_{m_a m_q M_{ij}} C^{j_b j_c J_2}_{m_b m_c M_2} C^{j_q j_k J_3}_{m_q m_k M_3} C^{J_2 \bar{J}_3 J_\nu}_{M_2 \bar{M}_3 M_\nu}$$

$= \hat{J}_2\hat{J}_3\hat{J}_{ab}\hat{J}_{ij}\hat{j}_1\hat{j}_2$

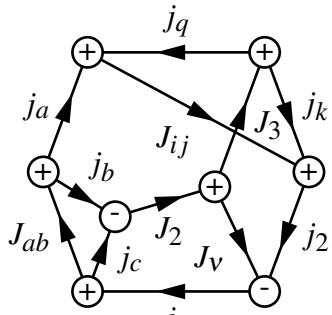

$= \hat{J}_2\hat{J}_3\hat{J}_{ab}\hat{J}_{ij}\hat{j}_1\hat{j}_2$

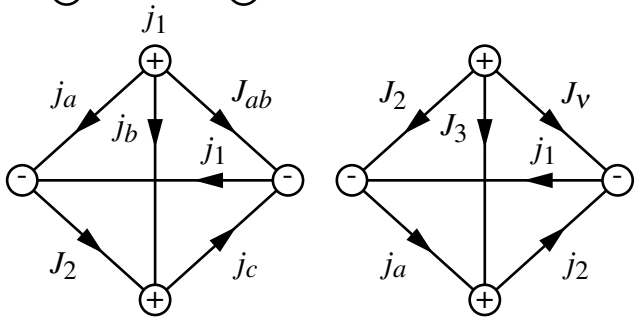

$\times$

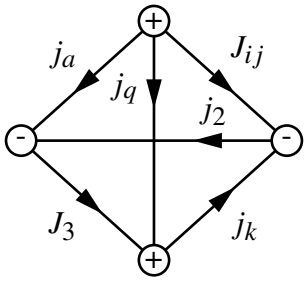

$(-1)^{(j_2+j_a+j_b+j_c+j_k+j_q+J_3+J_\nu)}$

$= \hat{J}_2\hat{J}_3\hat{J}_{ab}\hat{J}_{ij}\hat{j}_1\hat{j}_2(-1)^{(j_2+j_a+j_b+j_c+j_k+j_q+J_3+J_\nu)}$
$$\times \begin{Bmatrix} j_a & j_b & J_{ab} \\ j_c & j_1 & J_2 \end{Bmatrix} \begin{Bmatrix} J_2 & J_3 & J_\nu \\ j_2 & j_1 & j_a \end{Bmatrix} \begin{Bmatrix} j_a & j_q & J_{ij} \\ j_k & j_2 & J_3 \end{Bmatrix}, \tag{125}$$

Figure A.14 Derivation of induced three-body force with Jucys diagrams.

and thus

$$T_{1A} = \sum_q \sum_{J_2 J_3} = \hat{J}_2\hat{J}_3\hat{J}_{ab}\hat{J}_{ij}\hat{j}_1\hat{j}_2(-1)^{(j_2+j_a+j_b+j_c+j_k+j_q+J_3+J_\nu)}$$
$$\times \begin{Bmatrix} j_a & j_b & J_{ab} \\ j_c & j_1 & J_2 \end{Bmatrix} \begin{Bmatrix} J_2 & J_3 & J_\nu \\ j_2 & j_1 & j_a \end{Bmatrix} \begin{Bmatrix} j_a & j_q & J_{ij} \\ j_k & j_2 & J_3 \end{Bmatrix} \tilde{\Gamma}^{J_{ij}}_{aqij} \tilde{X}^{(J_2 J_3) J_\nu}_{bcqk} \tag{126}$$

The remainder of the terms may be computed with more or less the same procedure, and the full expression is given by

$$\langle[(ab)J_{ab}c]j_1||W^{J\nu}||[(ij)J_{ij}k]j_2\rangle = \sum_{N=1}^{9} T_N\,, \tag{127}$$

where

$$\begin{aligned}
T_1 = {} & \hat{j_1}\hat{j_2}\hat{J_{ab}} \sum_{\substack{J_1 J_2 q}} \hat{J_2}(-1)^{(j_c+j_b+j_q+j_2+J\nu)} \\
& \times \Bigg[\hat{J_1}\hat{J_{ij}}(-1)^{(j_a-j_k+J_2)} \begin{Bmatrix} j_a & j_b & J_{ab} \\ j_c & j_1 & J_1 \end{Bmatrix} \begin{Bmatrix} j_2 & j_a & J_2 \\ J_1 & J\nu & j_1 \end{Bmatrix} \begin{Bmatrix} j_a & j_q & J_{ij} \\ j_k & j_2 & J_2 \end{Bmatrix} \tilde{A}^{J_{ij}}_{aqij} \tilde{X}^{(J_1J_2)J\nu}_{bcqk} \\
& - \hat{J_2}\hat{J_1}(-1)^{J_1} \begin{Bmatrix} j_a & j_b & J_{ab} \\ j_c & j_1 & J_2 \end{Bmatrix} \begin{Bmatrix} j_2 & j_k & J_{ij} \\ J_1 & J\nu & j_1 \end{Bmatrix} \begin{Bmatrix} j_a & j_q & J_1 \\ j_k & j_1 & J_2 \end{Bmatrix} \tilde{X}^{(J_1J_{ij})J\nu}_{aqij} \tilde{A}^{J_2}_{bcqk} \Bigg]
\end{aligned} \tag{128}$$

$$\begin{aligned}
T_2 = {} & \hat{j_1}\hat{j_2}\hat{J_{ab}}\hat{J_{ij}} \sum_{\substack{qJ_1 \\ J_2J_3}} \hat{J_1}\hat{J_2}\hat{J_3}(-1)^{(j_b+j_c+j_j+j_k+j_q-j_2+J\nu)} \begin{Bmatrix} j_a & j_b & J_{ab} \\ j_c & j_1 & J_3 \end{Bmatrix} \begin{Bmatrix} j_i & j_j & J_{ij} \\ j_k & j_2 & J_2 \end{Bmatrix} \\
& \times \Bigg[\hat{J_2}(-1)^{(j_a-j_i+J_2+J_1)} \begin{Bmatrix} J_1 & J_3 & J\nu \\ j_1 & j_2 & j_a \end{Bmatrix} \begin{Bmatrix} j_a & j_q & J_2 \\ j_i & j_2 & J_1 \end{Bmatrix} \tilde{A}^{J_2}_{aqjk} \tilde{X}^{(J_3J_1)J\nu}_{bcqi} \\
& - \hat{J_3}(-1)^{(J_1+J_2)} \begin{Bmatrix} J_2 & J_1 & J\nu \\ j_1 & j_2 & j_i \end{Bmatrix} \begin{Bmatrix} j_a & j_1 & J_3 \\ j_i & j_q & J_1 \end{Bmatrix} \tilde{X}^{(J_1J_2)J\nu}_{aqjk} \tilde{A}^{J_3}_{bcqi} \Bigg]
\end{aligned} \tag{129}$$

$$\begin{aligned}
T_3 = {} & \hat{j_1}\hat{j_2}\hat{J_{ab}}\hat{J_{ij}} \sum_{\substack{qJ_1 \\ J_2J_3}} \hat{J_1}\hat{J_2}\hat{J_3}(-1)^{(j_b+j_c+j_i+j_q-j_2+J\nu+J_{ij})} \begin{Bmatrix} j_a & j_b & J_{ab} \\ j_c & j_1 & J_3 \end{Bmatrix} \begin{Bmatrix} j_i & j_j & J_{ij} \\ j_2 & j_k & J_2 \end{Bmatrix} \\
& \times \Bigg[\hat{J_2}(-1)^{(j_a+J_1)} \begin{Bmatrix} J_1 & J_3 & J\nu \\ j_1 & j_2 & j_a \end{Bmatrix} \begin{Bmatrix} j_a & j_q & J_2 \\ j_j & j_2 & J_1 \end{Bmatrix} \tilde{A}^{J_2}_{aqki} \tilde{X}^{(J_3J_1)J\nu}_{bcqj} \\
& - \hat{J_3}(-1)^{(j_j+J_1)} \begin{Bmatrix} J_1 & J_2 & J\nu \\ j_2 & j_1 & j_j \end{Bmatrix} \begin{Bmatrix} j_a & j_q & J_1 \\ j_j & j_1 & J_3 \end{Bmatrix} \tilde{X}^{(J_1J_2)J\nu}_{aqki} \tilde{A}^{J_3}_{bcqj} \Bigg]
\end{aligned} \tag{130}$$

$$T_4 = \hat{j_1}\hat{j_2}\hat{J_{ab}} \sum_{qJ_1J_2} \hat{J_1}\hat{J_2}(-1)^{(j_a+j_q+j_2+J_\nu+J_{ab}+J_1+J_2)}$$
$$\times \Bigg[\hat{J_{ij}}(-1)^{j_k} \begin{Bmatrix} j_a & j_b & J_{ab} \\ j_1 & j_c & J_1 \end{Bmatrix} \begin{Bmatrix} j_q & j_b & J_{ij} \\ j_2 & j_k & J_2 \end{Bmatrix} \begin{Bmatrix} J_1 & J_2 & J_\nu \\ j_2 & j_1 & j_b \end{Bmatrix} \tilde{A}^{J_{ij}}_{bqij} \tilde{X}^{(J_1J_2)J_\nu}_{caqk}$$
$$- \hat{J_2}(-1)^{j_b} \begin{Bmatrix} j_a & j_b & J_{ab} \\ j_1 & j_c & J_2 \end{Bmatrix} \begin{Bmatrix} j_q & j_b & J_1 \\ j_1 & j_k & J_2 \end{Bmatrix} \begin{Bmatrix} J_1 & J_{ij} & J_\nu \\ j_2 & j_1 & j_k \end{Bmatrix} \tilde{X}^{(J_1J_{ij})J_\nu}_{bqij} \tilde{A}^{J_2}_{caqk} \Bigg] \quad (131)$$

$$T_5 = \hat{j_1}\hat{j_2}\hat{J_{ab}}\hat{J_{ij}} \sum_{\substack{qJ_1 \\ J_2J_3}} \hat{J_1}\hat{J_2}\hat{J_3}(-1)^{(j_a+j_q+j_k+j_j-j_2+J_\nu+J_{ab}+J_1+J_2+J_3)}$$
$$\times \Bigg[\hat{J_1}(-1)^{j_i} \begin{Bmatrix} j_a & j_b & J_{ab} \\ j_1 & j_c & J_2 \end{Bmatrix} \begin{Bmatrix} j_i & j_j & J_{ij} \\ j_k & j_2 & J_1 \end{Bmatrix} \begin{Bmatrix} j_b & j_q & J_1 \\ j_i & j_2 & J_3 \end{Bmatrix} \begin{Bmatrix} J_3 & J_2 & J_\nu \\ j_1 & j_2 & j_b \end{Bmatrix} \tilde{A}^{J_1}_{bqjk} \tilde{X}^{(J_2J_3)J_\nu}_{caqi}$$
$$- \hat{J_3}(-1)^{j_b} \begin{Bmatrix} j_a & j_b & J_{ab} \\ j_1 & j_c & J_3 \end{Bmatrix} \begin{Bmatrix} j_b & j_q & J_1 \\ j_i & j_1 & J_3 \end{Bmatrix} \begin{Bmatrix} j_i & j_j & J_{ij} \\ j_k & j_2 & J_2 \end{Bmatrix} \begin{Bmatrix} J_2 & J_1 & J_\nu \\ j_1 & j_2 & j_i \end{Bmatrix} \tilde{X}^{(J_1J_2)J_\nu}_{bqjk} \tilde{A}^{J_3}_{caqi} \Bigg] \quad (132)$$

$$T_6 = \hat{j_1}\hat{j_2}\hat{J_{ab}}\hat{J_{ij}} \sum_{\substack{qJ_1 \\ J_2J_3}} \hat{J_1}\hat{J_2}\hat{J_3}(-1)^{(j_a+j_q+j_i+j_2+J_\nu+J_{ab}+J_{ij}+J_1+J_3)}$$
$$\times \Bigg[\hat{J_1}(-1)^{J_2+J_1} \begin{Bmatrix} j_a & j_b & J_{ab} \\ j_1 & j_c & J_2 \end{Bmatrix} \begin{Bmatrix} j_i & j_j & J_{ij} \\ j_2 & j_k & J_1 \end{Bmatrix} \begin{Bmatrix} j_b & j_q & J_1 \\ j_j & j_2 & J_3 \end{Bmatrix} \begin{Bmatrix} J_3 & J_2 & J_\nu \\ j_1 & j_2 & j_b \end{Bmatrix} \tilde{A}^{J_1}_{bqki} \tilde{X}^{(J_2J_3)J_\nu}_{caqj}$$
$$- \hat{J_3}(-1)^{(j_b-j_j)} \begin{Bmatrix} j_a & j_b & J_{ab} \\ j_1 & j_c & J_3 \end{Bmatrix} \begin{Bmatrix} j_b & j_q & J_1 \\ j_j & j_1 & J_3 \end{Bmatrix} \begin{Bmatrix} j_i & j_j & J_{ij} \\ j_2 & j_k & J_2 \end{Bmatrix} \begin{Bmatrix} J_2 & J_1 & J_\nu \\ j_1 & j_2 & j_j \end{Bmatrix} \tilde{X}^{(J_1J_2)J_\nu}_{bqki} \tilde{A}^{J_3}_{caqj} \Bigg] \quad (133)$$

$$T_7 = \hat{j_1}\hat{j_2}\sum_{qJ_1}\hat{J_1}(-1)^{(j_q-j_2+J_\nu+J_{ab}+J_1)}$$
$$\times[\hat{J_{ij}}(-1)^{(j_c-j_k)}\begin{Bmatrix} j_c & j_q & J_{ij} \\ j_k & j_2 & J_1 \end{Bmatrix}\begin{Bmatrix} J_1 & J_{ab} & J_\nu \\ j_1 & j_2 & j_c \end{Bmatrix}\tilde{A}^{J_{ij}}_{cqij}\tilde{X}^{(J_{ab}J_1)J_\nu}_{abqk}$$
$$-\hat{J_{ab}}\begin{Bmatrix} j_c & j_q & J_1 \\ j_k & j_1 & J_{ab} \end{Bmatrix}\begin{Bmatrix} J_1 & J_{ij} & J_\nu \\ j_2 & j_1 & j_k \end{Bmatrix}\tilde{X}^{(J_1J_{ij})J_\nu}_{cqij}\tilde{A}^{J_{ab}}_{abqk}\Big] \tag{134}$$

$$T_8 = \hat{j_1}\hat{j_2}\hat{J_{ij}}\sum_{qJ_1J_2}\hat{J_1}\hat{J_2}(-1)^{(j_k+j_q+j_j+j_2+J_\nu+J_{ab}+J_1+J_2)}$$
$$\times\Big[\hat{J_1}(-1)^{(j_c-j_i)}\begin{Bmatrix} j_q & j_i & J_2 \\ j_2 & j_c & J_1 \end{Bmatrix}\begin{Bmatrix} j_i & j_j & J_{ij} \\ j_k & j_2 & J_1 \end{Bmatrix}\begin{Bmatrix} J_{ab} & J_2 & J_\nu \\ j_2 & j_1 & j_c \end{Bmatrix}\tilde{A}^{J_1}_{cqjk}\tilde{X}^{(J_{ab}J_2)J_\nu}_{abqi}$$
$$-\hat{J_{ab}}\begin{Bmatrix} j_c & j_q & J_1 \\ j_i & j_1 & J_{ab} \end{Bmatrix}\begin{Bmatrix} j_i & j_j & J_{ij} \\ j_k & j_2 & J_2 \end{Bmatrix}\begin{Bmatrix} J_1 & J_2 & J_\nu \\ j_2 & j_1 & j_i \end{Bmatrix}\tilde{X}^{(J_1J_2)J_\nu}_{cqjk}\tilde{A}^{J_{ab}}_{abqi}\Big] \tag{135}$$

$$T_9 = \hat{j_1}\hat{j_2}\hat{J_{ij}}\sum_{qJ_1J_2}\hat{J_1}\hat{J_2}(-1)^{(j_q+j_i+j_2+J_\nu+J_{ab}+J_{ij})}$$
$$\times\Big[\hat{J_1}(-1)^{(j_c+J_2)}\begin{Bmatrix} j_c & j_q & J_1 \\ j_j & j_2 & J_2 \end{Bmatrix}\begin{Bmatrix} j_i & j_j & J_{ij} \\ j_2 & j_k & J_1 \end{Bmatrix}\begin{Bmatrix} J_{ab} & J_2 & J_\nu \\ j_2 & j_1 & j_c \end{Bmatrix}\tilde{A}^{J_1}_{cqki}\tilde{X}^{(J_{ab}J_2)J_\nu}_{abqj}$$
$$-\hat{J_{ab}}(-1)^{(J_1-j_j)}\begin{Bmatrix} j_c & j_q & J_1 \\ j_j & j_1 & J_{ab} \end{Bmatrix}\begin{Bmatrix} j_i & j_j & J_{ij} \\ j_2 & j_k & J_2 \end{Bmatrix}\begin{Bmatrix} J_1 & J_2 & J_\nu \\ j_2 & j_1 & j_j \end{Bmatrix}\tilde{X}^{(J_1J_2)J_\nu}_{cqki}\tilde{A}^{J_{ab}}_{abqj}\Big] \tag{136}$$

You can arrive at the expressions required for the ground state triples correction by taking $J_\nu \to 0$ and converting to non-reduced matrix elements.

BIBLIOGRAPHY

BIBLIOGRAPHY

[1] B.V. Pritychenko, M. Birch, B. Singh, and M. Horoi. Tables of E2 transition probabilities from the first 2^+ states in even–even nuclei. *At. Data Nucl. Data Tables*, 107:1, 2016.

[2] V. F. Weisskopf. Radiative transition probabilities in nuclei. *Phys. Rev.*, 83:1073, 1951.

[3] H. Hergert, S. K. Bogner, T. D. Morris, A. Schwenk, and K. Tsukiyama. The in-medium similarity renormalization group: A novel ab initio method for nuclei. *Phys. Rept.*, 621:165, 2016.

[4] R. Machleidt and D. R. Entem. Chiral effective field theory and nuclear forces. *Phys. Rept.*, 503:1, 2011.

[5] D. R. Entem and R. Machleidt. Accurate charge-dependent nucleon-nucleon potential at fourth order of chiral perturbation theory. *Phys. Rev. C*, 68:041001, 2003.

[6] T. D. Morris, N. M. Parzuchowski, and S. K. Bogner. Magnus expansion and in-medium similarity renormalization group. *Phys. Rev. C*, 92:034331, 2015.

[7] R. J. Furnstahl, G. Hagen, and T. Papenbrock. Corrections to nuclear energies and radii in finite oscillator spaces. *Phys. Rev. C*, 86:031301, 2012.

[8] S. N. More, A. Ekström, R. J. Furnstahl, G. Hagen, and T. Papenbrock. Universal properties of infrared oscillator basis extrapolations. *Phys. Rev. C*, 87:044326, 2013.

[9] E. D. Jurgenson, P. Navrátil, and R. J. Furnstahl. Evolution of nuclear many-body forces with the similarity renormalization group. *Phys. Rev. Lett.*, 103:082501, 2009.

[10] G. Audi, O. Bersillon, J. Blachot, and A. H. Wapstra. The nubase evaluation of nuclear and decay properties. *Nuc. Phys. A*, 729:3, 2003.

[11] I. Shavitt and R. J. Bartlett. *Many-Body Methods in Chemistry and Physics: MBPT and Coupled-Cluster Theory*. Cambridge University Press, 2009.

[12] Evaluated nuclear structure data file. `https://www.nndc.bnl.gov/ensdf/`. Accessed: 2017-02-20.

[13] P. Navrátil. Local three-nucleon interaction from chiral effective field theory. *Few-Body Systems*, 41:117, 2007.

[14] F. Ajzenberg-Selove. Energy levels of light nuclei A = 13–15. *Nucl. Phys. A*, 523:1, 1991.

[15] T. Kibédi and R. H. Spear. Reduced electric-octupole transition probabilities, $B(E3;0_1^+ \rightarrow 3_1^-)$ – an update. *At. Data Nucl. Data Tables*, 80:35, 2002.

[16] P. Navrátil, J. P. Vary, and B. R. Barrett. Large-basis ab initio no-core shell model and its application to ^{12}**C**. *Phys. Rev. C*, 62:054311, 2000.

[17] P. Navrátil, S. Quaglioni, I. Stetcu, and B. R. Barrett. Recent developments in no-core shell-model calculations. *J. Phys. G: Nucl. Part. Phys.*, 36:083101, 2009.

[18] B. R. Barrett, P. Navrátil, and J. P. Vary. Ab initio no core shell model. *Prog. Part. Nucl. Phys.*, 69:131, 2013.

[19] B. S. Pudliner, V. R. Pandharipande, J. Carlson, Steven C. Pieper, and R. B. Wiringa. Quantum Monte Carlo calculations of nuclei with $A \leq 7$. *Phys. Rev. C*, 56:1720, 1997.

[20] S. C. Pieper and R. B. Wiringa. Quantum Monte Carlo calculations of light nuclei 1. *Ann. Rev. Nucl. Part. Sci.*, 51:53, 2001.

[21] J. Carlson, S. Gandolfi, F. Pederiva, Steven C. Pieper, R. Schiavilla, K. E. Schmidt, and R. B. Wiringa. Quantum Monte Carlo methods for nuclear physics. *Rev. Mod. Phys.*, 87:1067, 2015.

[22] J. Hubbard. The description of collective motions in terms of many-body perturbation theory. In *Proceedings of the Royal Society of London A: Mathematical, Physical and Engineering Sciences*, volume 240, page 539. The Royal Society, 1957.

[23] N. M. Hugenholtz. Perturbation theory of large quantum systems. *Physica*, 23:481, 1957.

[24] H. F. Schaefer III. *Quantum Chemistry: The Development of Ab-Initio Methods in Molecular Electronic Structure Theory*. Dover Publications Inc., 2004.

[25] J. Cizek. On the correlation problem in atomic and molecular systems. calculation of wavefunction components in ursell-type expansion using quantum-field theoretical methods. *J. Chem. Phys.*, 45:4256, 1966.

[26] J. Cizek and J. Paldus. Coupled cluster approach. *Phys. Scripta*, 21:251, 1980.

[27] J. Cizek and J. Paldus. Correlation problems in atomic and molecular systems iii. rederivation of the coupled-pair many-electron theory using the traditional quantum chemical methodst. *Int. J. Quantum Chem.*, 5:359, 1971.

[28] P. Piecuch, K. Kowalski, I. S. O Pimienta, and M. J. Mcguire. Recent advances in electronic structure theory: Method of moments of coupled-cluster equations and renormalized coupled-cluster approaches. *Int. Rev. Phys. Chem.*, 21:527, 2002.

[29] F. Coester. Bound states of a many-particle system. *Nucl. Phys.*, 7:421, 1958.

[30] F. Coester and H. Kümmel. Short-range correlations in nuclear wave functions. *Nucl. Phys.*, 17:477, 1960.

[31] H. Kümmel, K. H. Lührmann, and J. G. Zabolitzky. Many-fermion theory in exps-(or coupled cluster) form. *Phys. Rept.*, 36:1, 1978.

[32] J. W. Negele and D. Vautherin. Density-matrix expansion for an effective nuclear Hamiltonian. *Phys. Rev. C*, 5:1472, 1972.

[33] T. T. S. Kuo and G. E. Brown. Structure of finite nuclei and the free nucleon-nucleon interaction: An application to ^{18}O and ^{18}F. *Nucl. Phys.*, 85:40, 1966.

[34] W. A. Richter, S. Mkhize, and B. Alex Brown. *sd*-shell observables for the usda and usdb Hamiltonians. *Phys. Rev. C*, 78:064302, 2008.

[35] T. H. R. Skyrme. The effective nuclear potential. *Nucl. Phys*, 9:615, 1958.

[36] D. Vautherin and D. M. Brink. Hartree-fock calculations with skyrme's interaction. i. spherical nuclei. *Phys. Rev. C*, 5:626, 1972.

[37] E. Epelbaum, H.-W. Hammer, and Ulf-G. Meißner. Modern theory of nuclear forces. *Rev. Mod. Phys.*, 81:1773, 2009.

[38] R. Machleidt and D. R. Entem. Chiral effective field theory and nuclear forces. *Phys. Rept.*, 503:1, 2011.

[39] S. K. Bogner, R. J. Furnstahl, and A. Schwenk. From low-momentum interactions to nuclear structure. *Prog. Part. Nucl. Phys.*, 65:94, 2010.

[40] R. Roth, J. Langhammer, A. Calci, S. Binder, and P. Navrátil. Similarity-transformed chiral $NN + 3N$ interactions for the *Ab Initio* description of ^{12}**C** and ^{16}**O**. *Phys. Rev. Lett.*, 107:072501, 2011.

[41] M. Włoch, D. J. Dean, J. R. Gour, M. Hjorth-Jensen, K. Kowalski, T. Papenbrock, and P. Piecuch. Ab-initio coupled-cluster study of o 16. *Phys. Rev. Lett.*, 94:212501, 2005.

[42] M. Wloch, J. R. Gour, P. Piecuch, D. J. Dean, M. Hjorth-Jensen, and T. Papenbrock. Coupled-cluster calculations for ground and excited states of closed- and open-shell nuclei using methods of quantum chemistry. *J. Phys. G*, 31:S1291, 2005.

[43] K. Tsukiyama, S. K. Bogner, and A. Schwenk. In-medium similarity renormalization group for nuclei. *Phys. Rev. Lett.*, 106:222502, 2011.

[44] K. Tsukiyama, S. K. Bogner, and A. Schwenk. In-medium similarity renormalization group for open-shell nuclei. *Phys. Rev. C*, 85:061304, 2012.

[45] H. Hergert, S. Binder, A. Calci, J. Langhammer, and R. Roth. *Ab Initio* calculations of even oxygen isotopes with chiral two-plus-three-nucleon interactions. *Phys. Rev. Lett.*, 110:242501, 2013.

[46] S. K. Bogner, H. Hergert, J. D. Holt, A. Schwenk, S. Binder, A. Calci, J. Langhammer, and R. Roth. Nonperturbative shell-model interactions from the in-medium similarity renormalization group. *Phys. Rev. Lett.*, 113:142501, 2014.

[47] H. Hergert, S. K. Bogner, T. D. Morris, S. Binder, A. Calci, J. Langhammer, and R. Roth. Ab initio multi-reference in-medium similarity renormalization group calculations of even calcium and nickel isotopes. *Phys. Rev. C*, 90:041302, 2014.

[48] H. Hergert. In-medium similarity renormalization group for closed and open-shell nuclei. *Physica Scripta*, 92:023002, 2017.

[49] G. R. Jansen, J. Engel, G. Hagen, P. Navratil, and A. Signoracci. Ab-initio coupled-cluster effective interactions for the shell model: Application to neutron-rich oxygen and carbon isotopes. *Phys. Rev. Lett.*, 113:142502, 2014.

[50] G. R. Jansen, A. Signoracci, G. Hagen, and P. Navrl. Open *sd*-shell nuclei from first principles. *Phys. Rev. C*, 94:011301, 2016.

[51] S. R. Stroberg, H. Hergert, J. D. Holt, S. K. Bogner, and A. Schwenk. Ground and excited states of doubly open-shell nuclei from ab initio valence-space Hamiltonians. *Phys. Rev. C*, 93:051301, 2016.

[52] S. R. Stroberg, A. Calci, H. Hergert, J. D. Holt, S. K. Bogner, R. Roth, and A. Schwenk. A nucleus-dependent valence-space approach to nuclear structure. *arXiv:1607.03229*, 2016.

[53] V. Somá, C. Barbieri, and T. Duguet. *Ab initio* gorkov-green's function calculations of open-shell nuclei. *Phys. Rev. C*, 87:011303, 2013.

[54] V. Somá, C. Barbieri, and T. Duguet. Ab initio self-consistent Gorkov-Green's function calculations of semi-magic nuclei: Numerical implementation at second order with a two-nucleon interaction. *Phys. Rev. C*, 89:024323, 2014.

[55] V. Somá, A. Cipollone, C. Barbieri, P. Navrátil, and T. Duguet. Chiral two- and three-nucleon forces along medium-mass isotope chains. *Phys. Rev. C*, 89:061301, 2014.

[56] F. Wienholtz, D. Beck, K. Blaum, Ch. Borgmann, M. Breitenfeldt, R. B. Cakirli, S. George, F. Herfurth, J. D. Holt, M. Kowalska, S. Kreim, D. Lunney, V. Manea, J. Menendez, D. Neidherr, M. Rosenbusch, L. Schweikhard, A. Schwenk, J. Simonis, J. Stanja, R. N. Wolf, and K. Zuber. Masses of exotic calcium isotopes pin down nuclear forces. *Nature*, 498:346, 2013.

[57] G. Hagen, A. Ekström, C. Forssen, G. R. Jansen, W. Nazarewicz, T. Papenbrock, K. A. Wendt, S. Bacca, N. Barnea, B. Carlsson, C. Drischler, K. Hebeler, M. Hjorth-Jensen, M. Miorelli, G. Orlandini, A. Schwenk, and J. Simonis. Neutron and weak-charge distributions of the ^{48}Ca nucleus. *Nature Physics*, advance online publication:–, 2015.

[58] K. Kowalski, D. J. Dean, M. Hjorth-Jensen, T. Papenbrock, and P. Piecuch. Coupled cluster calculations of ground and excited states of nuclei. *Phys. Rev. Lett.*, 92:132501, 2004.

[59] J. R. Gour, P. Piecuch, M. Hjorth-Jensen, M. Wloch, and D. J. Dean. Coupled-cluster calculations for valence systems around ^{16}O. *Phys. Rev. C*, 74:024310, 2006.

[60] S. Binder, P. Piecuch, A. Calci, J. Langhammer, P. Navrátil, and R. Roth. Extension of coupled-cluster theory with a noniterative treatment of connected triply excited clusters to three-body Hamiltonians. *Phys. Rev. C*, 88:054319, 2013.

[61] G. Hagen, T. Papenbrock, D. J. Dean, A. Schwenk, A. Nogga, M. Włoch, and P. Piecuch. Coupled-cluster theory for three-body Hamiltonians. *Phys. Rev. C*, 76:034302, 2007.

[62] V. Somá, A. Cipollone, C. Barbieri, P. Navrátil, and T. Duguet. Chiral two- and three-nucleon forces along medium-mass isotope chains. *Phys. Rev. C*, 89:061301, 2014.

[63] R. Roth, S. Binder, K. Vobig, A. Calci, J. Langhammer, and P. Navrátil. Medium-mass nuclei with normal-ordered chiral $NN+3N$ interactions. *Phys. Rev. Lett.*, 109:052501, 2012.

[64] H. Hergert, S.K. Bogner, S. Binder, A. Calci, J. Langhammer, et al. In-medium similarity renormalization group with chiral two- plus three-nucleon interactions. *Phys. Rev. C*, 87:034307, 2013.

[65] V. Somá, C. Barbieri, and T. Duguet. Ab-initio gorkov-green's function calculations of open-shell nuclei. *Phys. Rev. C*, 87:011303, 2013.

[66] E. Gebrerufael, K. Vobig, H. Hergert, and R. Roth. Ab Initio Description of Open-Shell Nuclei: Merging No-Core Shell Model and In-Medium Similarity Renormalization Group. *arXiv:1610.05254*, 2016.

[67] J. Engel and J. Menéndez. Status and future of nuclear matrix elements for neutrinoless double-beta decay: a review. *Rep. Prog. Phys.*, 80:046301, 2017.

[68] A. Ekström, G. R. Jansen, K. A. Wendt, G. Hagen, T. Papenbrock, et al. Effects of three-nucleon forces and two-body currents on gamow-teller strengths. *Phys. Rev. Lett.*, 113:262504, 2014.

[69] G. R. Jansen. Spherical coupled-cluster theory for open-shell nuclei. *Phys. Rev. C*, 88:024305, 2013.

[70] S. Bacca, N. Barnea, G. Hagen, M. Miorelli, G. Orlandini, and T. Papenbrock. Giant and pigmy dipole resonances in ^{4}He, ^{16,22}O, and ^{40}Ca from chiral nucleon-nucleon interactions. *Phys. Rev. C*, 90:064619, 2014.

[71] D. J. Rowe. Equations-of-motion method and the extended shell model. *Rev. Mod. Phys.*, 40:153, 1968.

[72] N. M. Parzuchowski, T. D. Morris, and S. K. Bogner. Ab initio excited states from the in-medium similarity renormalization group. *Phys. Rev. C*, 95:044304, 2017.

[73] K. Emrich. An extension of the coupled cluster formalism to excited states. *Nucl. Phys. A*, 351:397, 1981.

[74] K. Emrich and J. G. Zabolitzky. Negative parity states in ^{16}O from coupled-cluster equations. *Nucl. Phys. A*, 351:439, 1981.

[75] H. J. Monkhorst. Calculation of properties with the coupled-cluster method. *Int. J. Quantum Chem*, 12:421, 1977.

[76] J. F. Stanton and R. J. Bartlett. The equation of motion coupled-cluster method. a systematic biorthogonal approach to molecular excitation energies, transition probabilities, and excited state properties. *J. Chem. Phys.*, 98:7029, 1993.

[77] W. Kutzelnigg and D. Mukherjee. Normal order and extended wick theorem for a multiconfiguration reference wave function. *J. Chem. Phys.*, 107:432, 1997.

[78] B. A. Brown and W. A. Richter. New "usd" Hamiltonians for the *sd* shell. *Phys. Rev. C*, 74:034315, 2006.

[79] S. R. Beane, E. Chang, W. Detmold, H. W. Lin, T. C. Luu, K. Orginos, A. Parreño, M. J. Savage, A. Torok, and A. Walker-Loud. Deuteron and exotic two-body bound states from lattice QCD. *Phys. Rev. D*, 85:054511, 2012.

[80] T. Yamazaki, K. Ishikawa, Y. Kuramashi, and A. Ukawa. Helium nuclei, deuteron, and dineutron in 2+1 flavor lattice QCD. *Phys. Rev. D*, 86:074514, 2012.

[81] R. Machleidt, K. Holinde, and Ch. Elster. The bonn meson-exchange model for the nucleon—nucleon interaction. *Phys. Rept.*, 149:1, 1987.

[82] V. G. J. Stoks, R. A. M. Klomp, C. P. F. Terheggen, and J. J. de Swart. Construction of high-quality nn potential models. *Phys. Rev. C*, 49:2950, 1994.

[83] R. B. Wiringa, V. G. J. Stoks, and R. Schiavilla. Accurate nucleon-nucleon potential with charge-independence breaking. *Phys. Rev. C*, 51:38, 1995.

[84] E. Epelbaum, H.-W. Hammer, and Ulf-G. Meißner. Modern theory of nuclear forces. *Rev. Mod. Phys.*, 81:1773, 2009.

[85] K. Nakamura, Particle Data Group, et al. Review of particle physics. *J. Phys. G: Nucl. and Part. Phys.*, 37:075021, 2010.

[86] J. Beringer, J.-F. Arguin, R. M. Barnett, K. Copic, O. Dahl, D. E. Groom, C.-J. Lin, J. Lys, H. Murayama, C. G. Wohl, et al. Review of particle physics particle data group. *Phys. Rev. D*, 86, 2012.

[87] E. Epelbaum. Few-nucleon forces and systems in chiral effective field theory. *Prog. Part. Nucl. Phys.*, 57:654, 2006.

[88] K. Hebeler, H. Krebs, E. Epelbaum, J. Golak, and R. Skibiński. Efficient calculation of chiral three-nucleon forces up to N^3LO for ab initio studies. *Phys. Rev. C*, 91:044001, 2015.

[89] S. Binder, J. Langhammer, A. Calci, and R. Roth. Ab initio path to heavy nuclei. *Phys. Lett. B*, 736:119, 2014.

[90] V. Lapoux, V. Somà, C. Barbieri, H. Hergert, J. D. Holt, and S. R. Stroberg. Radii and binding energies in oxygen isotopes: A challenge for nuclear forces. *Phys. Rev. Lett.*, 117:052501, 2016.

[91] D. R. Entem, N. Kaiser, R. Machleidt, and Y. Nosyk. Dominant contributions to the nucleon-nucleon interaction at sixth order of chiral perturbation theory. *Phys. Rev. C*, 92:064001, 2015.

[92] A. Ekström, G. Baardsen, C. Forssén, G. Hagen, M. Hjorth-Jensen, G. R. Jansen, R. Machleidt, W. Nazarewicz, T. Papenbrock, J. Sarich, and S. M. Wild. Optimized chiral nucleon-nucleon interaction at next-to-next-to-leading order. *Phys. Rev. Lett.*, 110:192502, 2013.

[93] A. Ekström, G. R. Jansen, K. A. Wendt, G. Hagen, T. Papenbrock, B. D. Carlsson, C. Forssén, M. Hjorth-Jensen, P. Navrátil, and W. Nazarewicz. Accurate nuclear radii and binding energies from a chiral interaction. *Phys. Rev. C*, 91:051301, 2015.

[94] K. Hebeler, S. K. Bogner, R. J. Furnstahl, A. Nogga, and A. Schwenk. Improved nuclear matter calculations from chiral low-momentum interactions. *Phys. Rev. C*, 83:031301, 2011.

[95] P. Ring and P. Schuck. *The Nuclear Many-Body Problem*. Springer, 1st edition, 1980.

[96] N. Michel, W. Nazarewicz, M. Płoszajczak, and K. Bennaceur. Gamow shell model description of neutron-rich nuclei. *Phys. Rev. Lett.*, 89:042502, 2002.

[97] N. Michel, W. Nazarewicz, M. Płoszajczak, and J. Rotureau. Antibound states and halo formation in the gamow shell model. *Phys. Rev. C*, 74:054305, 2006.

[98] G. Hagen, D. J. Dean, M. Hjorth-Jensen, and T. Papenbrock. Complex coupled-cluster approach to an ab-initio description of open quantum systems. *Phys. Lett. B*, 656:169, 2007.

[99] G. Hagen, T. Papenbrock, and M. Hjorth-Jensen. Ab initio computation of the ^{17}F proton halo state and resonances in A= 17 nuclei. *Phys. Rev. Lett.*, 104:182501, 2010.

[100] A.L. Fetter and J.D. Walecka. *Quantum Theory of Many-particle Systems*. Dover Books on Physics. Dover Publications, 2003.

[101] W. H. Dickhoff and D. Van Neck. *Many-body theory exposed!: propagator description of quantum mechanics in many-body systems*. World Scientific Publishing Co Inc, 2008.

[102] S. Binder, J. Langhammer, A. Calci, P. Navrátil, and R. Roth. *Ab initio* calculations of medium-mass nuclei with explicit chiral 3*N* interactions. *Phys. Rev. C*, 87:021303, 2013.

[103] D. J. Thouless. Stability conditions and nuclear rotations in the hartree-fock theory. *Nucl. Phys.*, 21:225, 1960.

[104] E. R Davidson. Matrix eigenvector methods. In *Methods in Computational Molecular Physics*, pages 95–113. Springer, 1983.

[105] C. Lanczos. *An iteration method for the solution of the eigenvalue problem of linear differential and integral operators*. United States Governm. Press Office Los Angeles, CA, 1950.

[106] E. Epelbaum, H. Krebs, D. Lee, and U.-G. Meißner. Lattice effective field theory calculations for a= 3, 4, 6, 12 nuclei. *Phys. Rev. Lett.*, 104:142501, 2010.

[107] T. A. Lähde, E. Epelbaum, H. Krebs, D. Lee, U.-G. Meißner, and G. Rupak. Lattice effective field theory for medium-mass nuclei. *Phys. Lett. B*, 732:110, 2014.

[108] C. D. Sherrill and H. F Schaefer. The configuration interaction method: Advances in highly correlated approaches. *Adv. Quantum Chem.*, 34:143, 1999.

[109] R. Roth, P. Papakonstantinou, N. Paar, H. Hergert, T. Neff, and H. Feldmeier. Hartree-fock and many body perturbation theory with correlated realistic nn interactions. *Phys. Rev. C*, 73:044312, 2006.

[110] A. Tichai, J. Langhammer, S. Binder, and R. Roth. Hartree–fock many-body perturbation theory for nuclear ground-states. *Phys. Lett. B*, 756:283, 2016.

[111] K. A. Brueckner. Many-body problem for strongly interacting particles. ii. linked cluster expansion. *Phys. Rev.*, 100:36, 1955.

[112] J. Goldstone. Derivation of the Brueckner Many-Body Theory. *Proc. Roy. Soc. Lond. A Math. Phys. Eng. Sci.*, 239:267, 1957.

[113] R. Yaris. Linked-cluster theorem and unitarity. *J. Chem. Phys.*, 41:2419, 1964.

[114] B. H. Brandow. Linked-cluster expansions for the nuclear many-body problem. *Rev. Mod. Phys.*, 39:771, 1967.

[115] A. G. Taube and R. J. Bartlett. Improving upon CCSD(T): Lambda CCSD(T). I. potential energy surfaces. *J. Chem. Phys.*, 128:044110, 2008.

[116] G. Hagen, T. Papenbrock, D. J. Dean, and M. Hjorth-Jensen. Ab initio coupled-cluster approach to nuclear structure with modern nucleon-nucleon interactions. *Phys. Rev. C*, 82:034330, 2010.

[117] W. Magnus. On the exponential solution of differential equations for a linear operator. *Comm. Pure Appl. Math.*, 7:649, 1954.

[118] F. Wegner. Flow equations for Hamiltonians. *Ann. Phys. (Leipzig)*, 506:77, 1994.

[119] S. D. Glazek and K. G. Wilson. Renormalization of Hamiltonians. *Phys. Rev. D*, 48:5863, 1993.

[120] S. K. Bogner, R. J. Furnstahl, S. Ramanan, and A. Schwenk. Low-momentum interactions with smooth cutoffs. *Nucl. Phys. A*, 784:79, 2007.

[121] S. K. Bogner, R. J. Furnstahl, and R. J. Perry. Similarity renormalization group for nucleon-nucleon interactions. *Phys. Rev. C*, 75:061001, 2007.

[122] S. K. Bogner, R. J. Furnstahl, and R. J. Perry. Similarity renormalization group for nucleon-nucleon interactions. *Phys. Rev. C*, 75:061001(R), 2007.

[123] E. D. Jurgenson, P. Navrátil, and R. J. Furnstahl. Evolving nuclear many-body forces with the similarity renormalization group. *Phys. Rev. C*, 83:034301, 2011.

[124] E. D. Jurgenson, P. Maris, R. J. Furnstahl, P. Navrátil, W. E. Ormand, and J. P. Vary. Structure of p-shell nuclei using three-nucleon interactions evolved with the similarity renormalization group. *Phys. Rev. C*, 87:054312, 2013.

[125] S. C. Pieper, R. B. Wiringa, and J. Carlson. Quantum Monte Carlo calculations of excited states in $A = 6 - 8$ nuclei. *Phys. Rev. C*, 70:054325, 2004.

[126] J. W. Negele and H. Orland. *Quantum Many-Particle Systems*. Advanced Book Classics. Westview Press, 1998.

[127] R. Roth, A. Calci, J. Langhammer, and S. Binder. Evolved chiral $NN + 3N$ Hamiltonians for ab initio nuclear structure calculations. *Phys. Rev. C*, 90:024325, 2014.

[128] H. Hergert, S. K. Bogner, S. Binder, A. Calci, J. Langhammer, R. Roth, and A. Schwenk. In-medium similarity renormalization group with chiral two- plus three-nucleon interactions. *Phys. Rev. C*, 87:034307, 2013.

[129] V. Somá, T. Duguet, and C. Barbieri. *Ab initio* self-consistent Gorkov-Green's function calculations of semimagic nuclei: Formalism at second order with a two-nucleon interaction. *Phys. Rev. C*, 84:064317, 2011.

[130] K. Hebeler. Momentum-space evolution of chiral three-nucleon forces. *Phys. Rev. C*, 85:021002, 2012.

[131] K. A. Wendt. Similarity renormalization group evolution of three-nucleon forces in a hyperspherical momentum representation. *Phys. Rev. C*, 87:061001, 2013.

[132] S. R. White. Numerical canonical transformation approach to quantum many-body problems. *J. Chem. Phys.*, 117:7472, 2002.

[133] K. A. Brueckner and C. A. Levinson. Approximate reduction of the many-body problem for strongly interacting particles to a problem of self-consistent fields. *Phys. Rev.*, 97:1344, 1955.

[134] K. A. Brueckner and C. A. Levinson. Approximate Reduction of the Many-Body Problem for Strongly Interacting Particles to a Problem of Self-Consistent Fields. *Phys. Rev.*, 97:1344, 1955.

[135] H. A. Bethe. Nuclear many-body problem. *Phys. Rev.*, 103:1353, 1956.

[136] B. D. Day. Elements of the brueckner-goldstone theory of nuclear matter. *Rev. Mod. Phys.*, 39:719, 1967.

[137] LF Shampine and MK Gordon. Computer solution of ordinary differential equations: the initial value problem, 1975.

[138] R. F. Bishop, M. F. Flynn, M. C. Boscá, E. Buenda, and R. Guardiola. Translationally invariant coupled cluster theory for simple finite systems. *Phys. Rev. C*, 42:1341, 1990.

[139] A. Nogga, H. Kamada, W. Glöckle, and B. R. Barrett. The α particle based on modern nuclear forces. *Phys. Rev. C*, 65:054003, 2002.

[140] S. Bacca, N. Barnea, W. Leidemann, and G. Orlandini. Role of the final-state interaction and three-body force on the longitudinal response function of ^{4}He. *Phys. Rev. Lett.*, 102:162501, 2009.

[141] G. Hagen, T. Papenbrock, and D. J. Dean. Solution of the Center-Of-Mass Problem in Nuclear Structure Calculations. *Phys. Rev. Lett.*, 103(6):062503, 2009.

[142] D. H. Gloeckner and R. D. Lawson. Spurious center-of-mass motion. *Phys. Lett. B*, 53:313, 1974.

[143] R. J. Bartlett. Many-body perturbation theory and coupled cluster theory for electron correlation in molecules. *Annu. Rev. Phys. Chem.*, 32:359, 1981.

[144] G. Hagen, M. Hjorth-Jensen, G. R. Jansen, R. Machleidt, and T. Papenbrock. Continuum effects and three-nucleon forces in neutron-rich oxygen isotopes. *Phys. Rev. Lett.*, 108:242501, 2012.

[145] R. Roth and P. Navrátil. Ab initio study of ^{40}Ca with an importance-truncated no-core shell model. *Phys. Rev. Lett.*, 99:092501, 2007.

[146] R. Roth. Importance truncation for large-scale configuration interaction approaches. *Phys. Rev. C*, 79:064324, 2009.

[147] T. D. Morris. *Systematic Improvements of Ab-Initio In-Medium Similarity Renormalization Group Calculations*. PhD thesis, Michigan State University, East Lansing, Michigan, 2016.

[148] F. A. Evangelista. A driven similarity renormalization group approach to quantum many-body problems. *J. Chem. Phys.*, 141:054109, 2014.

[149] P. Papakonstantinou and R. Roth. Second random phase approximation and renormalized realistic interactions. *Phys. Lett. B*, 671:356, 2009.

[150] C. Yannouleas. Zero-temperature second random phase approximation and its formal properties. *Phys. Rev. C*, 35:1159, 1987.

[151] J. Sous, P. Goel, and M. Nooijen. Similarity transformed equation of motion coupled cluster theory revisited: a benchmark study of valence excited states. *Mol. Phys.*, 112:616, 2014.

[152] G. Hagen, T. Papenbrock, and D. J. Dean. Solution of the center-of-mass problem in nuclear structure calculations. *Phys. Rev. Lett.*, 103:062503, 2009.

[153] G. Hagen, T. Papenbrock, M. Hjorth-Jensen, and D. J. Dean. Coupled-cluster computations of atomic nuclei. *Rept. Prog. Phys.*, 77:096302, 2014.

[154] K. Emrich. An extension of the coupled cluster formalism to excited states (I). *Nucl. Phys. A*, 351:379, 1981.

[155] J. Langhammer, P. Navrátil, S. Quaglioni, G. Hupin, A. Calci, and R. Roth. Continuum and three-nucleon force effects on ^{9}Be energy levels. *Phys. Rev. C*, 91:021301, 2015.

[156] G. Audi, A. H. Wapstra, and C. Thibault. The AME2003 atomic mass evaluation:(II). Tables, graphs and references. *Nucl. Phys. A*, 729:337, 2003.

[157] P. Navrátil, J. P. Vary, W. E. Ormand, and B. R. Barrett. Six-nucleon spectroscopy from a realistic nonlocal Hamiltonian. *Phys. Rev. Lett.*, 87:172502, 2001.

[158] I. Stetcu, B. R. Barrett, P. Navrátil, and J. P. Vary. Effective operators within the ab initio no-core shell model. *Phys. Rev. C*, 71:044325, 2005.

[159] R. B. Wiringa, Steven C. Pieper, J. Carlson, and V. R. Pandharipande. Quantum Monte Carlo calculations of $A = 8$ nuclei. *Phys. Rev. C*, 62:014001, 2000.

[160] S. Pastore, S. C. Pieper, R. Schiavilla, and R. B. Wiringa. Quantum Monte Carlo calculations of electromagnetic moments and transitions in A$\leq$9 nuclei with meson-exchange currents derived from chiral effective field theory. *Phys. Rev. C*, 87:035503, 2013.

[161] J. Engel, S. Pittel, and P. Vogel. Nuclear physics of dark matter detection. *Int. J. Mod. Phys. E*, 01:1, 1992.

[162] P. Klos, J. Menéndez, D. Gazit, and A. Schwenk. Large-scale nuclear structure calculations for spin-dependent wimp scattering with chiral effective field theory currents. *Phys. Rev. D*, 88:083516, 2013.

[163] J. Suhonen. *From Nucleons to Nucleus. Concepts of Microscopic Nuclear Theory*. Springer, Berlin, 1st edition, 2007.

[164] J. M. Eisenberg, W. Greiner, and M. Hamermesh. Excitation mechanisms of the nucleus, nuclear theory series, vol. 2. *Physics Today*, 24:51, 1971.

[165] B. A. Brown and B. H. Wildenthal. Status of the nuclear shell model. *Annu. Rev. Nucl. and Part. Sci.*, 38:29, 1988.

[166] P. G. Thirolf, B. V. Pritychenko, B. A. Brown, P. D. Cottle, M. Chromik, T. Glasmacher, G. Hackman, R. W. Ibbotson, K. W. Kemper, T. Otsuka, L. A. Riley, and H. Scheit. Spectroscopy of the 2_1^+ state in ^{22}O and shell structure near the neutron drip line. *Phys. Lett. B*, 485:16, 2000.

[167] B. A. Brown and B. H. Wildenthal. Empirically optimum m1 operator for sd-shell nuclei. *Nucl. Phys. A*, 474:290, 1987.

[168] G. Martínez-Pinedo, A. Poves, E. Caurier, and A. P. Zuker. Effective g A in the pf shell. *Phys. Rev. C*, 53(6):R2602–R2605, 1996.

[169] B. A. Brown and B. H. Wildenthal. Corrections to the free-nucleon values of the single-particle matrix elements of the M 1 and Gamow-Teller operators, from a comparison of shell-model predictions with sd -shell data. *Phys. Rev. C*, 28(6):2397, 1983.

[170] A. Ekström, G. R. Jansen, K. A. Wendt, G. Hagen, T. Papenbrock, S. Bacca, B. Carlsson, and D. Gazit. Effects of three-nucleon forces and two-body currents on Gamow-Teller strengths. *Phys. Rev. Lett.*, 113(26):262504, 2014.

[171] G. F. Bertsch and I. Hamamoto. Gamow-teller strength at high excitations. *Phys. Rev. C*, 26:1323, 1982.

[172] I. S. Towner. Quenching of spin matrix elements in nuclei. *Phys. Rept.*, 155:263, 1987.

[173] E. Caurier, A. Poves, and A. P. Zuker. Missing and quenched gamow-teller strength. *Phys. Rev. Lett.*, 74:1517, 1995.

[174] T.-S. Park, H. Jung, and D.-P. Min. In-medium effective axial-vector coupling constant. *Phys. Lett. B*, 409:26, 1997.

[175] D. H. Gloeckner and R. D. Lawson. Spurious center-of-mass motion. *Phys. Lett. B*, 53(4):313–318, 1974.

[176] L. E. Marcucci, Muslema Pervin, Steven C. Pieper, R. Schiavilla, and R. B. Wiringa. Quantum Monte Carlo calculations of magnetic moments and $M1$ transitions in $A \leqslant 7$ nuclei including meson-exchange currents. *Phys. Rev. C*, 78:065501, 2008.

[177] A. Ekström, G. R. Jansen, K. A. Wendt, G. Hagen, T. Papenbrock, B. D. Carlsson, C. Forssén, M. Hjorth-Jensen, P. Navrátil, and W. Nazarewicz. Accurate nuclear radii and binding energies from a chiral interaction. *Phys. Rev. C*, 91(5):051301, 2015.

[178] Y. Kanada-En'yo and Y. Hidaka. Tetrahedral shape and surface density wave of ^{16}O caused by α-cluster correlations. *arXiv:1608.03642*, 2016.

[179] B. A. Brown and W. D. M. Rae. The shell-model code NuShellX@ MSU. *Nucl. Data Sheets*, 120:115, 2014.

[180] E. R. Anderson, S. K. Bogner, R. J. Furnstahl, and R. J. Perry. Operator evolution via the similarity renormalization group: The deuteron. *Phys. Rev. C*, 82:054001, 2010.

[181] M. D. Schuster, S. Quaglioni, C. W. Johnson, E. D. Jurgenson, and P. Navrátil. Operator evolution for ab initio theory of light nuclei. *Phys. Rev. C*, 90:011301, 2014.

[182] P. E. S. Wormer and J. Paldus. Angular momentum diagrams. *Adv. Quantum Chem.*, 51:59, 2006.

[183] D. A. Varshalovich, A. N. Moskalev, and V. K. Khersonskii. *Quantum theory of angular momentum*. World scientific, 1988.